Structure-property relationships in flow formed discontinuous fiber reinforced composites

Vlastimil Kunc

Dissertation submitted to the Faculty of the
Virginia Polytechnic Institute and State University
in partial fulfillment of the requirements for the degree of

Doctor of Philosophy
in
Engineering Mechanics

Scott W. Case, Chair
David A. Dillard
Romesh C. Batra
Mayuresh J. Patil
Raffaella De Vita

November 5, 2013
Blacksburg, Virginia

Keywords: Composites, Discontinuous Fiber Microstructure, Stiffness Tensor, Fiber Curvature

Copyright 2013 by Vlastimil Kunc

Structure-property relationships in flow formed discontinuous fiber reinforced composites

Vlastimil Kunc

Abstract

The research presented in this dissertation provides advances to the state of the art in the area of discontinuous fiber composites. The focus of this work is on stiffness prediction for materials containing curved fibers with quasi-random orientation in space. The dissertation contains five papers highlighting newly developed model formulation accounting for curved fibers, experimental techniques, and experimental results for comparison with model predictions.

Exploratory experiments with injection-molded samples suggested the presence of curved fibers. The effect of fiber curvature on composite stiffness had not been rigorously addressed prior to the developments detailed in this dissertation. A new definition of fiber configuration and configuration averaging allows us to calculate the fully anisotropic stiffness tensor for discontinuous fiber composites. The development of X-ray and optical based experimental techniques was also necessary to provide quantifiable data for model-experiment comparison. The experimental results are obtained using novel X-ray micro-tomography setup allowing observation of material microstructure under load. It is demonstrated that new model provides better match with experimental results when compared to theory relying on the assumption of straight fibers.

Acknowledgments

This dissertation represents a process that has changed me as an engineer and as a person. Throughout this process, I was inspired and guided by many outstanding individuals and supported by several organizations. It is impossible to acknowledge every person and to express enough gratitude without extending this lengthy process even further. I only make an attempt to list individuals with the most profound influence on this work and a large portion of my life.

I would like to thank Prof. Scott Case for his patient and enduring guidance. Scott gave me years of honest feedback, suggestions and help. I will never forget his kindness. I could always count on Srdjan Simunovic of Oak Ridge National Laboratory (ORNL) for a constructive feedback on my ideas and help with technical and funding obstacles, regardless of his busy schedule.

Prof. David Dillard recruited me to Virginia Tech during his sabbatical at ORNL, hence provided the impetus to this entire process. I would like to thank Prof. Romesh Batra, Prof. Mayuresh Patil and Prof. Raffaella De Vita for serving on my committee.

I would like to thank Dr. Martin Keller, Dr. Craig Blue, Dr. Lonnie Love, and Dr. Chad Duty for their help and insistence on timely completion of this work. I would like to thank Bob Norris for showing me how to work long hours in a challenging environment and Dr. Donald Erdman for giving me a chance in his laboratory many years ago.

The work of Prof. Charles Tucker and his students from University of Illinois provided an inspiration and a benchmark for my work. It has been a privilege to know Prof. Tucker personally and to have the opportunity to work with him on several projects related to this dissertation. I have been also fortunate to work along Dr. Nghiep Nguyen and Mark Smith of Pacific North National Laboratory, Dr. Peter Foss of General Motors and Dr. Michael Wyzgoski, all of whom have taught me something useful for this dissertation.

There are two people who I can't appreciate or acknowledge enough. Nobody taught me more than Dr. Gabriela Kuncova, my mother, and Dr. Pavel Kunc, my father.

Contents

1 Introduction 1
2 Discontinuous Fiber Reinforced Composites - Overview 1
2.1 Structure 2
2.2 Structure-Property Relations 5
2.3 Time Dependent Properties 7
2.4 Failure Modes 8
2.5 Application In Design 11
3 Stiffness Model Background 12
3.1 Introduction 12
3.2 Elasticity 12
3.3 Voigt and Kelvin Notation 14
3.3.1 Kelvin Notation [Kelvin 1856] 14
3.3.2 Voigt Notation [Voigt 1910] 15
3.4 Coordinate Transformations 17
3.4.1 Transformation in Kelvin Notation 18
3.4.2 Transformation in Voigt Notation 19
3.4.3 Euler Angles 20
3.4.4 Vector Rotation Using Euler Angles 24
3.4.5 Euler Angles from Vector Components 26
3.5 Kelvin Moduli and Eigen-States 27
3.6 Material Symmetry 29
3.7 Stiffness Tensor Decomposition 34
3.7.1 Decomposition of Stiffness Tensor for Transversely Isotropic Material 41
3.7.2 Decomposition of Stiffness Tensor for Orthotropic Material 44
3.8 Orientation Tensors and Stiffness of Straight Fiber 49
3.9 Transversely Isotropic Constants from Halpin-Tsai-Kardos Equations 53
4. Stiffness Model for Curved Fiber 57

4.1. Curved Fiber Model – Introduction 57
4.2. Configuration of a Single Curved Fiber 57
4.3. Configuration Distribution Function 61
4.4. Orthotropic Stiffness Tensor for Material with Fibers in Single Configuration 62
4.5. Configuration Averaging for Material with Arbitrary Fiber Configuration 64
4.6. Geometric Configuration Tensors 72
4.6.1. Fiber Orientation Tensors 73
4.6.2. Fiber Curvature Tensors 77
4.6.3. Mixed Tensor 81
4.7. Obtaining Material Parameters for Material in Single Configuration 84
5 Experimental Measurement of Fiber Architecture in Injection Molded Plaques 96
5.1 Introduction 96
5.2 Fiber Orientation Measurement 96
5.3 Fiber Length Measurement 107
6 Articles 113
6.1 The Stiffness Tensor for Composites with Curved Discontinuous Fibers Part 1: A Formulation 113
6.2 The Stiffness Tensor for Composite with Curved Discontinuous Fibers Part 2: Effect of Curvature, Representative Volume and Comparison with Experiment 132
6.3 Observation of Composite Materials Using Coupled Mechanical Testing and Computed Tomography 150
6.4 Tensile Specimen Design and Experimental Procedures for Characterizing Polymeric Composites Using X-Ray Based Micro-Tomography 171
6.5 On Fiber Curvature Measurements From Non-Elliptical Cross-Sections 186
7 Conclusions 207
7.1 Review 207
7.2 Development 207
7.3 Summary 207
7.4 Future Work 208
8 Appendixes 213
8.1 Appendix A: Curved Fiber Stiffness Model Verification Cases 213
8.1.1 Introduction 213

8.1.2 Halpin-Tsai-Kardos Equations 213
8.1.3 Material with Fibers in Single Configuration 214
8.1.4 Geometric Tensors for Material with fibers in Single Configuration 215
8.1.5 Parameters for a Material with Fibers in Single Configuration 220
8.1.6 Stiffness tensor for Material in Single Confguration 223
8.1.7 Material with Fibers in Finite Set of Configurations 226
8.1.8 Geometric Tensors for Material With Fibers in Finite Set of Configurations 227
8.1.9 Parameters for a Material with Fibers in Finite Set of Configurations 231
8.1.10 Stiffness Tensor for Material with Fibers in Finite Set of Configurations 232
8.1.11 Material with Continuous Distribution of Fiber Configurations 233
8.1.12 Constant δ Sequence Function 233
8.1.13 Geometric Tensors for Material with Fibers Represented by Constant δ Sequence Function 235
8.1.14 Parameters for Material with Fibers Represented by Constant δ Sequence Function 239
8.1.15 Stiffness Tensor for Material with Fibers Represented by Constant δ Sequence Function 240
8.2 Appendix B: Solutions for toroid cross-sections 243

List of Figures

Figure 2-1. X-ray of injection molded tensile bar..... 3
Figure 2-2. Polished cross-section of injection molded composite 3
Figure 2-3. X-ray computed tomography reconstruction for injection molded composite 4
Figure 2-4. Typical fiber length distributions for long fiber injection molded material..... 4
Figure 2-5. Creep and recovery response of injection molded 30%glass/Polypropylene material at room temperature. 8
Figure 2-6. Fracture surfaces of glass/PA6,6 injection molded material tested in tension..... 10
Figure 2-7. Scanning electron micrographs showing matrix residue on glass fibers after fracture of glass/PA6,6 injection molded material tested in tension. 10
Figure 3-1. Rotation Rijz by angle α 21
Figure 3-2. Rotation Rijy by angle β 22
Figure 3-3. Rotation Rijx by angle γ 23
Figure 3-4. Coordinate system and definition of θ,ϕ and orientation vector **p** 50
Figure 4-1. Straight cylindrical fiber with coordinate system **f = (p**,**q**,**s)** 58
Figure 4-2. Bent fiber with radius R 58
Figure 4-3. Limit case of straight fiber (Rmax=∞), with Euler angles α, β and coordinate system defined in Advani-Tucker [8] 60
Figure 4-4. Bent fiber with coordinate system **f** = (**p**,**q**,**s**), defined by Euler angles α,β,γ 61
Figure 4-5. Material with fibers in single configuration 63
Figure 4-6. Orientation vector p for a segment of bent fiber 85
Figure 5-1. Coordinate system and definition of θ,ϕ and orientation vector **p** 97
Figure 5-2. Typical digital image of polished and etched with white fibers and black matrix 100
Figure 5-3. Typical digital image of polished and etched with white fibers and black matrix 100
Figure 5-4. Digital image showing solid white fibers, with blask “shadows” indicating fiber ends extending above the etched surface 101
Figure 5-5. Digital image showing solid white fibers, with black “shadows” indicating fiber ends extending above the etched surface 101
Figure 5-6. Section coordinate systems hf and hc and global coordinate system e_1,e_2,e_3 102
Figure 5-7 Raw distribution of angle α for fibers measured in flow direction sample expressed in flow sample coordinate system 103
Figure 5-8. Raw distribution of angle β for fibers measured in flow direction sample expressed in flow sample coordinate system 103
Figure 5-9. Raw distribution of angle α for fibers measured in cross flow direction sample expressed in cross flow sample coordinate system 104
Figure 5-10. Raw distribution of angle β for fibers measured in cross flow direction sample expressed in cross flow sample coordinate system 104
Figure 5-11. Combined results for all measured fibers as a function of normalized thickness 106
Figure 5-12. Fiber orientation tensor component A_{11} for flow and cross flow sample 106

Figure 5-13. Fiber orientation tensor component A_{22} for flow and cross flow sample 107
Figure 5-14. Netrork of glass fibers after fully constrained pyrolysis 108
Figure 5-15. Network of carbon fibers after unconstrained pyrolysis 109
Figure 5-16. Isolated fibers with epoxy cylinder 109
Figure 5-17. Digital image of dispersed carbon fibers obtained with a scanner 110
Figure 5-18. Sampling region of diameter d with three fibers captured for experimental measurement and only two centroids within the sampling region 111
Figure 6-1. Injection molded composite containing glass fibers. Left: Polished cross-section - three cross-sections whose deviation from elliptical shape indicates fiber curvature are highlighted. Right: Entangled mass of curved fibers after matrix burn-off 115
Figure 6-2. Left: Straight cylindrical fiber with coordinate system **f** = (**p**,**q**,**s**) Right: Bent fiber with radius R 116
Figure 6-3. Curved fiber with coordinate system **f** = (**p**,**q**,**s**), defined by Euler angles α,β,γ ... 117
Figure 6-4. Material with fibers in single configuration 119
Figure 6-5. Orientation vector p for a segment of bent fiber 123
Figure 6-6.. Material constants as a function of curvature η for a material in with fibers single configuration having aspect ratio ξ=100 and constituent properties listed in Table 1 126
Figure 6-7 Engineering constants as a function of curvature η for a material in with fibers single configuration having aspect ratio ξ=100 and constituent properties listed in Table 1 127
Figure 6.2-1. Material constants for orthotropic material with fibers in single configuration and aspect ratio X=100 136
Figure 6.2-2. Young's moduli, shear Moduli and Poisson's ratios for orthotropic material with fibers in single configuration and aspect ratio X=100 137
Figure 6.2-3. Isotropic Young's moduli for 10 randomly generated ensembles of fibers with shape parameters X=100,H=π/4 141
Figure 6.2-4. Error err for material with perfectly random rotation of straight (x) and curved (o) fibers approximated by a finite set of randomly generated fibers N_f 142
Figure 6.2-5. Weighted experimentally measured fiber length distribution 143
Figure 6.2-6. Histogram of fiber radius measured using x-ray micro-tomography 144
Figure 6.2-7. Stress-strain curves from digital image correlation 145
Figure 6.2-8.. Predicted sample Young's moduli Ec and Es for curved fibers and straight fibers respectively 147
Figure 6.3-1. Schematic of fiber form within a specimen with continuous fiber tow loops 152
Figure 6.3-2. Schematic of fiber form within a specimen with interrupted fiber tow loops 152
Figure 6.3-3. Untested specimen, specimen with pulled out grip piece, specimen with gage length grip failure and initial specimen design 153
Figure 6.3-4. Cross-section of final design of the grip piece 153
Figure 6.3-5. Fiber form with cured epoxy maintaining the shape 154
Figure 6.3-6. Fiber form (right) was inserted in Teflon tube and bottom sealed with clay (middle) to produce a specimen (left) 154
Figure 6.3-7. Testing machine within x-ray micro-tomography unit 155

Figure 6.3-8. Horizontal wobble of alignment ball through 150 degrees of rotation 157
Figure 6.3-9. Vertical wobble of alignment ball through 150 degrees of rotation 157
Figure 6.3-10. X-ray image of fiber form with interrupted tow (CutLoop1) 158
Figure 6.3-11. X-ray of FullLoopMoldRel1 specimen showing observable gage length 160
Figure 6.3-12. Load-displacement curve for the entire test of FullLoopMoldRel1..... 160
Figure 6.3-13. Initial ten minutes of loading leading up to tomography imaging at approximately 29 lb 161
Figure 6.3-14. Relaxation of specimen during tomography imaging 161
Figure 6.3-15. Loading after tomography taken at 29 lb with extended observation at 42 lb and failure 162
Figure 6.3-16. Detail of x-ray image of sample before loading..... 162
Figure 6.3-17. Detail of x-ray image of sample carrying approximately 29 lb of load 163
Figure 6.3-18. Detail of tomography reconstruction at no load - horizontal slice of the loop 163
Figure 6.3-19. Detail of tomography reconstruction of sample subjected to load - horizontal slice of the loop..... 163
Figure 6.3-20. Vertical slice of tomography reconstruction at no load 164
Figure 6.3-21. Vertical slice of tomography reconstruction of specimen under load showing crack within the specimen not observable prior to loading 164
Figure 6.3-22. Rendering of fiber form at no load 165
Figure 6.3-23. Rendering of fiber form inside specimen subjected to load..... 165
Figure 6.3-24. Rendering of fiber form after failure..... 166
Figure 6.3-25. Rendering of fiber form and voids of specimen at no load, view from the top..... 166
Figure 6.3-26. Rendering of fiber form and voids of specimen subjected to load, view from the top..... 167
Figure 6.3-27. Rendering of fiber form and matrix after failure 167
Figure 6.3-28.Selection of slices from a sequence of reconstruction slices showing failed specimen 168
Figure 6.4-1. Miniature tensile sample 172
Figure 6.4-2. X-ray of failed miniature sample showing dark glass fibers and gray epoxy..... 173
Figure 6.4-3. Reconstructions of filaments within a sample 173
Figure 6.4-4. The miniature double dog-bone tensile specimen E2-1 175
Figure 6.4-5. Grips for extracted samples..... 175
Figure 6.4-6. Assembly of grip and sample (shown in red) for finite element analysis 176
Figure 6.4-7. Power law fit of results from creep experiments for glass/polypropylene injection molded material 177
Figure 6.4-8. Contour plots of Von-Mises stress within E2-1 with corresponding shoulder radius, maximum Von-Misses stress and grip displacement 178
Figure 6.4-9. D2-3 samples (from left to right) untested, failed in gage length, grip failure and pull-out 180
Figure 6.4-10. Mesh of axisymmetric model of D2-3 specimen 181
Figure 6.4-11. von Mises stress in a D2-3 specimen rod with perfect adhesion 182

Figure 6.4-12. Pull-out gap in D2-3 specimen with no adhesion between the specimen rod and grip subjected to tensile load 182
Figure 6.5-1. Standard assumption about fiber shape and definition or angles defining orientation vector **p** 188
Figure 6.5-2. Non-elliptical cross section formed by intersection of toroid with an arbitrary plane 188
Figure 6.5-3. Black elliptical cross section for $\alpha = 0$ and $\beta = 20°$, gray non-elliptical cross sections for $9.398\ 10^{-5} < \rho < 4.758\ 10^{-2}$and $0 \leq \gamma < 2\pi$ 193
Figure 6.5-4. Normalized distance between center of non-elliptical cross section q and center of best fit ellipse q_e for sections with $\beta = 20°$ 194
Figure 6.5-5. Difference between $\beta = 20°$ for non-elliptical cross sections and $\beta_e$of best fit ellipse 195
Figure 6.5-6. Area of non-elliptical cross sections for $\beta = 20°$ normalized with respect to the area of circular cross section for the same fiber 196
Figure 6.5-7. Normalized deviation $\bar{\delta}$ for fiber with $\beta = 20°$ 197
Figure 6.5-8. Normalized deviation δ_{max} for fiber with $\beta = 20°$ 197
Figure 6.5-9. Minimum of normalized $\bar{\delta}$ deviation as a function of curvature for a range of angles β 198
Figure 6.5-10. Minimum of normalized δ_{max} deviation as a function of curvature for a range of angles β..... 199
Figure 6.5-11. Minimum of normalized $\bar{\delta}$ deviation as a function of curvature for a range of angles β with dotted line indicating optical microscope spatial resolution at 1000x magnification 200
Figure 6.5-12. Minimum of normalized δ_{max} deviation as a function of curvature for a range of angles β with dotted line indicating optical microscope spatial resolution at 1000x magnification 201
Figure 6.5-13. Example fiber cross-sections showing white fibers, dark shadows identifying fiber end protruding above the etched surface and rough matrix surface obtained by etching 202
Figure 6.5-14. Illustration of automated shadow detection 203
Figure 6.5-15. Fibers (gray) with overlay of ellipse fit (points) and curved fiber fit (solid line) 203

List of Tables

Table 6.1-1 Fiber and matrix properties from reference [8] 125

Table 6.1-2 Orthotropic material constants for a material with curved fibers in single configuration given by shape parameters ξ=100 for straight fiber η=0 and curved fiber with $\eta=\pi/4$ 126

Table 6.1-3. Geometric configuration parameters for three fibers 128

Table 6.2-1. Constituent Material Properties 135

Table 6.2-2. Parameters k_1, k_2 and k_3 for orthotropic material with fibers in single configuration and aspect ratio X=100 135

Table 6.2-3. Orthotropic material constants for material in single configuration given by shape parameters X=100,H=π/4 and material with straight fibers X=100,H→0 136

Table 6.2-4. Tangential Young's moduli from digital image correlation of x-ray images of loaded samples 145

Table 6.2-5. Constituent Material Properties for Injection Molded PA6,6 Containing 50% Glass Fibers By Weight 146

Table 6.3-1. Test Matrix 159

Table 6.4-1. Results of static analysis for E2-1 specimen 179

Table 6.4-2. Results of visco-elastic analysis for E2-1 specimen..... 180

Table 6.4-3. Results of analysis for D2-3 specimen with perfect adhesion..... 182

Table 6.4-4. Results of analysis for D2-3 specimen with no adhesion 183

Table 6.5-1. Parameters for six fibers shown in Figure 6.5-15 204

Table 8.1-1. Fiber and matrix properties from [1] 213

Table 8.1-2. Composite engineering properties calculated from Halpin-Tsai Equations 213

Table 8.1-3. Composite material constants 214

1 Introduction

Micro-mechanical models for flow molded discontinuous fiber composites (DFCs) are used sparsely because predicted macro-scale results generally do not correspond well to real life observations. This shortcoming for DFCs is recognized by the industry and has led to funding of research which is largely responsible for the work performed to date as well as work proposed herein.

It is here suggested that the discrepancy in observed and predicted behavior is in part due to an inaccurate description of the physical microstructure as well as inappropriate models of behavior and interaction of fiber and matrix within DFC composites. Over the past several years, practical observations of DFCs response were made in the laboratory resulting in data useful for completion of this work as well as identification of gaps in current state of the art needed for better predictability of DFCs.

2 Discontinuous Fiber Reinforced Composites - Overview

Discontinuous fiber reinforced composites (DFCs) represent a large class of materials which is gaining popularity because of favorable tradeoffs between material properties, design options, and processing cost. DFCs are materials in which the fibers are not long enough to be considered continuous, but in which they are not short enough to be considered as just filler in a homogeneous material. The most commonly used fibers in DFCs are glass and carbon fibers, which come in tows of many (usually thousands) of fibers. The fibers (except for their lengths) are either identical or very similar to those used in continuous fiber composites. Fibers intended for DFCs are usually sized with a special sizing that not only promotes fiber-matrix adhesion, but also assists in wet-out and fiber dispersion during processing of DFCs. The surface of fibers is treated and sized while the fibers are still in the form of a continuous tow [1]. The discontinuity is introduced only subsequently to allow rapid pre-form production and molding of complex geometry; therefore fiber ends in DFCs are unsized and un-treated.

Fiber fragments with sized and unsized surface area of approximately the same order may be considered as fillers since there can be only limited load transfer between fibers via shearing of the matrix. Therefore, the order of L/D ratio of such fragments is 10^0, where L is the length of the fiber and D is the fiber diameter. These fragments can be oriented in any direction within a sample of realistic thickness. Fibers that can be assumed to remain approximately straight and that can be modeled approximately as straight cylinders are called short fibers. Typically, the L/D ratio of short fibers is 10^1-10^2. Short fiber length enables dispersion and prevents entanglement. Long fibers with an L/D ratio on the order of 10^3 typically remain undispersed in the form of bundles or form entangled mass of bent fibers. Fibers with L/D of 10^4 and greater are usually used in laminae, weaves, or braids because they do not lend themselves to flow forming processes.

Realistic flow-formed DFCs contain long and short fibers as well as fragments. The fiber length or L/D ratio can be used to describe a DFC prior to flow molding or in an average sense. However, capturing fiber length distribution (FLD) is necessary if one wishes to faithfully represent the microstructure of DFC. Theories and experiments typically focus on the two extremes of the fiber length spectrum discussed above (fillers and long fibers). Most composite materials literature focuses on continuous fibers with DFCs being treated as a special case [2]. The plastics literature treats the reinforcing fibers as a special class of fillers [3]. In either case, the finer details of DFCs are not considered.

2.1 Structure

It is common to distinguish among micro, meso, and macro scale features and properties in the study of composites. These scales can be neatly defined for laminated composites [4]. Geometry and properties of individual fibers embedded in matrix are considered on the micro-scale, laminae with distinct interlaminar boundaries are considered on the meso-scale, and laminates accounting for all of the above in an average sense can be analyzed and tested on the macro-scale.

The internal structure of DFCs is commonly referred to as microstructure even if the material features under consideration are clearly not on the microscopic scale. This is probably due to the fact that the definitions of scales may not always be apparent due to the nature of DFCs. The entangled and sometimes partially dispersed structure of flow molded DFCs makes separation of scales non-trivial. The fiber diameter is on the order of 10^{-5} m, with observable voids, impurities and possibly micro-cracks on the order of 10^{-6} m to 10^{-5} m. With typical part thickness of 2 to 6 mm, layer thicknesses with distinct preferential orientation is of 10^{-4} m to 10^{-3} m scale. Fiber length spans 10^{-5} m to 10^{-2} m scale, therefore single fiber can span several features in the meso-scale and in the case of un-dispersed fiber bundles, it can be considered macro-scale feature.

Figure 2-1 shows an X-ray image of a tensile bar. The bar is 12.7 mm (0.5 in.) wide and 3 mm (0.12 in.) thick, made of 40% of glass fibers by weight in polypropylene matrix. The darker regions in the image indicate the presence of glass fibers. Preferential local fiber orientation and imperfect dispersion of fibers stand out as the major features of the macro-scale structure.

Figure 2-2 shows polished cross-section of a typical long fiber reinforced injection molded thermoplastic plaque where cross-sections of cylindrical fibers appear as ellipses. It is apparent that there is preferred orientation as a function of position through the thickness. Three regions can be observed in injection molded composites: the skin, the shell, and the core. In addition to varying fiber orientation, the fiber length distribution can also vary as a function of position through the thickness. The structure of skin shell and core could be considered as meso-scale for DFCs. Boundaries between regions may be well defined as in the case of short fiber reinforced injection molded composite or they

may be difficult to define as in the case of compression molded composite reinforced with undispersed long fiber bundles.

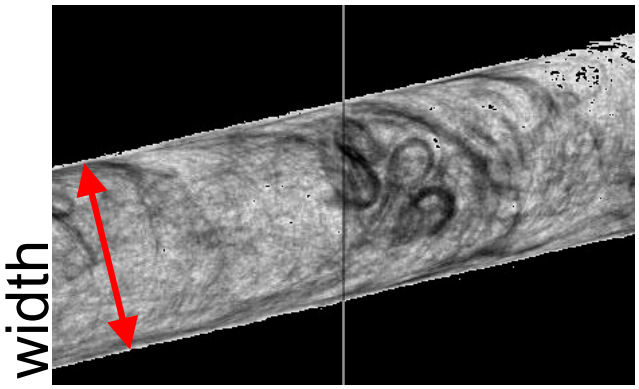

Figure 2-1. X-ray of injection molded tensile bar.

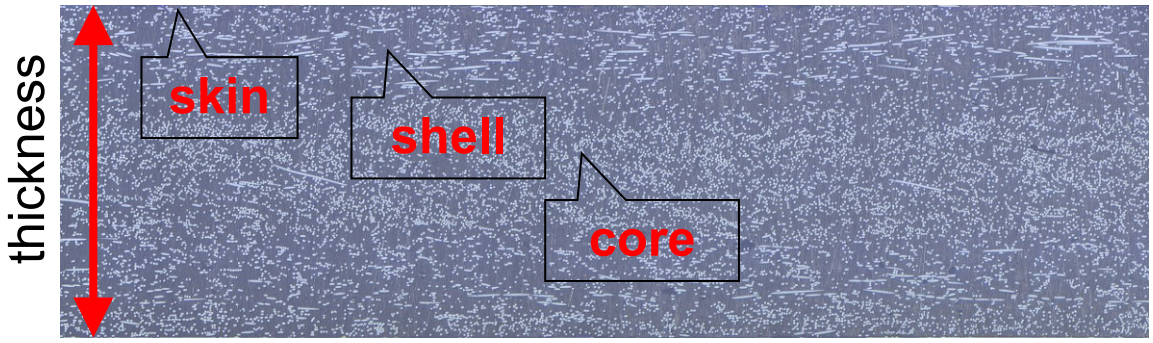

Figure 2-2. Polished cross-section of injection molded composite.

Closer examination of the figure reveals voids in the matrix, numerous non-elliptical fragments of fibers as well as impurities. A careful observer would also conclude that fiber diameters are not the same for every filament, rather, there is a narrow distribution of fiber diameters. Such features of the structure would belong to the micro-scale. Figure 2-3 shows X-ray computed tomography reconstruction of 2 mm x 2 mm injection molded sample. Just like in the previous figure, it is apparent that there is preferred orientation. However, the figure also shows more clearly that the filament lengths differ significantly and that longer filaments do not remain straight.

Because of the complex structure of DFCs, it is not always apparent how one should describe the microstructure of the material. Clearly, each fiber has certain length and it is positioned with respect to the part and other fibers. In the literature, the microstructure of

DFCs is described primarily by measures of fiber length and fiber orientation with fiber fraction assumed to be constant in a part.

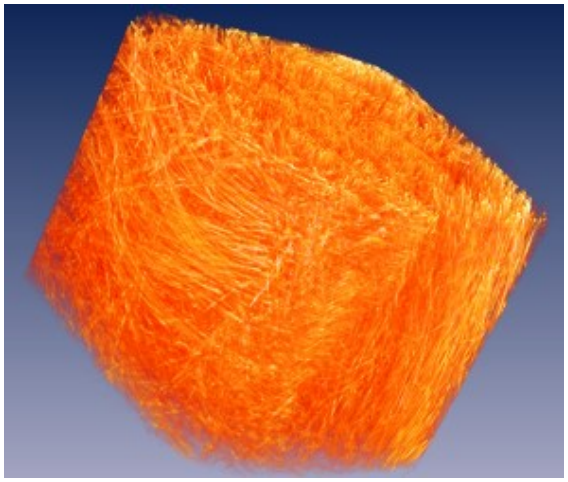

Figure 2-3. X-ray computed tomography reconstruction for injection molded composite.

The fiber length as defined by the length of a centerline of an individual fiber can be measured and the fiber length distribution (FLD) can be assigned in an average sense to a region within a part. Techniques for measurement and description of the FLD as well as results for various flow molded DFCs are discussed for example by Thomason [5, 6] and Kunc [7]. Figure 2-4 shows a typical FLD for injection-molded sample molded using long pellets.

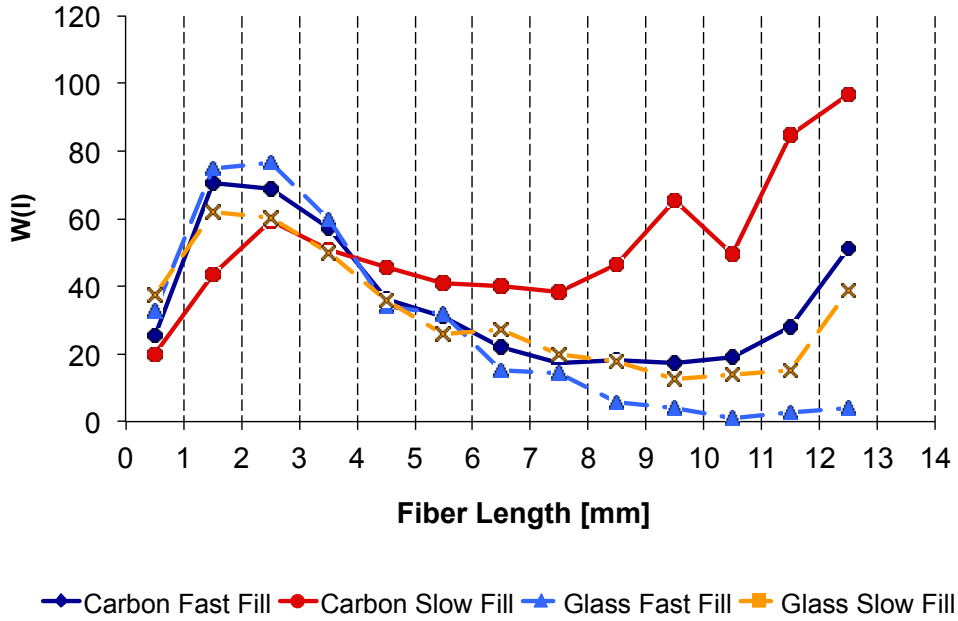

Figure 2-4. Typical FLD for long fiber injection molded material.

There are several difficulties with obtaining and interpreting FLD. Samples must contain enough fibers for the result to be statistically significant. Depending on individual company or institutional practice, researchers tend to select between several hundred to tens of thousands of fibers. Choices on either end of the spectrum are valid; however, the result and significance of FLD measurement will depend on the method of sample selection and its size. Samples containing tens of thousands of fibers may occupy a large enough region within a composite part that the FLD is an average of FLDs for multiple meso-scale layers. On the other hand, a sample of several hundred fibers may either be selected from a very small region within a part or it may be a subset selected from larger region. Selection of a very small sample would seem to be the best choice for characterizing microstructure at a point in the meso-scale. However, there is a danger of selecting a sample that is not representative especially in a material with incomplete fiber bundle dispersion. Measuring a subset of a larger sample is valid only if one applies appropriate randomization technique and avoids skewing results. In either case, the size of the region from which a sample was selected must be accounted for in a correction factor applied to the results to avoid bias towards long fibers [7], otherwise the FLD is skewed based depending on the size of the selected region. Considering fibers with single diameter, longer fibers occupy greater volume compared to short fiber. Therefore, it is more likely that longer fibers will be in the measurement sample. FLDs reported by various researchers will also differ depending on the treatment of very short fibers and fragments. The length of fragment with L/D=~1 may not be well defined and it is certainly difficult to measure. Measuring the volume or the weight of such fragment would solve the problem of defining its length. However, it is impractical to perform such measurements for many fragments. Neglecting fragments is as common as it is incorrect, and is detrimental to the accuracy of any analysis based on these results. Fragments must be accounted for if they constitute non-trivial portion of fiber fraction.

Advani and Tucker [8, 9] describe measures of fiber orientation and fiber orientation distribution (FOD). An optical technique for measuring FOD with this definition from a polished section of a sample is discussed by Clarke [10] and VerWeyst [11] and reconstruction of FOD from computed tomography is discussed by several researchers [12, 13]. Advani and Tucker's definition of fiber orientation was developed for short fiber injection molded composites and it may not appear to be completely suitable for a long curved fibers. Baird [14] discuses alternative measures such as fiber end to end orientation and average curvature, which would provide more faithful measure for entangled microstructure of long fibers within DFCs. However, definition and measurement techniques for fiber curvature are non-existent in literature dealing with DFCs.

2.2 Structure-Property Relations

In the eyes of a structural engineer, DFCs will be always inferior to continuous fiber reinforced composites which have greater stiffness, strength, fatigue resistance, etc. However, a process engineer may consider materials with fibers of any significant length expensive and difficult to work with, resulting in products with inconsistent dimensions,

material properties and surface appearance. Yet applications of DFCs are growing due to favorable balance among properties, manufacturing considerations, and cost for many products. DFCs can be found in nearly all types of products ranging from planes, cars, consumer and sporting goods and defense articles.

Linking property and structure of DFCs requires the use of micro-mechanics. Micro-mechanics solutions often rely on strict assumptions and provide varying degree of agreement with experimental results. Reputable textbooks urge caution and stress limitations of micromechanics [15, 16]. Composite properties are derived from the constituent properties and geometry. Unfortunately, the measurement of mechanical properties of constituents is difficult due to the scale at which tests have to be performed. It is usually not necessary to measure properties of common reinforcement fibers. Textbook/handbook values for glass fiber should be sufficiently accurate, while properties of carbon fiber have to be estimated for a given grade. There is no evidence that properties of glass or carbon fibers change due to molding; therefore, measurements for any given fiber type need only be performed once regardless of end composite system. Obtaining matrix properties within flow molded DFCs may be challenging because it is generally not possible to obtain plaques of neat matrix material with the same properties. Although the matrix material is generally assumed to be homogeneous and isotropic, the material usually possesses microstructure of its own with properties varying as a function of distance from the fiber based on the sizing applied to the fibers. This is especially true for flow-formed DFCs as significant amount of lubricant in sizing may be designed to disperse in the polymeric matrix. Crystallinity, crystallite orientation, and polymer chain structure is affected by the presence of fibers. Standard measures and techniques can be found for example in [17]. Using properties measured on neat resin plaque for prediction of composite properties usually does not work even for the simplest elastic modulus predictions. It is common practice to test composite properties of a particular composite system with well known microstructure, calibrate matrix properties for a given model, and subsequently use these properties for similar composite systems. This approach is practical and appears to provide reasonable predictions.

Understanding of load transfer in DFCs requires analysis of fiber loading, matrix loading, and load transfer between fibers through the matrix. The work of Cox, Rosen, and Batdorf [18-21] is most commonly cited in connection with loading along a fiber and load transfer between fibers. The Kelly-Tyson model [22] is most commonly used for prediction of strength for unidirectional composite.

Analytical property predictions accounting for fiber orientation can be achieved using methods based on the equivalent inclusion principle [23], average matrix strain [24] and orientation averaging [25, 26] models have shown accurate stiffness predictions for short fiber composites. More information on models relevant to short fiber composites can be found in a study performed by Tucker and Linang [27]. A significant body of work dealing with injection molded materials has been published by Thomason [28-33]. The issue of fiber curvature was addressed in [34] by using finite element unit cell approach as well as orientation averaging technique similar to the technique noted above [26].

These results are not validated because fiber curvature measurements do not exist at this time and the authors considered only fiber bundles.

2.3 Time Dependent Properties

The response of a typical polymeric material to external loading is the combined response of fluid and solid. The time-dependent response of glass and carbon fibers can be neglected when examining DFCs, therefore only response of the matrix will be considered. Viscoelastic response of DFCs is not the primary focus of this work, however viscoelastic response plays an important role in radiographic and tomography experiments.

Both linear and non-linear viscoelastic models can be applied to DFCs. A viscoelastic material is said to be linear if strain is proportional to stress at given time and if the Boltzman superposition principle applies. Linear viscoelasticity is generally applicable at low stress levels. Once a linear viscoelastic region is established by for example performing a set of creep and recovery experiments, an abstract model of the material can be developed using a set of springs and dashpots with various stiffness and viscosity coefficients.

At high stress levels, linear viscoelastic models do not provide an adequate representation of time dependent material response and non-linear viscoelastic models must be used. The most widely used non-linear model is that of Schapery [35]. This model contains total of six parameters which must be determined from experiments. It should be emphasized that these experiments must be carried out on the matrix material and that the uncertainty of actual material properties discussed earlier still applies.

Figure 2-5 shows typical creep and recovery response of DFC material. In this test a specimen is loaded to a given load level and this load level is held for a given period of time. The specimen elongates with time until the load is removed. When the load is removed, the specimen does not immediately return to its initial configuration, rather it gradually recovers.

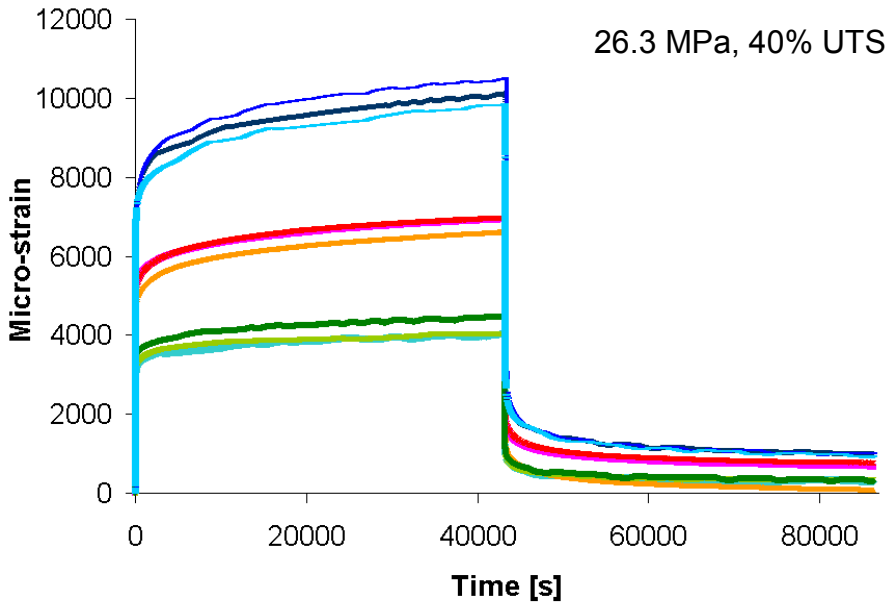

Figure 2-5. Creep and recovery response of injection molded 30%glass/Polypropylene material at room temperature.

The other type of experiment which can be used to establish time dependent behavior of materials is stress relaxation test. In this test, a sample is loaded to a given strain level and held there for an extended period of time. The measured load (hence stress in the sample) decreases as a function of time. This is the loading scenario of interest while one performs radiographic and tomography experiments of specimens subjected to load. In these experiments, it is necessary to pause loading for the duration of image acquisition. This may be several seconds for a single image or several hours for a tomography experiment. As indicated above, the state of samples will not remain the same over this period of time even if the overall displacement is held constant, which reduces the achievable resolution obtained from samples subjected to load.

2.4 Failure Modes

Predicting strength and energy released during failure is difficult for any material and it invariably leads to examination of the underlying material structure. Composite engineers emphasize the difficulty of predicting strength and progressive damage in composites by pointing out the relative simplicity of self-similar propagating crack in metals in comparison to all the possible failure modes that laminated composite can exhibit. This is only partially justified as intergranular cavitation, transgranular fracture, grain boundary sliding etc. are certainly considered in metal fracture [36]. The scale at which these processes occur (10^{-6} to 10^{-4} m) allows for the development of phenomenological laws that effectively average many events at a (macroscopic) point (continuum). This fact makes analysis of plasticity, damage and fracture in metal structures tractable. In composites, the in-plane and out-of plane failure modes [2] of fiber fracture, matrix

micro-cracking, fiber-matrix debonding, fiber pullout, matrix shear failure, micro-buckling, kinking, delamination etc. may be observed on scales spanning 10-6 to 10-2 m with multiple failure modes active at the same time. Statistical and fracture size effects should be considered in progressive failure analysis, leading to the application of non-local approaches [37]. The above mentioned complications contribute to the fact that even predicting failure in a well-defined laminated composite has not solved the problem [38].

The situation is even more complicated for DFCs. The uncertainty about actual material structure and inherent fiber waviness makes DFC damage mechanisms intricate [2]. There is, however, a clear correspondence between internal structure and damage of DFCs. Figure 2-6 shows fracture surfaces of glass/PA6,6 injection molded material that was tested in tension. The internal core-shell-skin structure shown in Figure 2-2 is clearly reflected on the fracture surface shown in Figure 2-6.

Fiber/matrix adhesion plays a prominent role in DFCs. Load transfer from fiber to fiber is often interrupted by the presence of fiber ends and curvature in fibers. It has been shown that that strength of thermoplastic DFC can be increased by more than 50% if proper coupling agent facilitates fiber matrix adhesion [39]. Figure 2-7 shows PA6,6 residue on glass fibers after quasi-static tensile tests indicating appropriate sizing and adequate fiber-matrix adhesion.

Two types of processes are usually considered when accounting for macroscopic non-linear response of DFCs which cannot be explained by viscoelastic response: plasticity and damage. Coupled continuum plasticity and damage models accounting for size effects have been developed studied for metals as well as composite materials [40]. An extensive summary of statistical, micromechanical, and continuum damage models is included in [41]. [42] applied coupled elasto-plastic and damage model to DFCs and concluded that inter-fiber interactions and multiple damage mechanisms must be reflected in a more representative model. [43] applied a very similar approach compared to experiments on injection molded material.

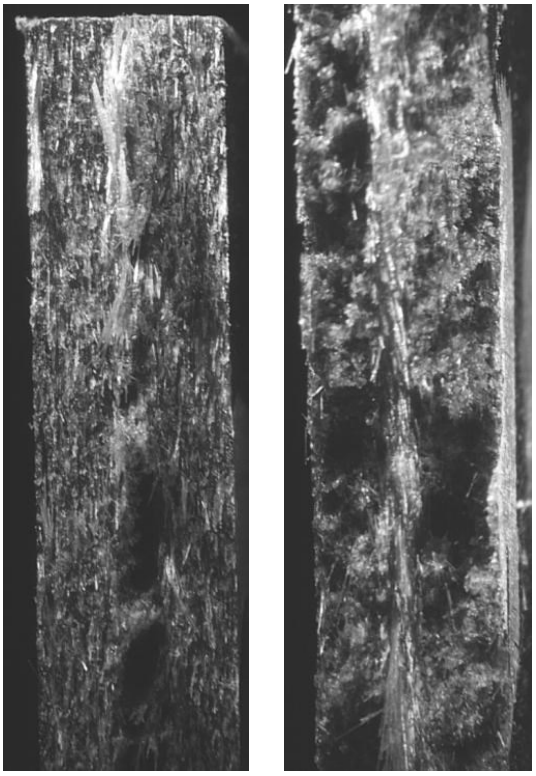

Figure 2-6. Fracture surfaces of glass/PA6,6 injection molded material tested in tension.

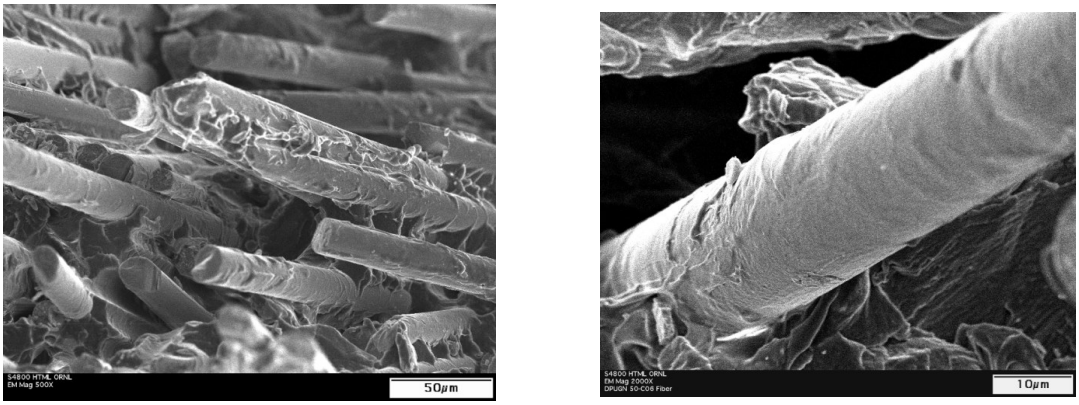

Figure 2-7. Scanning electron micrographs showing matrix residue on glass fibers after fracture of glass/PA6,6 injection molded material tested in tension.

Damage models can be linked to experimental results either through direct observation of damage or through global stress-strain response of a coupon specimen. Global response can be used to establish damage evolution for damage models through inverse or iterative techniques. However, this approach is justified only if the damage processes are well understood. This is not the case for DFCs at this time. Therefore, damage parameters are

simply parameters that are used to fit the behavior of a particular material system with some mechanistic or thermodynamic justification.

Damage in DFCs can be established through various destructive and non-destructive methods [44, 45]. The strain field can be established with photoelasticity, digital image correlation, Moire methods, holographic methods, and brittle coatings. Due to decreasing cost of digital cameras and computing power, 2D and 3D digital image correlation (DIC) techniques are becoming prevalent. An overview of the theory of operation and applications of DIC can be found in [46]. Non destructive evaluation (NDE) techniques are usually used to detect a flow or damage, but in some cases the same techniques can evaluate the type and size of damage. NDE techniques include radiography, ultrasonic methods, thermography and acoustic emission.

2.5 Application in design

There structural characteristics usually drive design: stiffness, strength and energy absorbed in catastrophic loading. From private discussion with practitioners, it appears that the driving factor in design with DFCs is overwhelmingly stiffness. Energy absorption is important in some automotive applications. It appears that once desired stiffness is achieved, strength requirements are automatically satisfied in most cases provided good design practices are obeyed. The focus of the subsequent discussion is therefore on improving prediction of stiffness tensor for DFCs.

1 Introduction 1
2 Discontinuous Fiber Reinforced Composites - Overview 1
2.1 STRUCTURE 2
2.2 STRUCTURE-PROPERTY RELATIONS 5
2.3 TIME DEPENDENT PROPERTIES 7
2.4 FAILURE MODES 8
2.5 APPLICATION IN DESIGN 11

1 Introduction

Micro-mechanical models for flow molded discontinuous fiber composites (DFCs) are used sparsely because predicted macro-scale results generally do not correspond well to real life observations. This shortcoming for DFCs is recognized by the industry and has led to funding of research which is largely responsible for the work performed to date as well as work proposed herein.

It is here suggested that the discrepancy in observed and predicted behavior is in part due to an inaccurate description of the physical microstructure as well as inappropriate models of behavior and interaction of fiber and matrix within DFC composites. Over the past several years, practical observations of DFCs response were made in the laboratory resulting in data useful for completion of this work as well as identification of gaps in current state of the art needed for better predictability of DFCs.

2 Discontinuous Fiber Reinforced Composites - Overview

Discontinuous fiber reinforced composites (DFCs) represent a large class of materials which is gaining popularity because of favorable tradeoffs between material properties, design options, and processing cost. DFCs are materials in which the fibers are not long enough to be considered continuous, but in which they are not short enough to be considered as just filler in a homogeneous material. The most commonly used fibers in DFCs are glass and carbon fibers, which come in tows of many (usually thousands) of fibers. The fibers (except for their lengths) are either identical or very similar to those used in continuous fiber composites. Fibers intended for DFCs are usually sized with a special sizing that not only promotes fiber-matrix adhesion, but also assists in wet-out and fiber dispersion during processing of DFCs. The surface of fibers is treated and sized while the fibers are still in the form of a continuous tow [1]. The discontinuity is introduced only subsequently to allow rapid pre-form production and molding of complex geometry; therefore fiber ends in DFCs are unsized and un-treated.

Fiber fragments with sized and unsized surface area of approximately the same order may be considered as fillers since there can be only limited load transfer between fibers via shearing of the matrix. Therefore, the order of L/D ratio of such fragments is 10^0, where L is the length of the fiber and D is the fiber diameter. These fragments can be oriented in any direction within a sample of realistic thickness. Fibers that can be assumed to remain approximately straight and that can be modeled approximately as straight cylinders are called short fibers. Typically, the L/D ratio of short fibers is 10^1-10^2. Short fiber length enables dispersion and prevents entanglement. Long fibers with an L/D ratio on the order of 10^3 typically remain undispersed in the form of bundles or form entangled mass of bent fibers. Fibers with L/D of 10^4 and greater are usually used in laminae, weaves, or braids because they do not lend themselves to flow forming processes.

Realistic flow-formed DFCs contain long and short fibers as well as fragments. The fiber length or L/D ratio can be used to describe a DFC prior to flow molding or in an average sense. However, capturing fiber length distribution (FLD) is necessary if one wishes to faithfully represent the microstructure of DFC. Theories and experiments typically focus on the two extremes of the fiber length spectrum discussed above (fillers and long fibers). Most composite materials literature focuses on continuous fibers with DFCs being treated as a special case [2]. The plastics literature treats the reinforcing fibers as a special class of fillers [3]. In either case, the finer details of DFCs are not considered.

2.1 Structure

It is common to distinguish among micro, meso, and macro scale features and properties in the study of composites. These scales can be neatly defined for laminated composites [4]. Geometry and properties of individual fibers embedded in matrix are considered on the micro-scale, laminae with distinct interlaminar boundaries are considered on the meso-scale, and laminates accounting for all of the above in an average sense can be analyzed and tested on the macro-scale.

The internal structure of DFCs is commonly referred to as microstructure even if the material features under consideration are clearly not on the microscopic scale. This is probably due to the fact that the definitions of scales may not always be apparent due to the nature of DFCs. The entangled and sometimes partially dispersed structure of flow molded DFCs makes separation of scales non-trivial. The fiber diameter is on the order of 10^{-5} m, with observable voids, impurities and possibly micro-cracks on the order of 10^{-6} m to 10^{-5} m. With typical part thickness of 2 to 6 mm, layer thicknesses with distinct preferential orientation is of 10^{-4} m to 10^{-3} m scale. Fiber length spans 10^{-5} m to 10^{-2} m scale, therefore single fiber can span several features in the meso-scale and in the case of un-dispersed fiber bundles, it can be considered macro-scale feature.

Figure 2-1 shows an X-ray image of a tensile bar. The bar is 12.7 mm (0.5 in.) wide and 3 mm (0.12 in.) thick, made of 40% of glass fibers by weight in polypropylene matrix. The darker regions in the image indicate the presence of glass fibers. Preferential local fiber orientation and imperfect dispersion of fibers stand out as the major features of the macro-scale structure.

Figure 2-2 shows polished cross-section of a typical long fiber reinforced injection molded thermoplastic plaque where cross-sections of cylindrical fibers appear as ellipses. It is apparent that there is preferred orientation as a function of position through the thickness. Three regions can be observed in injection molded composites: the skin, the shell, and the core. In addition to varying fiber orientation, the fiber length distribution can also vary as a function of position through the thickness. The structure of skin shell and core could be considered as meso-scale for DFCs. Boundaries between regions may be well defined as in the case of short fiber reinforced injection molded composite or they

may be difficult to define as in the case of compression molded composite reinforced with undispersed long fiber bundles.

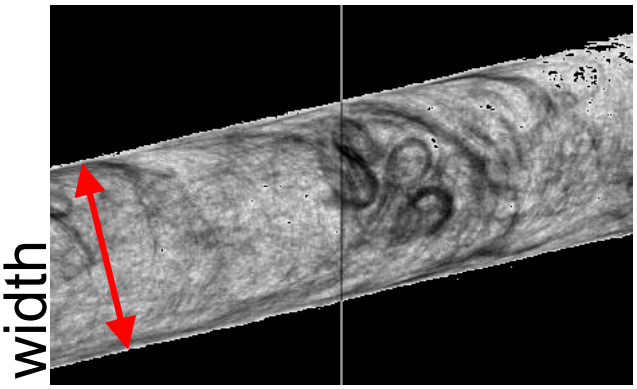

Figure 2-1. X-ray of injection molded tensile bar.

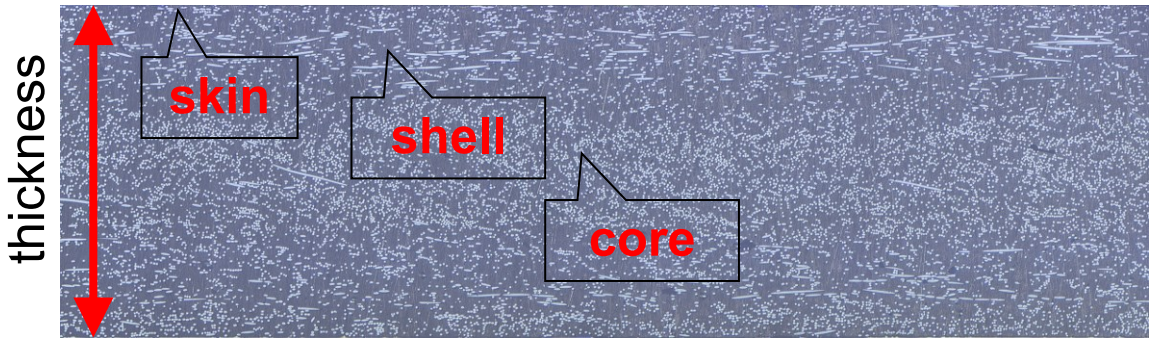

Figure 2-2. Polished cross-section of injection molded composite.

Closer examination of the figure reveals voids in the matrix, numerous non-elliptical fragments of fibers as well as impurities. A careful observer would also conclude that fiber diameters are not the same for every filament, rather, there is a narrow distribution of fiber diameters. Such features of the structure would belong to the micro-scale. Figure 2-3 shows X-ray computed tomography reconstruction of 2 mm x 2 mm injection molded sample. Just like in the previous figure, it is apparent that there is preferred orientation. However, the figure also shows more clearly that the filament lengths differ significantly and that longer filaments do not remain straight.

Because of the complex structure of DFCs, it is not always apparent how one should describe the microstructure of the material. Clearly, each fiber has certain length and it is positioned with respect to the part and other fibers. In the literature, the microstructure of

DFCs is described primarily by measures of fiber length and fiber orientation with fiber fraction assumed to be constant in a part.

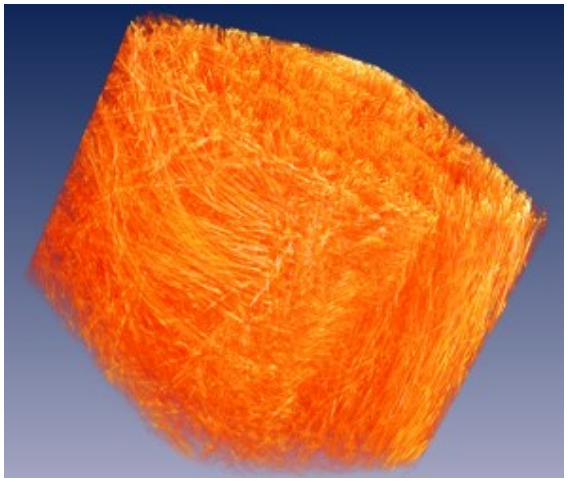

Figure 2-3. X-ray computed tomography reconstruction for injection molded composite.

The fiber length as defined by the length of a centerline of an individual fiber can be measured and the fiber length distribution (FLD) can be assigned in an average sense to a region within a part. Techniques for measurement and description of the FLD as well as results for various flow molded DFCs are discussed for example by Thomason [5, 6] and Kunc [7]. Figure 2-4 shows a typical FLD for injection-molded sample molded using long pellets.

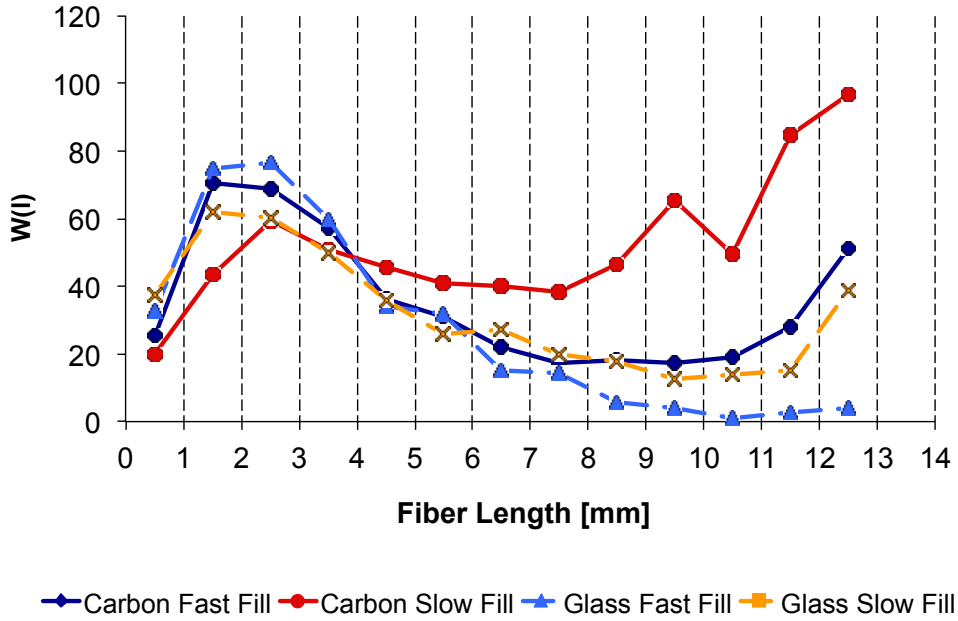

Figure 2-4. Typical FLD for long fiber injection molded material.

There are several difficulties with obtaining and interpreting FLD. Samples must contain enough fibers for the result to be statistically significant. Depending on individual company or institutional practice, researchers tend to select between several hundred to tens of thousands of fibers. Choices on either end of the spectrum are valid; however, the result and significance of FLD measurement will depend on the method of sample selection and its size. Samples containing tens of thousands of fibers may occupy a large enough region within a composite part that the FLD is an average of FLDs for multiple meso-scale layers. On the other hand, a sample of several hundred fibers may either be selected from a very small region within a part or it may be a subset selected from larger region. Selection of a very small sample would seem to be the best choice for characterizing microstructure at a point in the meso-scale. However, there is a danger of selecting a sample that is not representative especially in a material with incomplete fiber bundle dispersion. Measuring a subset of a larger sample is valid only if one applies appropriate randomization technique and avoids skewing results. In either case, the size of the region from which a sample was selected must be accounted for in a correction factor applied to the results to avoid bias towards long fibers [7], otherwise the FLD is skewed based depending on the size of the selected region. Considering fibers with single diameter, longer fibers occupy greater volume compared to short fiber. Therefore, it is more likely that longer fibers will be in the measurement sample. FLDs reported by various researchers will also differ depending on the treatment of very short fibers and fragments. The length of fragment with L/D=~1 may not be well defined and it is certainly difficult to measure. Measuring the volume or the weight of such fragment would solve the problem of defining its length. However, it is impractical to perform such measurements for many fragments. Neglecting fragments is as common as it is incorrect, and is detrimental to the accuracy of any analysis based on these results. Fragments must be accounted for if they constitute non-trivial portion of fiber fraction.

Advani and Tucker [8, 9] describe measures of fiber orientation and fiber orientation distribution (FOD). An optical technique for measuring FOD with this definition from a polished section of a sample is discussed by Clarke [10] and VerWeyst [11] and reconstruction of FOD from computed tomography is discussed by several researchers [12, 13]. Advani and Tucker's definition of fiber orientation was developed for short fiber injection molded composites and it may not appear to be completely suitable for a long curved fibers. Baird [14] discuses alternative measures such as fiber end to end orientation and average curvature, which would provide more faithful measure for entangled microstructure of long fibers within DFCs. However, definition and measurement techniques for fiber curvature are non-existent in literature dealing with DFCs.

2.2 Structure-Property Relations

In the eyes of a structural engineer, DFCs will be always inferior to continuous fiber reinforced composites which have greater stiffness, strength, fatigue resistance, etc. However, a process engineer may consider materials with fibers of any significant length expensive and difficult to work with, resulting in products with inconsistent dimensions,

material properties and surface appearance. Yet applications of DFCs are growing due to favorable balance among properties, manufacturing considerations, and cost for many products. DFCs can be found in nearly all types of products ranging from planes, cars, consumer and sporting goods and defense articles.

Linking property and structure of DFCs requires the use of micro-mechanics. Micro-mechanics solutions often rely on strict assumptions and provide varying degree of agreement with experimental results. Reputable textbooks urge caution and stress limitations of micromechanics [15, 16]. Composite properties are derived from the constituent properties and geometry. Unfortunately, the measurement of mechanical properties of constituents is difficult due to the scale at which tests have to be performed. It is usually not necessary to measure properties of common reinforcement fibers. Textbook/handbook values for glass fiber should be sufficiently accurate, while properties of carbon fiber have to be estimated for a given grade. There is no evidence that properties of glass or carbon fibers change due to molding; therefore, measurements for any given fiber type need only be performed once regardless of end composite system. Obtaining matrix properties within flow molded DFCs may be challenging because it is generally not possible to obtain plaques of neat matrix material with the same properties. Although the matrix material is generally assumed to be homogeneous and isotropic, the material usually possesses microstructure of its own with properties varying as a function of distance from the fiber based on the sizing applied to the fibers. This is especially true for flow-formed DFCs as significant amount of lubricant in sizing may be designed to disperse in the polymeric matrix. Crystallinity, crystallite orientation, and polymer chain structure is affected by the presence of fibers. Standard measures and techniques can be found for example in [17]. Using properties measured on neat resin plaque for prediction of composite properties usually does not work even for the simplest elastic modulus predictions. It is common practice to test composite properties of a particular composite system with well known microstructure, calibrate matrix properties for a given model, and subsequently use these properties for similar composite systems. This approach is practical and appears to provide reasonable predictions.

Understanding of load transfer in DFCs requires analysis of fiber loading, matrix loading, and load transfer between fibers through the matrix. The work of Cox, Rosen, and Batdorf [18-21] is most commonly cited in connection with loading along a fiber and load transfer between fibers. The Kelly-Tyson model [22] is most commonly used for prediction of strength for unidirectional composite.

Analytical property predictions accounting for fiber orientation can be achieved using methods based on the equivalent inclusion principle [23], average matrix strain [24] and orientation averaging [25, 26] models have shown accurate stiffness predictions for short fiber composites. More information on models relevant to short fiber composites can be found in a study performed by Tucker and Linang [27]. A significant body of work dealing with injection molded materials has been published by Thomason [28-33]. The issue of fiber curvature was addressed in [34] by using finite element unit cell approach as well as orientation averaging technique similar to the technique noted above [26].

These results are not validated because fiber curvature measurements do not exist at this time and the authors considered only fiber bundles.

2.3 Time Dependent Properties

The response of a typical polymeric material to external loading is the combined response of fluid and solid. The time-dependent response of glass and carbon fibers can be neglected when examining DFCs, therefore only response of the matrix will be considered. Viscoelastic response of DFCs is not the primary focus of this work, however viscoelastic response plays an important role in radiographic and tomography experiments.

Both linear and non-linear viscoelastic models can be applied to DFCs. A viscoelastic material is said to be linear if strain is proportional to stress at given time and if the Boltzman superposition principle applies. Linear viscoelasticity is generally applicable at low stress levels. Once a linear viscoelastic region is established by for example performing a set of creep and recovery experiments, an abstract model of the material can be developed using a set of springs and dashpots with various stiffness and viscosity coefficients.

At high stress levels, linear viscoelastic models do not provide an adequate representation of time dependent material response and non-linear viscoelastic models must be used. The most widely used non-linear model is that of Schapery [35]. This model contains total of six parameters which must be determined from experiments. It should be emphasized that these experiments must be carried out on the matrix material and that the uncertainty of actual material properties discussed earlier still applies.

Figure 2-5 shows typical creep and recovery response of DFC material. In this test a specimen is loaded to a given load level and this load level is held for a given period of time. The specimen elongates with time until the load is removed. When the load is removed, the specimen does not immediately return to its initial configuration, rather it gradually recovers.

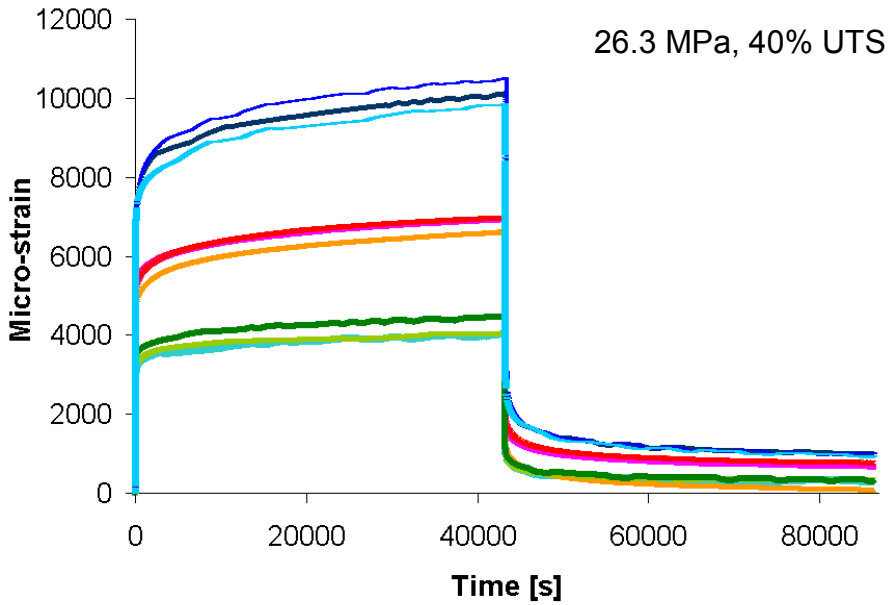

Figure 2-5. Creep and recovery response of injection molded 30%glass/Polypropylene material at room temperature.

The other type of experiment which can be used to establish time dependent behavior of materials is stress relaxation test. In this test, a sample is loaded to a given strain level and held there for an extended period of time. The measured load (hence stress in the sample) decreases as a function of time. This is the loading scenario of interest while one performs radiographic and tomography experiments of specimens subjected to load. In these experiments, it is necessary to pause loading for the duration of image acquisition. This may be several seconds for a single image or several hours for a tomography experiment. As indicated above, the state of samples will not remain the same over this period of time even if the overall displacement is held constant, which reduces the achievable resolution obtained from samples subjected to load.

2.4 Failure Modes

Predicting strength and energy released during failure is difficult for any material and it invariably leads to examination of the underlying material structure. Composite engineers emphasize the difficulty of predicting strength and progressive damage in composites by pointing out the relative simplicity of self-similar propagating crack in metals in comparison to all the possible failure modes that laminated composite can exhibit. This is only partially justified as intergranular cavitation, transgranular fracture, grain boundary sliding etc. are certainly considered in metal fracture [36]. The scale at which these processes occur (10^{-6} to 10^{-4} m) allows for the development of phenomenological laws that effectively average many events at a (macroscopic) point (continuum). This fact makes analysis of plasticity, damage and fracture in metal structures tractable. In composites, the in-plane and out-of plane failure modes [2] of fiber fracture, matrix

micro-cracking, fiber-matrix debonding, fiber pullout, matrix shear failure, micro-buckling, kinking, delamination etc. may be observed on scales spanning 10-6 to 10-2 m with multiple failure modes active at the same time. Statistical and fracture size effects should be considered in progressive failure analysis, leading to the application of non-local approaches [37]. The above mentioned complications contribute to the fact that even predicting failure in a well-defined laminated composite has not solved the problem [38].

The situation is even more complicated for DFCs. The uncertainty about actual material structure and inherent fiber waviness makes DFC damage mechanisms intricate [2]. There is, however, a clear correspondence between internal structure and damage of DFCs. Figure 2-6 shows fracture surfaces of glass/PA6,6 injection molded material that was tested in tension. The internal core-shell-skin structure shown in Figure 2-2 is clearly reflected on the fracture surface shown in Figure 2-6.

Fiber/matrix adhesion plays a prominent role in DFCs. Load transfer from fiber to fiber is often interrupted by the presence of fiber ends and curvature in fibers. It has been shown that that strength of thermoplastic DFC can be increased by more than 50% if proper coupling agent facilitates fiber matrix adhesion [39]. Figure 2-7 shows PA6,6 residue on glass fibers after quasi-static tensile tests indicating appropriate sizing and adequate fiber-matrix adhesion.

Two types of processes are usually considered when accounting for macroscopic non-linear response of DFCs which cannot be explained by viscoelastic response: plasticity and damage. Coupled continuum plasticity and damage models accounting for size effects have been developed studied for metals as well as composite materials [40]. An extensive summary of statistical, micromechanical, and continuum damage models is included in [41]. [42] applied coupled elasto-plastic and damage model to DFCs and concluded that inter-fiber interactions and multiple damage mechanisms must be reflected in a more representative model. [43] applied a very similar approach compared to experiments on injection molded material.

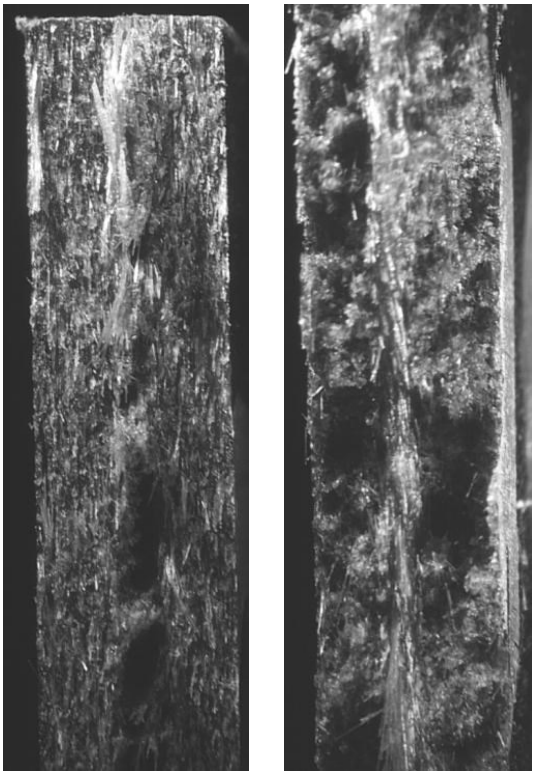

Figure 2-6. Fracture surfaces of glass/PA6,6 injection molded material tested in tension.

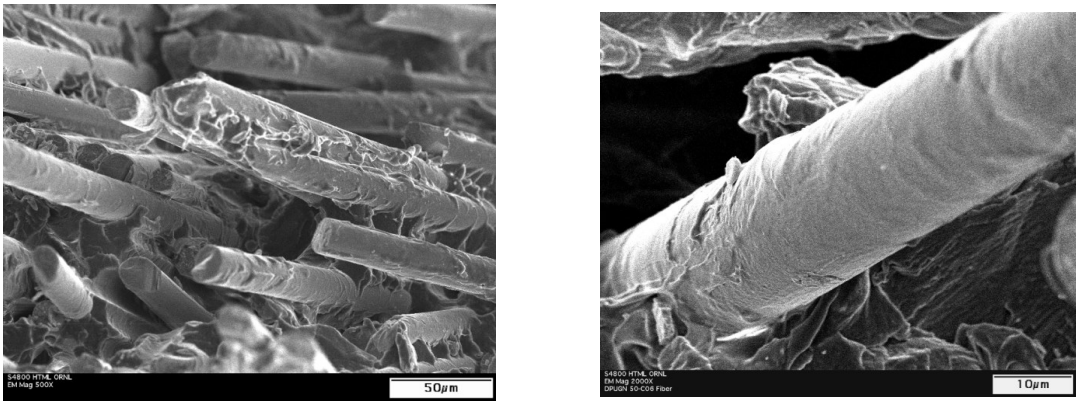

Figure 2-7. Scanning electron micrographs showing matrix residue on glass fibers after fracture of glass/PA6,6 injection molded material tested in tension.

Damage models can be linked to experimental results either through direct observation of damage or through global stress-strain response of a coupon specimen. Global response can be used to establish damage evolution for damage models through inverse or iterative techniques. However, this approach is justified only if the damage processes are well understood. This is not the case for DFCs at this time. Therefore, damage parameters are

simply parameters that are used to fit the behavior of a particular material system with some mechanistic or thermodynamic justification.

Damage in DFCs can be established through various destructive and non-destructive methods [44, 45]. The strain field can be established with photoelasticity, digital image correlation, Moire methods, holographic methods, and brittle coatings. Due to decreasing cost of digital cameras and computing power, 2D and 3D digital image correlation (DIC) techniques are becoming prevalent. An overview of the theory of operation and applications of DIC can be found in [46]. Non destructive evaluation (NDE) techniques are usually used to detect a flow or damage, but in some cases the same techniques can evaluate the type and size of damage. NDE techniques include radiography, ultrasonic methods, thermography and acoustic emission.

2.5 Application in design

There structural characteristics usually drive design: stiffness, strength and energy absorbed in catastrophic loading. From private discussion with practitioners, it appears that the driving factor in design with DFCs is overwhelmingly stiffness. Energy absorption is important in some automotive applications. It appears that once desired stiffness is achieved, strength requirements are automatically satisfied in most cases provided good design practices are obeyed. The focus of the subsequent discussion is therefore on improving prediction of stiffness tensor for DFCs.

3 Stiffness Model Background

3.1 Introduction

The objective of this section is to establish a stiffness model for composite material reinforced with discontinuous curved fibers. The theoretical background covering relevant concepts of linear elasticity is provided in the following section. Although the focus of this work is strictly on predicting and understanding of stiffness tensor under the assumption of linear elasticity, this work provides the foundation for more general models. Subsequent sections list assumptions used for derivation of a model suitable for stiffness prediction of flow molded composite.

3.2 Elasticity

We shall assume that composite material reinforced with discontinuous curved fibers is linear elastic. This assumption appears to be reasonable and valid for low strain levels. In rectangular Cartesian basis $\boldsymbol{e} = \{\boldsymbol{e}_1, \boldsymbol{e}_1, \boldsymbol{e}_1\}$ linear elastic problem is governed by the Equation of motion

$$\sigma_{ij,j} - \rho \frac{\partial^2 u_i}{\partial t^2} + F_i = 0 \qquad i,j = 1,2,3 \tag{3.2-1}$$

the generalized Hooke's law

$$\sigma_{ij} = C_{ijkl}\varepsilon_{kl} \qquad i,j,k,l = 1,2,3 \tag{3.2-2}$$

and the strain-displacement gradient formula

$$2\varepsilon_{kl} = u_{l,k} + u_{k,l} \qquad k,l = 1,2,3 \tag{3.2-3}$$

Throughout this document, a comma in the index notation denotes spatial derivative with respect to the marked subscript and Einstein summation convention applies over repeated indexes unless otherwise noted.

In Equations 3.2-1 through 3.2-3, u_i are the components of displacement, F_i are the components of body force, t is time, ρ is density of material, σ_{ij} and ε_{kl} are the components of second rank stress and strain tensors respectively. Our primary focus is on the establishment of components C_{ijkl} in Equation 3.2-2 which is a fourth order stiffness tensor in three dimensional space.

Equation 3.2-2 can be inverted

$$\varepsilon_{ij} = S_{ijkl}\sigma_{kl} \qquad i,j,k,l = 1,2,3 \tag{3.2-4}$$

where the compliance tensor S_{ijkl} is the inverse of the stiffness tensor

$$C_{ijpq}S_{pqkl} = I_{ijkl} \qquad i,j,k,l,p,q = 1,2,3 \tag{3.2-5}$$

The identity tensor can be defined as

$$I_{ijkl} = \delta_{ijkl} = \frac{1}{2}(\delta_{ik}\delta_{jl} + \delta_{il}\delta_{jk}) \qquad i,j,k,l = 1,2,3 \tag{3.2-6}$$

using Kronecker delta

$$\delta_{ij} = \begin{cases} 1 \; when \; i = j \\ 0 \; when \; i \neq j \end{cases} \tag{3.2-7}$$

We shall further assume that our material is hyperelastic with strain energy density

$$\Omega = \frac{1}{2}\sigma_{ij}\varepsilon_{ij} = \frac{1}{2}C_{ijkl}\varepsilon_{ij}\varepsilon_{kl} \qquad i,j,k,l = 1,2,3 \tag{3.2-8}$$

The stiffness tensor C_{ijkl} in Equation 3.2-2 has $3^4 = 81$ components. Since the stress tensor is symmetric [47] and symmetry of the strain tensor is apparent from Equation 3.2-3, the stiffness tensor has the following property

$$C_{ijkl} = C_{jikl} = C_{jilk} \qquad i,j,k,l = 1,2,3 \tag{3.2-9}$$

Furthermore, the existence of strain energy density defined in Equation 3.2-8 results in

$$C_{ijkl} = C_{jikl} = C_{klij} \qquad i,j,k,l = 1,2,3 \tag{3.2-10}$$

which reduces the number of distinct components in C_{ijkl} from 81 to 21.

3.3 Voigt and Kelvin Notation

The above noted symmetries allow transformation of σ_{ij} and ε_{ij} from second order three dimensional tensors to first order six dimensional tensors or 6x1 vectors and transformation of C_{ijkl} from fourth order three dimensional tensor to second order six dimensional tensor or 6x6 symmetric matrix.

Let us use the following scheme to assign the indexes during the transformation from three dimensional space to six dimensional space [48]:

$$\begin{gathered} 11 \rightarrow 1, 22 \rightarrow 2, 33 \rightarrow 3, 23 = 32 \rightarrow 4, \\ 31 = 13 \rightarrow 5, 12 = 21 \rightarrow 6 \end{gathered} \tag{3.3-1}$$

For the stiffness tensor, this scheme is used for the first two and last two subscripts.

There are two six dimensional representations of the stiffness tensor used in the literature, both of which preserve the strain energy density.

3.3.1 Kelvin Notation [Kelvin 1856]

Equation 3.3-2 shows the stiffness tensor represented in Kelvin notation.

$$\begin{bmatrix} \sigma_1 \\ \sigma_2 \\ \sigma_3 \\ \sigma_4 \\ \sigma_5 \\ \sigma_6 \end{bmatrix} = \begin{bmatrix} C_{11} & C_{12} & C_{13} & \sqrt{2}C_{14} & \sqrt{2}C_{15} & \sqrt{2}C_{16} \\ & C_{22} & C_{23} & \sqrt{2}C_{24} & \sqrt{2}C_{25} & \sqrt{2}C_{26} \\ & & C_{33} & \sqrt{2}C_{34} & \sqrt{2}C_{35} & \sqrt{2}C_{36} \\ & & & 2C_{44} & 2C_{45} & 2C_{46} \\ & sym. & & & 2C_{55} & 2C_{56} \\ & & & & & 2C_{66} \end{bmatrix} \begin{bmatrix} \varepsilon_1 \\ \varepsilon_2 \\ \varepsilon_3 \\ \varepsilon_4 \\ \varepsilon_5 \\ \varepsilon_6 \end{bmatrix} \tag{3.3-2}$$

With the stress and strain mapped as

$$\begin{bmatrix}\sigma_1\\ \sigma_2\\ \sigma_3\\ \sigma_4\\ \sigma_5\\ \sigma_6\end{bmatrix}=\begin{bmatrix}\sigma_{11}\\ \sigma_{22}\\ \sigma_{33}\\ \sqrt{2}\sigma_{23}\\ \sqrt{2}\sigma_{13}\\ \sqrt{2}\sigma_{12}\end{bmatrix},\qquad \begin{bmatrix}\varepsilon_1\\ \varepsilon_2\\ \varepsilon_3\\ \varepsilon_4\\ \varepsilon_5\\ \varepsilon_6\end{bmatrix}=\begin{bmatrix}\varepsilon_{11}\\ \varepsilon_{22}\\ \varepsilon_{33}\\ \sqrt{2}\varepsilon_{23}\\ \sqrt{2}\varepsilon_{13}\\ \sqrt{2}\varepsilon_{12}\end{bmatrix} \tag{3.3-3}$$

Again, we can use the following mapping rules to obtain Kelvin representation of the stiffness tensor:

$$p = i\,\delta_{ij} + \left(1-\delta_{ij}\right)(9-i-j) \qquad i,j = 1,2,3 \tag{3.3-4}$$

$$q = i\,\delta_{ij} + \left(1-\delta_{ij}\right)(9-i-j) \qquad i,j = 1,2,3 \tag{3.3-5}$$

$$\begin{gathered}\hat{\sigma}_p = \left(\delta_{ij} + \sqrt{2}\left(1-\delta_{ij}\right)\right)\sigma_{ij}, \hat{\varepsilon}_q = \left(\delta_{kl} + \sqrt{2}(1-\delta_{kl})\right)\varepsilon_{kl},\\ \hat{C}_{pq} = \left(\delta_{ij} + \sqrt{2}\left(1-\delta_{ij}\right)\right)\left(\delta_{kl} + \sqrt{2}(1-\delta_{kl})\right)C_{ijkl} \;\; i,j,k,l = 1,2,3\end{gathered} \tag{3.3-6}$$

This representation is used less commonly in the literature and hat accent will be used throughout this document for Kelvin notation. The disadvantage of this mapping is that the stiffness components are changed and the mapping does not appear natural. Stress and strain is treated identically and we can take advantage of tensor algebra.

3.3.2 Voigt Notation [Voigt 1910]

Equation 3.3-7 shows the stiffness tensor represented in Voigt notation.

$$\begin{bmatrix}\sigma_1\\ \sigma_2\\ \sigma_3\\ \sigma_4\\ \sigma_5\\ \sigma_6\end{bmatrix}=\begin{bmatrix}C_{11} & C_{12} & C_{13} & C_{14} & C_{15} & C_{16}\\ & C_{22} & C_{23} & C_{24} & C_{25} & C_{26}\\ & & C_{33} & C_{34} & C_{35} & C_{36}\\ & & & C_{44} & C_{45} & C_{46}\\ & sym. & & & C_{55} & C_{56}\\ & & & & & C_{66}\end{bmatrix}\begin{bmatrix}\varepsilon_1\\ \varepsilon_2\\ \varepsilon_3\\ \varepsilon_4\\ \varepsilon_5\\ \varepsilon_6\end{bmatrix} \tag{3.3-7}$$

With the stress and strain mapped as

$$\begin{bmatrix}\sigma_1\\ \sigma_2\\ \sigma_3\\ \sigma_4\\ \sigma_5\\ \sigma_6\end{bmatrix}=\begin{bmatrix}\sigma_{11}\\ \sigma_{22}\\ \sigma_{33}\\ \sigma_{23}\\ \sigma_{13}\\ \sigma_{12}\end{bmatrix},\qquad \begin{bmatrix}\varepsilon_1\\ \varepsilon_2\\ \varepsilon_3\\ \varepsilon_4\\ \varepsilon_5\\ \varepsilon_6\end{bmatrix}=\begin{bmatrix}\varepsilon_{11}\\ \varepsilon_{22}\\ \varepsilon_{33}\\ 2\varepsilon_{23}\\ 2\varepsilon_{13}\\ 2\varepsilon_{12}\end{bmatrix} \tag{3.3-8}$$

Alternatively, we can use the following mapping rules to obtain Voigt representation of the stiffness tensor:

$$p = i\,\delta_{ij} + \left(1-\delta_{ij}\right)(9-i-j) \qquad i,j = 1,2,3 \tag{3.3-9}$$

$$q = i\,\delta_{ij} + \left(1-\delta_{ij}\right)(9-i-j) \qquad i,j = 1,2,3 \tag{3.3-10}$$

$$\sigma_p = \sigma_{ij}, \varepsilon_q = (2-\delta_{kl})\varepsilon_{kl}, C_{pq} = C_{ijkl} \;\; i,j,k,l = 1,2,3 \tag{3.3-11}$$

This representation is the standard representation throughout engineering literature in the 20th century. The benefits include preservation of stress values, engineering representation of strains and preservation of stiffness components. However, stresses and strains are treated differently, the norms of the tensors are not preserved and the benefits of tensor algebra are lost.

As noted above, both representations preserve the strain energy density given in Equation 3.2-8

$$\Omega = \frac{1}{2}\sigma_p\varepsilon_q = \frac{1}{2}\hat{\sigma}_p\hat{\varepsilon}_q \qquad p,q = 1,2,\ldots,6 \tag{3.3-12}$$

Conversion between Voigt and Kelvin notations can be accomplished by using matrix notation and defining

$$\boldsymbol{\chi} = [1 \quad 1 \quad 1 \quad \sqrt{2} \quad \sqrt{2} \quad \sqrt{2}], \qquad \boldsymbol{\chi}^{-1} = \left[1 \quad 1 \quad 1 \quad \frac{1}{\sqrt{2}} \quad \frac{1}{\sqrt{2}} \quad \frac{1}{\sqrt{2}}\right] \tag{3.3-13}$$

then

$$\hat{\boldsymbol{\sigma}} = \boldsymbol{\sigma} * \boldsymbol{\chi},\ \hat{\boldsymbol{\varepsilon}} = \boldsymbol{\varepsilon} * \boldsymbol{\chi}^{-1}, \boldsymbol{\sigma} = \hat{\boldsymbol{\sigma}} * \boldsymbol{\chi}^{-1},\ \boldsymbol{\varepsilon} = \hat{\boldsymbol{\varepsilon}} * \boldsymbol{\chi} \tag{3.3-14}$$

Where * denotes component-wise multiplication. Using $\otimes$ for outer product, the conversion of stiffness components between the two notations can be accomplished using

$$\hat{\boldsymbol{C}} = (\boldsymbol{\chi} \otimes \boldsymbol{\chi}) * \boldsymbol{C} \tag{3.3-15}$$

It is important to realize that compliance matrix in Voigt notation should be obtained by inverting the stiffness matrix, because mapping noted above, along with Equation 3.3-15 applies only to the stiffness matrix.

3.4 Coordinate Transformations

Since stress, strain, stiffness and compliance in three-dimensional space and in Kelvin notation are tensors, we can use simple orthogonal transformation rules for representation of these quantities in different coordinate systems. Transformations for Voigt notation are also straightforward. Relevant expressions of this section are expressed both in index notation and matrix form to facilitate implementation into code.

First, we consider orthogonal transformation α_{ij} between **x** and **x'** system in three dimensions

$$x'_j = \alpha_{ij} x_i,\ \ \alpha_{ij}\alpha_{ik} = \delta_{jk} \qquad i, j, k = 1, 2, 3 \tag{3.4-1}$$

in matrix form

$$\boldsymbol{x}' = [\boldsymbol{\alpha}]^T \boldsymbol{x},\ \ [\boldsymbol{\alpha}]^T [\boldsymbol{\alpha}] = [\boldsymbol{I}] \tag{3.4-2}$$

with second order stress and strain tensors transformations

$$\varepsilon'_{kl} = \alpha_{ik}\alpha_{jl}\varepsilon_{ij}, \qquad \sigma'_{kl} = \alpha_{ik}\alpha_{jl}\sigma_{ij} \qquad i, j, k, l = 1, 2, 3 \tag{3.4-3}$$

in matrix form

$$[\boldsymbol{\varepsilon}'] = [\boldsymbol{\alpha}]^T[\boldsymbol{\varepsilon}][\boldsymbol{\alpha}], \qquad [\boldsymbol{\sigma}'] = [\boldsymbol{\alpha}]^T[\boldsymbol{\sigma}][\boldsymbol{\alpha}] \tag{3.4-4}$$

and fourth order stiffness and compliance tensors transformations

$$C'_{pqrs} = \alpha_{ip}\alpha_{iq}C_{ijkl}\alpha_{kr}\alpha_{ls}, \qquad S'_{pqrs} = \alpha_{ip}\alpha_{iq}S_{ijkl}\alpha_{kr}\alpha_{ls}\ i,j,k,l,p,q,r,s = 1,2,3 \tag{3.4-5}$$

Clearly, we cannot write Equation 3.4-5 in matrix form, because stiffness and compliance are fourth order tensors. Therefore we use six-dimensional representation of these quantities along with corresponding forms of coordinate transformations.

3.4.1 Transformation in Kelvin Notation

Following Annin [49], we can use orthogonal matrix in the following form

$$\hat{\alpha}_{ij} = \begin{bmatrix} \alpha_{11}^2 & \alpha_{12}^2 & \alpha_{13}^2 & \sqrt{2}\alpha_{12}\alpha_{13} & \sqrt{2}\alpha_{11}\alpha_{13} & \sqrt{2}\alpha_{11}\alpha_{12} \\ \alpha_{21}^2 & \alpha_{22}^2 & \alpha_{23}^2 & \sqrt{2}\alpha_{22}\alpha_{23} & \sqrt{2}\alpha_{21}\alpha_{23} & \sqrt{2}\alpha_{21}\alpha_{22} \\ \alpha_{31}^2 & \alpha_{32}^2 & \alpha_{33}^2 & \sqrt{2}\alpha_{32}\alpha_{33} & \sqrt{2}\alpha_{31}\alpha_{33} & \sqrt{2}\alpha_{31}\alpha_{32} \\ \sqrt{2}\alpha_{21}\alpha_{31} & \sqrt{2}\alpha_{22}\alpha_{32} & \sqrt{2}\alpha_{23}\alpha_{33} & \alpha_{22}\alpha_{33} + \alpha_{23}\alpha_{32} & \alpha_{21}\alpha_{33} + \alpha_{23}\alpha_{31} & \alpha_{21}\alpha_{32} + \alpha_{22}\alpha_{31} \\ \sqrt{2}\alpha_{11}\alpha_{31} & \sqrt{2}\alpha_{12}\alpha_{32} & \sqrt{2}\alpha_{13}\alpha_{33} & \alpha_{12}\alpha_{33} + \alpha_{13}\alpha_{32} & \alpha_{11}\alpha_{33} + \alpha_{13}\alpha_{31} & \alpha_{11}\alpha_{32} + \alpha_{12}\alpha_{31} \\ \sqrt{2}\alpha_{11}\alpha_{21} & \sqrt{2}\alpha_{12}\alpha_{22} & \sqrt{2}\alpha_{13}\alpha_{23} & \alpha_{12}\alpha_{23} + \alpha_{13}\alpha_{22} & \alpha_{11}\alpha_{23} + \alpha_{13}\alpha_{21} & \alpha_{11}\alpha_{22} + \alpha_{12}\alpha_{21} \end{bmatrix} \tag{3.4-6}$$

to transform first order stress and strain tensors in Kelvin notation

$$\hat{\varepsilon}'_i = \hat{\alpha}_{ki}\hat{\varepsilon}_k, \qquad \hat{\sigma}'_i = \hat{\alpha}_{ki}\hat{\sigma}_k \qquad i,j,k = 1,2,\ldots,6 \tag{3.4-7}$$

in matrix form with stress and strain being vectors

$$\hat{\boldsymbol{\varepsilon}}' = [\hat{\boldsymbol{\alpha}}]^T\hat{\boldsymbol{\varepsilon}}, \qquad \hat{\boldsymbol{\sigma}}' = [\hat{\boldsymbol{\alpha}}]^T\hat{\boldsymbol{\sigma}} \tag{3.4-8}$$

and fourth order stiffness and compliance tensors in six dimensional space

$$\hat{C}'_{ij} = \hat{\alpha}_{si}\hat{C}_{sk}\hat{\alpha}_{kj}, \qquad \hat{S}'_{ij} = \hat{\alpha}_{si}\hat{S}_{sk}\hat{\alpha}_{kj} \qquad i,j,s,k = 1,2,\ldots,6 \tag{3.4-9}$$

which is now written in matrix form.

3.4.2 Transformation in Voigt Notation

In Voigt notation, we will use matrix notation and define transformation matrix $[\alpha_{(\sigma)}]$

$$[\alpha_{(\sigma)ij}] = \begin{bmatrix} \alpha_{11}^2 & \alpha_{12}^2 & \alpha_{13}^2 & 2\,\alpha_{12}\alpha_{13} & 2\alpha_{11}\alpha_{13} & 2\alpha_{11}\alpha_{12} \\ \alpha_{21}^2 & \alpha_{22}^2 & \alpha_{23}^2 & 2\alpha_{22}\alpha_{23} & 2\alpha_{21}\alpha_{23} & 2\alpha_{21}\alpha_{22} \\ \alpha_{31}^2 & \alpha_{32}^2 & \alpha_{33}^2 & 2\alpha_{32}\alpha_{33} & 2\alpha_{31}\alpha_{33} & 2\alpha_{31}\alpha_{32} \\ \alpha_{21}\alpha_{31} & \alpha_{22}\alpha_{32} & \alpha_{23}\alpha_{33} & (\alpha_{22}\alpha_{33} + \alpha_{23}\alpha_{32}) & (\alpha_{21}\alpha_{33} + \alpha_{23}\alpha_{31}) & (\alpha_{21}\alpha_{32} + \alpha_{22}\alpha_{31}) \\ \alpha_{11}\alpha_{31} & \alpha_{12}\alpha_{32} & \alpha_{13}\alpha_{33} & (\alpha_{12}\alpha_{33} + \alpha_{13}\alpha_{32}) & (\alpha_{11}\alpha_{33} + \alpha_{13}\alpha_{31}) & (\alpha_{11}\alpha_{32} + \alpha_{12}\alpha_{31}) \\ \alpha_{11}\alpha_{21} & \alpha_{12}\alpha_{22} & \alpha_{13}\alpha_{23} & (\alpha_{12}\alpha_{23} + \alpha_{13}\alpha_{22}) & (\alpha_{11}\alpha_{23} + \alpha_{13}\alpha_{21}) & (\alpha_{11}\alpha_{22} + \alpha_{12}\alpha_{21}) \end{bmatrix} \tag{3.4-10}$$

Which transforms stress between **x** and **x'** system

$$[\sigma'] = [\alpha_{(\sigma)ij}][\sigma] \tag{3.4-11}$$

Following the path set out by Reuter [50], we define matrix [M]

$$[\alpha_{(\sigma)}] = \begin{bmatrix} 1 & 0 & 0 & 0 & 0 & 0 \\ 0 & 1 & 0 & 0 & 0 & 0 \\ 0 & 0 & 1 & 0 & 0 & 0 \\ 0 & 0 & 0 & 2 & 0 & 0 \\ 0 & 0 & 0 & 0 & 2 & 0 \\ 0 & 0 & 0 & 0 & 0 & 2 \end{bmatrix} \tag{3.4-12}$$

and note that the transformation for strain has the following form

$$[\varepsilon'] = [M]\left[\alpha_{(\sigma)}\right][\mathrm{M}]^{-1}[\varepsilon] = \left[\alpha_{(\varepsilon)}\right][\varepsilon] \tag{3.4-13}$$

where

$$[\alpha_{(\varepsilon)}] = \begin{bmatrix} \alpha_{11}^2 & \alpha_{12}^2 & \alpha_{13}^2 & \alpha_{12}\alpha_{13} & \alpha_{11}\alpha_{13} & \alpha_{11}\alpha_{12} \\ \alpha_{21}^2 & \alpha_{22}^2 & \alpha_{23}^2 & \alpha_{22}\alpha_{23} & \alpha_{21}\alpha_{23} & \alpha_{21}\alpha_{22} \\ \alpha_{31}^2 & \alpha_{32}^2 & \alpha_{33}^2 & \alpha_{32}\alpha_{33} & \alpha_{31}\alpha_{33} & \alpha_{31}\alpha_{32} \\ 2\alpha_{21}\alpha_{31} & 2\alpha_{22}\alpha_{32} & 2\alpha_{23}\alpha_{33} & (\alpha_{22}\alpha_{33}+\alpha_{23}\alpha_{32}) & (\alpha_{21}\alpha_{33}+\alpha_{23}\alpha_{31}) & (\alpha_{21}\alpha_{32}+\alpha_{22}\alpha_{31}) \\ 2\alpha_{11}\alpha_{31} & 2\alpha_{12}\alpha_{32} & 2\alpha_{13}\alpha_{33} & (\alpha_{12}\alpha_{33}+\alpha_{13}\alpha_{32}) & (\alpha_{11}\alpha_{33}+\alpha_{13}\alpha_{31}) & (\alpha_{11}\alpha_{32}+\alpha_{12}\alpha_{31}) \\ 2\alpha_{11}\alpha_{21} & 2\alpha_{12}\alpha_{22} & 2\alpha_{13}\alpha_{23} & (\alpha_{12}\alpha_{23}+\alpha_{13}\alpha_{22}) & (\alpha_{11}\alpha_{23}+\alpha_{13}\alpha_{21}) & (\alpha_{11}\alpha_{22}+\alpha_{12}\alpha_{21}) \end{bmatrix} \tag{3.4-14}$$

Noting that $\left[\alpha_{(\sigma)}\right]^{-1} = \left[\alpha_{(\varepsilon)}\right]^T$, we can write transformation for stiffness tensor in Voigt notation

$$[C'] = \left[\alpha_{(\varepsilon)}\right]^T [C]\left[\alpha_{(\varepsilon)}\right] \tag{3.4-15}$$

and for compliance

$$[S'] = \left[\alpha_{(\sigma)}\right]^T [S]\left[\alpha_{(\sigma)}\right] \tag{3.4-16}$$

Since arbitrary orientation of material with respect to laboratory system does not change characteristics of the material, we can choose three free parameters of α_{ij} and reduce the number of independent components of the stiffness tensor from 21 to 18. For example, one could use Euler angles as the three parameters for successive rotations.

3.4.3 Euler Angles

In view of latter sections, we use three Euler angles α,β,γ as the three parameters for successive rotations and we also express relevant relations in terms of alternate set of parameters, where

$$\phi = \alpha \tag{3.4-17}$$

$$\theta = \frac{\pi}{2} - \beta \tag{3.4-18}$$

$$\gamma = \gamma \tag{3.4-19}$$

We describe arbitrary orientation of a Cartesian coordinate system **x'''** with respect to laboratory Cartesian coordinate system **x** = (x_1,x_2,x_3) as the following sequence of rotations:

1. Rotation of around x_3 in mathematically positive sense by angle α (Figure 3-1).

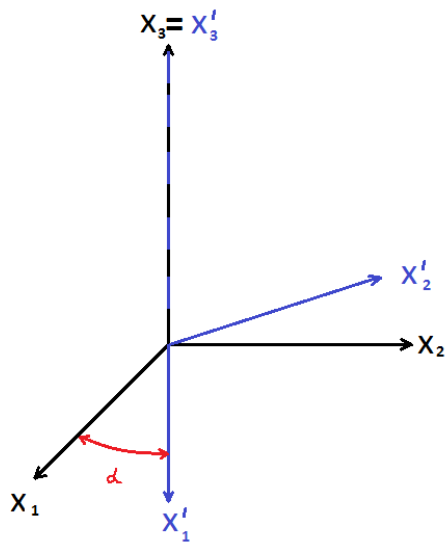

Figure 3-1. Rotation R_{ij}^{z} by angle α.

This rotation is represented by

$$x_j' = R_{ij}^{z} x_i, \qquad R_{ij}^{z} = \begin{bmatrix} \cos\alpha & \sin\alpha & 0 \\ -\sin\alpha & \cos\alpha & 0 \\ 0 & 0 & 1 \end{bmatrix} = \begin{bmatrix} \cos\phi & \sin\phi & 0 \\ -\sin\phi & \cos\phi & 0 \\ 0 & 0 & 1 \end{bmatrix} \tag{3.4-20}$$

In matrix notation

$$\boldsymbol{x}' = [\boldsymbol{R}^{\boldsymbol{z}}]^T \boldsymbol{x} \tag{3.4-21}$$

2. Rotation of around x_2' in mathematically positive sense by angle β (Figure 3-2).

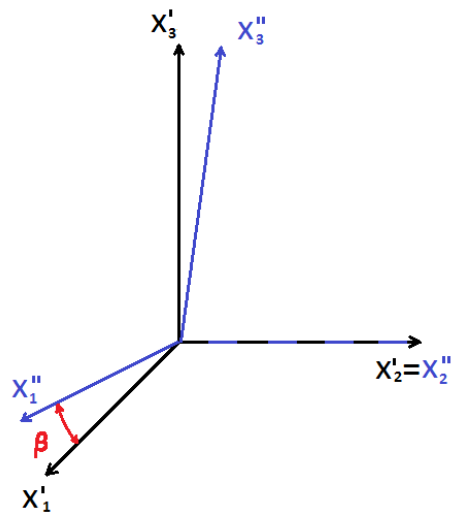

Figure 3-2. Rotation R_{ij}^{y} by angle β.

This rotation is represented by

$$x_k'' = R_{jk}^{y} x_j', \qquad R_{jk}^{y} = \begin{bmatrix} \cos\beta & 0 & \sin\beta \\ 0 & 1 & 0 \\ -\sin\beta & 0 & \cos\beta \end{bmatrix} = \begin{bmatrix} \sin\theta & 0 & \cos\theta \\ 0 & 1 & 0 \\ -\cos\theta & 0 & \sin\theta \end{bmatrix} \tag{3.4-22}$$

in matrix notation

$$\boldsymbol{x}'' = [\boldsymbol{R}^{\boldsymbol{y}}]^T \boldsymbol{x}' \tag{3.4-23}$$

3. Rotation of around x_1'' in mathematically positive sense by angle γ.

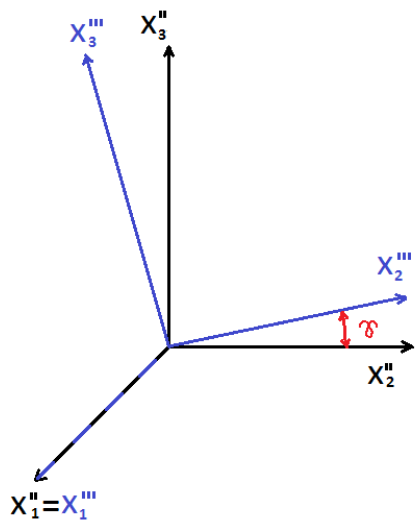

Figure 3-3. Rotation R_{ij}^{x} by angle γ.

This rotation is represented by

$$x_l''' = R_{kl}^{x} x_k'', \qquad R_{kl}^{x} = \begin{bmatrix} 1 & 0 & 0 \\ 0 & \cos\gamma & \sin\gamma \\ 0 & -\sin\gamma & \cos\gamma \end{bmatrix} \tag{3.4-24}$$

in matrix notation

$$\boldsymbol{x}''' = [\boldsymbol{R}^{x}]^{T} \boldsymbol{x}'' \tag{3.4-25}$$

The total rotation can be described as

$$x_l''' = R_{il}^{xyz} x_i = R_{kl}^{x} R_{jk}^{y} R_{ij}^{z} x_i, \qquad i, j, k, l = 1, 2, 3 \tag{3.4-26}$$

where

$$R_{il}^{xyz}$$

$$= \begin{bmatrix} \cos\alpha\cos\beta & \cos\beta\sin\alpha & \sin\beta \\ -\cos\gamma\sin\alpha - \cos\alpha\sin\beta\sin\gamma & \cos\alpha\cos\gamma - \sin\alpha\sin\beta\sin\gamma & \cos\beta\sin\gamma \\ -\cos\alpha\cos\gamma\sin\beta + \sin\alpha\sin\gamma & -\cos\gamma\sin\alpha\sin\beta - \cos\alpha\sin\gamma & \cos\beta\cos\gamma \end{bmatrix}$$

$$= \begin{bmatrix} \cos\alpha\sin\theta & \sin\theta\sin\alpha & \cos\theta \\ -\cos\gamma\sin\alpha - \cos\alpha\cos\theta\sin\gamma & \cos\alpha\cos\gamma - \sin\alpha\cos\theta\sin\gamma & \sin\theta\sin\gamma \\ -\cos\alpha\cos\gamma\cos\theta + \sin\alpha\sin\gamma & -\cos\gamma\sin\alpha\cos\theta - \cos\alpha\sin\gamma & \sin\theta\cos\gamma \end{bmatrix} \quad (3.4\text{-}27)$$

Equation 3.4-27 can be written in matrix notation as

$$\boldsymbol{x}''' = [\boldsymbol{R}^{xyz}]^T\boldsymbol{x} = [\boldsymbol{R}^{x}]^T[\boldsymbol{R}^{y}]^T[\boldsymbol{R}^{z}]^T\boldsymbol{x} = [[\boldsymbol{R}^{z}][\boldsymbol{R}^{y}][\boldsymbol{R}^{x}]]^T\boldsymbol{x} \quad (3.4\text{-}28)$$

Transformation matrix for a 6 dimensional space can be constructed with components of R_{ij}^{xyz} using Equation 3.4-10 or Equation 3.4-14. It is easy to verify that these transformations are orthogonal

$$R_{ij}^{x}R_{ik}^{x} = R_{ij}^{y}R_{ik}^{y} = R_{ij}^{z}R_{ik}^{z} = R_{ij}^{xyz}R_{ik}^{xyz} = \delta_{jk}, \qquad i,j,k = 1,2,3 \quad (3.4\text{-}29)$$

3.4.4 Vector Rotation Using Euler Angles

We will find it useful to describe any unit vector by rotating the first basis vector

$$(e_1)_i = \delta_{i1}, \qquad i = 1,2,3 \quad (3.4\text{-}30)$$

We can obtain any unit vector by performing two rotations

$$p_i = R_{jk}^{y}R_{ij}^{z}\delta_{i1}, \qquad i,j,k = 1,2,3 \quad (3.4\text{-}31)$$

Note that if we perform third rotation about **p**, then **p** does not change and we can write

$$p_i = R^y_{jk} R^z_{ij} \delta_{i1} = R^x_{kl} R^y_{jk} R^z_{ij} \delta_{i1}, \qquad i, j, k = 1, 2, 3 \tag{3.4-32}$$

The unit vector **p** is then fully specified by two angles and by the condition |**p**|=1. The components of **p** can be written as

$$p_1 = \cos\alpha \cos\beta = \cos\phi \sin\theta \tag{3.4-33}$$

$$p_2 = \sin\alpha \cos\beta = \sin\phi \sin\theta \tag{3.4-34}$$

$$p_3 = \sin\beta = \cos\theta \tag{3.4-35}$$

We will also want to find a unit vector, which is perpendicular to **p** and defined by angle γ, measured in a plane normal to unit vector **p**. We can obtain this vector by rotating the second basis vector

$$(e_2)_i = \delta_{i2}, \qquad i = 1, 2, 3 \tag{3.4-36}$$

which is orthogonal to the first basis vector by definition

$$(e_1)_i (e_2)_i = \delta_{i1} \delta_{i2} = 0, \qquad i = 1, 2, 3 \tag{3.4-37}$$

This vector has the following form

$$q_i = R^x_{kl} R^y_{jk} R^z_{ij} \delta_{i2}, \qquad i, j, k = 1, 2, 3 \tag{3.4-28}$$

where

$$q_1 = -\sin\alpha \cos\gamma - \cos\alpha \sin\beta \sin\gamma = -\sin\phi \cos\gamma - \cos\phi \cos\theta \sin\gamma \tag{3.4-39}$$

$$q_2 = \cos\alpha\cos\gamma - \sin\alpha\sin\beta\sin\gamma = \cos\phi\cos\gamma - \sin\phi\cos\theta\sin\gamma \tag{3.4-40}$$

$$q_3 = \cos\beta\sin\gamma = \sin\theta\sin\gamma \tag{3.4-41}$$

It is easy to verify that the vectors are orthogonal by **p**.**q**=0.

3.4.5 Euler Angles from Vector Components

Now we want to solve the reverse problem of calculating Euler angles knowing the components of **p** and **q**. Using Equation 3.4-34 and Equation 3.4-33 we can obtain

$$\alpha = ArcTan\left(\frac{p_2}{p_1}\right) \tag{3.4-42}$$

If $p_1 = 0$, then we decide if $\alpha = 0$ or $\beta = \frac{\pi}{2}$ from Equation 3.4-34 and Equation 3.4-35. Similarly from Equation 3.4-35 and Equation 3.4-33, we can write

$$\beta = ArcTan\left(\frac{p_3}{p_2}Sin(\alpha)\right) \tag{3.4-43}$$

Again, in the case of p_2, we decide if $\alpha = 0$ or $\beta = \frac{\pi}{2}$. We could also look at this problem as finding spherical coordinates, given known Cartesian coordinates and write

$$\theta = ArcCos(p_3) \tag{3.4-44}$$

and

$$\phi = \begin{cases} ArcSin\left(\frac{p_2}{S_p}\right) & if\ 0 \le p_1 \\ \pi - ArcSin\left(\frac{p_2}{S_p}\right) & if\ p_1 < 0 \end{cases} \tag{3.4-45}$$

To resolve the last angle, we note that $\gamma = 0$ when $q_3 = 0$, otherwise

$$\gamma = ArcTan\left(\left(-\frac{Cos(\beta)}{Sin(\alpha)}\left(\frac{q_1}{q_3} + Cos(\alpha)Tan(\beta)\right)\right)^{-1}\right) \tag{3.4-46}$$

This allows us to calculate Euler angles knowing **p** and **q** expressed in an arbitrary coordinate system.

3.5 Kelvin Moduli and Eigen-States

The Kelvin notation introduced in Section 3.3.1 allows us to use tensor algebra to gain deeper understanding of the structure of anisotropic stiffness tensor. This understanding is necessary to establish the number of material parameters, dimensionless and geometrical coefficients fully defining the stiffness tensor. The concept of elastic eigen-values was first established by Lord Kelvin [51], however this work was poorly reviewed and forgotten [52]. Rychlewski [52] and perhaps other researchers re-developed the concept in the late 20th century. Annin [49] provides a historical summary with focus on review of Russian literature, which contains useful works.

It was shown in Section 3.2 that there are 21 independent elastic constants in the stiffness tensor for general linear elastic body. Three of these constants define orientation of the material with respect to the laboratory system. We can choose Euler angles α,β,γ introduced in Section 3.4.3 for this purpose. In the following discussion, we show that six of the remaining eighteen parameters are invariants of the stiffness tensor with the unit of stress, and twelve are dimensionless invariants.

For the purpose of brevity, we proceed directly in six-dimensional space using Kelvin notation and presume that $\widehat{\boldsymbol{\omega}}$ exists, so that

$$\hat{C}_{ij}\widehat{\omega}_j = \lambda\widehat{\omega}_i \qquad i,j = 1,2,\ldots,6 \tag{3.5-1}$$

The eigen-values λ of the system are the roots of sixth-degree equation

$$\mathrm{Det}(\hat{C}_{ij} - \lambda\delta_{ji}) = 0 \qquad i,j = 1,2,\ldots,6 \tag{3.5-2}$$

Therefore, we obtain six eigen-values λ_K and six corresponding eigen-vectors $\widehat{\boldsymbol{\omega}}_K$. From now on, capital Latin indices run through values $1,2,\ldots,6$ and Einstein summation does not apply to

them. Eigen-values λ_K with the unit of stress are called Kelvin moduli, and vectors $\widehat{\boldsymbol{\omega}}_{\boldsymbol{K}}$ are called elastic eigen-states.

We note that the $\widehat{\boldsymbol{\omega}}_K$ formed an orthonormed bases in six-dimensional Euclidean space

$$\widehat{\boldsymbol{\omega}}_K \widehat{\boldsymbol{\omega}}_L = \delta_{KL} \qquad K, L = 1, 2, \dots, 6 \tag{3.5-3}$$

We can then de-compose stress

$$\widehat{\boldsymbol{\sigma}} = \sigma_1 \widehat{\boldsymbol{\omega}}_1 + \sigma_2 \widehat{\boldsymbol{\omega}}_2 + \cdots + \sigma_6 \widehat{\boldsymbol{\omega}}_6 \tag{3.5-4}$$

and strain

$$\widehat{\boldsymbol{\varepsilon}} = \varepsilon_1 \widehat{\boldsymbol{\omega}}_1 + \varepsilon_2 \widehat{\boldsymbol{\omega}}_2 + \cdots + \varepsilon_6 \widehat{\boldsymbol{\omega}}_6 \tag{3.5.5}$$

where $\sigma_1, \dots, \sigma_6$ and $\varepsilon_1, \dots, \varepsilon_6$ are constants.

Similarly, the stiffness tensor can be written in terms of the bases and Kelvin moduli

$$\widehat{\boldsymbol{C}} = \lambda_1 \widehat{\boldsymbol{\omega}}_1 \otimes \widehat{\boldsymbol{\omega}}_1 + \lambda_2 \widehat{\boldsymbol{\omega}}_2 \otimes \widehat{\boldsymbol{\omega}}_2 + \cdots + \lambda_6 \widehat{\boldsymbol{\omega}}_6 \otimes \widehat{\boldsymbol{\omega}}_6 \tag{3.5-6}$$

Since $\widehat{\boldsymbol{C}}$ is positive definite, then $\lambda_K > 0$ and we can write the compliance as

$$\widehat{\boldsymbol{S}} = \frac{1}{\lambda_1} \widehat{\boldsymbol{\omega}}_1 \otimes \widehat{\boldsymbol{\omega}}_1 + \frac{1}{\lambda_2} \widehat{\boldsymbol{\omega}}_2 \otimes \widehat{\boldsymbol{\omega}}_2 + \cdots + \frac{1}{\lambda_6} \widehat{\boldsymbol{\omega}}_6 \otimes \widehat{\boldsymbol{\omega}}_6 \tag{3.5-7}$$

From Equations 3.5-35 and 3.5-4, we see that

$$\sigma_K = \widehat{\boldsymbol{\sigma}} . \widehat{\boldsymbol{\omega}}_K, \varepsilon_K = \widehat{\boldsymbol{\varepsilon}} . \widehat{\boldsymbol{\omega}}_K \qquad K, L = 1, 2, \dots, 6 \tag{3.5-8}$$

and using Equation 3.5-6, we can write Hooke's law for a generic anisotropic material as six scalar equations

$$\sigma_K = \lambda_K \varepsilon_K \qquad K, L = 1, 2, \ldots, 6 \tag{3.5-9}$$

Therefore, of the 21 independent constants of a stiffness tensor, we now have three Euler angles defining orientation with respect to the laboratory system and six Kelvin moduli.

Notice that Equations 3.5-1 through 3.5-9 written for six-dimensional space can be used in three dimensional space after applying transformations noted in Section 3.3. It is convenient to transform six first order tensor eigen states $\widehat{\boldsymbol{\omega}}_{\boldsymbol{K}}$ from a six dimensional space to six second order tensor eigen states $\boldsymbol{\omega}_{\boldsymbol{K}}$ in three dimensions. With $tr\ \boldsymbol{\omega}_{\boldsymbol{K}}{}^{\mathbf{2}} \equiv \boldsymbol{\omega}_{\boldsymbol{K}} . \boldsymbol{\omega}_{\boldsymbol{K}} = \omega_{\boldsymbol{ij}(\boldsymbol{K})} \omega_{\boldsymbol{ij}(\boldsymbol{K})} = 1$ being the normalizing condition corresponding to Equation 3.5-3, we can use

$$tr\ \boldsymbol{\omega}_{\boldsymbol{K}}\ and\ tr\ \boldsymbol{\omega}_{\boldsymbol{K}}{}^{\mathbf{3}} \qquad K = 1, 2, \ldots, 6 \tag{3.5-10}$$

to obtain the remaining twelve dimensionless invariants.

Rychlevski [52] shows that elastic solids can be categorized into 11 classes depending on multiplicity of Kelvin moduli. Extreme cases of allowable materials consist of a general anisotropic body with 6 distinct Kelvin moduli and 12 distinct dimensionless invariants and three orientation angles, and an isotropic body with one Kelvin modulus, one dimensionless invariant (Poisson's ratio).

3.6 Material Symmetry

The introduction of fiber curvature reduces symmetry of the internal material structure within discontinuous fiber composites. This section shows forms of stiffness tensor resulting from symmetries applicable to the discontinuous fiber composites. It is also shown that if material contains two planes of symmetry, a third plane of symmetry is implied [48]. This fact has significant implications for development of a model allowing us to estimate discontinuous fiber composite properties from constituent properties of fibers and matrix. Through the following section, we follow Chadwick [48] starting with definition of symmetry transformation l

$$l_{ij} = \boldsymbol{e}'_i . \boldsymbol{e}_j \quad i, j = 1, 2, 3 \tag{3.6-1}$$

Between orthonormal bases $e = \{\boldsymbol{e}_1, \boldsymbol{e}_2, \boldsymbol{e}_3\}$ and $e' = \{\boldsymbol{e}'_1, \boldsymbol{e}'_2, \boldsymbol{e}'_3\}$ under which the components of the stiffness tensor C_{ijkl} are invariant. This condition can be expressed as

$$C_{pqrs} = l_{ip} l_{iq} C_{ijkl} l_{kr} l_{ls}, \quad i,j,k,l,p,q,r,s = 1,2,3 \tag{3.6-2}$$

It can be verified that if l and m are orthogonal symmetry transformations, so is l^{-1} and lm, therefore a set of symmetry transformations for given material forms a linear group. The identity transformation and its opposite always form a symmetry sub-group $\{\delta_{ij}, -\delta_{ij}\}$.

Let a unit vector $\boldsymbol{a}$ be a normal vector to a material plane of symmetry. Then transformation

$$R_{ij}(\boldsymbol{a}) = \delta_{ij} - a_i a_j \qquad i,j = 1,2,3 \tag{3.6-3}$$

is a reflection with respect to this plane.

We can introduce notation

$$\boldsymbol{r_i}(\theta) = \sin\theta\, \boldsymbol{e}_j + \cos\theta\, \boldsymbol{e}_k \tag{3.6-4}$$

where {i,j,k} is a cyclic permutation of {1,2,3}. Then identities

$$R(\boldsymbol{e}_j)R(\boldsymbol{r_i}(\theta))R(\boldsymbol{e}_j) = R(\boldsymbol{e}_k)R(\boldsymbol{r_i}(\theta))R(\boldsymbol{e}_k) = R(\boldsymbol{r_i}(\pi - \theta)) \tag{3.6-5}$$

and

$$R(\boldsymbol{r_i}(\theta))R\left(\boldsymbol{r_i}\left(\theta + \frac{1}{2}\pi\right)\right) = -R(\boldsymbol{e}_i) \tag{3.6-6}$$

follow from definition in Equation 3.6-3.

We now examine monoclinic material with single plane of symmetry characterized by reflection $R(\boldsymbol{e}_2)$, Using Equations 3.6-1 and 3.6-3, we obtain $\boldsymbol{e}_1' = \boldsymbol{e}_1, \boldsymbol{e}_2' = -\boldsymbol{e}_2, \boldsymbol{e}_3' = \boldsymbol{e}_3$. By examining Equation 3.6-2, we conclude that components of the stiffness tensor with one or three suffixes equal to 3 are zero. Therefore, in Voigt notation, the stiffness tensor in Equation 3.3-7 reduces to

$$\begin{bmatrix}\sigma_1\\ \sigma_2\\ \sigma_3\\ \sigma_4\\ \sigma_5\\ \sigma_6\end{bmatrix} = \begin{bmatrix} C_{11} & C_{12} & C_{13} & 0 & C_{15} & 0 \\ & C_{22} & C_{23} & 0 & C_{25} & 0 \\ & & C_{33} & 0 & C_{35} & 0 \\ & & & C_{44} & 0 & C_{46} \\ & sym. & & & C_{55} & 0 \\ & & & & & C_{66} \end{bmatrix} \begin{bmatrix}\varepsilon_1\\ \varepsilon_2\\ \varepsilon_3\\ \varepsilon_4\\ \varepsilon_5\\ \varepsilon_6\end{bmatrix} \tag{3.6-7}$$

By suitable choice of rotation, one more component may be made to vanish [48] and the number of distinct components in the stiffness tensor is reduced to 12.

Using the same approach, we find zero terms and obtain stiffness tensor corresponding to a single reflection $R(\boldsymbol{e}_3)$:

$$\begin{bmatrix}\sigma_1\\ \sigma_2\\ \sigma_3\\ \sigma_4\\ \sigma_5\\ \sigma_6\end{bmatrix} = \begin{bmatrix} C_{11} & C_{12} & C_{13} & 0 & 0 & C_{16} \\ & C_{22} & C_{23} & 0 & 0 & C_{26} \\ & & C_{33} & 0 & 0 & C_{36} \\ & & & C_{44} & C_{45} & 0 \\ & sym. & & & C_{55} & 0 \\ & & & & & C_{66} \end{bmatrix} \begin{bmatrix}\varepsilon_1\\ \varepsilon_2\\ \varepsilon_3\\ \varepsilon_4\\ \varepsilon_5\\ \varepsilon_6\end{bmatrix} \tag{3.6-8}$$

We can now examine symmetry with two reflections with normal enclosing angle θ. With e and e' as the bases

$$\boldsymbol{e}_1' = \boldsymbol{r}_3\left(\theta + \frac{1}{2}\pi\right), \boldsymbol{e}_2' = \boldsymbol{r}_3(\theta), \boldsymbol{e}_3' = \boldsymbol{e}_3 \tag{3.6-9}$$

And using $R(\boldsymbol{e}_2)$ and $R(\boldsymbol{e}_2')$ as reflections, we can use Equations 3.4-10 and 3.6-1 through 3.6-4 to obtain

$$c_{14}' = \{c_{25}sin^2\theta + (c_{15} - 2c_{46})cos^2\theta\}sin\theta \tag{3.6-10}$$

$$c_{16}' = -\{(c_{22} - c_{12} - 2c_{66})sin^2\theta - (c_{11} - c_{12} - 2c_{66})cos^2\}sin\theta cos\theta \tag{3.6-11}$$

$$c'_{24} = \{c_{15}sin^2\theta + (c_{25} + 2c_{46})cos^2\}sin\theta \tag{3.6-12}$$

$$c'_{26} = \{(c_{11} - c_{12} - 2c_{66})sin^2\theta - (c_{22} - c_{12} - 2c_{66})cos^2\}sin\theta cos\theta \tag{3.6-13}$$

$$c'_{34} = c_{35}sin\theta \tag{3.6-14}$$

$$c'_{36} = (c_{13} - c_{23})sin\theta cos\theta \tag{3.6-15}$$

$$c'_{45} = -(c_{44} - 2c_{55})sin\theta cos\theta \tag{3.6-16}$$

$$c'_{56} = \{c_{46}sin^2\theta + (c_{15} - c_{25} - c_{46})cos^2\theta\}sin\theta \tag{3.6-17}$$

Since $sin\theta \neq 0$ for two distinct planes of symmetry, we obtain the following conditions

$$c_{25}sin^2\theta + (c_{15} - 2c_{46})cos^2\theta = 0 \tag{3.6-18}$$

(3.6-1)

$$\{(c_{22} - c_{12} - 2c_{66})sin^2\theta - (c_{11} - c_{12} - 2c_{66})cos^2\}cos\theta = 0$$

(3.6-19)

$$c_{15}sin^2\theta + (c_{25} + 2c_{46})cos^2 = 0 \tag{3.6-20}$$

$$\{(c_{11} - c_{12} - 2c_{66})sin^2\theta - (c_{22} - c_{12} - 2c_{66})cos^2\}cos\theta = 0 \tag{3.6-21}$$

$$c_{35} = 0 \tag{3.6-22}$$

$$(c_{13} - c_{23})cos\theta = 0 \tag{3.6-23}$$

$$(c_{44} - 2c_{55})cos\theta = 0 \tag{3.6-24}$$

$$c_{46}sin^2\theta + (c_{15} - c_{25} - c_{46})cos^2\theta = 0 \tag{3.6-24}$$

We can then obtain the following solutions

$$\theta = \frac{1}{4}\pi \; or \; \frac{3}{4}\pi, c_{11} = c_{22},\; c_{13} = c_{23}, c_{44} = c_{55}, c_{15} = c_{25} = c_{35} = c_{46} = 0 \tag{3.6-26}$$

$$\theta = \frac{1}{3}\pi \; or \; \frac{2}{3}\pi, c_{11} = c_{22},\; c_{13} = c_{23}, c_{44} = c_{55}, c_{66} = \frac{1}{2}(c_{11} - c_{12}), \qquad c_{35} = 0, \\ c_{25} = c_{46} = -c_{15} \tag{3.6-27}$$

$$\theta = \frac{1}{2}\pi, \qquad c_{15} = c_{25} = c_{35} = c_{46} = 0 \tag{3.6-28}$$

$$\theta \neq \left\{\frac{1}{4}\pi, \frac{1}{3}\pi, \frac{1}{2}\pi, \frac{2}{3}\pi, \frac{3}{4}\pi\right\}, c_{11} = c_{22},\; c_{13} = c_{23}, c_{44} = c_{55}, \\ c_{66} = \frac{1}{2}(c_{11} - c_{12}), \qquad c_{15} = c_{25} = c_{35} = c_{46} = 0 \tag{3.6-29}$$

Now we examine case of reflections with normals $\boldsymbol{e}_2$ and $\boldsymbol{r_3}\left(\frac{1}{2}\pi\right) = \boldsymbol{e}_1$, which will be used later in the document for material with two planes of symmetry enclosing $\theta = \frac{1}{2}\pi$. We note that the identity of Equation 3.6-6 induces a third reflection. This is confirmed by the fact that zero terms of the stiffness tensor in Equations 3.6-7 and 3.6-28 correspond to zero terms for $R(\boldsymbol{e}_2)$ and $R(\boldsymbol{e}_3)$ reflections given in Equations 3.6-7 and 3.6-8 correspondingly, therefore, we obtain orthotropic material, which contains three mutually orthogonal planes of symmetry. Using Equations 3.6-7 and 3.6-28, we obtain the stiffness matrix for orthotropic material

$$\begin{bmatrix}\sigma_1\\ \sigma_2\\ \sigma_3\\ \sigma_4\\ \sigma_5\\ \sigma_6\end{bmatrix} = \begin{bmatrix} C_{11} & C_{12} & C_{13} & 0 & 0 & 0 \\ & C_{22} & C_{23} & 0 & 0 & 0 \\ & & C_{33} & 0 & 0 & 0 \\ & & & C_{44} & 0 & 0 \\ & sym. & & & C_{55} & 0 \\ & & & & & C_{66} \end{bmatrix} \begin{bmatrix}\varepsilon_1\\ \varepsilon_2\\ \varepsilon_3\\ \varepsilon_4\\ \varepsilon_5\\ \varepsilon_6\end{bmatrix} \tag{3.6-30}$$

The stiffness matrix in Equation 3.6-30 contains nine distinct components. The fact of third plane of symmetry being induced by the presence of two orthogonal planes of symmetry is a key finding by Chadwick [48] used in this work.

We also note the case of transverse isotropy resulting from Equations 3.6-7 and 3.6-29. Transverse isotropy with five distinct stiffness tensor components has a key role in development models containing straight fibers and obtaining components of stiffness tensor for curved fiber model presented in this work. From Equations 3.6-7 and 3.6-29, we obtain

$$\begin{bmatrix}\sigma_1\\ \sigma_2\\ \sigma_3\\ \sigma_4\\ \sigma_5\\ \sigma_6\end{bmatrix} = \begin{bmatrix} C_{11} & C_{12} & C_{13} & 0 & & 0 & 0 \\ & C_{11} & C_{13} & 0 & & 0 & 0 \\ & & C_{33} & 0 & & 0 & 0 \\ & & & C_{44} & & 0 & 0 \\ & sym. & & & C_{44} & & 0 \\ & & & & & \frac{1}{2}(C_{11}-C_{12}) & \end{bmatrix}\begin{bmatrix}\varepsilon_1\\ \varepsilon_2\\ \varepsilon_3\\ \varepsilon_4\\ \varepsilon_5\\ \varepsilon_6\end{bmatrix} \tag{3.6-31}$$

which can be reproduced in three dimensions by

$$\begin{aligned} C_{ijkl} = \; & c_{12}\delta_{ij}\delta_{kl} + \frac{1}{2}(c_{11}-c_{12})\left(\delta_{ik}\delta_{jl}+\delta_{il}\delta_{jk}\right) \\ & - (c_{12}-c_{13})\left(\delta_{ij}\delta_{k3}\delta_{l3}+\delta_{kl}\delta_{i3}\delta_{j3}\right) \\ & - \frac{1}{2}(c_{11}-c_{12}-2c_{44})\left(\delta_{ik}\delta_{j3}\delta_{l3}+\delta_{il}\delta_{j3}\delta_{k3}+\delta_{jl}\delta_{i3}\delta_{k3}+\delta_{jk}\delta_{i3}\delta_{l3}\right) \\ & + (c_{11}+c_{33}-2c_{13}-4c_{44})\delta_{i3}\delta_{j3}\delta_{k3}\delta_{l3} \qquad i,j,k,l = 1,2,3 \end{aligned} \tag{3.6-32}$$

3.7 Stiffness Tensor Decomposition

We now turn our attention to forms of stiffness tensor expressed as a sum of base tensors, similar to Equation 3.6-32. Decomposition of the stiffness tensor provides us with greater understanding of its structure and it will allow us to construct stiffness tensor for a given microstructure with certain symmetries. Annin and Ostrosablin [49] show a general decomposition into volumetric, deviatoric and nonor parts

$$C_{ijkl} = \lambda^* \delta_{ij}\delta_{kl} + \mu^*\left(\delta_{ik}\delta_{jl} + \delta_{il}\delta_{jk}\right) + \left(M_{ij}\delta_{kl} + M_{kl}\delta_{ij}\right) + \left(P_{ik}\delta_{jl} + P_{lj}\delta_{ik} + P_{il}\delta_{jk} + P_{jk}\delta_{il}\right) + N_{ijkl} \qquad i,j,k,l = 1,2,3 \tag{3.7-1}$$

where

$$\lambda^* = \frac{2C_{iikk} - C_{ikki}}{15} \qquad i,j,k,l = 1,2,3 \tag{3.7-2}$$

$$\mu^* = \frac{3C_{ikki} - C_{iikk}}{30} \qquad i,k = 1,2,3 \tag{3.7-3}$$

$$M_{ij} = \frac{\left[5\left(C_{ijkk} - \frac{C_{sskk}\delta_{ij}}{3}\right) - 4\left(C_{ikkj} - \frac{C_{skks}\delta_{ij}}{3}\right)\right]}{7} \qquad i,j,k,l,s = 1,2,3 \tag{3.7-4}$$

$$P_{ij} = \frac{\left[-2\left(C_{ijkk} - \frac{C_{sskk}\delta_{ij}}{3}\right) + 3\left(C_{ikkj} - \frac{C_{skks}\delta_{ij}}{3}\right)\right]}{7} \qquad i,j,k,l,s = 1,2,3 \tag{3.7-5}$$

and the following equalities hold

$$M_{ii} = P_{ii} = 0, \qquad N_{ijkk} = 0 \qquad i,j,k = 1,2,3 \tag{3.7-6}$$

Ostrosablin [53] provides a complete decomposition for the fully anisotropic stiffness tensor in the following form.

$$
\begin{aligned}
C_{ijkl} = \; & H\frac{1}{3}\left(\delta_{ij}\delta_{kl} + 2\delta_{ijkl}\right) + 2h\frac{1}{3}\left(\delta_{ij}\delta_{kl} - \delta_{ijkl}\right) \\
& + \frac{1}{6}\left(H_{ij}\delta_{kl} + H_{kl}\delta_{ij} + H_{lj}\delta_{ik} + H_{il}\delta_{jk} + H_{jk}\delta_{il}\right) + \frac{1}{3}\left(h_{ij}\delta_{kl} + h_{kl}\delta_{ij}\right) \\
& - \frac{1}{6}\left(h_{ik}\delta_{lj} + h_{lj}\delta_{ik} + h_{il}\delta_{jk} + h_{jk}\delta_{il}\right) + N_{ijkl} \qquad i,j,k,l = 1,2,3
\end{aligned}
\tag{3.7-7}
$$

where components with H, H_{ij} and N_{ijkl} belong to the fully symmetric part $C_{(ijkl)}$ of the stiffness tensor

$$
C_{(ijkl)} = \frac{1}{3}\left(C_{ijkl} + C_{iklj} + C_{iljk}\right) \qquad i,j,k,l = 1,2,3 \tag{3.7-8}
$$

and components with h and h_{ik} belong to the asymmetric part A_{ijkl} of the stiffness tensor

$$
A_{ijkl} = C_{ijkl} - C_{(ijkl)} = \frac{1}{3}\left(2C_{ijkl} - C_{iklj} - C_{iljk}\right) \qquad i,j,k,l = 1,2,3 \tag{3.7-9}
$$

It follows that

$$
C_{(ijkl)}A_{ijkl} = 0 \qquad i,j,k,l = 1,2,3 \tag{3.7-10}
$$

and

$$
A_{ijkl} + A_{iklj} + A_{iljk} = 0 \qquad i,j,k,l = 1,2,3 \tag{3.7-11}
$$

Noting that $h_{ij} = h_{ji}$, we can use the following mapping

$$\begin{bmatrix} h_1 \\ h_2 \\ h_3 \\ h_4 \\ h_5 \\ h_6 \end{bmatrix} = \begin{bmatrix} h_{11} \\ h_{22} \\ h_{33} \\ \sqrt{2}h_{23} \\ \sqrt{2}h_{13} \\ \sqrt{2}h_{12} \end{bmatrix} \tag{3.7-12}$$

to write this decomposition in Kelvin notation.

The coefficients on the right hand side can be calculated from the stiffness matrix coefficient

$$
\hat{C}_{ij} = \frac{H}{3}\begin{bmatrix} 3 & & & & & \\ 1 & 3 & & sym & & \\ 1 & 1 & 3 & & & \\ 0 & 0 & 0 & 2 & & \\ 0 & 0 & 0 & 0 & 2 & \\ 0 & 0 & 0 & 0 & 0 & 2 \end{bmatrix} + \frac{2h}{3}\begin{bmatrix} 0 & & & & & \\ 1 & 0 & & sym & & \\ 1 & 1 & 0 & & & \\ 0 & 0 & 0 & -1 & & \\ 0 & 0 & 0 & 0 & -1 & \\ 0 & 0 & 0 & 0 & 0 & -1 \end{bmatrix}
$$

$$
+\frac{1}{6}\begin{bmatrix} 6H_1 & & & & & \\ -H_3 & 6H_2 & & sym & & \\ -H_2 & -H_1 & 6H_3 & & & \\ H_4 & 3H_4 & 3H_4 & -2H_1 & & \\ 3H_5 & H_5 & 3H_5 & \sqrt{2}H_6 & -2H_2 & \\ 3H_6 & 3H_6 & H_6 & \sqrt{2}H_5 & \sqrt{2}H_4 & -2H_3 \end{bmatrix}
$$

$$
+\frac{1}{3}\begin{bmatrix} 0 & & & & & \\ -h_3 & 0 & & sym & & \\ -h_2 & -h_1 & 0 & & & \\ h_4 & 0 & 0 & h_1 & & \\ 0 & h_5 & 0 & -\frac{1}{\sqrt{2}}h_6 & h_2 & \\ 0 & 0 & h_6 & -\frac{1}{\sqrt{2}}h_5 & -\frac{1}{\sqrt{2}}h_4 & h_3 \end{bmatrix} \tag{3.7-1}
$$

$$
+\begin{bmatrix} N_{11} & & & & & \\ N_{21} & N_{22} & & sym & & \\ N_{31} & N_{32} & N_{33} & & & \\ N_{41} & N_{42} & N_{43} & 2N_{32} & & \\ N_{51} & N_{52} & N_{53} & \sqrt{2}N_{63} & 2N_{31} & \\ N_{61} & N_{62} & N_{63} & \sqrt{2}N_{52} & \sqrt{2}N_{41} & -2N_{21} \end{bmatrix}
$$

$$H = \frac{1}{15}\left[3\left(\hat{C}_{11} + \hat{C}_{22} + \hat{C}_{33}\right) + 2\left(\hat{C}_{21} + \hat{C}_{31} + \hat{C}_{32} + \hat{C}_{44} + \hat{C}_{55} + \hat{C}_{66}\right)\right],$$

$$h = \frac{1}{6}\left[2\left(\hat{C}_{21} + \hat{C}_{31} + \hat{C}_{32}\right) - \left(\hat{C}_{44} + \hat{C}_{55} + \hat{C}_{66}\right)\right];$$

$$H_1 = H_{11} = \frac{2}{21}\left(6\hat{C}_{11} + \hat{C}_{21} + \hat{C}_{31} - 3\hat{C}_{22} - 2\hat{C}_{32} - 3\hat{C}_{33} - 2\hat{C}_{44} + \hat{C}_{55} + \hat{C}_{66}\right),$$

$$H_2 = H_{22} = \frac{2}{21}\left(-3\hat{C}_{11} + \hat{C}_{21} - 2\hat{C}_{31} + 6\hat{C}_{22} + \hat{C}_{32} - 3\hat{C}_{33} + \hat{C}_{44} - 2\hat{C}_{55} + \hat{C}_{66}\right),$$

$$H_3 = H_{33} = \frac{2}{21}\left(-3\hat{C}_{11} - 2\hat{C}_{21} + \hat{C}_{31} - 3\hat{C}_{22} + \hat{C}_{32} + 6\hat{C}_{33} + \hat{C}_{44} + \hat{C}_{55} - 2\hat{C}_{66}\right),$$

$$H_4 = \sqrt{2}H_{32} = \frac{2}{7}\left[3\left(\hat{C}_{42} + \hat{C}_{43}\right) + \hat{C}_{41} + \sqrt{2}\hat{C}_{65}\right],$$

$$H_5 = \sqrt{2}H_{31} = \frac{2}{7}\left[3\left(\hat{C}_{51} + \hat{C}_{53}\right) + \hat{C}_{52} + \sqrt{2}\hat{C}_{64}\right],$$

$$H_6 = \sqrt{2}H_{21} = \frac{2}{7}\left[3\left(\hat{C}_{61} + \hat{C}_{62}\right) + \hat{C}_{63} + \sqrt{2}\hat{C}_{54}\right]; \tag{3.7-14}$$

$$h_1 = h_{11} = \frac{1}{3}\left[2\left(\hat{C}_{21} + \hat{C}_{31} - 2\hat{C}_{32} + \hat{C}_{44}\right) - \hat{C}_{55} - \hat{C}_{66}\right],$$

$$h_2 = h_{22} = \frac{1}{3}\left[2\left(\hat{C}_{21} - 2\hat{C}_{31} + \hat{C}_{32} + \hat{C}_{55}\right) - \hat{C}_{44} - \hat{C}_{66}\right],$$

$$h_3 = h_{33} = \frac{1}{3}\left[2\left(-2\hat{C}_{21} + \hat{C}_{31} + \hat{C}_{32} + \hat{C}_{66}\right) - \hat{C}_{44} - \hat{C}_{55}\right],$$

$$h_4 = \sqrt{2}h_{32} = 2\hat{C}_{41} - \sqrt{2}\hat{C}_{65}, h_5 = \sqrt{2}h_{31} = 2\hat{C}_{52} - \sqrt{2}\hat{C}_{64}, h_6 = \sqrt{2}h_{21} = 2\hat{C}_{63} - \sqrt{2}\hat{C}_{54};$$

$$N_{11} = \frac{1}{35}\left[8\left(\hat{C}_{11} - \hat{C}_{21} - \hat{C}_{31} - \hat{C}_{55} - \hat{C}_{66}\right) + 3\left(\hat{C}_{22} + \hat{C}_{33}\right) + 2\left(\hat{C}_{32} + \hat{C}_{44}\right)\right],$$

$$N_{21} = \frac{1}{35}(-4\hat{C}_{11} + 9\hat{C}_{21} - \hat{C}_{31} - 4\hat{C}_{22} - \hat{C}_{32} + \hat{C}_{33} - \hat{C}_{44} - \hat{C}_{55} + 9\hat{C}_{66}),$$

$$N_{31} = \frac{1}{35}(-4\hat{C}_{11} - \hat{C}_{21} + 9\hat{C}_{31} + \hat{C}_{22} - \hat{C}_{32} - 4\hat{C}_{33} - \hat{C}_{44} + 9\hat{C}_{55} - \hat{C}_{66}),$$

$$N_{41} = \frac{1}{7}\left[2\left(\hat{C}_{41} + \sqrt{2}\hat{C}_{65}\right) - \hat{C}_{42} - \hat{C}_{43}\right],$$

$$N_{51} = \frac{1}{7}(4\hat{C}_{51} - \hat{C}_{52} - 3\hat{C}_{53} - \sqrt{2}\hat{C}_{64}),$$

$$N_{61} = \frac{1}{7}(4\hat{C}_{61} - 3\hat{C}_{62} - \hat{C}_{63} - \sqrt{2}\hat{C}_{54}),$$

$$N_{22} = \frac{1}{35}\left[8\left(\hat{C}_{22} - \hat{C}_{21} - \hat{C}_{32} - \hat{C}_{44} - \hat{C}_{66}\right) + 3\left(\hat{C}_{11} + \hat{C}_{33}\right) + 2\left(\hat{C}_{31} + \hat{C}_{55}\right)\right], \quad (3.7\text{-}14)$$

$$N_{32} = \frac{1}{35}(\hat{C}_{11} - \hat{C}_{21} - \hat{C}_{31} - 4\hat{C}_{22} + 9\hat{C}_{32} - 4\hat{C}_{33} + 9\hat{C}_{44} - \hat{C}_{55} - \hat{C}_{66}), \quad \text{continued}$$

$$N_{42} = \frac{1}{7}(-\hat{C}_{41} + 4\hat{C}_{42} - 3\hat{C}_{43} - \sqrt{2}\hat{C}_{65}),$$

$$N_{52} = \frac{1}{7}\left[2\left(\hat{C}_{52} + \sqrt{2}\hat{C}_{64}\right) - \hat{C}_{51} - \hat{C}_{53}\right],$$

$$N_{62} = \frac{1}{7}(-3\hat{C}_{61} + 4\hat{C}_{62} - \hat{C}_{63} - \sqrt{2}\hat{C}_{54});$$

$$N_{33} = \frac{1}{35}\left[8\left(\hat{C}_{33} - \hat{C}_{31} - \hat{C}_{32} - \hat{C}_{44} - \hat{C}_{55}\right) + 3\left(\hat{C}_{11} + \hat{C}_{22}\right) + 2\left(\hat{C}_{21} + \hat{C}_{66}\right)\right],$$

$$N_{43} = \frac{1}{7}(-\hat{C}_{41} - 3\hat{C}_{42} + 4\hat{C}_{43} - \sqrt{2}\hat{C}_{65}),$$

$$N_{53} = \frac{1}{7}(-3\hat{C}_{51} - \hat{C}_{52} + 4\hat{C}_{53} - \sqrt{2}\hat{C}_{64}),$$

$$N_{63} = \frac{1}{7}\left[2\left(\hat{C}_{63} + \sqrt{2}\hat{C}_{54}\right) - \hat{C}_{61} - \hat{C}_{62}\right]$$

Since there are no conditions on the form of anisotropy for decomposition listed in Equations 3.7-13 and 3.7-14, we can obtain stiffness tensor decomposition for any material symmetry.

Lubarda and Chen [54] studied orthogonal of stiffness and compliance tensors with transversely isotropic and orthotropic symmetry. These symmetries are most useful for this work, therefore we summarize the work.

3.7.1 Decomposition of Stiffness Tensor for Transversely Isotropic Material

The stiffness tensor for material with unit vector **p** parallel to the axis of transverse isotropy can be defined as a sum of six base tensors $\mathbf{I}_r$ scaled by six parameters τ, five of which are independent

$$\boldsymbol{C} = \tau_1\mathbf{I}_1 + \tau_2\mathbf{I}_2 + \cdots + \tau_6\mathbf{I}_6 \tag{3.7-15}$$

where

$$(\mathbf{I_1})_{ijkl} = \frac{1}{2}(\delta_{ik}\delta_{jl} + \delta_{il}\delta_{jk}) \qquad i,j,k,l = 1,2,3 \tag{3.7-16}$$

$$(\mathbf{I_2})_{ijkl} = \delta_{ij}\delta_{kl} \qquad i,j,k,l = 1,2,3 \tag{3.7-17}$$

$$(\mathbf{I_3})_{ijkl} = p_i p_j \delta_{kl} \qquad i,j,k,l = 1,2,3 \tag{3.7-18}$$

$$(\mathbf{I_4})_{ijkl} = p_k p_l \delta_{ij} \qquad i,j,k,l = 1,2,3 \tag{3.7-19}$$

$$(\mathbf{I_5})_{ijkl} = \frac{1}{2}(\delta_{ik}p_j p_l + \delta_{il}p_j p_k + \delta_{jl}p_i p_k + \delta_{jk}p_i p_l) \qquad i,j,k,l = 1,2,3 \tag{3.7-20}$$

$$(\mathbf{I_6})_{ijkl} = p_i p_j p_k p_l \qquad i,j,k,l = 1,2,3 \tag{3.7-21}$$

and parameters τ

$$\tau_1 = 2\mu, \tau_2 = \lambda, \tau_3 = \tau_4 = \alpha_\lambda, \tau_5 = 2(\mu_0 - \mu), \tau_6 = \beta_\lambda \tag{3.7-22}$$

Parameters μ and λ are Lamé constants within the plane of isotropy, μ_0 is the out of plane shear modulus, and $\alpha_\lambda$and β_λ are remaining elastic properties in the plane of isotropy and perpendicular to it.

Note that even though the form of Equation 3.7-15 is the same as for Equation 3.5-6, the base tensors $\mathbf{I}_r$ are not orthogonal as required by Equation 3.5-3 and do not correspond to stiffness tensor eigen-states. Also note that Equation 3.6-32 is a special case of Equation 3.7-15 with **p**=e3.

We can generate an alternative set of tensors $\mathbf{J}_r$ scaled by six parameters $\bar{\tau}$, five of which are independent

$$\boldsymbol{C} = \bar{\tau}_1\mathbf{J}_1 + \bar{\tau}_2\mathbf{J}_2 + \cdots + \bar{\tau}_6\mathbf{J}_6 \tag{3.7-23}$$

where

$$\mathbf{J}_1 = \mathbf{I}_6 \tag{3.7-24}$$

$$\mathbf{J}_2 = \frac{1}{2}(\mathbf{I}_2 - \mathbf{I}_3 - \mathbf{I}_4 + \mathbf{I}_6) \tag{3.7-25}$$

$$\mathbf{J}_3 = \frac{1}{\sqrt{2}}(\mathbf{I}_3 - \mathbf{I}_6) \tag{3.7-26}$$

$$\mathbf{J}_4 = \frac{1}{\sqrt{2}}(\mathbf{I}_4 - \mathbf{I}_6) \tag{3.7-27}$$

$$\mathbf{J}_5 = \frac{1}{2}(2\mathbf{I}_1 - \mathbf{I}_2 + \mathbf{I}_3 + \mathbf{I}_4 - 2\mathbf{I}_5 + \mathbf{I}_6) \tag{3.7-28}$$

$$\mathbf{J}_6 = \mathbf{I}_5 - 2\mathbf{I}_6 \tag{3.7-29}$$

and parameters $\bar{\tau}$ are given by

$$\bar{\tau}_1 = \tau_1 + \tau_2 + 2\tau_3 + 2\tau_5 + \tau_6 = \lambda + 4\mu_0 - 2\mu + 2\alpha_\lambda + \beta_\lambda \tag{3.7-30}$$

$$\bar{\tau}_2 = \tau_1 + 2\tau_2 = 2(\lambda + \mu) \tag{3.7-31}$$

$$\bar{\tau}_3 = \bar{\tau}_4 = \sqrt{2}(\tau_2 + \tau_3) = \sqrt{2}(\lambda + \alpha_\lambda) \tag{3.7-32}$$

$$\bar{\tau}_5 = \tau_1 = 2\mu \tag{3.7-33}$$

$$\bar{\tau}_6 = \tau_1 + \tau_5 = 2\mu_0 \tag{3.7-34}$$

We can also write the compliance tensor in terms of tensor bases $\mathbf{J}_r$ scaled by parameters $\bar{\varsigma}_r$

$$\boldsymbol{S} = \boldsymbol{C}^{-1} = \bar{\varsigma}_1\mathbf{J}_1 + \bar{\varsigma}_2\mathbf{J}_2 + \cdots + \bar{\varsigma}_6\mathbf{J}_6 \tag{3.7-35}$$

where parameters $\bar{\varsigma}_r$ are related to parameters $\bar{\tau}$

$$\bar{\varsigma}_1 = \frac{\bar{\tau}_2}{\bar{\tau}}, \bar{\varsigma}_2 = \frac{\bar{\tau}_1}{\bar{\tau}}, \bar{\varsigma}_3 = \bar{\varsigma}_4 = -\frac{\bar{\tau}_3}{\bar{\tau}}, \bar{\varsigma}_5 = \frac{1}{\bar{\tau}_5}, \bar{\varsigma}_6 = \frac{1}{\bar{\tau}_6} \tag{3.7-36}$$

and where

$$\bar{\tau} = \bar{\tau}_1\bar{\tau}_2 - \bar{\tau}_3{}^2 \tag{3.7-37}$$

Alternatively, we can write

$$\boldsymbol{S} = \boldsymbol{C}^{-1} = \varsigma_1\mathbf{I}_1 + \varsigma_2\mathbf{I}_2 + \cdots + \varsigma_6\mathbf{I}_6 \tag{3.7-38}$$

where

$$\varsigma_1 = \bar{\varsigma}_5, \varsigma_2 = \frac{1}{2}(\bar{\varsigma}_2 - \bar{\varsigma}_5), \varsigma_3 = \varsigma_4 = \frac{1}{\sqrt{2}}\bar{\varsigma}_3 - \frac{1}{2}(\bar{\varsigma}_2 - \bar{\varsigma}_5), \varsigma_5 = \bar{\varsigma}_6 - \bar{\varsigma}_5, \varsigma_6 = \bar{\varsigma}_1 - \frac{1}{2}\bar{\varsigma}_2 - \sqrt{2}\bar{\varsigma}_3 + \frac{1}{2}\bar{\varsigma}_5 - 2\bar{\varsigma}_6 \tag{3.7-39}$$

3.7.2 Decomposition of Stiffness Tensor for Orthotropic Material

Similarly, we can write stiffness tensor decomposition for orthotropic material with principal axes of orthotropy along the directions given by unit vectors **p** , **q** and **s**, arbitrarily oriented with respect to the laboratory system as a sum of twelve base tensors $\mathbf{U}_r$ scaled by twelve parameters ϑ, nine of which are independent

$$\boldsymbol{C} = \vartheta_1\mathbf{U}_1 + \vartheta_2\mathbf{U}_2 + \cdots + \vartheta_{12}\mathbf{U}_{12} \tag{3.7-40}$$

where

$$(\mathbf{U_1})_{ijkl} = \frac{1}{2}(\delta_{ik}\delta_{jl} + \delta_{il}\delta_{jk}) \qquad i,j,k,l = 1,2,3 \tag{3.7-41}$$

$$(\mathbf{U_2})_{ijkl} = \delta_{ij}\delta_{kl} \qquad i,j,k,l = 1,2,3 \tag{3.7-42}$$

$$(\mathbf{U_3})_{ijkl} = p_i p_j \delta_{kl} \qquad i,j,k,l = 1,2,3 \tag{3.7-43}$$

$$(\mathbf{U_4})_{ijkl} = \delta_{ij} p_k p_l \qquad i,j,k,l = 1,2,3 \tag{3.7-44}$$

$$(\mathbf{U_5})_{ijkl} = q_i q_j \delta_{kl} \qquad i,j,k,l = 1,2,3 \tag{3.7-45}$$

$$(\mathbf{U_6})_{ijkl} = \delta_{ij} q_k q_l \qquad i,j,k,l = 1,2,3 \tag{3.7-46}$$

$$(\mathbf{U_7})_{ijkl} = \delta_{ik}p_j p_l + \delta_{il}p_j p_k + \delta_{jl}p_i p_k + \delta_{jk}p_i p_l \qquad i,j,k,l = 1,2,3 \tag{3.7-47}$$

$$(\mathbf{U_8})_{ijkl} = \delta_{ik}q_jq_l + \delta_{il}q_jq_k + \delta_{jl}q_iq_k + \delta_{jk}q_iq_l \quad i,j,k,l = 1,2,3 \tag{3.7-48}$$

$$(\mathbf{U_9})_{ijkl} = p_ip_jp_kp_l \quad i,j,k,l = 1,2,3 \tag{3.7-49}$$

$$(\mathbf{U_{10}})_{ijkl} = q_iq_jq_kq_l \quad i,j,k,l = 1,2,3 \tag{3.7-50}$$

$$(\mathbf{U_{11}})_{ijkl} = p_ip_jq_kq_l \quad i,j,k,l = 1,2,3 \tag{3.7-51}$$

$$(\mathbf{U_{12}})_{ijkl} = q_iq_jp_kp_l \quad i,j,k,l = 1,2,3 \tag{3.7-52}$$

and parameters ϑ are given by

$$\vartheta_1 = 2\mu, \vartheta_2 = \lambda, \vartheta_3 = \vartheta_4 = \alpha_{\lambda 1}, \vartheta_5 = \vartheta_6 = \alpha_{\lambda 2}, \vartheta_7 = 2\mu_1, \vartheta_8 = 2\mu_2, \vartheta_9 = \beta_{\lambda 1}, \vartheta_{10} = \beta_{\lambda 2}, \vartheta_{11} = \vartheta_{12} = \beta_{\lambda 3} \tag{3.7-53}$$

We can write the compliance in terms of tensor bases $\mathbf{U}_r$ scaled by parameters $\varkappa_r$

$$\boldsymbol{S} = \boldsymbol{C}^{-1} = \varkappa_1\mathbf{U}_1 + \varkappa_2\mathbf{U}_2 + \cdots + \varkappa_{12}\mathbf{U}_{12} \tag{3.7-54}$$

and we can generate a set of twelve alternative bases $\mathbf{W}_{rs}$ and scaled them by twelve parameters κ_{rs} to produce the compliance tensor

$$\boldsymbol{S} = \boldsymbol{C}^{-1} = \sum_{r,s=1}^{3} \kappa_{rs}\mathbf{W}_{rs} + \kappa_{44}\mathbf{W}_{44} + \kappa_{55}\mathbf{W}_{55} + \kappa_{66}\mathbf{W}_{66} \tag{3.7-55}$$

The bases $\mathbf{W}_{rs}$ in Equation 3.7-55 are defined in terms of unit vectors **p** , **q** and **s** specifying the direction of orthotropy.

$$(\boldsymbol{W_{11}})_{ijkl} = p_i p_j p_k p_l \qquad i,j,k,l = 1,2,3 \tag{3.7-56}$$

$$(\boldsymbol{W_{22}})_{ijkl} = q_i q_j q_k q_l \qquad i,j,k,l = 1,2,3 \tag{3.5-57}$$

$$(\mathbf{W_{33}})_{ijkl} = s_i s_j s_k s_l \qquad i,j,k,l = 1,2,3 \tag{3.7-58}$$

$$(\mathbf{W_{12}})_{ijkl} = p_i p_j q_k q_l \qquad i,j,k,l = 1,2,3 \tag{3.7-59}$$

$$(\boldsymbol{W_{13}})_{ijkl} = p_i p_j s_k s_l \qquad i,j,k,l = 1,2,3 \tag{3.7-60}$$

$$(\boldsymbol{W_{21}})_{ijkl} = q_i q_j p_k p_l \qquad i,j,k,l = 1,2,3 \tag{3.7-61}$$

$$(\boldsymbol{W_{31}})_{ijkl} = s_i s_j p_k p_l \qquad i,j,k,l = 1,2,3 \tag{3.7-62}$$

$$(\boldsymbol{W_{23}})_{ijkl} = q_i q_j s_k s_l \qquad i,j,k,l = 1,2,3 \tag{3.7-63}$$

$$(\boldsymbol{W_{32}})_{ijkl} = s_i s_j q_k q_l \qquad i,j,k,l = 1,2,3 \tag{3.7-64}$$

$$(\boldsymbol{W_{44}})_{ijkl} = \frac{1}{2}(q_i q_k s_j s_l + q_i q_l s_j s_k + q_j q_l s_i s_k + q_j q_k s_i s_l) \qquad i,j,k,l = 1,2,3 \tag{3.7-65}$$

$$(\boldsymbol{W_{55}})_{ijkl} = \frac{1}{2}(s_i s_k p_j p_l + s_i s_l p_j p_k + s_j s_l p_i p_k + s_j s_k p_i p_l) \qquad i,j,k,l = 1,2,3 \tag{3.7-66}$$

$$(\boldsymbol{W_{66}})_{ijkl} = \frac{1}{2}(p_i p_k q_j q_l + p_i p_l q_j q_k + p_j p_l q_i q_k + p_j p_k q_i q_l) \qquad i,j,k,l = 1,2,3 \tag{3.7-67}$$

and the scaling factors κ_{rs} are given in a simple form involving engineering constants of orthotropic materials defined with respect to **p**, **q** and **s**

$$\kappa_{11} = \frac{1}{E_p}, \kappa_{22} = \frac{1}{E_q}, \kappa_{33} = \frac{1}{E_s}, \kappa_{12} = -\frac{\nu_{pq}}{E_p}, \kappa_{13} = -\frac{\nu_{ps}}{E_p}, \kappa_{23} = -\frac{\nu_{qs}}{E_q}, \kappa_{44} = \frac{1}{2G_{qs}}, \kappa_{55} = \frac{1}{2G_{ps}}, \kappa_{66} = \frac{1}{2G_{pq}} \tag{3.7-68}$$

We can now write scaling factors $\varkappa_r$ in terms of κ_{rs}

$$\begin{aligned}
&\varkappa_1 = \kappa_{55} + \kappa_{66} - \kappa_{44}, \qquad \varkappa_2 = \kappa_{33} + \kappa_{44} - \kappa_{55} - \kappa_{66}, \\
&\varkappa_3 = \varkappa_4 = \kappa_{13} - \kappa_{33} - \kappa_{44} + \kappa_{55} + \kappa_{66}, \\
&\varkappa_5 = \varkappa_6 = \kappa_{23} - \kappa_{33} - \kappa_{44} + \kappa_{55} + \kappa_{66}, \\
&\varkappa_7 = \kappa_{44} - \kappa_{55}, \ \ \varkappa_8 = \kappa_{44} - \kappa_{66}, \ \ \varkappa_9 = \kappa_{11} - 2\kappa_{31} + \kappa_{33} - 2\kappa_{66}, \ \ \varkappa_{10} \\
&= \kappa_{22} - 2\kappa_{23} + \kappa_{33} - 2\kappa_{55}, \\
&\varkappa_{11} = \varkappa_{12} = \kappa_{21} - \kappa_{23} - \kappa_{31} + \kappa_{33} + \kappa_{44} - \kappa_{55} - \kappa_{66},
\end{aligned} \tag{3.7-69}$$

and we can base tensors $\mathbf{U}_r$ in terms of $\mathbf{W}_{rs}$

$$\mathbf{U}_1 = \mathbf{W}_{11} + \mathbf{W}_{22} + \mathbf{W}_{33} + \mathbf{W}_{44} + \mathbf{W}_{55} + \mathbf{W}_{66} \tag{3.7-70}$$

$$\mathbf{U_2} = \mathbf{W}_{11} + \mathbf{W}_{12} + \mathbf{W}_{13} + \mathbf{W_{21}} + \mathbf{W_{22}} + \mathbf{W_{23}} + \mathbf{W_{31}} + \mathbf{W_{32}} + \mathbf{W_{33}} \tag{3.7-71}$$

$$\mathbf{U_3} = \mathbf{W}_{11} + \mathbf{W}_{12} + \mathbf{W}_{13} \tag{3.7-72}$$

$$\mathbf{U_4} = \mathbf{W}_{11} + \mathbf{W_{21}} + \mathbf{W_{31}} \tag{3.7-73}$$

$$\mathbf{U_5} = \mathbf{W}_{21} + \mathbf{W}_{22} + \mathbf{W}_{23} \tag{3.7-74}$$

$$\mathbf{U_6} = \mathbf{W}_{12} + \mathbf{W_{22}} + \mathbf{W}_{32} \tag{3.7-75}$$

$$\mathbf{U_7} = \mathbf{2W_{11}} + \mathbf{W_{55}} + \mathbf{W_{66}} \tag{3.7-76}$$

$$\mathbf{U_8} = \mathbf{2W_{22}} + \mathbf{W_{44}} + \mathbf{W_{66}} \tag{3.7-77}$$

$$\mathbf{U_9} = \mathbf{W}_{11} \tag{3.7-78}$$

$$\mathbf{U_{10}} = \mathbf{W_{22}} \tag{3.7-79}$$

$$\mathbf{U_{11}} = \mathbf{W_{12}} \tag{3.7-80}$$

$$\mathbf{U_{12}} = \mathbf{W}_{21} \tag{3.7-81}$$

With the inverse relationships of $\mathbf{W}_{rs}$ in terms of $\mathbf{U}_r$ are easily obtainable. We can then clearly re-write Equation 3.7-40 as

$$\boldsymbol{C} = \sum_{r,s=1}^{3} \chi_{rs}\mathbf{W}_{rs} + \chi_{44}\mathbf{W}_{44} + \chi_{55}\mathbf{W}_{55} + \chi_{66}\mathbf{W}_{66} \tag{3.7-82}$$

where

$$\begin{aligned} &\chi_{11} = \lambda + 2\mu + 4\mu_1 + 2\alpha_{\lambda 1} + \beta_{\lambda 1}, \qquad \chi_{22} = \lambda + 2\mu + 4\mu_2 + 2\alpha_{\lambda 2} + \beta_{\lambda 2}\,, \\ &\chi_{33} = \lambda + 2\mu, \qquad \chi_{12} = \lambda + \alpha_{\lambda 1} + \alpha_{\lambda 2} + \beta_{\lambda 3}, \qquad \chi_{23} = \lambda + \alpha_{\lambda 2}, \\ &\chi_{31} = \lambda + \alpha_{\lambda 1}, \qquad \chi_{44} = 2(\mu + \mu_2), \qquad \chi_{55} = 2(\mu + \mu_1), \\ &\chi_{66} = 2(\mu + \mu_1 + \mu_2) \end{aligned} \tag{3.7-83}$$

To obtain the inverse of **C** to obtain **S**, we can use

$$\kappa_{11} = \frac{\chi_{22}\chi_{33} - {\chi_{22}}^2}{\chi}, \kappa_{12} = \kappa_{21} = \frac{\chi_{31}\chi_{23} - \chi_{12}\chi_{33}}{\chi}, \kappa_{22} = \frac{\chi_{11}\chi_{33} - {\chi_{31}}^2}{\chi}, \kappa_{23} = \kappa_{32} = \frac{\chi_{12}\chi_{31} - \chi_{11}\chi_{23}}{\chi}, \kappa_{31} = \kappa_{13} = \frac{\chi_{12}\chi_{23} - \chi_{31}\chi_{22}}{\chi}, \kappa_{33} = \frac{\chi_{11}\chi_{22} - {\chi_{12}}^2}{\chi}, \kappa_{44} = \frac{1}{\chi_{44}}, \kappa_{55} = \frac{1}{\chi_{55}}, \kappa_{66} = \frac{1}{\chi_{66}} \tag{3.7-84}$$

where

$$\chi = \chi_{11}\chi_{22}\chi_{33} + 2\chi_{12}\chi_{23}\chi_{31} - \chi_{11}{\chi_{23}}^2 - \chi_{22}{\chi_{31}}^2 - \chi_{33}{\chi_{12}}^2 \tag{3.7-85}$$

A transversely isotropic material can be recovered by taking

$$\chi_{22} = \chi_{11}, \chi_{23} = \chi_{31}, \chi_{55} = \chi_{44} = \chi_{11} - \chi_{12} \qquad 3.7\text{-}86)$$

3.8 Orientation Tensors and Stiffness of Straight Fiber

The concept of orientation tensor is introduced for straight rigid fiber and relationship between orientation tensors and stiffness tensor is elucidated in this section. The work of Advani and Tucker [8] is followed.

First, we introduce a unit orientation vector **p** to describe orientation of straight rigid fiber

$$p_1 = \sin\theta\cos\phi \tag{3.8-1}$$

$$p_2 = \sin\theta\sin\phi \tag{3.8-2}$$

$$p_3 = \cos\theta \tag{3.8-3}$$

where angles θ and ϕ are defined in Figure 3-4.

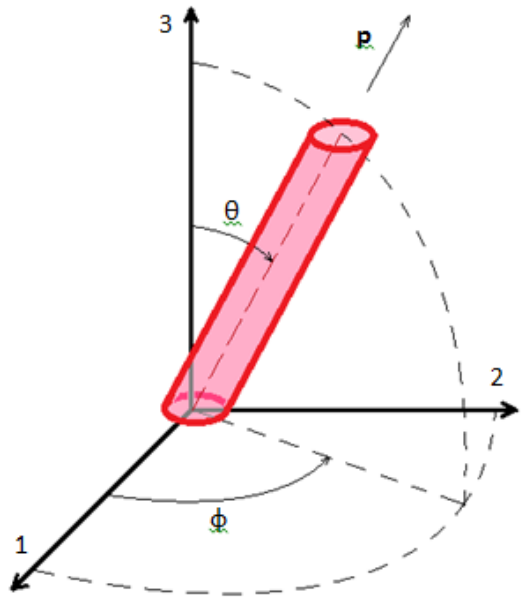

Figure 3-4. Coordinate system and definition of θ, ϕ and orientation vector **p**.

The orientation of an ensemble of fibers can be described by probability density function $\psi(\theta, \phi)$ or equivalently $\psi(\boldsymbol{p})$, which we will call orientation distribution function. $\psi(\theta, \phi)$ is defined so that the probability of finding a fiber between angles θ_1 and $\theta_1 + d\theta$, and ϕ_1 and $\phi_1 + d\phi$ is given by

$$P(\theta_1 \leq \theta \leq \theta_1 + d\theta, \phi_1 \leq \phi \leq \phi_1 + d\phi) = \psi(\theta_1, \phi_1) \sin\theta_1 \, d\theta d\phi \tag{3.8-4}$$

The function ψ must be periodic

$$\psi(\theta, \phi) = \psi(\pi - \theta, \phi + \pi) \; or \; \psi(\boldsymbol{p}) = \psi(-\boldsymbol{p}) \tag{3.8-5}$$

and normalized, since every fiber has some orientation.

$$\int_{\theta=0}^{\pi} \int_{\phi=0}^{2\pi} \psi(\theta, \phi) \sin\theta \, d\theta d\phi = \oint \psi(\boldsymbol{p}) d\boldsymbol{p} = 1 \tag{3.8-6}$$

The orientation distribution function ψ is a complete description of fiber orientation, however it does not lend itself to easy numerical computation. Following Advani and Tucker [8], we can

define a set of orientation tensors by forming dyadic product of vector **p** and then integrating the product of these tensors with the distribution function over all possible directions. Only even-order integrals are non-zero due to ψ being even as apparent in Equation 3.8-5, therefore we can write second and fourth order orientation tensors as

$$a_{ij} = \langle p_i p_j \rangle \;=\; \oint p_i p_j \psi(\boldsymbol{p}) d\boldsymbol{p} \quad i,j = 1,2,3 \tag{3.8-7}$$

$$a_{ijkl} = \langle p_i p_j p_k p_l \rangle \;=\; \oint p_i p_j p_k p_l \psi(\boldsymbol{p}) d\boldsymbol{p} \quad i,j,k,l = 1,2,3 \tag{3.8-8}$$

From these definitions, we note the tensorial nature and symmetry

$$a_{ij} = a_{ji} \tag{3.8-9}$$

$$a_{ijkl} = a_{jikl} = a_{kijl} = a_{lijk} = a_{klij}, \qquad etc. \tag{3.8-10}$$

From normalization condition in Equation 3.8-6, we see that

$$a_{ii} = 1 \tag{3.8-11}$$

And we can prove that higher order orientation tensor contains information about lower order orientation tensor, such as

$$a_{ijkk} = a_{ij} \tag{3.8-12}$$

Advani and Tucker [8] state that fourth order tensor with symmetries given in Equation 3.2-10, with transverse isotropy about the direction **p**, the tensor must have the following form

$$C_{ijkl}(\boldsymbol{p}) = B_1(p_i p_j p_k p_l) + B_2(p_i p_j \delta_{kl} + p_k p_l \delta_{ij}) + B_3(p_i p_k \delta_{jl} + p_i p_l \delta_{ik} + p_j p_l \delta_{ik} + p_j p_k \delta_{il}) + B_4(\delta_{ij}\delta_{kl}) + B_5(\delta_{ik}\delta_{jl} + \delta_{il}\delta_{jk}) \qquad i,j,k,l = 1,2,3 \tag{3.8-13}$$

where we write the fourth order tensor directly as the stiffness tensor with scalars B_i, given by the components of a stiffness tensor $\overline{C_{ij}}$ for a material with fibers aligned with $\boldsymbol{e}_1$:

$$B_1 = \overline{C_{11}} + \overline{C_{22}} - 2\overline{C_{12}} - 4\overline{C_{66}} \tag{3.8-14}$$

$$B_2 = \overline{C_{12}} - \overline{C_{23}} \tag{3.8-15}$$

$$B_3 = \overline{C_{66}} + \frac{1}{2}(\overline{C_{23}} - \overline{C_{22}}) \tag{3.8-16}$$

$$B_4 = \overline{C_{23}} \tag{3.8-17}$$

$$B_5 = \frac{1}{2}(\overline{C_{22}} - \overline{C_{23}}) \tag{3.8-18}$$

We can observe that in Equation 3.8-13, we have simply re-stated Equation 3.7-15.

To obtain stiffness tensor for continuum containing an ensemble of fibers, Advani and Tucker [8] use the notion of orientation averaging

$$\langle C \rangle_{ijkl} = B_1 < p_i p_j p_k p_l > + B_2 < p_i p_j \delta_{kl} + p_k p_l \delta_{ij} > + B_3 < p_i p_k \delta_{jl} + p_i p_l \delta_{ik} + p_j p_l \delta_{ik} + p_j p_k \delta_{il} > + B_4(\delta_{ij}\delta_{kl}) + B_5(\delta_{ik}\delta_{jl} + \delta_{il}\delta_{jk}) \qquad i,j,k,l = 1,2,3 \tag{3.8-19}$$

which using definitions 3.8-7 and 3.8-8 can be written as

$$\langle C\rangle_{ijkl} = B_1 a_{ijkl} + B_2(a_{ij}\delta_{kl} + a_{kl}\delta_{ij})$$

$$+B_3(a_{ik}\delta_{jl} + a_{il}\delta_{ik} + a_{jl}\delta_{ik} + a_{jk}\delta_{il}) + B_4(\delta_{ij}\delta_{kl}) \tag{3.8-20}$$

$$+B_5(\delta_{ik}\delta_{jl} + \delta_{il}\delta_{jk}) \qquad i,j,k,l = 1,2,3$$

It is therefore apparent that fourth order orientation tensor is sufficient for calculation of stiffness tensor if we use orientation averaging in a continuum containing an ensemble of fibers. A higher order orientation tensor would provide more accurate description of the probability density function ψ. However this information would not be reflected in calculation of the orientation average from the fourth order orientation tensor using Equations 3.8-20 and 3.8-12.

3.9 Transversely Isotropic Constants from Halpin-Tsai-Kardos Equations

We now wish to determine stiffness of composite reinforced with straight fibers of uniform ratio of length to diameter $\xi = \frac{L}{d}$. This can be done experimentally, numerically or using semi-empirical Halpin-Tsai Equations with parameter ξ_{HK} as shown by Halpin and Kardos [55]. We realize that this material is transversely isotropic and that we can write its compliance tensor in Voigt notation assuming fibers aligned in the x_1 direction [1]

$$\mathbf{S} = \begin{bmatrix} S_{11} & S_{12} & S_{12} & 0 & 0 & 0 \\ & S_{22} & S_{23} & 0 & 0 & 0 \\ & & S_{22} & 0 & 0 & 0 \\ & & & 2(S_{22}-S_{23}) & 0 & 0 \\ & sym. & & & S_{55} & 0 \\ & & & & & S_{55} \end{bmatrix} \tag{3.9-1}$$

where

$$S_{11} = \frac{1}{E_1}, S_{12} = -\frac{\nu_{12}}{E_1}, S_{22} = \frac{1}{E_2}, S_{23} = -\frac{\nu_{23}}{E_2}, S_{55} = \frac{1}{G_{12}} \tag{3.9-2}$$

We assume isotropic material properties for matrix and fibers with known Young's moduli E_m, E_f and Poisson's ratio ν_m, ν_f, which are the constituents for a composite of fiber volume fraction V_f. We can calculate shear modulus of the constituents using

$$G_m = \frac{E_m}{2(1+\nu_m)}, G_f = \frac{E_f}{2(1+\nu_m)} \tag{3.9-3}$$

We can now use the following formula to establish material constant Q of the composite material using [55]

$$Q = Q_m \frac{1+\xi_{HK}\eta_{HK}V_f}{1-\eta_{HK}V_f} \tag{3.9-4}$$

where

$$\eta_{HK} = (\frac{Q_f}{Q_m} - 1)/(\frac{Q_f}{Q_m} + \xi_{HK}) \tag{3.9-5}$$

and where ξ_{HK} depends on the material constant Q.

For longitudinal composite modulus E_1, we set $Q = E_1, Q_m = E_m, Q_f = E_f$ with

$$\xi_{HK} = 2\frac{L}{d} = 2\xi \tag{3.9-6}$$

For transverse modulus E_2 in the plane of isotropy, we set $Q = E_2, Q_m = E_m, Q_f = E_f$ with

$$\xi_{HK} = 2\frac{d}{d} = 2 \tag{3.9-7}$$

For shear modulus G_{12} in the plane of isotropy, we set $Q = G_{12}, Q_m = G_m, Q_f = G_f$ with

$$\xi_{HK} = 1 \tag{3.9-8}$$

For shear modulus $G_{23} = \frac{E_2}{2(1+\nu_{23})}$, we follow Advani and Tucker [8] and set $Q = G_{23}, Q_m = G_m$, $Q_f = G_f$ with

$$\xi_{HK} = \frac{K_m/G_m}{(K_m/G_m + 2)} \tag{3.9-9}$$

where K_m is the matrix bulk modulus

$$K_m = \frac{E_m}{3(1 - 2\nu_m)} \tag{3.9-10}$$

We can calculate the remaining Poisson's coefficient using

$$\nu_{12} = \nu_f V_f + \nu_m (1 - V_f) \tag{3.9-11}$$

Therefore, we now have five independent constants that can be used in Equations 3.9-1 and 3.9-2. We wish to find $\mu, \lambda, \alpha_\lambda, \mu_0, \beta_\lambda$in Equations 3.7-15 through 3.7-22 as a function of $E_1, E_2, G_{12,}G_{23}, \nu_{12}$. To accomplish this, we set $p_i = \delta_{i1}$ in Equations 3.7-15 through 3.7-22 so that our material would be aligned x_1 direction as in Equation 3.9-1 and contract into Voigt notation. We find that

$$S_{11} = -\frac{\lambda + \mu}{{\alpha_\lambda}^2 - 2\alpha_\lambda\mu + \lambda\mu + 2\mu^2 - \beta_\lambda(\lambda + \mu) - 4\lambda\mu_0 - 4\mu\mu_0} \quad ,$$

$$S_{12} = \frac{\alpha_\lambda + \lambda}{2({\alpha_\lambda}^2 - 2\alpha_\lambda\mu + \lambda\mu + 2\mu^2 - \beta_\lambda(\lambda + \mu) - 4\lambda\mu_0 - 4\mu\mu_0)} \quad ,$$

$$S_{22} = \frac{{\alpha_\lambda}^2 - 4\alpha_\lambda\mu - \beta_\lambda(\lambda + 2\mu) + 4(\mu^2 - \lambda\mu_0 - 2\mu\mu_0)}{4\mu({\alpha_\lambda}^2 - 2\alpha_\lambda\mu + \lambda\mu + 2\mu^2 - \beta_\lambda(\lambda + \mu) - 4\lambda\mu_0 - 4\mu\mu_0)} \quad ,$$

$$S_{23} = \frac{-{\alpha_\lambda}^2 + \lambda(\beta_\lambda - 2\mu + 4\mu_0)}{4\mu({\alpha_\lambda}^2 - 2\alpha_\lambda\mu + \lambda\mu + 2\mu^2 - \beta_\lambda(\lambda + \mu) - 4\lambda\mu_0 - 4\mu\mu_0)} \quad , \tag{3.9-12}$$

$$S_{44} = \frac{1}{\mu} \quad ,$$

$$S_{55} = \frac{1}{\mu_0}$$

Now we can equate Equation 3.9-2 with Equation 3.9-12 and obtain

$$\mu = G_{23}, \qquad \mu_0 = G_{12}, \qquad \lambda = \frac{E_2(E_2{\nu_{12}}^2 + E_1\nu_{23})}{(2E_2{\nu_{12}}^2 + E_1(\nu_{23} - 1))(1 + \nu_{23})},$$

$$\alpha_\lambda = \frac{E_2(E_2{\nu_{12}}^2 - E_1(\nu_{12} + (\nu_{12} - 1)\nu_{23})}{(2E_2{\nu_{12}}^2 + E_1(\nu_{23} - 1))(1 + \nu_{23})}, \tag{3.9-13}$$

$$\beta_\lambda = E_1 - 4G_{12} - \frac{E_1E_2(1 - \nu_{23})^2}{4E_2{\nu_{12}}^2 + 2E_1(\nu_{23} - 1)} + G_{23}$$

These are five material constants that will be used in formulation of transversely isotropic stiffness tensor.

4. Stiffness Model for Curved Fiber

4.1. Curved Fiber Model - Introduction

In this section, we make assumptions about the microstructure of discontinuous fiber composite containing curved fibers and provide method for obtaining the stiffness tensor, which accounts for fiber curvature in a systematic manner. This approach is novel and to the knowledge of the authors the first model allowing investigation of the nature of anisotropy induced by fiber curvature in this manner. Other approaches given in literature make assumptions about the nature of anisotropy first and subsequently modify coefficients in the stiffness tensor of an assumed form.

We begin by obtaining bent fiber in general configuration with respect to laboratory coordinates by performing four successive operations. We discuss parameters of this configuration and continue by providing probability distribution function describing an ensemble of fibers with arbitrary configuration. We then show that an ensemble of fibers with single configuration possesses orthotropic symmetry, which allows us to use decomposed form of stiffness (or compliance) tensor in a suitable form. We then perform configuration averaging, analogous to orientation averaging, performed by Advani and Tucker [8] for straight rigid fibers. This gives us an anisotropic stiffness (or compliance) for an ensemble of fibers in terms of nine parameters defining properties of orthotropic material with fibers in single configuration. We discuss the possibilities for obtaining these parameters and provide a solution based on orientation averaging and semi-empirical Halpin-Kardos [55] Equations.

4.2. Configuration of a Single Curved Fiber

We first define a fiber coordinate system $f = (\mathbf{p},\mathbf{q},\mathbf{s})$ as a Cartesian coordinate system defined by orthonormal vectors **p**, **q** and **s**. We assume straight cylindrical fiber of length L and diameter d and place it so that the center of the fiber coincides with the origin of f and fiber centerline is parallel to **p** as shown in Figure 4-1.

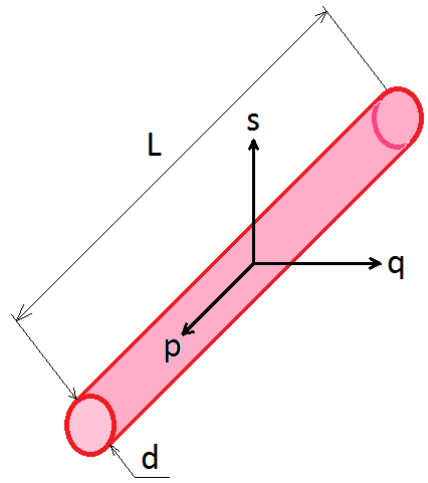

Figure 4-1. Straight cylindrical fiber with coordinate system $f = (\mathbf{p},\mathbf{q},\mathbf{s})$.

Note that this geometry is symmetric with respect to planes intersecting origin of f given by normals **p**, **q** and **s**. Therefore reflections $R_{ij}(\boldsymbol{p}), R_{ij}(\boldsymbol{q})$ and $R_{ij}(\boldsymbol{s})$ defined in Equation 3.6-3 project the geometry of fiber on itself and that this configuration is defined by a single dimensionless parameter $= \frac{L}{d}$.

We can now perform four successive operations that will give us bent fiber in general configuration with respect to laboratory coordinate system.

1. We bend the fiber so that the oriented curvature $\boldsymbol{\rho}$ is given by $= \frac{1}{R}\boldsymbol{q}$, where R is the radius of curvature. This is equivalent to describing a section of toroid in cylindrical coordinates $(r, \varphi, \bar{z})$ with system origin at R**q** , z axis aligned with **s** and F_i measured from $\bar{x}$ in mathematically positive sense as shown in Figure 4-2.

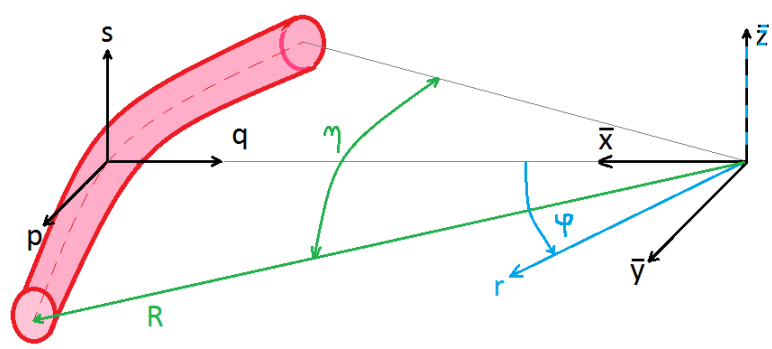

Figure 4-2. Bent fiber with radius R.

The length of the centerline remains L, diameter remains d and **p** remains tangent to the centerline at the center of the fiber. This configuration is given by two dimensionless parameters $\xi = \frac{L}{d}$ and $\eta = \frac{L}{R}$. This geometry is still symmetric with respect to $R_{ij}(\boldsymbol{p})$ and $R_{ij}(\boldsymbol{s})$ however $R_{ij}(\boldsymbol{q})$ no longer projects this configuration on itself.

We will only consider non-degenerate cases, where every fiber has two ends and does not form a toroid. Our limits on radius of curvature consist of a straight fiber ($R_{max} = \infty$), and minimum curvature for fiber near its elastic limit in bending. Using mechanics of materials approach to calculate maximum strain ε_m for a fiber in pure bending

$$\varepsilon_m = \frac{\frac{d}{2}}{R} \tag{4.2-1}$$

Therefore maximum stress σ_m for a fiber of isotropic, homogeneous material with Young's modulus E, subjected to pure bending can be written as

$$\sigma_m = \frac{E}{R}\frac{d}{2} \tag{4.2-2}$$

This results in minimum radius for curvature

$$R_{min} = \frac{E}{\sigma_u}\frac{d}{2} \tag{4.2-3}$$

where σ_u is ultimate stress for the fiber material.

2. Rotate fiber coordinate system f = (**p,q,s**) around **s** by α. This rotation is described by Equation 3.4-20.
3. Rotate fiber coordinate system f = (**p,q,s**) around **q** by β. This rotation is described by Equation 3.4-22. Note that tor the limit case of a straight fiber ($\eta = 0$), we obtain coordinate system as described by Advani and Tucker. The angles are illustrated in Figure 4-3.

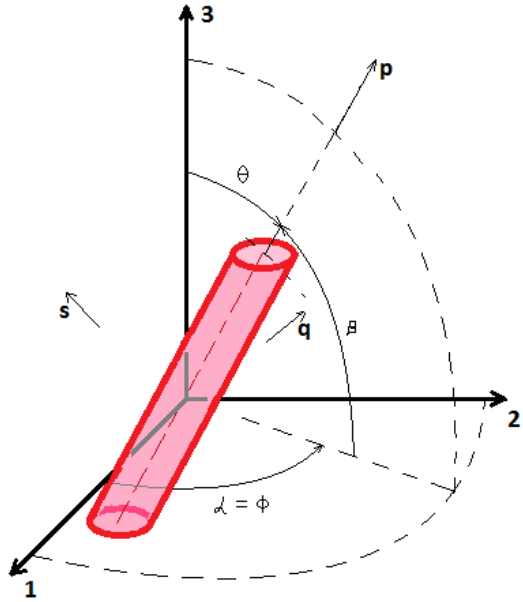

Figure 4-3. Limit case of straight fiber ($R_{max} = \infty$), with Euler angles α, β and coordinate system defined in Advani-Tucker [8].

The Euler angles can be converted to angles defined by Advani-Tucker [8]:

$$\phi = \alpha \tag{4.2-4}$$

$$\theta = \frac{\pi}{2} - \beta \tag{4.2-5}$$

Notice that orientation vector **p** conveniently coincides with vector **p** defining fiber coordinate system.

4. Rotate fiber coordinate system f = (**p**,**q**,**s**) around **p** by γ. This rotation is described by Equation 3.4-24 and results in coordinate system shown in Figure 4-4.

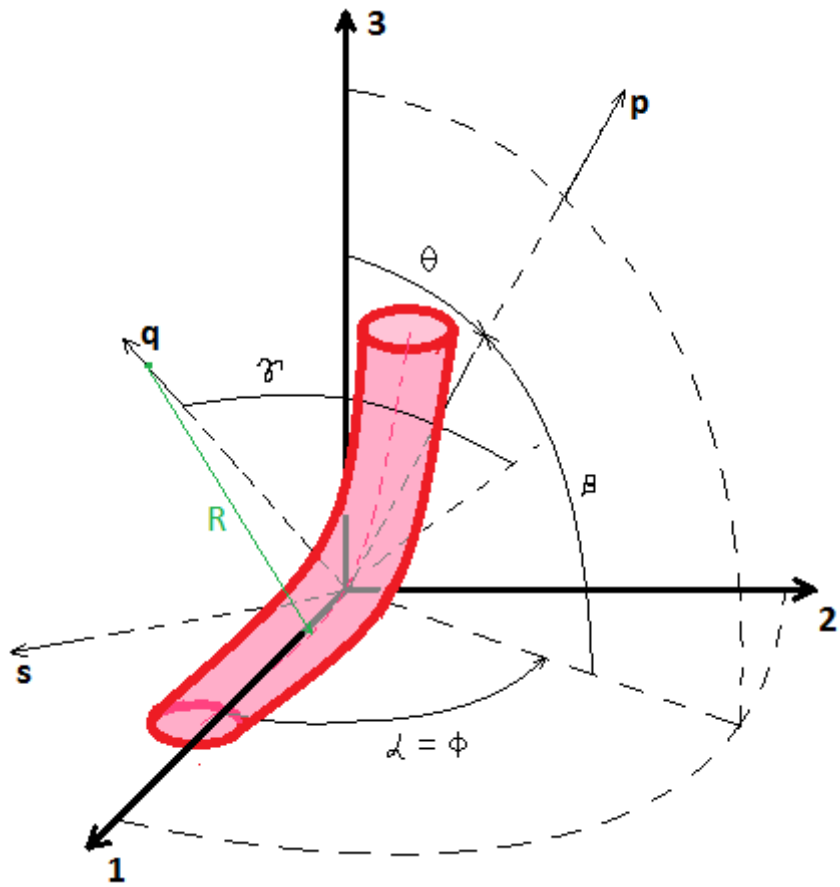

Figure 4-4. Bent fiber with coordinate system f = (**p**,**q**,**s**), defined by Euler angles α, β, γ.

The configuration of a curved fiber with centerline length L, diameter d and radius of curvature R positioned arbitrarily in the laboratory system can be described by five non-dimensional parameters $\alpha, \beta, \gamma, \xi, \eta$. Equivalently, we can describe configuration of a fiber by unit vectors **p**, **q** and parameters ξ, η. Three components of vector **p** are defined from two Euler angles α, β and normalization condition |**p**|=1. Three components of vector **q** are defined by Euler angle γ, normalization condition |**q**|=1 and orthogonality $\mathbf{p}.\mathbf{q} = 0$.

Note that for $\eta = 0$, configuration remains the same regardless of angle γ as shown in Equation 3.4-32, and we obtain standard description for straight fiber using orientation vector **p** and ratio ξ. The correspondence of Euler angles α, β and orientation angles ϕ, θ is given in Equations 4.2-4 and 4.2-5.

4.3. Configuration Distribution Function

We now describe configuration of an ensemble of fibers using probability density function $\psi_C(\alpha, \beta, \gamma, \xi, \eta)$. We can also write $\psi_C(\mathbf{p}, \mathbf{q}, \xi, \eta)$or $\psi_C(\mathbf{p}, \mathbf{s}, \xi, \eta)$ or $\psi_C(\mathbf{q}, \mathbf{s}, \xi, \eta)$ since angles α, β, γ define fiber coordinate system f = (**p**,**q**,**s**). We define this function so that probability of

finding a fiber with configuration given by angles and parameters $\alpha, \beta, \gamma, \xi, \eta$ between $\alpha_1, \alpha_1 + d\alpha_1;\ \beta_1, \beta_1 + d\beta_1; \gamma_1, \gamma_1 + d\gamma_1; \xi_1, \xi_1 + d\xi_1; \eta_1, \eta_1 + d\eta_1$ is given by

$$\begin{aligned} P(\alpha_1 \le \alpha \le \alpha_1 + d\alpha_1, \beta_1 \le \beta \le \beta_1 + d\beta_1, \gamma_1 \le \gamma \le \gamma_1 + d\gamma_1, \xi_1 \le \xi \\ \le +\xi_1 + d\xi_1, \eta_1 \le \eta \le +\eta_1 + d\eta_1) \\ = \psi(\alpha_1, \beta_1, \gamma_1, \xi_1, \eta_1) \cos\beta_1 \ d\alpha d\beta d\gamma d\xi d\eta \end{aligned} \tag{4.3.1}$$

and call ψ configuration distribution function. We can use Equation 4.2-5 and show that

$$\psi(\alpha, \beta, \gamma, \xi, \eta) \cos\beta \ d\alpha d\beta d\gamma d\xi d\eta = \psi\left(\phi, \frac{\pi}{2} - \theta, \gamma, \xi, \eta\right) \sin\theta \ d\theta d\phi d\gamma d\xi d\eta \tag{4.3-2}$$

If we assume straight fiber with constant $\xi = \frac{L}{d}$ as was done by Advani and Tucker [8], the right hand side of Equation 4.3-2 reduces orientation distribution function given in Equation 3.8-4.

The configuration function is normalized

$$\begin{aligned} &\int_{\eta=0}^{\infty} \int_{\xi=0}^{\infty} \int_{\gamma=0}^{2\pi} \int_{\theta=0}^{\pi} \int_{\phi=0}^{2\pi} \psi_C(\phi, \theta, \gamma, \xi, \eta) \sin\theta \ d\phi d\theta d\gamma d\xi d\eta \\ &= \int_{\eta=0}^{\infty} \int_{\xi=0}^{\infty} \int_{\gamma=0}^{2\pi} \int_{\beta=-\pi/2}^{\pi/2} \int_{\alpha=0}^{2\pi} \psi_C(\alpha, \beta, \gamma, \xi, \eta) \cos\beta \ d\alpha d\beta d\gamma d\xi d\eta = 1 \end{aligned} \tag{4.3-3}$$

with the following property being apparent from the geometric symmetry as illustrated in Figure 4-4.

$$\psi_C(\mathbf{p}, \mathbf{q}, \xi, \eta) = \psi_C(-\mathbf{p}, \mathbf{q}, \xi, \eta) \ and \ \psi_C(\mathbf{p}, \mathbf{s}, \xi, \eta) = \psi_C(-\mathbf{p}, -\mathbf{s}, \xi, \eta) \tag{4.3-4}$$

4.4. Orthotropic Stiffness Tensor for Material with Fibers in Single Configuration

We now imagine material consisting of an ensemble of uniformly dispersed fibers of a single configuration within a matrix as illustrated in Figure 4-5.

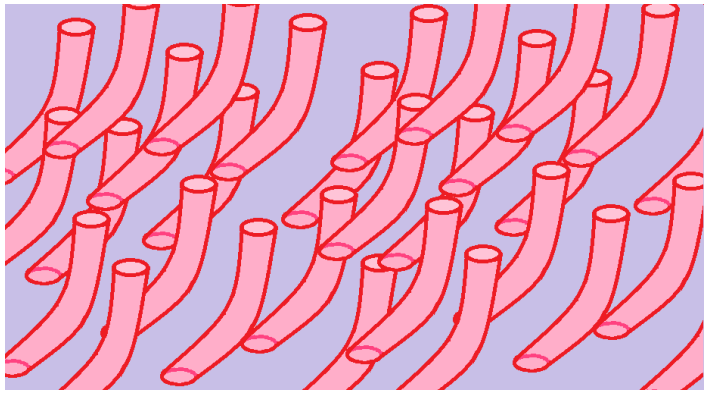

Figure 4-5. Material with fibers in single configuration.

A single fiber shown in Figure 4-4 would then be a representative volume for such material. We can inspect Figure 4-4 and conclude that there exists geometrical symmetry with respect to a plane with normal **p** and to a plane with normal s. Since our imaginary material consists of fibers in single configuration, the resulting material will also have two material planes of symmetry. Using Equation 3.6-3, we can write two transformations under which a stiffness tensor remains invariant

$$R_{ij}(\boldsymbol{p}) = \delta_{ij} - p_i p_j \qquad i,j = 1,2,3 \tag{4.4-1}$$

$$R_{ij}(\boldsymbol{s}) = \delta_{ij} - s_i s_j \qquad i,j = 1,2,3 \tag{4.4-2}$$

We note that vectors **p** and **s** enclose angle of $\frac{1}{2}\pi$ which was shown to imply third plane of symmetry and result in orthotropic material with nine constants as shown in Section 3.6. Using Equations 3.7-40 through 3.7-53, we can write the form of material containing fibers in single configuration

$$\begin{gathered}\tilde{C}_{ijkl} = \mu\left(\delta_{ik}\delta_{jl} + \delta_{il}\delta_{jk}\right) + \lambda\delta_{ij}\delta_{kl} + \alpha_{\lambda 1}\left(p_i p_j \delta_{kl} + \delta_{ij} p_k p_l\right) + \alpha_{\lambda 2}\left(q_i q_j \delta_{kl} + \right. \\ \left. \delta_{ij} q_k q_l\right) + 2\mu_1\left(\delta_{ik} p_j p_l + \delta_{il} p_j p_k + \delta_{jl} p_i p_k + \delta_{jk} p_i p_l\right) + 2\mu_2\left(\delta_{ik} q_j q_l + \delta_{il} q_j q_k + \right. \\ \left. \delta_{jl} q_i q_k + \delta_{jk} q_i q_l\right) + \beta_{\lambda 1} p_i p_j p_k p_l + \beta_{\lambda 2} q_i q_j q_k q_l + \beta_{\lambda 3}\left(p_i p_j q_k q_l + q_i q_j p_k p_l\right) \\ i,j,k,l = 1,2,3\end{gathered} \tag{4.4-3}$$

We can observe that for straight fiber, the material does not change with arbitrary choice of γ, which defines vector **q**. After removing terms containing vector **q**, which is undefined for straight fiber, the form of Equation 4.4-3 for orthotropic material reduces to the form given by

Advani and Tucker [8] in Equation 3.8-13 for transversely isotropic material with corresponding reduction in material constants from 9 to 5.

4.5. Configuration Averaging for Material with Arbitrary Fiber Configuration

We now perform configuration averaging to obtain the stiffness tensor for material containing fibers described by configuration distribution function ψ. This procedure is analogous to orientation averaging and we define configuration average of stiffness tensor as

$$\langle\langle\langle\langle C_{ijkl}\rangle\rangle\rangle\rangle = \int_{\eta=0}^{\infty}\int_{\xi=0}^{\infty}\int_{\gamma=0}^{2\pi}\int_{\theta=0}^{\pi}\int_{\phi=0}^{2\pi} \tilde{C}_{ijkl}\psi_C(\phi,\theta,\gamma,\xi,\eta)\sin\theta \;\; d\theta d\phi d\gamma d\xi d\eta \qquad i,j,k,l = 1,2,3 \tag{4.5-1}$$

Where we used quadruple brackets to indicate configuration averaging. Combining Equation 4.4-3 and 4.5-1 results in the most general form of stiffness tensor for material containing curved fibers with assumptions listed in this document. Such expression would appear to be cumbersome in numerical calculations and experimental measurement of $\psi(\phi,\theta,\gamma,\xi,\eta)$, where parameters of the configuration distribution function are not independent, appears intractable at this time.

We therefore make an assumption about the form of ψ, which would allow us to perform easier calculations and physical measurements. A convenient form would appear to be

$$\psi_C(\phi,\theta,\gamma,\xi,\eta) = \psi_R(\phi,\theta,\gamma)\psi_S(\xi,\eta) \tag{4.5-2}$$

Where we assume the rotation of fiber coordinate system with respect to laboratory system given by three angles and the shape of a fiber given by parameters ξ,η are independent for an arbitrary configuration. We place the following normalization conditions on the rotation distribution function ψ_R and shape distribution function ψ_S

$$\int_{\gamma=0}^{2\pi}\int_{\theta=0}^{\pi}\int_{\phi=0}^{2\pi} \psi_R(\phi,\theta,\gamma)\sin\theta \;\; d\theta d\phi d\gamma = 1 \tag{4.5-3}$$

$$\int_{\eta=0}^{\infty}\int_{\xi=0}^{\infty}\psi_S(\xi,\eta)d\xi d\eta = 1 \tag{4.5.4}$$

Equation 4.3-3 is clearly satisfied. It is useful to view rotation distribution function as a product of probability of finding orientation vector **p** given by angles ϕ,θ and probability of finding vector **q** in the plane defined by vector **p** and angle γ. If we integrate ψ_R over all possible angles γ, we are left with the fiber orientation distribution function

$$\psi(\phi,\theta) = \int_{\gamma=0}^{2\pi}\psi_R(\phi,\theta,\gamma)d\gamma \tag{4.5-5}$$

For material with straight fibers of constant $\xi = \frac{L}{d}$, configuration averaging reduces to orientation averaging.

We started exploring averaged stiffness tensor by realizing that material constants in Equation 4.4-3 are independent of orientation of fiber coordinate system with respect to laboratory system, however, they depend on parameters ξ and η for a particular configuration. Therefore we can write

$$\mu = \mu(\xi,\eta) \tag{4.5-6}$$

$$\lambda = \lambda(\xi,\eta) \tag{4.5-7}$$

$$\mu_1 = \mu_1(\xi,\eta) \tag{4.5-8}$$

$$\mu_2 = \mu_2(\xi,\eta) \tag{4.5-9}$$

$$\alpha_{\lambda 1} = \alpha_{\lambda 1}(\xi,\eta) \tag{4.5-10}$$

$$\alpha_{\lambda 2} = \alpha_{\lambda 2}(\xi,\eta) \tag{4.5-11}$$

$$\beta_{\lambda 1} = \beta_{\lambda 1}(\xi, \eta) \tag{4.5-12}$$

$$\beta_{\lambda 2} = \beta_{\lambda 2}(\xi, \eta) \tag{4.5-13}$$

$$\beta_{\lambda 3} = \beta_{\lambda 3}(\xi, \eta) \tag{4.5-14}$$

In the previous section, we have also shown that orientation vector **p** for any configuration is obtained by two rotations through angles α, β or ϕ, θ. The curvature vector **q** is then obtained by additional rotation around **p** through angle γ. We can therefore write

$$\boldsymbol{p} = \boldsymbol{p}(\alpha, \beta\ )\ or\ \boldsymbol{p} = \boldsymbol{p}(\phi, \theta) \tag{4.5-15}$$

$$\boldsymbol{q} = \boldsymbol{q}(\alpha, \beta\ , \gamma)\ or\ \boldsymbol{q} = \boldsymbol{q}(\phi, \theta, \gamma) \tag{4.5-16}$$

where the form of **p** and **q** can be found in Equations 3.4-33 through 3.4-35 and 3.4-39 through 3.4-41.

We can now perform configuration averaging on each term of Equation 4.4-3 separately. We note that the terms will have one of the following forms

$$k(\xi, \eta)\delta_{ij}\delta_{kl} \tag{4.5-17}$$

$$k(\xi, \eta)\left(p_i(\phi, \theta)p_j(\phi, \theta)\right)\delta_{kl} \tag{4.5-18}$$

$$k(\xi, \eta)\left(q_i(\phi, \theta, \gamma)q_j(\phi, \theta, \gamma)\right)\delta_{kl} \tag{4.5-19}$$

$$k(\xi, \eta)\left(p_i(\phi, \theta)p_j(\phi, \theta)p_k(\phi, \theta)p_l(\phi, \theta)\right) \tag{4.5-20}$$

$$k(\xi, \eta)\left(q_i(\phi, \theta, \gamma)q_j(\phi, \theta, \gamma)q_k(\phi, \theta, \gamma)q_l(\phi, \theta, \gamma)\right) \tag{4.5-21}$$

$$k(\xi,\eta)\left(p_i(\phi,\theta)p_j(\phi,\theta)q_k(\phi,\theta,\gamma)q_l(\phi,\theta,\gamma)\right) \tag{4.5-22}$$

where material constant from Equations 4.5-6 through 4.5-14 can be used in place of k.

Configuration averaging of the form given in Equation 4.5-17 results in

$$\begin{aligned}
&\langle\langle\langle\langle k\ \delta_{ij}\delta_{kl}\rangle\rangle\rangle\rangle \\
&= \int_{\eta=0}^{\infty}\int_{\xi=0}^{\infty}\int_{\gamma=0}^{2\pi}\int_{\theta=0}^{\pi}\int_{\phi=0}^{2\pi} k(\xi,\eta)\delta_{ij}\delta_{kl}\psi_C(\phi,\theta\ ,\gamma,\xi,\eta)\sin\theta\ d\theta d\phi d\gamma d\xi d\eta \\
&= \delta_{ij}\delta_{kl}\int_{\eta=0}^{\infty}\int_{\xi=0}^{\infty} k(\xi,\eta)\psi_S(\xi,\eta)d\left(\frac{L}{d}\right)d\eta\int_{\gamma=0}^{2\pi}\int_{\theta=0}^{\pi}\int_{\phi=0}^{2\pi}\psi_R(\phi,\theta,\gamma)\sin\theta\ \ d\theta d\phi d\gamma \\
&= \delta_{ij}\delta_{kl}\int_{\eta=0}^{\infty}\int_{\xi=0}^{\infty} k(\xi,\eta)\psi_S(\xi,\eta)d\xi d\eta = \bar{k}\ \delta_{ij}\delta_{kl} \quad i,j,k,l = 1,2,3
\end{aligned} \tag{4.5-23}$$

where we used Equation 4.5-3 and defined

$$\bar{k} = \langle\langle\langle k\rangle\rangle\rangle = \int_{\eta=0}^{\infty}\int_{\xi=0}^{\infty} k\ \psi_S d\xi d\eta \tag{4.5-24}$$

where we denote shape averaging by triple brackets. Configuration averaging of the form given in Equation 4.5-18 results in

$$\langle\langle\langle\langle kp_ip_j\delta_{kl}\rangle\rangle\rangle\rangle$$

$$= \int_{\eta=0}^{\infty}\int_{\xi=0}^{\infty}\int_{\gamma=0}^{2\pi}\int_{\theta=0}^{\pi}\int_{\phi=0}^{2\pi} k(\xi,\eta)\left(p_i(\phi,\theta)p_j(\phi,\theta)\right)\delta_{kl}\psi_C(\phi,\theta,\gamma,\xi,\eta)\sin\theta\, d\theta d\phi d\gamma d\xi d\eta$$

$$= \delta_{kl}\int_{\eta=0}^{\infty}\int_{\xi=0}^{\infty} k(\xi,\eta)\psi_S(\xi,\eta)d\xi d\eta \int_{\gamma=0}^{2\pi}\int_{\theta=0}^{\pi}\int_{\phi=0}^{2\pi} p_i(\phi,\theta)p_j(\phi,\theta)\psi_R(\phi,\theta,\gamma)\sin\theta\ d\theta d\phi d\gamma$$

$$= \delta_{kl}\bar{k}\int_{\phi=0}^{2\pi}\int_{\theta=0}^{\pi} p_i(\phi,\theta)p_j(\phi,\theta)\int_{\gamma=0}^{2\pi}\psi_R(\phi,\theta,\gamma)d\gamma\ \sin\theta\ d\theta d\phi = \bar{k}\, a_{ij}\delta_{kl} \tag{4.5-25}$$

$$i,j,k,l = 1,2,3$$

where we can use Equation 4.5-5 we wrote

$$a_{ij} = \langle\langle p_ip_j\rangle\rangle = \int_{\gamma=0}^{2\pi}\int_{\theta=0}^{\pi}\int_{\phi=0}^{2\pi} p_i(\phi,\theta)p_j(\phi,\theta)\psi_R(\phi,\theta,\gamma)\sin\theta\ d\theta d\phi d\gamma$$

$$= \int_{\phi=0}^{2\pi}\int_{\theta=0}^{\pi} p_i(\phi,\theta)p_j(\phi,\theta)\psi(\phi,\theta)\sin\theta\ d\theta d\phi = \langle p_ip_j\rangle \tag{4.5-26}$$

$$i,j = 1,2,3$$

Double brackets indicate rotation averaging and single brackets have been defined as orientation averaging in Equation 3.8-7, following Advani and Tucker [8].

Configuration averaging of the form given in Equation 4.5-19 results in

$$\langle\langle\langle\langle kq_iq_j\delta_{kl}\rangle\rangle\rangle\rangle$$

$$= \int_{\eta=0}^{\infty}\int_{\xi=0}^{\infty}\int_{\gamma=0}^{2\pi}\int_{\theta=0}^{\pi}\int_{\phi=0}^{2\pi} k(\xi,\eta)\left(q_i(\phi,\theta,\gamma)q_j(\phi,\theta,\gamma)\right)\delta_{kl}\psi_C(\phi,\theta\ ,\gamma,\xi,\eta)\sin\theta\ d\theta d\phi d\gamma d\xi d\eta$$

$$= \delta_{kl}\int_{\eta=0}^{\infty}\int_{\xi=0}^{\infty} k(\xi,\eta)\psi_S(\xi,\eta)d\xi d\eta \int_{\gamma=0}^{2\pi}\int_{\theta=0}^{\pi}\int_{\phi=0}^{2\pi} q_i(\phi,\theta,\gamma)q_j(\phi,\theta,\gamma)\psi_R(\phi,\theta,\gamma)\sin\theta\ \ d\theta d\phi d\gamma \tag{4.5-27}$$

$$= \bar{k}\ b_{ij}\delta_{kl} \quad i,j,k,l = 1,2,3$$

where

$$b_{ij} = \langle\langle q_iq_j\rangle\rangle \int_{\gamma=0}^{2\pi}\int_{\theta=0}^{\pi}\int_{\phi=0}^{2\pi} q_i(\phi,\theta,\gamma)q_j(\phi,\theta,\gamma)\psi_R(\phi,\theta,\gamma)\sin\theta\ \ d\theta d\phi d\gamma \tag{4.5-29}$$

$$i,j = 1,2,3$$

Configuration averaging of the form given in Equation 4.5-20 results in

$$\langle\langle\langle\langle kp_ip_jp_kp_l\rangle\rangle\rangle\rangle$$

$$= \int_{\eta=0}^{\infty}\int_{\xi=0}^{\infty}\int_{\gamma=0}^{2\pi}\int_{\theta=0}^{\pi}\int_{\phi=0}^{2\pi} k(\xi,\eta)\left(p_i(\phi,\theta)p_j(\phi,\theta)p_k(\phi,\theta)p_l(\phi,\theta)\right)\psi_C\sin\theta\ d\theta d\phi d\gamma d\xi d\eta$$

$$= \int_{\eta=0}^{\infty}\int_{\xi=0}^{\infty} k\psi_S d\xi d\eta \int_{\gamma=0}^{2\pi}\int_{\theta=0}^{\pi}\int_{\phi=0}^{2\pi} p_i(\phi,\theta)p_j(\phi,\theta)p_k(\phi,\theta)p_l(\phi,\theta)\psi_R(\phi,\theta,\gamma)\sin\theta\ \ d\theta d\phi d\gamma$$

$$= \bar{k}\int_{\phi=0}^{2\pi}\int_{\theta=0}^{\pi} p_i(\phi,\theta)p_j(\phi,\theta)p_k(\phi,\theta)p_l(\phi,\theta)\int_{\gamma=0}^{2\pi}\psi_R(\phi,\theta,\gamma)d\gamma\ \sin\theta\ \ d\theta d\phi \tag{4.5-29}$$

$$= \bar{k}\ a_{ijkl} \quad i,j,k,l = 1,2,3$$

where we can use Equation 4.5-15 we wrote

$$a_{ijkl} = \langle\langle p_i p_j p_k p_l \rangle\rangle$$

$$= \int_{\gamma=0}^{2\pi} \int_{\theta=0}^{\pi} \int_{\phi=0}^{2\pi} p_i(\phi,\theta) p_j(\phi,\theta) p_k(\phi,\theta) p_l(\phi,\theta)\ \psi_R(\phi,\theta,\gamma) \sin\theta\ \ d\theta d\phi d\gamma$$

$$= \int_{\phi=0}^{2\pi} \int_{\theta=0}^{\pi} p_i(\phi,\theta) p_j(\phi,\theta) p_k(\phi,\theta) p_l(\phi,\theta)\ \psi(\phi,\theta) \sin\theta\ \ d\theta d\phi \tag{4.5-30}$$

$$= \langle p_i p_j p_k p_l \rangle \quad i,j,k,l = 1,2,3$$

Configuration averaging of the form given in Equation 4.5-21 results in

$$\langle\langle\langle\langle k q_i q_j q_k q_l \rangle\rangle\rangle\rangle = \int_{\eta=0}^{\infty} \int_{\xi=0}^{\infty} \int_{\gamma=0}^{2\pi} \int_{\theta=0}^{\pi} \int_{\phi=0}^{2\pi} k q_i q_j q_k q_l\ \sin\theta\, d\theta d\phi d\gamma d\xi d\eta$$

$$= \int_{\eta=0}^{\infty} \int_{\xi=0}^{\infty} k\psi_S d\xi d\eta \int_{\gamma=0}^{2\pi} \int_{\theta=0}^{\pi} \int_{\phi=0}^{2\pi} q_i q_j q_k q_l \psi_R \sin\theta\, d\theta d\phi d\gamma \tag{4.5-31}$$

$$= \bar{k}\, b_{ijkl} \quad i,j,k,l = 1,2,3$$

where

$$b_{ijkl} = \langle\langle q_i q_j q_k q_l \rangle\rangle$$

$$= \int_{\gamma=0}^{2\pi} \int_{\theta=0}^{\pi} \int_{\phi=0}^{2\pi} q_i(\phi,\theta,\gamma) q_j(\phi,\theta,\gamma) q_k(\phi,\theta,\gamma) q_l(\phi,\theta,\gamma) \psi_R(\phi,\theta,\gamma) \sin\theta\ \ d\theta d\phi d\gamma \tag{4.5-32}$$

$$= 1,2,3$$

Configuration averaging of the form given in Equation 4.5-22 results in

$$\langle\langle\langle\langle kp_ip_jq_kq_l\rangle\rangle\rangle\rangle = \int_{\eta=0}^{\infty}\int_{\xi=0}^{\infty}\int_{\gamma=0}^{2\pi}\int_{\theta=0}^{\pi}\int_{\phi=0}^{2\pi} kp_ip_jq_kq_l\psi_C \sin\theta \, d\theta d\phi d\gamma d\xi d\eta$$

$$= \int_{\eta=0}^{\infty}\int_{\xi=0}^{\infty} k\psi_S d\xi d\eta \int_{\gamma=0}^{2\pi}\int_{\theta=0}^{\pi}\int_{\phi=0}^{2\pi} kp_ip_jq_kq_l\psi_R \sin\theta \, d\theta d\phi d\gamma \tag{4.5-33}$$

$$= \bar{k}\, c_{ijkl} \quad i,j,k,l = 1,2,3$$

where

$$c_{ijkl} = \langle\langle p_ip_jq_kq_l\rangle\rangle$$

$$= \int_{\gamma=0}^{2\pi}\int_{\theta=0}^{\pi}\int_{\phi=0}^{2\pi} p_i(\phi,\theta)p_j(\phi,\theta)q_k(\phi,\theta,\gamma)q_l(\phi,\theta,\gamma)\psi_R(\phi,\theta,\gamma)\sin\theta \;\; d\theta d\phi d\gamma \tag{4.5-34}$$

$$\mathrm{i}, j,k,l = 1,2,3$$

We can now write Equation 4.5-1 as

$$\langle\langle\langle\langle C_{ijkl}\rangle\rangle\rangle\rangle = \bar{\mu}\left(\delta_{ik}\delta_{jl} + \delta_{il}\delta_{jk}\right) + \bar{\lambda}\delta_{ij}\delta_{kl} + \overline{\alpha_{\lambda 1}}\left(a_{ij}\delta_{kl} + \delta_{ij}a_{kl}\right) + \overline{\alpha_{\lambda 2}}\left(b_{ij}\delta_{kl} + \delta_{ij}b_{kl}\right) + 2\overline{\mu_1}\left(\delta_{ik}a_{jl} + \delta_{il}a_{jk} + \delta_{jl}a_{ik} + \delta_{jk}a_{il}\right) + 2\overline{\mu_2}\left(\delta_{ik}b_{jl} + \delta_{il}b_{jk} + \delta_{jl}b_{ik} + \delta_{jk}b_{il}\right) + \overline{\beta_{\lambda 1}}a_{ijkl} + \overline{\beta_{\lambda 2}}b_{ijkl} + \overline{\beta_{\lambda 3}}(c_{ijkl} + c_{klij}) \quad i,j,k,l = 1,2,3 \tag{4.5-35}$$

where

$$\bar{\mu} = \langle\langle\langle\mu\rangle\rangle\rangle = \int_{\xi=0}^{\infty}\int_{\eta=0}^{\infty} \mu(\xi,\eta)\psi_S(\xi,\eta) \;\; d\xi d\eta \tag{4.5-36}$$

$$\bar{\lambda} = \langle\langle\langle\lambda\rangle\rangle\rangle = \int_{\xi=0}^{\infty}\int_{\eta=0}^{\infty} \lambda(\xi,\eta)\psi_S(\xi,\eta)\ d\xi d\eta \tag{4.5-37}$$

$$\overline{\mu_1} = \langle\langle\langle\mu_1\rangle\rangle\rangle = \int_{\xi=0}^{\infty}\int_{\eta=0}^{\infty} \mu_1(\xi,\eta)\psi_S(\xi,\eta)\ d\xi d\eta \tag{4.5-38}$$

$$\overline{\mu_2} = \langle\langle\langle\mu_2\rangle\rangle\rangle = \int_{\xi=0}^{\infty}\int_{\eta=0}^{\infty} \mu_2(\xi,\eta)\psi_S(\xi,\eta)\ d\xi d\eta \tag{4.5-39}$$

$$\overline{\alpha_{\lambda 1}} = \langle\langle\langle\alpha_{\lambda 1}\rangle\rangle\rangle = \int_{\xi=0}^{\infty}\int_{\eta=0}^{\infty} \alpha_{\lambda 1}(\xi,\eta)\psi_S(\xi,\eta)\ d\xi d\eta \tag{4.5-40}$$

$$\overline{\alpha_{\lambda 2}} = \langle\langle\langle\alpha_{\lambda 2}\rangle\rangle\rangle = \int_{\xi=0}^{\infty}\int_{\eta=0}^{\infty} \alpha_{\lambda 2}(\xi,\eta)\psi_S(\xi,\eta)\ d\xi d\eta \tag{4.5-41}$$

$$\overline{\beta_{\lambda 1}} = \langle\langle\langle\beta_{\lambda 1}\rangle\rangle\rangle = \int_{\xi=0}^{\infty}\int_{\eta=0}^{\infty} \beta_{\lambda 1}(\xi,\eta)\psi_S(\xi,\eta)\ d\xi d\eta \tag{4.5-42}$$

$$\overline{\beta_{\lambda 2}} = \langle\langle\langle\beta_{\lambda 2}\rangle\rangle\rangle = \int_{\xi=0}^{\infty}\int_{\eta=0}^{\infty} \beta_{\lambda 2}(\xi,\eta)\psi_S(\xi,\eta)\ d\xi d\eta \tag{4.5-43}$$

$$\overline{\beta_{\lambda 3}} = \langle\langle\langle\beta_{\lambda 3}\rangle\rangle\rangle = \int_{\xi=0}^{\infty}\int_{\eta=0}^{\infty} \beta_{\lambda 3}(\xi,\eta)\psi_S(\xi,\eta)\ d\xi d\eta \tag{4.5-44}$$

4.6. Geometric Configuration Tensors

In this section we explore properties second and fourth order orientation tensors a_{ij} and a_{ijkl}, second and fourth order curvature tensors b_{ij} and b_{ijkl}, and mixed tensor c_{ijkl}. We could define

higher order tensors and show how these tensors reproduce distribution functions, similarly to the work presented in Advani and Tucker [8], however performing this work is not necessary for our present discussion. We simply focus on properties of second and fourth order tensors, which will enable us to obtain components of stiffness tensor for a material containing curved fibers.

4.6.1. Fiber orientation Tensors

Since definitions of a_{ij} and a_{ijkl} given in Equations 4.5-26 and Equation 4.5-30 reduce to definitions identical to those provided by Advani and Tucker [8], properties of a_{ij} and a_{ijkl} remain unchanged and in the absence of fiber curvature, all of the equations above reduce to previously developed theories. Some properties of orientation tensors are given in Equations 3.8-9 through 3.8-12. We will show these properties and explore the tensor in more detail.

We start by listing components of unit vector **p**, which can be viewed as rotated bases vector for fiber coordinate system or as a unit tangent vector to the fiber centerline at the middle of the fiber. Repeating Equations 3.4-33 through 3.4-35.

$$p_1 = \cos\alpha\cos\beta = \cos\phi\sin\theta \tag{4.6-1}$$

$$p_2 = \sin\alpha\cos\beta = \sin\phi\sin\theta \tag{4.6-2}$$

$$p_3 = \sin\beta = \cos\theta \tag{4.6-3}$$

where corresponding angles are shown in Figure 4-4. We can write the definition of second and fourth order tensor in the following form

$$a_{ij}$$

$$= \langle\langle p_i p_j \rangle\rangle = \int_{\gamma=0}^{2\pi} \int_{\theta=0}^{\pi} \int_{\phi=0}^{2\pi} p_i p_j \psi_R(\phi,\theta,\gamma) \sin\theta \; d\theta d\phi d\gamma$$

$$= \int_{\phi=0}^{2\pi} \int_{\theta=0}^{\pi} p_i p_j \psi(\phi,\theta\,) \sin\theta \; d\theta d\phi = \langle p_i p_j \rangle = \oint p_i p_j \psi(\boldsymbol{p}) d\boldsymbol{p} \tag{4.6-4}$$

$$= \int_{\beta=-\frac{\pi}{2}}^{\frac{\pi}{2}} \int_{\alpha=0}^{2\pi} p_i p_j \psi(\alpha,\beta\,) \cos\beta \;\; d\alpha d\beta \qquad i,j = 1,2,3$$

$$a_{ijkl} = \langle\langle p_i p_j p_k p_l \rangle\rangle = \int_{\gamma=0}^{2\pi} \int_{\theta=0}^{\pi} \int_{\phi=0}^{2\pi} p_i p_j p_k p_l \; \psi_R(\phi,\theta,\gamma) \sin\theta \; d\theta d\phi d\gamma$$

$$= \int_{\phi=0}^{2\pi} \int_{\theta=0}^{\pi} p_i p_j p_k p_l \; \psi(\phi,\theta) \sin\theta \; d\theta d\phi = \langle p_i p_j p_k p_l \rangle$$

$$= \oint p_i p_j p_k p_l \psi(\boldsymbol{p}) d\boldsymbol{p} \tag{4.6-5}$$

$$= \int_{\beta=-\pi/2}^{\pi/2} \int_{\alpha=0}^{2\pi} p_i p_j p_k p_l \psi(\alpha,\beta\,) \cos\beta \;\; d\alpha d\beta \qquad i,j,k,l = 1,2,3$$

Complete symmetry of these tensors noted in Equations 3.8-9 and 3.8-10 is clear from definition

$$a_{ij} = \oint p_i p_j \psi(\boldsymbol{p}) d\boldsymbol{p} = \oint p_j p_i \psi(\boldsymbol{p}) d\boldsymbol{p} = a_{ji} \tag{4.6-6}$$

$$a_{ijkl} = \oint p_i p_j p_k p_l \psi(\boldsymbol{p}) d\boldsymbol{p} = \oint p_j p_i p_k p_l \psi(\boldsymbol{p}) d\boldsymbol{p} = a_{jikl} = a_{kijl} = a_{lijk} = a_{klij}, \qquad etc. \tag{4.6-7}$$

We can then write unique components of $\boldsymbol{p}_{(2)} = p_i p_j$, which would appear in these definitions

$$p_{(2)_{11}} = \sin^2\theta\ \cos^2\phi = \cos^2\alpha\cos^2\beta \tag{4.6-8}$$

$$p_{(2)_{22}} = \sin^2\theta\ \sin^2\phi = \sin^2\alpha\cos^2\beta \tag{4.6-9}$$

$$p_{(2)_{33}} = \cos^2\theta\ = \sin^2\beta \tag{4.6-10}$$

$$p_{(2)_{23}} = p_{(2)_{32}} = \sin\phi\sin\theta\cos\theta = \sin\alpha\sin\beta\cos\beta \tag{4.6-11}$$

$$p_{(2)_{13}} = p_{(2)_{31}} = \cos\phi\sin\theta\cos\theta = \cos\alpha\sin\beta\cos\beta \tag{4.6-12}$$

$$p_{(2)_{12}} = p_{(2)_{21}} = \cos\phi\sin\phi\sin^2\theta = \sin\alpha\sin\beta\cos^2\beta \tag{4.6-13}$$

Of 81 components in $\boldsymbol{p}_{(4)} = p_i p_j p_k p_l$, the number of unique components is 15. We write $\boldsymbol{p}_{(4)}$ in Voigt notation

$$\boldsymbol{p}_{(4)} = \begin{bmatrix} p_{(4)_{11}} & p_{(4)_{66}} & p_{(4)_{55}} & p_{(4)_{14}} & p_{(4)_{15}} & p_{(4)_{16}} \\ & p_{(4)_{22}} & p_{(4)_{44}} & p_{(4)_{24}} & p_{(4)_{25}} & p_{(4)_{26}} \\ & & p_{(4)_{33}} & p_{(4)_{34}} & p_{(4)_{35}} & p_{(4)_{36}} \\ & & & p_{(4)_{44}} & p_{(4)_{36}} & p_{(4)_{25}} \\ & sym. & & & p_{(4)_{55}} & p_{(4)_{14}} \\ & & & & & p_{(4)_{66}} \end{bmatrix} \tag{4.6-14}$$

where

$$p_{(4)_{11}} = \cos^4\phi\sin^4\theta\ = \cos^4\alpha\cos^4\beta \tag{4.6-15}$$

$$p_{(4)_{22}} = \sin^4\phi\sin^4\theta\ = \sin^4\alpha\cos^4\beta \tag{4.6-16}$$

$$p_{(4)_{33}} = \cos^4\theta \ = \sin^4\beta \tag{4.6-17}$$

$$p_{(4)_{44}} = \sin^2\phi\cos^2\theta\sin^2\theta = \sin^2\alpha\sin^2\beta\cos^2\beta \tag{4.6-18}$$

$$p_{(4)_{55}} = \cos^2\phi\cos^2\theta\sin^2\theta = \cos^2\alpha\sin^2\beta\cos^2\beta \tag{4.6-19}$$

$$p_{(4)_{66}} = \sin^2\phi\cos^2\phi\sin^4\theta = \sin^2\alpha\cos^2\alpha\cos^4\beta \tag{4.6-20}$$

$$p_{(4)_{14}} = \sin\phi\cos^2\phi\cos\theta\sin^3\theta \ = \sin\alpha\cos^2\alpha\sin\beta\cos^3\beta \tag{4.6-21}$$

$$p_{(4)_{15}} = \cos^3\phi\cos\theta\sin^3\theta \ = \cos^3\alpha\sin\beta\cos^3\beta \tag{4.6-22}$$

$$p_{(4)_{16}} = \sin\phi\cos^3\phi\sin^4\theta \ = \sin\alpha\cos^3\alpha\cos^4\beta \tag{4.6-23}$$

$$p_{(4)_{24}} = \sin^3\phi\cos\theta\sin^3\theta = \sin^3\alpha\sin\beta\cos^3\beta \tag{4.6-24}$$

$$p_{(4)_{25}} = \sin^2\phi\cos\alpha\cos\theta\sin^3\theta = \sin^2\alpha\cos\alpha\sin\beta\cos^3\beta \tag{4.6-25}$$

$$p_{(4)_{26}} = \sin^3\phi\cos\phi\cos^3\theta = \sin^3\alpha\cos\alpha\sin^3\beta \tag{4.6-26}$$

$$p_{(4)_{34}} = \sin\phi\cos^3\theta\sin\theta = \sin\alpha\sin^3\beta\cos\beta \tag{4.6-27}$$

$$p_{(4)_{35}} = \cos\phi\sin\theta\cos^3\theta = \cos\alpha\cos\beta\sin^3\beta \tag{4.6-28}$$

$$p_{(4)_{36}} = \sin\phi\cos\phi\cos^2\theta\sin^2\theta = \sin\alpha\cos\alpha\sin^2\beta\cos^2\beta \tag{4.6-29}$$

Then we can show directly

$$a_{ii} = 1 \tag{4.6-30}$$

$$a_{ijkk} = a_{ij} \tag{4.6-31}$$

4.6.2. Fiber Curvature Tensors

The fiber curvature tensor is defined in this work for the first time, therefore there is no previous research which could be referenced. Again we start the investigation of curvature tensor by listing components of unit vector q, which is perpendicular to vector **p** and defined by angle γ. The vector **q** can be viewed as rotated bases vector for fiber coordinate system or as a unit vector normal to the fiber centerline at the middle of the fiber, pointing in the direction of center of curvature as illustrated in Figure 4-4. Repeating Equations 3.4-39 through 3.4-41

$$q_1 = -\sin\alpha\cos\gamma - \cos\alpha\sin\beta\sin\gamma = -\sin\phi\cos\gamma - \cos\phi\cos\theta\sin\gamma \tag{4.6-32}$$

$$q_2 = \cos\alpha\cos\gamma - \sin\alpha\sin\beta\sin\gamma = \cos\phi\cos\gamma - \sin\phi\cos\theta\sin\gamma \tag{4.6-33}$$

$$q_3 = \cos\beta\sin\gamma = \sin\theta\sin\gamma \tag{4.6-34}$$

where angles are shown in Figure 4-4.

We can write the definitions of curvature tensors given in Equations 4.5-28 and 4.5-32 as follows

$$\begin{aligned} b_{ij} = \langle\langle q_i q_j \rangle\rangle &= \int_{\gamma=0}^{2\pi}\int_{\theta=0}^{\pi}\int_{\phi=0}^{2\pi} q_i q_j \psi_R(\phi,\theta,\gamma)\sin\theta \; d\theta d\phi d\gamma \\ &= \int_{\gamma=0}^{2\pi}\int_{\beta=-\pi/2}^{\pi/2}\int_{\alpha=0}^{2\pi} q_i q_j \psi_R(\alpha,\beta,\gamma)\cos\beta \;\; d\alpha d\beta d\gamma \qquad i,j = 1,2,3 \end{aligned} \tag{4.6-35}$$

$$b_{ijkl} = \langle\langle q_i q_j q_k q_l \rangle\rangle = \int_{\gamma=0}^{2\pi} \int_{\theta=0}^{\pi} \int_{\phi=0}^{2\pi} q_i q_j q_k q_l \psi_R(\phi,\theta,\gamma) \sin\theta \; d\theta d\phi d\gamma$$
$$= \int_{\gamma=0}^{2\pi} \int_{\beta=-\frac{\pi}{2}}^{\frac{\pi}{2}} \int_{\alpha=0}^{2\pi} q_i q_j q_k q_l \psi_R(\alpha,\beta,\gamma) \cos\beta \;\; d\alpha d\beta d\gamma \qquad i,j,k,l = 1,2,3 \tag{4.6-36}$$

Just like the orientation tensors, curvature tensors are completely symmetric. We can show this from the definition

$$b_{ij} = \int_{\gamma=0}^{2\pi} \int_{\theta=0}^{\pi} \int_{\phi=0}^{2\pi} q_i q_j \psi_R(\phi,\theta,\gamma) \sin\theta \; d\theta d\phi d\gamma$$
$$= \int_{\gamma=0}^{2\pi} \int_{\theta=0}^{\pi} \int_{\phi=0}^{2\pi} q_j q_i \psi_R(\phi,\theta,\gamma) \sin\theta \; d\theta d\phi d\gamma = b_{ji} \tag{4.6-37}$$

$$b_{ijkl} = \int_{\gamma=0}^{2\pi} \int_{\theta=0}^{\pi} \int_{\phi=0}^{2\pi} q_i q_j q_k q_l \psi_R(\phi,\theta,\gamma) \sin\theta \; d\theta d\phi d\gamma$$
$$= \int_{\gamma=0}^{2\pi} \int_{\theta=0}^{\pi} \int_{\phi=0}^{2\pi} q_j q_i q_k q_l \psi_R(\phi,\theta,\gamma) \sin\theta \; d\theta d\phi d\gamma = b_{jikl} = b_{kijl} = b_{lijk} = b_{klij}, \qquad etc. \tag{4.6-38}$$

We can then write unique components of $\boldsymbol{q}_{(2)} = q_i q_j$, which would appear in these definitions

$$q_{(2)_{11}} = (\cos\gamma \sin\alpha + \cos\alpha \sin\beta \sin\gamma)^2 \tag{4.6-39}$$

$$q_{(2)_{22}} = (\cos\alpha\cos\gamma - \sin\alpha\sin\beta\sin\gamma)^2 \tag{4.6-40}$$

$$q_{(2)_{33}} = (\cos\beta)^2(\sin\gamma)^2 \tag{4.6-41}$$

$$q_{(2)_{23}} = q_{(2)_{32}} = \cos\beta\sin\gamma\,(\cos\alpha\cos\gamma - \sin\alpha\sin\beta\sin\gamma) \tag{4.6-42}$$

$$q_{(2)_{13}} = q_{(2)_{31}} = -\cos\beta\sin\gamma\,(\cos\gamma\sin\alpha + \cos\alpha\sin\beta\sin\gamma) \tag{4.6-43}$$

$$q_{(2)_{12}} = q_{(2)_{21}} = (\cos\gamma\sin\alpha + \cos\alpha\sin\beta\sin\gamma)(\sin\alpha\sin\beta\sin\gamma - \cos\alpha\cos\gamma) \tag{4.6-44}$$

Of 81 components in $\boldsymbol{q}_{(4)} = q_i q_j q_k q_l$, the number of unique components is 15. We write $\boldsymbol{q}_{(4)}$ in Voigt notation

$$\boldsymbol{q}_{(4)} = \begin{bmatrix} q_{(4)_{11}} & q_{(4)_{66}} & q_{(4)_{55}} & q_{(4)_{14}} & q_{(4)_{15}} & q_{(4)_{16}} \\ & q_{(4)_{22}} & q_{(4)_{44}} & q_{(4)_{24}} & q_{(4)_{25}} & q_{(4)_{26}} \\ & & q_{(4)_{33}} & q_{(4)_{34}} & q_{(4)_{35}} & q_{(4)_{36}} \\ & & & q_{(4)_{44}} & q_{(4)_{36}} & q_{(4)_{25}} \\ & sym. & & & q_{(4)_{55}} & q_{(4)_{14}} \\ & & & & & q_{(4)_{66}} \end{bmatrix} \tag{4.6-45}$$

where

$$q_{(4)_{11}} = (\cos\gamma\sin\alpha + \cos\alpha\sin\beta\sin\gamma)^4 \tag{4.6-46}$$

$$q_{(4)_{22}} = (\cos\alpha\cos\gamma - \sin\alpha\sin\beta\sin\gamma)^4 \tag{4.6-47}$$

$$q_{(4)_{33}} = (\cos\beta)^4(\sin\gamma)^4 \tag{4.6-48}$$

$$q_{(4)_{44}} = (\cos\beta)^2\,(\sin\gamma)^2\,(\cos\alpha\cos\gamma - \sin\alpha\sin\beta\sin\gamma)^2 \tag{4.6-49}$$

$$q_{(4)_{55}} = (\cos\beta)^2(\sin\gamma)^2(\cos\gamma\sin\alpha + \cos\alpha\sin\beta\sin\gamma)^2 \tag{4.6-50}$$

$$q_{(4)_{66}} = (\cos\gamma\sin\alpha + \cos\alpha\sin\beta\sin\gamma)^2(\cos\alpha\cos\gamma - \sin\alpha\sin\beta\sin\gamma)^2 \tag{4.651}$$

$$q_{(4)_{14}} = \cos\beta\sin\gamma\,(\cos\gamma\sin\alpha + \cos\alpha\sin\beta\sin\gamma)^2(\cos\alpha\cos\gamma - \sin\alpha\sin\beta\sin\gamma) \tag{4.6-52}$$

$$q_{(4)_{15}} = -\cos\beta\sin\gamma\,(\cos\gamma\sin\alpha + \cos\alpha\sin\beta\sin\gamma)^3 \tag{4.6-53}$$

$$q_{(4)_{16}} = (\cos\gamma\sin\alpha + \cos\alpha\sin\beta\sin\gamma)^3(\sin\alpha\sin\beta\sin\gamma - \cos\alpha\cos\gamma) \tag{4.6-54}$$

$$q_{(4)_{24}} = \cos\beta\sin\gamma\,(\cos\alpha\cos\gamma - \sin\alpha\sin\beta\sin\gamma)^3 \tag{4.6-55}$$

$$q_{(4)_{25}} = -\cos\beta\sin\gamma\,(\cos\gamma\sin\alpha + \cos\alpha\sin\beta\sin\gamma)(\sin\alpha\sin\beta\sin\gamma - \cos\alpha\cos\gamma)^2 \tag{4.6-56}$$

$$q_{(4)_{26}} = (\cos\gamma\sin\alpha + \cos\alpha\sin\beta\sin\gamma)(\sin\alpha\sin\beta\sin\gamma - \cos\alpha\cos\gamma)^3 \tag{4.6-57}$$

$$q_{(4)_{34}} = (\cos\beta)^3(\sin\gamma)^3(\cos\alpha\cos\gamma - \sin\alpha\sin\beta\sin\gamma) \tag{4.6-58}$$

$$q_{(4)_{35}} = -(\cos\beta)^3(\sin\gamma)^3\,(\cos\gamma\sin\alpha + \cos\alpha\sin\beta\sin\gamma) \tag{4.6-59}$$

$$q_{(4)_{36}} = (\cos\beta)^2\,(\sin\gamma)^2(\cos\gamma\sin\alpha + \cos\alpha\sin\beta\sin\gamma)(\sin\alpha\sin\beta\sin\gamma - \cos\alpha\cos\gamma) \tag{4.6-60}$$

Then we can show directly

$$b_{ii} = 1 \tag{4.6-61}$$

$$b_{ijkk} = b_{ij} \tag{4.6-62}$$

4.6.3. Mixed Tensor

Equation 4.5-34 provides definition for a mixed tensor appearing in configuration averaged stiffness tensor

$$\begin{aligned} c_{ijkl} = \langle\langle p_i p_j q_k q_l \rangle\rangle &= \int_{\gamma=0}^{2\pi} \int_{\theta=0}^{\pi} \int_{\phi=0}^{2\pi} p_i p_j q_k q_l \psi_R(\phi,\theta,\gamma) \sin\theta \; d\theta d\phi d\gamma \\ &= \int_{\gamma=0}^{2\pi} \int_{\beta=-\pi/2}^{\pi/2} \int_{\alpha=0}^{2\pi} p_i p_j q_k q_l \psi_R(\alpha,\beta,\gamma) \cos\beta \;\; d\alpha d\beta d\gamma \quad i,j,k,l \\ &= 1,2,3 \end{aligned} \tag{4.6-63}$$

The mixed tensor is not completely symmetric as was the case for fourth order orientation and curvature tensors, however it is symmetric with respect to the first pair and last pair of indexes. We can show this from the definition

$$\begin{aligned} c_{ijkl} &= \int_{\gamma=0}^{2\pi} \int_{\theta=0}^{\pi} \int_{\phi=0}^{2\pi} p_i p_j q_k q_l \psi_R(\phi,\theta,\gamma) \sin\theta \; d\theta d\phi d\gamma \\ &= \int_{\gamma=0}^{2\pi} \int_{\theta=0}^{\pi} \int_{\phi=0}^{2\pi} p_j p_i q_k q_l \psi_R(\phi,\theta,\gamma) \sin\theta \; d\theta d\phi d\gamma = c_{jikl} \\ &= \int_{\gamma=0}^{2\pi} \int_{\theta=0}^{\pi} \int_{\phi=0}^{2\pi} p_i p_j q_l q_k \psi_R(\phi,\theta,\gamma) \sin\theta \; d\theta d\phi d\gamma = c_{ijlk} = c_{jilk} \end{aligned} \tag{4.6-64}$$

There are 36 unique components in c_{ijkl}. However we can inspect Equation 4.4-3 and note that we gain additional symmetry by finding

$$s_{ijkl} = (c_{ijkl} + c_{klij}) \quad i,j,k,l = 1,2,3 \tag{4.6-65}$$

Which would be equivalent to defining s_{ijkl} by performing rotation averaging

$$s_{ijkl} = \langle\langle p_i p_j q_k q_l + p_k p_l q_i q_j \rangle\rangle \; i,j,k,l = 1,2,3 \tag{4.6-66}$$

The tensor s_{ijkl} has the same symmetry as the elastic tensor and has 21 distinct components. We can then write unique components of $m_{(4)} = p_i p_j q_k q_l + p_k p_l q_i q_j$, which would appear in these definitions.

$$m_{(4)_{11}} = 2\,(\cos\alpha)^2\,(\cos\beta)^2(\cos\gamma\sin\alpha + \cos\alpha\sin\beta\sin\gamma)^2 \tag{4.6-67}$$

$$m_{(4)_{22}} = 2(\cos\beta)^2(\sin\alpha)^2(\cos\alpha\cos\gamma - \sin\alpha\sin\beta\sin\gamma)^2 \tag{4.6-68}$$

$$m_{(4)_{33}} = 2(\cos\beta)^2(\sin\beta)^2(\sin\gamma)^2 \tag{4.6-69}$$

$$m_{(4)_{44}} = 2(\cos\beta)^2\sin\alpha\sin\beta\sin\gamma\,(\cos\alpha\cos\gamma - \sin\alpha\sin\beta\sin\gamma) \tag{4.6-70}$$

$$m_{(4)_{55}} = -2\cos\alpha\,(\cos\beta)^2\sin\beta\sin\gamma\,(\cos\gamma\sin\alpha + \cos\alpha\sin\beta\sin\gamma) \tag{4.6-71}$$

$$\begin{aligned} m_{(4)_{66}} = {} & -2\cos\alpha\,(\cos\beta)^2\sin\alpha\,(\cos\gamma\sin\alpha + \cos\alpha\sin\beta\sin\gamma)(\cos\alpha\cos\gamma \\ & - \sin\alpha\sin\beta\sin\gamma) \end{aligned} \tag{4.6-72}$$

$$\begin{aligned} m_{(4)_{12}} = {} & (\cos\beta)^2(\sin^2\alpha\,(\cos\gamma\sin\alpha + \cos\alpha\sin\beta\sin\gamma)^2 \\ & + (\cos\alpha)^2\,(\cos\alpha\cos\gamma - \sin\alpha\sin\beta\sin\gamma)^2) \end{aligned} \tag{4.6-73}$$

$$m_{(4)_{13}} = (\cos\alpha)^2\,(\cos\beta)^4(\sin\gamma)^2 + (\sin\beta)^2(\cos\gamma\sin\alpha + \cos\alpha\sin\beta\sin\gamma])^2 \tag{4.6-74}$$

$$m_{(4)_{14}} = \cos\beta \sin\alpha \sin\beta \, (\cos\gamma \sin\alpha + \cos\alpha \sin\beta \sin\gamma)^2 + (\cos\alpha)^2 (\cos\beta)^3 \sin\gamma \, (\cos\alpha \cos\gamma - \sin\alpha \sin\beta \sin\gamma) \tag{4.6-75}$$

$$m_{(4)_{15}} = \cos\alpha \cos\beta \, (\cos\gamma \sin\alpha \sin\beta - \cos\alpha \cos 2\beta \sin\gamma)(\cos\gamma \sin\alpha + \cos\alpha \sin\beta \sin\gamma) \tag{4.6-76}$$

$$m_{(4)_{16}} = -\cos\alpha \, (\cos\beta)^2 (\cos\gamma \sin\alpha + \cos\alpha \sin\beta \sin\gamma)((\cos\alpha)^2 \cos\gamma - \cos\gamma \, (\sin\alpha)^2 - 2\cos\alpha \sin\alpha \sin\beta \sin\gamma) \tag{4.6-77}$$

$$m_{(4)_{23}} = (\cos\beta)^4 ((\sin\alpha)^2 \, (\sin\gamma)^2 + (\sin\beta)^2 (\cos\alpha \cos\gamma - \sin\alpha \sin\beta \sin\gamma)^2 \tag{4.6-78}$$

$$m_{(4)_{24}} = \cos\beta \sin\alpha \, (\cos\alpha \cos\gamma \sin\beta + \cos 2\beta \sin\alpha \sin\gamma)(\cos\alpha \cos\gamma - \sin\alpha \sin\beta \sin\gamma) \tag{4.6-79}$$

$$m_{(4)_{25}} = -(\cos\beta)^3 (\sin\alpha)^2 \sin\gamma \, (\cos\gamma \sin\alpha + \cos\alpha \sin\beta \sin\gamma) + \cos\alpha \cos\beta \sin\beta \, (\cos\alpha \cos\gamma - \sin\alpha \sin\beta \sin\gamma)^2 \tag{4.6-80}$$

$$m_{(4)_{26}} = (\cos\beta)^2 \sin\alpha \, (-\cos\alpha \cos\gamma + \sin\alpha \sin\beta \sin\gamma)(-(\cos\alpha)^2 \cos\gamma + \cos\gamma \, (\sin\alpha)^2 + \sin 2\alpha \sin\beta \sin\gamma) \tag{4.6-81}$$

$$m_{(4)_{34}} = \cos\beta \sin\beta \sin\gamma \, (\cos\alpha \cos\gamma \sin\beta + \cos 2\beta \sin\alpha \sin\gamma) \tag{4.6-82}$$

$$m_{(4)_{35}} = \cos\beta \sin\beta \sin\gamma \, (-\cos\gamma \sin\alpha \sin\beta + \cos\alpha \cos 2\beta \sin\gamma) \tag{4.6-83}$$

$$m_{(4)_{36}} = \cos\alpha \, (\cos\beta)^4 \sin\alpha \, (\sin\gamma)^2 + (\sin\beta)^2 (\cos\gamma \sin\alpha + \cos\alpha \sin\beta \sin\gamma)(-\cos\alpha \cos\gamma + \sin\alpha \sin\beta \sin\gamma) \tag{4.6-84}$$

$$m_{(4)_{45}} = (\cos\beta)^2 \sin\beta \sin\gamma \left((\cos\alpha)^2 \cos\gamma - \cos\gamma\,(\sin\alpha)^2 - 2\cos\alpha \sin\alpha \sin\beta \sin\gamma\right) \tag{4.6-85}$$

$$m_{(4)_{46}} = \cos\beta \sin\alpha\,(\cos\gamma \sin\alpha \sin\beta - \cos\alpha \cos 2\beta \sin\gamma)(\sin\alpha \sin\beta \sin\gamma - \cos\alpha \cos\gamma) \tag{4.6-86}$$

$$m_{(4)_{56}} = -\cos\alpha \cos\beta\,(\cos\alpha \cos\gamma \sin\beta + \cos 2\beta \sin\alpha \sin\gamma)(\cos\gamma \sin\alpha + \cos\alpha \sin\beta \sin\gamma) \tag{4.6-87}$$

4.7. Obtaining Material Parameters for Material in Single Configuration

We now want to obtain material parameters in Equations 4.5-36 through 4.5-44. If a given material contains fibers in a limited range of configurations, these constants could be obtained experimentally. However this empirical approach would be impractical for realistic DFCs, and therefore we suggest two approaches to obtaining the constants and develop one of them in this section. The first approach would be numerical simulation of unit cells containing bent fibers in configurations of interest. Resulting orthotropic symmetry would allow generation of straightforward cuboidal unit cell with three planes of symmetry.

We explore an approach based on orientation averaging and semi-empirical Halpin-Kardos [55] equations. We can imagine a curved fiber in an arbitrary configuration to be composed of segments of straight fibers. We can therefore assign an orientation tensor to any given configuration. We will first develop planar orientation tensor for a curved fiber with shape given by ξ, η in fiber coordinate system f = (**p,q,s**) and subsequently rotate the result to obtain solution for arbitrary configuration. From Figure 4-6, we note that $\phi = \varphi$ and $\theta = \frac{\pi}{2}$ for a segment of bent fiber.

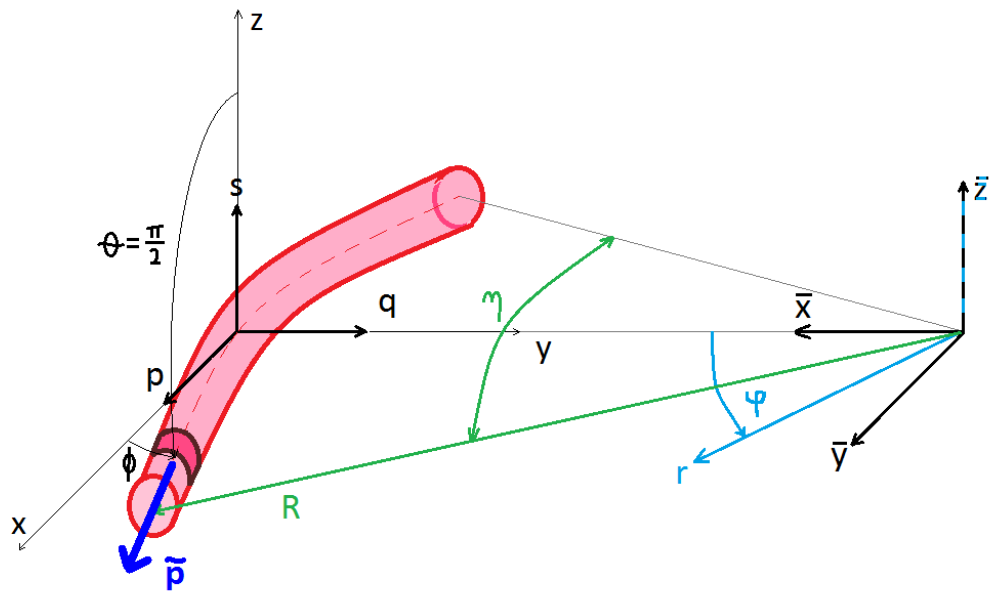

Figure 4-6. Orientation vector $\tilde{\mathbf{p}}$ for a segment of bent fiber.

Then Equations 3.8-1 through 3.8-3 give us segment orientation vector $\tilde{\mathbf{p}}$ components in the fiber coordinate system

$$\tilde{p}_1 = \cos\phi \tag{4.7-1}$$

$$\tilde{p}_2 = \sin\phi \tag{4.7-2}$$

$$\tilde{p}_3 = 0 \tag{4.7-3}$$

and the probability of finding a segment with given orientation is given by

$$\tilde{\psi}(\eta) = \begin{cases} \dfrac{1}{\pi\eta} & for\ \phi \in < -\dfrac{\eta}{2}, \dfrac{\eta}{2} > \\ 0 & elswhere \end{cases} \tag{4.7-4}$$

where we used normalization condition in Equation 3.8-6

$$\int_{\theta=0}^{\pi}\int_{\phi=0}^{2\pi}\tilde{\psi}\sin\theta\, d\theta d\phi = \int_{\theta=0}^{\pi}\int_{\phi=-\frac{\eta}{2}}^{\frac{\eta}{2}}\tilde{\psi}\sin\frac{\pi}{2}\, d\theta d\phi = 1 \tag{4.7-5}$$

In Equation 4.7-5, we have used even limits for $\phi \in \langle -\frac{\eta}{2}, \frac{\eta}{2}\rangle$ instead of integrating for $\phi \in \langle 0, \frac{\eta}{2}\rangle$ and $\phi \in \langle 2\pi - \frac{\eta}{2}, 2\pi\rangle$. We can use these even limits because function $\tilde{\psi}$ is periodic with a period of π. We use the same logic below for integrals containing $\tilde{\psi}$ powers of $\sin\phi$ and $\cos\phi$. All of these functions have period of 2π, therefore we can use even limits $\phi \in \langle -\frac{\eta}{2}, \frac{\eta}{2}\rangle$, to evaluate the integrals.

Now we can evaluate components of orientation tensor $\tilde{a}_{ij}$ corresponding to segments of bent fiber from definitions given in Equation 3.8-7

$$\tilde{a}_{11} = \int_{\theta=0}^{\pi}\int_{\phi=-\frac{\eta}{2}}^{\frac{\eta}{2}}\tilde{p}_1\tilde{p}_1\tilde{\psi}\sin\theta\, d\theta d\phi = \int_{\theta=0}^{\pi}\int_{\phi=-\frac{\eta}{2}}^{\frac{\eta}{2}}\cos^2\phi\,\frac{1}{\pi\eta}\, d\theta d\phi = \frac{\eta+\sin\eta}{2\eta} \tag{4.7-6}$$

$$\tilde{a}_{22} = \int_{\theta=0}^{\pi}\int_{\phi=-\frac{\eta}{2}}^{\frac{\eta}{2}}\tilde{p}_2\tilde{p}_2\tilde{\psi}\sin\theta\, d\theta d\phi = \int_{\theta=0}^{\pi}\int_{\phi=-\frac{\eta}{2}}^{\frac{\eta}{2}}\sin^2\phi\,\frac{1}{\pi\eta}\, d\theta d\phi = \frac{\eta-\sin\eta}{2\eta} \tag{4.7-7}$$

$$\tilde{a}_{12} = \tilde{a}_{21} = \int_{\theta=0}^{\pi}\int_{\phi=-\frac{\eta}{2}}^{\frac{\eta}{2}}\tilde{p}_1\tilde{p}_2\tilde{\psi}\sin\theta\, d\theta d\phi = \int_{\theta=0}^{\pi}\int_{\phi=-\frac{\eta}{2}}^{\frac{\eta}{2}}\sin\phi\cos\phi\,\frac{1}{\pi\eta}\, d\theta d\phi = 0 \tag{4.7-8}$$

The value of the last integral can be obtained without evaluation by examining symmetry of the problem or noting that we are evaluating odd function over even limits. We have therefore obtained two distinct values for two components of second order orientation tensor.

We can check that these values make sense by observing that Equation 3.8-11 is satisfied since

$$\tilde{a}_{11} + \tilde{a}_{22} = 1 \tag{4.7-9}$$

and noticing that for straight fiber

$$\lim_{\eta \to 0} \tilde{a}_{11} = \lim_{\eta \to 0} \frac{\eta + \sin \eta}{2\eta} = 1 \tag{4.7-10}$$

$$\lim_{\eta \to 0} \tilde{a}_{22} = \lim_{\eta \to 0} \frac{\eta - \sin \eta}{2\eta} = 0 \tag{4.7-11}$$

The components of a_{ijkl} can be calculated from definition given in Equation 3.8-8. All components containing odd powers of $\sin \eta$ evaluate to zero, therefore we are left with these non-zero components.

$$\begin{aligned} \tilde{a}_{1111} &= \int_{\theta=0}^{\pi} \int_{\phi=-\frac{\eta}{2}}^{\frac{\eta}{2}} \tilde{p}_1 \tilde{p}_1 \tilde{p}_1 \tilde{p}_1 \tilde{\psi} \sin \theta \, d\theta d\phi = \int_{\theta=0}^{\pi} \int_{\phi=-\frac{\eta}{2}}^{\frac{\eta}{2}} \cos^4 \phi \, \frac{1}{\pi\eta} d\theta d\phi \\ &= \frac{3\eta + (4 + \cos \eta) \sin \eta}{8\eta} \end{aligned} \tag{4.7-12}$$

$$\begin{aligned} \tilde{a}_{2222} &= \int_{\theta=0}^{\pi} \int_{\phi=-\frac{\eta}{2}}^{\frac{\eta}{2}} \tilde{p}_2 \tilde{p}_2 \tilde{p}_2 \tilde{p}_2 \tilde{\psi} \sin \theta \, d\theta d\phi = \int_{\theta=0}^{\pi} \int_{\phi=-\frac{\eta}{2}}^{\frac{\eta}{2}} \sin^4 \phi \, \frac{1}{\pi\eta} d\theta d\phi \\ &= \frac{3\eta + (-4 + \cos \eta) \sin \eta}{8\eta} \end{aligned} \tag{4.7-13}$$

$$\tilde{a}_{1122} = \tilde{a}_{2211} = \tilde{a}_{1212} = \tilde{a}_{2112} = \tilde{a}_{2121} = \tilde{a}_{1221} = \int_{\theta=0}^{\pi} \int_{\phi=-\frac{\eta}{2}}^{\frac{\eta}{2}} \tilde{p}_1\tilde{p}_1\tilde{p}_2\tilde{p}_2\tilde{\psi} \sin\theta \, d\theta d\phi$$

$$= \int_{\theta=0}^{\pi} \int_{\phi=-\frac{\eta}{2}}^{\frac{\eta}{2}} \cos^2\phi \sin^2\phi \, \frac{1}{\pi\eta} d\theta d\phi = \frac{\eta - \sin\eta\cos\eta}{8\eta} \tag{4.7-14}$$

We have therefore obtained three distinct values for eight non-zero components of fourth order orientation tensor. We can confirm that

$$\tilde{a}_{1111} + \tilde{a}_{2222} + \tilde{a}_{1122} + \tilde{a}_{2211} = 1 \tag{4.7-15}$$

and that fourth order orientation tensor contains information about second order orientation tensor

$$\tilde{a}_{11kk} = \tilde{a}_{1111} + \tilde{a}_{1122} = \frac{\eta + \sin\eta}{2\eta} = \tilde{a}_{11} \tag{4.7-16}$$

$$\tilde{a}_{22kk} = \tilde{a}_{2211} + \tilde{a}_{2222} = \frac{\eta - \sin\eta}{2\eta} = \tilde{a}_{22} \tag{4.7-17}$$

Again, we can show that for straight fiber, we only have one non-zero component

$$\lim_{\eta\to 0} \tilde{a}_{1111} = \lim_{\eta\to 0} \frac{3\eta + (4 + \cos\eta)\sin\eta}{8\eta} = 1 \tag{4.7-18}$$

$$\lim_{\eta\to 0} \tilde{a}_{2222} = \lim_{\eta\to 0} \frac{3\eta + (-4 + \cos\eta)\sin\eta}{8\eta} = 0 \tag{4.7-19}$$

$$\lim_{\eta\to 0}\tilde{a}_{1122} = \lim_{\eta\to 0}\tilde{a}_{2211} = etc. = \lim_{\eta\to 0}\frac{\eta - \sin\eta\cos\eta}{8\eta} = 0 \tag{4.7-20}$$

We can now use Equation 3.8-20 to perform orientation averaging to obtain properties in for a material containing bent fibers. We note that Equation 3.8-20 was derived from Equation 3.8-19, which is equivalent to Equations 3.7-40 through 3.7-53. We choose material constant notation from Equation 3.7-53 and write stiffness tensor for material containing bent fiber

$$\begin{aligned}\langle\check{C}\rangle_{ijkl} = {} & \mu_s\left(\delta_{ik}\delta_{jl} + \delta_{il}\delta_{jk}\right) + \lambda_s\left(\delta_{ij}\delta_{kl}\right) + \alpha_\lambda(\tilde{a}_{ij}\delta_{kl} + \tilde{a}_{kl}\delta_{ij}) \\ & +(\mu_0 - \mu_s)(\tilde{a}_{ik}\delta_{jl} + \tilde{a}_{il}\delta_{jk} + \tilde{a}_{jl}\delta_{ik} + \tilde{a}_{jk}\delta_{il}) + \beta_\lambda\tilde{a}_{ijkl} \\ & i, j, k, l = 1, 2, 3\end{aligned} \tag{4.7-21}$$

where subscript in μ_s and λ_s denotes that these constants are for straight fiber. We write out terms of Equation 4.7-21 in Voigt notation

$$\langle\check{C}\rangle = \mu_s\begin{bmatrix}2 & 0 & 0 & 0 & 0 & 0\\ 0 & 2 & 0 & 0 & 0 & 0\\ 0 & 0 & 2 & 0 & 0 & 0\\ 0 & 0 & 0 & 1 & 0 & 0\\ 0 & 0 & 0 & 0 & 1 & 0\\ 0 & 0 & 0 & 0 & 0 & 1\end{bmatrix} + \lambda_s\begin{bmatrix}1 & 1 & 1 & 0 & 0 & 0\\ 1 & 1 & 1 & 0 & 0 & 0\\ 1 & 1 & 1 & 0 & 0 & 0\\ 0 & 0 & 0 & 0 & 0 & 0\\ 0 & 0 & 0 & 0 & 0 & 0\\ 0 & 0 & 0 & 0 & 0 & 0\end{bmatrix}$$

$$\alpha_\lambda\begin{bmatrix}2\tilde{a}_{11} & \tilde{a}_{11}+\tilde{a}_{22} & \tilde{a}_{11} & 0 & 0 & 0\\ \tilde{a}_{11}+\tilde{a}_{22} & 2\tilde{a}_{22} & \tilde{a}_{22} & 0 & 0 & 0\\ \tilde{a}_{11} & \tilde{a}_{22} & 0 & 0 & 0 & 0\\ 0 & 0 & 0 & 0 & 0 & 0\\ 0 & 0 & 0 & 0 & 0 & 0\\ 0 & 0 & 0 & 0 & 0 & 0\end{bmatrix} \tag{4.7-22}$$

$$(\mu_0 - \mu_s)\begin{bmatrix}4\tilde{a}_{11} & 0 & 0 & 0 & 0 & 0\\ 0 & 4\tilde{a}_{22} & 0 & 0 & 0 & 0\\ 0 & 0 & 0 & 0 & 0 & 0\\ 0 & 0 & 0 & \tilde{a}_{22} & 0 & 0\\ 0 & 0 & 0 & 0 & \tilde{a}_{11} & 0\\ 0 & 0 & 0 & 0 & 0 & \tilde{a}_{11}+\tilde{a}_{22}\end{bmatrix}$$

$$+(\mu_0-\mu_s)\begin{bmatrix} 4\tilde{a}_{11} & 0 & 0 & 0 & 0 & 0 \\ 0 & 4\tilde{a}_{22} & 0 & 0 & 0 & 0 \\ 0 & 0 & 0 & 0 & 0 & 0 \\ 0 & 0 & 0 & \tilde{a}_{22} & 0 & 0 \\ 0 & 0 & 0 & 0 & \tilde{a}_{11} & 0 \\ 0 & 0 & 0 & 0 & 0 & \tilde{a}_{11}+\tilde{a}_{22} \end{bmatrix}$$

$$+\beta_\lambda\begin{bmatrix} \tilde{a}_{1111} & \tilde{a}_{1122} & 0 & 0 & 0 & 0 \\ \tilde{a}_{1122} & \tilde{a}_{2222} & 0 & 0 & 0 & 0 \\ 0 & 0 & 0 & 0 & 0 & 0 \\ 0 & 0 & 0 & 0 & 0 & 0 \\ 0 & 0 & 0 & 0 & 0 & 0 \\ 0 & 0 & 0 & 0 & 0 & \tilde{a}_{1122} \end{bmatrix}$$

then

$$\langle\check{C}\rangle=\begin{bmatrix} \check{C}_{11} & \check{C}_{12} & \check{C}_{13} & 0 & 0 & 0 \\ & \check{C}_{22} & \check{C}_{23} & 0 & 0 & 0 \\ & & \check{C}_{33} & 0 & 0 & 0 \\ & & & \check{C}_{44} & 0 & 0 \\ & sym. & & & \check{C}_{55} & 0 \\ & & & & & \check{C}_{66} \end{bmatrix} \tag{4.7-23}$$

where

$$\check{C}_{11}=\lambda_s+2\mu_s+2\tilde{a}_{11}(\alpha_\lambda+2(\mu_0-\mu_s))+\tilde{a}_{1111} \tag{4.7-24}$$

$$\check{C}_{22}=\lambda_s+2\mu_s+2\tilde{a}_{22}(\alpha_\lambda+2(\mu_0-\mu_s))+\tilde{a}_{2222} \tag{4.7-25}$$

$$\check{C}_{33}=\lambda_s+2\mu_s \tag{4.7-26}$$

$$\check{C}_{44}=\mu_s+\tilde{a}_{22}(\mu_0-\mu_s) \tag{4.7-27}$$

$$\check{C}_{55}=\mu_s+\tilde{a}_{11}(\mu_0-\mu_s) \tag{4.7-28}$$

$$\check{C}_{66} = \mu_s + (\tilde{a}_{11} + \tilde{a}_{22})(\mu_0 - \mu_s) + \tilde{a}_{1122} \tag{4.7-29}$$

$$\check{C}_{23} = \lambda_s + \tilde{a}_{22}\, \alpha_\lambda \tag{4.7-30}$$

$$\check{C}_{13} = \lambda_s + \tilde{a}_{11}\, \alpha_\lambda \tag{4.7-31}$$

$$\check{C}_{12} = \lambda_s + (\tilde{a}_{11} + \tilde{a}_{22})\alpha_\lambda + \tilde{a}_{1122} \tag{4.7-32}$$

Clearly, this is an orthotropic material with principal axes aligned with those of the laboratory coordinate system. We know that regardless of the method used for obtaining stiffness tensor for a material with fibers in single configuration, we should obtain orthotropic stiffness tensor. We can therefore conclude that orientation averaging of transversely isotropic tensor performed above resulted in the correct form of orthotropic stiffness tensor. It is important to realize that we could have simply performed orientation averaging and arrived at the same result without studying the symmetry of the problem first. However, the result would be in question, because it may not be intuitively obvious that orthotropic material with three planes of symmetry can have a characteristic volume with two planes of symmetry. For clarity, we copy the form of orthotropic stiffness tensor given in Equation 4.4-3 below.

$$\begin{gathered}\tilde{C}_{ijkl} = \mu\left(\delta_{ik}\delta_{jl} + \delta_{il}\delta_{jk}\right) + \lambda\delta_{ij}\delta_{kl} + \alpha_{\lambda 1}\left(p_i p_j \delta_{kl} + \delta_{ij} p_k p_l\right) + \alpha_{\lambda 2}\left(q_i q_j \delta_{kl} + \right. \\ \left. \delta_{ij} q_k q_l\right) + 2\mu_1\left(\delta_{ik} p_j p_l + \delta_{il} p_j p_k + \delta_{jl} p_i p_k + \delta_{jk} p_i p_l\right) + 2\mu_2\left(\delta_{ik} q_j q_l + \delta_{il} q_j q_k + \right. \\ \left. \delta_{jl} q_i q_k + \delta_{jk} q_i q_l\right) + \beta_{\lambda 1} p_i p_j p_k p_l + \beta_{\lambda 2} q_i q_j q_k q_l + \beta_{\lambda 3}\left(p_i p_j q_k q_l + q_i q_j p_k p_l\right) \\ i, j, k, l = 1, 2, 3\end{gathered} \tag{4.7-33}$$

where unit vectors **p** and **q** denote normals for planes of symmetry. During our orientation averaging procedure, these vectors were aligned with the laboratory system. For consistency, we select **p** = (1,0,0) and **q** = (0,1,0) and write out the terms of this tensor in Voigt notation

$$
\tilde{C} = \mu \begin{bmatrix} 2 & 0 & 0 & 0 & 0 & 0 \\ 0 & 2 & 0 & 0 & 0 & 0 \\ 0 & 0 & 2 & 0 & 0 & 0 \\ 0 & 0 & 0 & 1 & 0 & 0 \\ 0 & 0 & 0 & 0 & 1 & 0 \\ 0 & 0 & 0 & 0 & 0 & 1 \end{bmatrix} + \lambda \begin{bmatrix} 1 & 1 & 1 & 0 & 0 & 0 \\ 1 & 1 & 1 & 0 & 0 & 0 \\ 1 & 1 & 1 & 0 & 0 & 0 \\ 0 & 0 & 0 & 0 & 0 & 0 \\ 0 & 0 & 0 & 0 & 0 & 0 \\ 0 & 0 & 0 & 0 & 0 & 0 \end{bmatrix} + \alpha_{\lambda 1} \begin{bmatrix} 2 & 1 & 1 & 0 & 0 & 0 \\ 1 & 0 & 0 & 0 & 0 & 0 \\ 1 & 0 & 0 & 0 & 0 & 0 \\ 0 & 0 & 0 & 0 & 0 & 0 \\ 0 & 0 & 0 & 0 & 0 & 0 \\ 0 & 0 & 0 & 0 & 0 & 0 \end{bmatrix}
$$

$$
+\alpha_{\lambda 2} \begin{bmatrix} 0 & 1 & 0 & 0 & 0 & 0 \\ 1 & 2 & 1 & 0 & 0 & 0 \\ 0 & 1 & 0 & 0 & 0 & 0 \\ 0 & 0 & 0 & 0 & 0 & 0 \\ 0 & 0 & 0 & 0 & 0 & 0 \\ 0 & 0 & 0 & 0 & 0 & 0 \end{bmatrix} + 2\mu_1 \begin{bmatrix} 4 & 0 & 0 & 0 & 0 & 0 \\ 0 & 0 & 0 & 0 & 0 & 0 \\ 0 & 0 & 0 & 0 & 0 & 0 \\ 0 & 0 & 0 & 0 & 0 & 0 \\ 0 & 0 & 0 & 0 & 1 & 0 \\ 0 & 0 & 0 & 0 & 0 & 1 \end{bmatrix}
$$

$$
+2\mu_2 \begin{bmatrix} 0 & 0 & 0 & 0 & 0 & 0 \\ 0 & 4 & 0 & 0 & 0 & 0 \\ 0 & 0 & 0 & 0 & 0 & 0 \\ 0 & 0 & 0 & 1 & 0 & 0 \\ 0 & 0 & 0 & 0 & 0 & 0 \\ 0 & 0 & 0 & 0 & 0 & 1 \end{bmatrix} + \beta_{\lambda 1} \begin{bmatrix} 1 & 0 & 0 & 0 & 0 & 0 \\ 0 & 0 & 0 & 0 & 0 & 0 \\ 0 & 0 & 0 & 0 & 0 & 0 \\ 0 & 0 & 0 & 0 & 0 & 0 \\ 0 & 0 & 0 & 0 & 0 & 0 \\ 0 & 0 & 0 & 0 & 0 & 0 \end{bmatrix} \tag{4.7-34}
$$

$$
+\beta_{\lambda 2} \begin{bmatrix} 0 & 0 & 0 & 0 & 0 & 0 \\ 0 & 1 & 0 & 0 & 0 & 0 \\ 0 & 0 & 0 & 0 & 0 & 0 \\ 0 & 0 & 0 & 0 & 0 & 0 \\ 0 & 0 & 0 & 0 & 0 & 0 \\ 0 & 0 & 0 & 0 & 0 & 0 \end{bmatrix} + \beta_{\lambda 3} \begin{bmatrix} 0 & 1 & 0 & 0 & 0 & 0 \\ 1 & 0 & 0 & 0 & 0 & 0 \\ 0 & 0 & 0 & 0 & 0 & 0 \\ 0 & 0 & 0 & 0 & 0 & 0 \\ 0 & 0 & 0 & 0 & 0 & 0 \\ 0 & 0 & 0 & 0 & 0 & 0 \end{bmatrix}
$$

then

$$
\tilde{C} = \begin{bmatrix} \tilde{C}_{11} & \tilde{C}_{12} & \tilde{C}_{13} & 0 & 0 & 0 \\ & \tilde{C}_{22} & \tilde{C}_{23} & 0 & 0 & 0 \\ & & \tilde{C}_{33} & 0 & 0 & 0 \\ & & & \tilde{C}_{44} & 0 & 0 \\ & sym. & & & \tilde{C}_{55} & 0 \\ & & & & & \tilde{C}_{66} \end{bmatrix} \tag{4.7-35}
$$

where

$$
\tilde{C}_{11} = \lambda + 2\mu + 8\mu_1 + 2\alpha_{\lambda 1} + \beta_{\lambda 1} \tag{4.7-36}
$$

$$\tilde{C}_{22} = \lambda + 2\mu + 8\mu_2 + 2\alpha_{\lambda 2} + \beta_{\lambda 2} \tag{4.7-37}$$

$$\tilde{C}_{33} = \lambda + 2\mu \tag{4.7-38}$$

$$\tilde{C}_{44} = \mu + 2\mu_2 \tag{4.7-39}$$

$$\tilde{C}_{55} = \mu + 2\mu_1 \tag{4.7-40}$$

$$\tilde{C}_{66} = \mu + 2\mu_1 + 2\mu_2 \tag{4.7-41}$$

$$\tilde{C}_{23} = \lambda + \alpha_{\lambda 2} \tag{4.7-42}$$

$$\tilde{C}_{13} = \lambda + \alpha_{\lambda 1} \tag{4.7-43}$$

$$\tilde{C}_{12} = \lambda + \alpha_{\lambda 1} + \alpha_{\lambda 2} + \beta_{\lambda 3} \tag{4.7-44}$$

This is an orthotropic stiffness tensor and we note that stiffness tensors $\langle \check{C} \rangle_{ijkl}$ is the same as $\tilde{C}_{ijkl}$ and that we have obtained nine material constants by planar orientation averaging of transversely isotropic stiffness tensor. equating each non-zero component of these tensors gives us nine Equations to obtain nine material constants

$$\mu = \mu_s - \beta_\lambda \, \tilde{a}_{1122} \tag{4.7-45}$$

$$\lambda = \lambda_s + 2 \, \beta_\lambda \, \tilde{a}_{1122} \tag{4.7-46}$$

$$\alpha_{\lambda 1} = \alpha_\lambda \tilde{a}_{11} - 2 \, \tilde{a}_{1122} \, \beta_\lambda \tag{4.7-47}$$

$$\alpha_{\lambda 2} = \alpha_\lambda \tilde{a}_{22} - 2 \, \tilde{a}_{1122} \, \beta_\lambda \tag{4.7-48}$$

$$\mu_1 = \frac{1}{2}((\mu_0 - \mu_s)\tilde{a}_{11} + \tilde{a}_{1122}\,\beta_\lambda) \tag{4.7-49}$$

$$\mu_2 = \frac{1}{2}((\mu_0 - \mu_s)\tilde{a}_{22} + \tilde{a}_{1122}\,\beta_\lambda) \tag{4.7-50}$$

$$\beta_{\lambda 1} = \tilde{a}_{1111}\,\beta_\lambda \tag{4.7-51}$$

$$\beta_{\lambda 2} = \tilde{a}_{2222}\beta_\lambda \tag{4.7-52}$$

$$\beta_{\lambda 3} = 3\tilde{a}_{1122}\,\beta_\lambda \tag{4.7-53}$$

Note that one could write the above Equations only in terms of $\tilde{a}_{1111}$ and $\tilde{a}_{2222}$, with the remaining components being obtained from Equations 4.6-30 and 4.6-31. For straight fiber, $\eta \to 0$, we use Equations 4.7-10, 4.7-11 and 4.7-18 through 4.7-20 to show that

$$\mu(\eta \to 0) = \mu_s \tag{4.7-54}$$

$$\lambda(\eta \to 0) = \lambda_s \tag{4.7-55}$$

$$\alpha_{\lambda 1}(\eta \to 0) = \alpha_\lambda \tag{4.7-56}$$

$$\alpha_{\lambda 2}(\eta \to 0) = 0 \tag{4.7-57}$$

$$\mu_1(\eta \to 0) = \frac{1}{2}(\mu_s - \mu_0) \tag{4.7-58}$$

$$\mu_2(\eta \to 0) = 0 \tag{4.7-59}$$

$$\beta_{\lambda 1}(\eta \to 0) = \beta_\lambda \tag{4.7-60}$$

$$\beta_{\lambda 2}(\eta \to 0) = 0 \tag{4.7-61}$$

$$\beta_{\lambda 3}(\eta \to 0) = 0 \tag{4.7-62}$$

These constants reduce the form of Equation 4.7-33 to the form of Equation in 4.7-21. Therefore for a material containing straight fibers in single orientation given by vector **p**, we obtain transverse isotropy as expected.

To obtain μ_s , $\mu_0, \lambda_s, \alpha_\lambda, \beta_\lambda$, we can use experimental data, numerical simulations or we can use Halpin-Tsai-Kardos Equations. In general, all five material constants depend on the properties of matrix M_m, properties of fiber M_f, fiber volume fraction V_f and fiber aspect ratio ξ. In the case of Halpin-Tsai-Kardos [55] Equations, μ_s , μ_0 are independent of ξ.

5 Experimental Measurement of Fiber Architecture in Injection Molded Plaques

5.1 Introduction

Observation of fiber microstructure within DFCs described in earlier sections of this dissertation reveals significant complexity on multiple scales. The focus of this chapter is on quantitative measurements of fiber microstructure parameters relevant for newly developed stiffness model. An ideal measurement technique would provide us with all three measures for a large number of fibers at any point within our sample, thereby giving us complete information about the state of fiber configuration within a region of interest. Since 2005, numerous exploratory experiments were performed with various pieces of equipment, none of which could provide such information. The techniques included x-ray transmission imaging, x-ray micro-tomography, magnetic resonance imaging, neutron imaging, electron microscope imaging and optical imaging with and without various methods of matrix removal. None of these techniques were capable of generating full quantitative configuration dataset for realistic materials of interest. It is possible to gain qualitative appreciation for the nature of microstructure within materials of interest and to perform comparisons, however producing quantitative data for configuration is currently not possible. It is possible to use these methods separately to provide information about fiber orientation, fiber length and fiber curvature. This leaves us with uncorrelated data set of our microstructure measures and necessitates introduction of additional assumptions for comparison of results.

5.2 Fiber Orientation Measurement

The fiber orientation measurement technique used in this dissertation relies on optical measurement of individual filament cross-sections with method of ellipses (MoE). This technique has been extensively studied and applied for short fiber reinforced thermoplastics. Bay and Tucker [56] provide detailed mathematical background with examples. Automation of this method is described by Hine [57]. Velez [58] removes ambiguity in resolving fiber orientation from elliptical cross-section by using fiber shadows over an etched surface and generates example data with manual measurement. Details of sample preparation are discussed by Velez [59]. The following section highlights automation of this technique allowing generation of unambiguous fiber orientation results in reasonable amount of time.

For the purpose of fiber orientation measurement, we assume that fibers are straight cylinders described by orientation vector **p**. This vector is traditionally given by two angles θ and ϕ as shown in Figure 5-1.

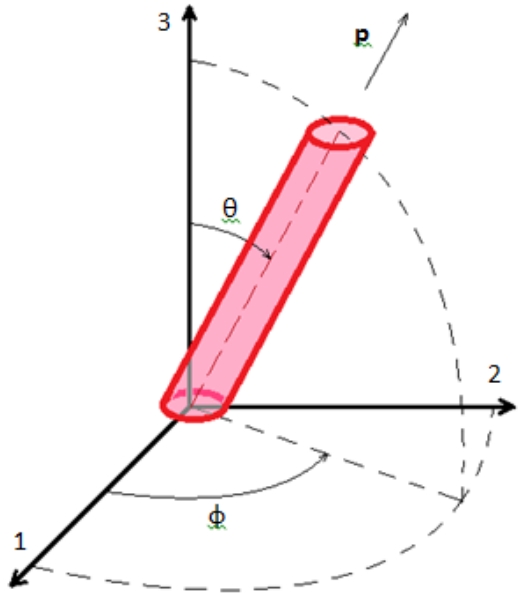

Figure 5-1. Coordinate system and definition of θ, ϕ and orientation vector **p**.

Then the components of the orientation vector can be written as

$$p_1 = \sin\theta \cos\phi \tag{5.2-1}$$

$$p_2 = \sin\theta \sin\phi \tag{5.2-2}$$

$$p_3 = \cos\theta \tag{5.2-3}$$

We note that these angles are directly related to Euler angles discussed in previous sections and that either set of angles α, β or ϕ, θ can be used to describe fiber orientation vector.

$$\phi = \alpha \tag{5.2-4}$$

$$\theta = \frac{\pi}{2} - \beta \tag{5.2-5}$$

To characterize orientation state for an ensemble of fibers, we use a set of even order orientation tensors. For correlated fiber length and fiber orientation, Bay and Tucker [56] propose definition of weighed fiber orientation tensor

$$a^t_{ij,k\ldots l} = \frac{\int_{L=0}^{\infty}\int_{\theta=0}^{\pi}\int_{\phi=0}^{2\pi} p_i p_j p_k \ldots p_l L^t \psi_S(\phi,\theta\,,L)\sin\theta \;\; d\phi d\theta dL}{\int_{L=0}^{\infty}\int_{\theta=0}^{\pi}\int_{\phi=0}^{2\pi} L^t \psi_S(\phi,\theta\,,L)\; d\phi d\theta dL} \qquad i,j,k,\ldots l = 1,2,3;\; t = 0\; or\; 1 \tag{5.2-6}$$

Where the number of subscripts i,j,k…l indicates the rank of the tensor L is fiber length and t is an exponent. When t is zero, each fiber has equal weight and $a^0_{ij,k..l}$ represents number average orientation. When t is equal to one, each fiber has weight equal to its length (or weight – assuming identical fiber diameters) and $a^1_{ij,k..l}$represents weight-average fiber orientation tensor. This assumption results in equality of number-average and weight-average tensor measures

$$\psi_S(\phi,\theta\,,L) = \psi_S(L)\psi(\phi,\theta\,) \rightarrow\; a^0_{ij,k..l} = a^1_{ij,k..l} \qquad i,j,k,\ldots l = 1,2,3; \tag{5.2-7}$$

Since measurement of physical samples consist of measurements of a large number of discrete fibers, integration in Equation 5.2-6 is replaced by summation with parameters discretized into k intervals

$$a^t_{ijk\ldots l} = \frac{\sum\left(p_i p_j p_k \ldots p_l\right)_k L^t F_k}{\sum L^t F_k} \qquad i,j,k,\ldots l = 1,2,3 \tag{5.2-8}$$

where F_k represents the number of fibers in kth interval. When we obtain measurements from a polished cross-section, we need to introduce a weighing function F_n to correct a bias caused by higher probability of finding fibers with nearly circular cross-section compared to the probability of finding a fiber with elongated ellipse cross-section. The weighing function is proportional to the useful projected height as proposed by Konicek [60]

$$F_n = \frac{1}{L_n\cos\theta_n + d_n\sin\theta_n} \tag{5.2-9}$$

or by Bay [56]

$$F_n = \frac{1}{L_n \cos\theta_n} \tag{5.2-10}$$

Using the latter weighing function in weight-averaged definition of orientation, the dependence on fiber length is eliminated and we are left with

$$a_{ijk\ldots l} = \frac{\sum\left(p_i p_j p_k \ldots p_l\right)_n \frac{1}{\cos\theta_n}}{\sum \frac{1}{\cos\theta_n}} \qquad i, j, k, \ldots l = 1, 2, 3 \tag{5.2-11}$$

For physical sample preparation, any metallographic technique is acceptable as long as fiber fracturing and fiber pull-out is minimized providing a smooth surface for etching. Velez [59] provides detailed guide for sample preparation using thermoplastic binder. Araldyte GY 502 epoxy with Hysol HD3416 hardener to mount specimens was used to mount specimens presented in this work. The mounting is followed by grinding and polishing on Struers equipment, starting with 500-4000 grade SiC paper in 30 to 60 second cycles at 150 RPM at 20-25N pressure. This is followed by 6μm MD Largo composite disc for 5 minutes at 15N, 3μm DAC cloth for 10 minutes at 30N and 1μm DUR cloth for 6 to 8 minutes at 30N pressure. Final polish is performed with diamond polishing assisted by purple lube. This procedure results in a sample with flat surface without contrast between fiber and matrix. To increase the contrast to allow for automated fiber orientation measurement, the sample is etched to generate rougher and less reflective matrix. Oxygen plasma etching is used when possible to retain good control over the process. Chemical etching is necessary for some material systems. Etching may result not only in rougher surface, but also removal of a thin layer of matrix material exposing the polished fiber ends.

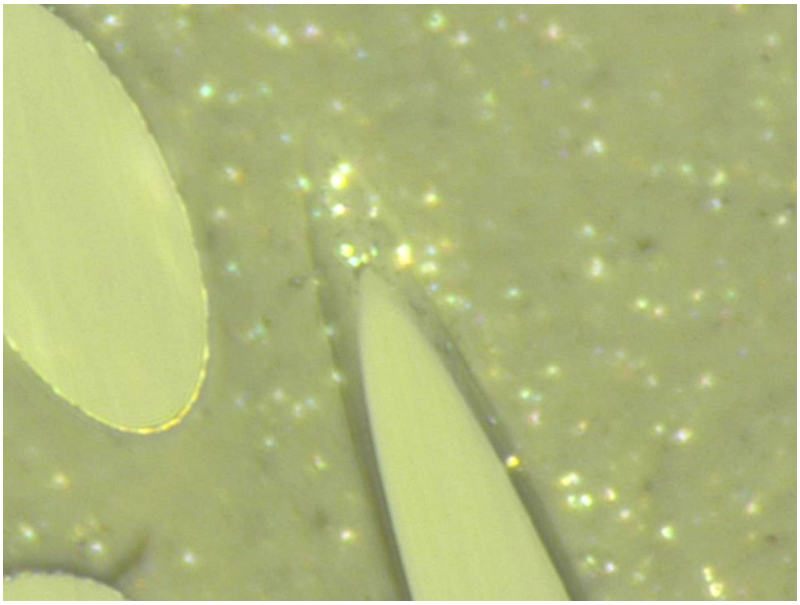

Figure 5-2. Typical digital image of polished and etched with white fibers and black matrix.

Subsequent procedure consists of generating microscope images and fitting ellipses to the fiber cross-sections. Automated systems [57] generally rely on the contrast between fiber and matrix material as seen in a digital image shown in Figure 5-3. To enhance this contrast beyond the level achieved by etching, the sample may be sputter coated with gold or silver.

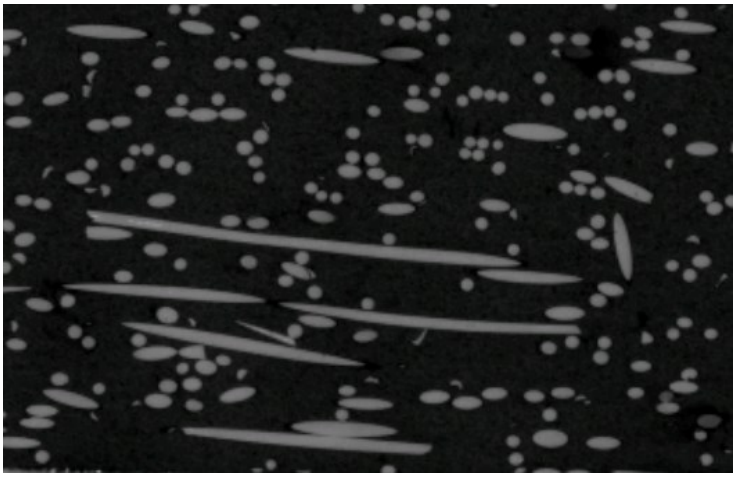

Figure 5-3. Typical digital image of polished and etched with white fibers and black matrix.

The information from Figure 5-3 is then thresholded and, after isolation of individual fiber cross sections end eliminating fragments, ellipses are fitted to the white regions in

the image. The new approach outlined herein relies on identical sample preparation, however the image is acquired with ligting showing fibers as solid white objects, fiber ends extending above the etched matrix as black “shadows” and matrix as gray. A typical image is shown in Figure 5-4.

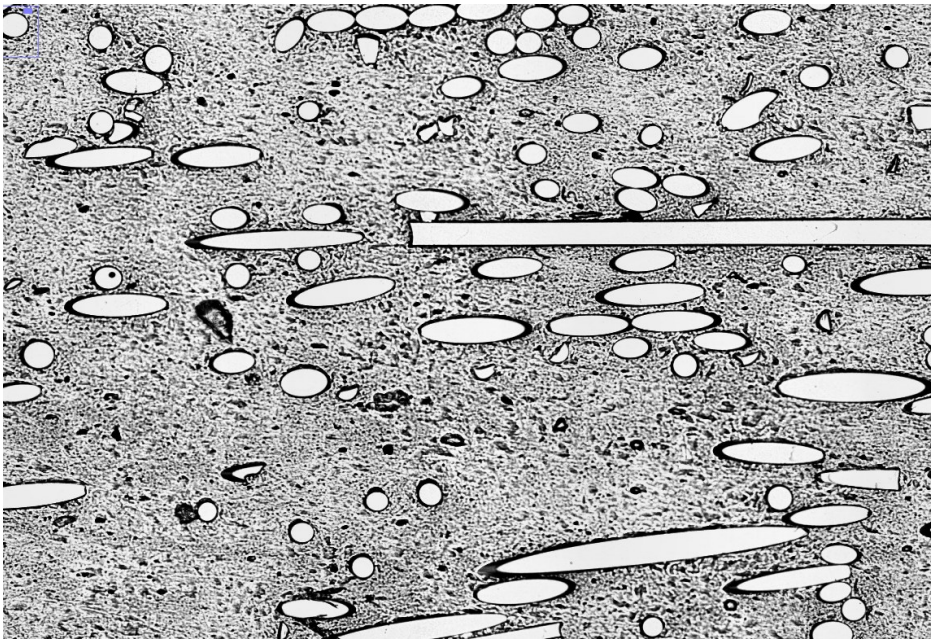

Figure 5-4. Digital image showing solid white fibers, with blask “shadows” indicating fiber ends extending above the etched surface.

An automated algorithm can be used to detect the shadow and determine unambiguous fiber orientation as shown in Figure 5-5.

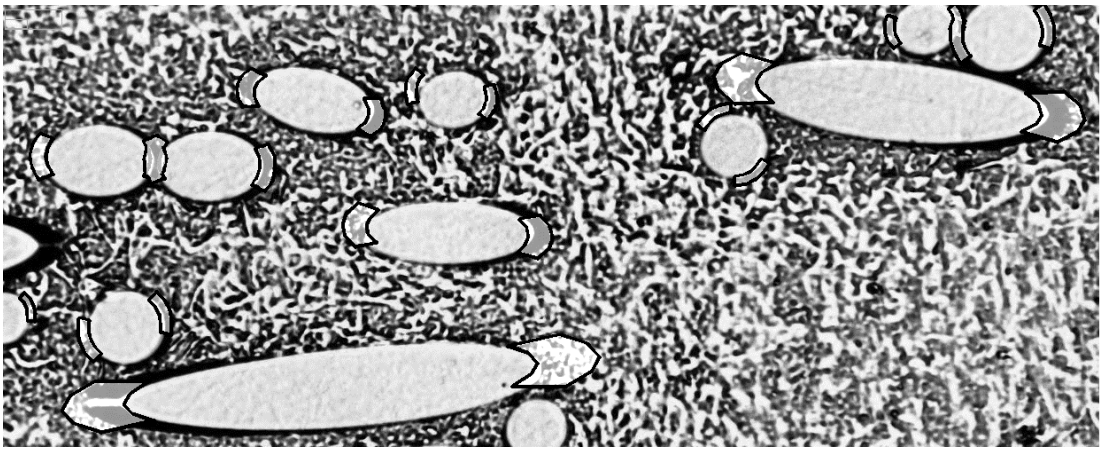

Figure 5-5. Digital image showing solid white fibers, with black “shadows” indicating fiber ends extending above the etched surface.

We can now present measurement results for an injection molded plaque with polypropylene and 40% glass fiber content by weight. The measurements must be performed on two physical samples collected from approximately identical location and the measurement and for the purpose of this discussion, we assume that the measurements are performed over the same area in both samples. Figure 5.6 shows coordinate system (e_1, e_2, e_3) and two coordinate systems h^f and h^c associated with two perpendicular planes. Direction of the first h^f axis corresponds to the flow direction in the sample, while the direction of the first h^c axis corresponds to the cross-flow direction.

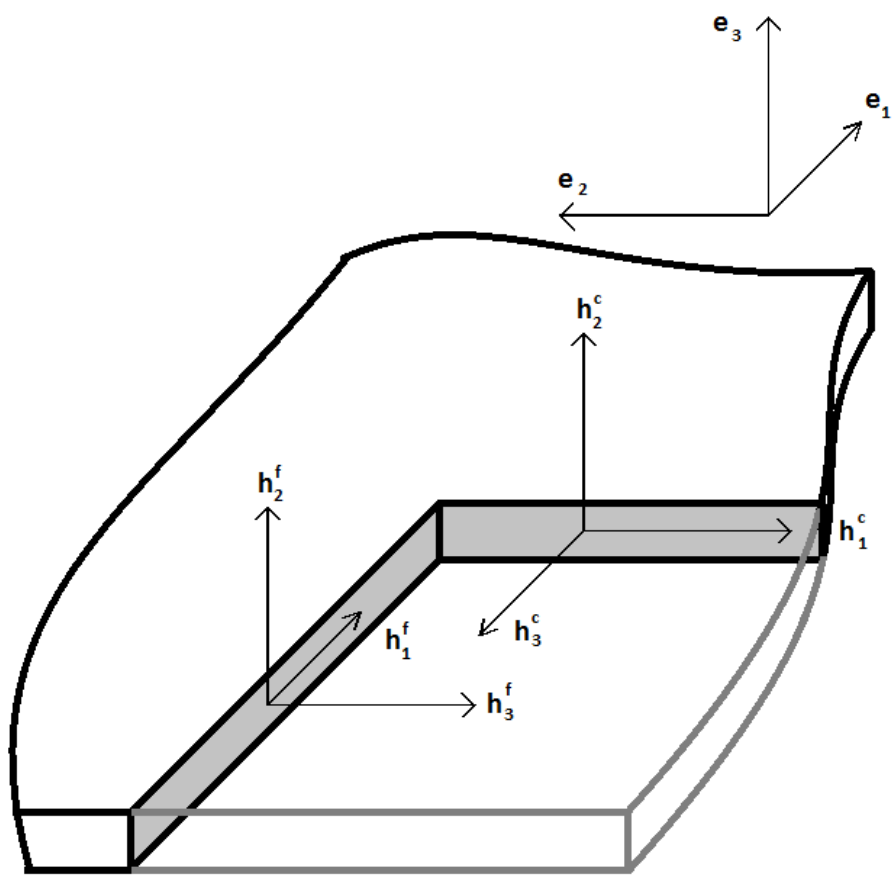

Figure 5-6. Section coordinate systems h^f and h^c and global coordinate system (e_1, e_2, e_3).

We can start exploring results by looking at raw angle distributions as measured from samples. Figure 5-7 through Figure 5-10 show as measured fiber angle histograms for flow direction sample with ten degree binning. The distribution for angle α shows that most fibers lay in the plane of the sample. The distribution for angle β clearly demonstrates that the likelihood of finding a fiber increases with the absolute value of β and correction is necessary to visualize unbiased distribution near $\beta = 0$.

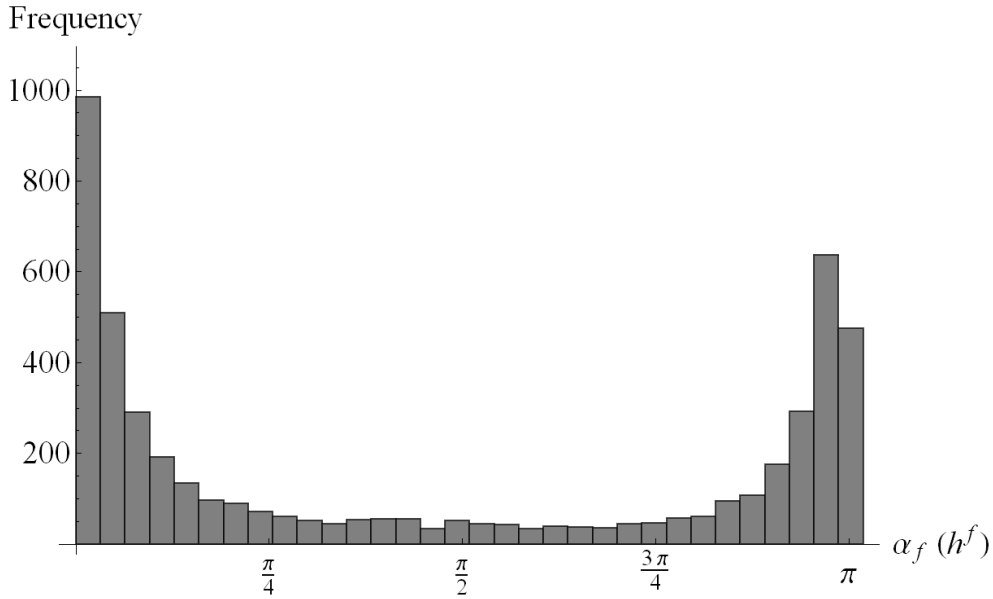

Figure 5-7 Raw distribution of angle α for fibers measured in flow direction sample expressed in flow sample coordinate system.

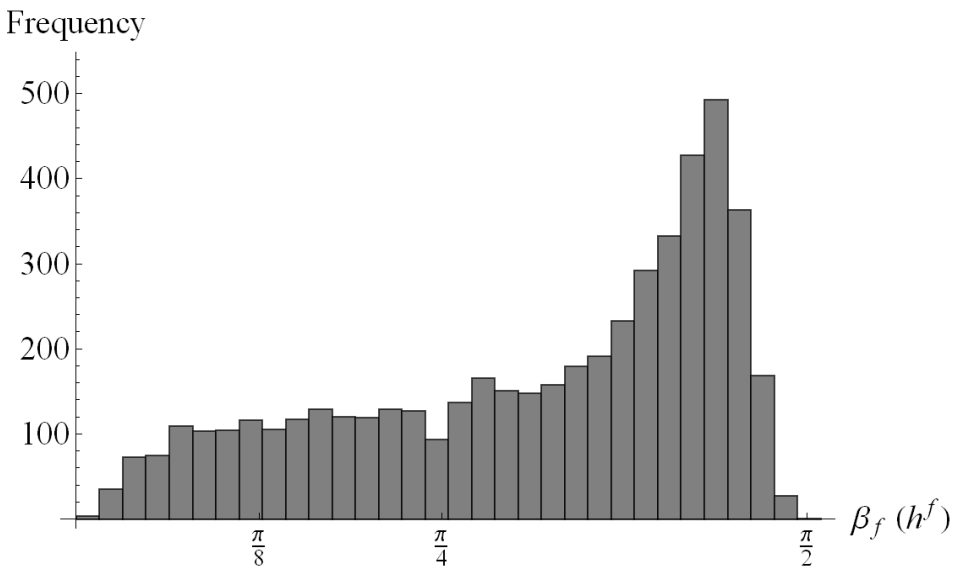

Figure 5-8. Raw distribution of angle β for fibers measured in flow direction sample expressed in flow sample coordinate system.

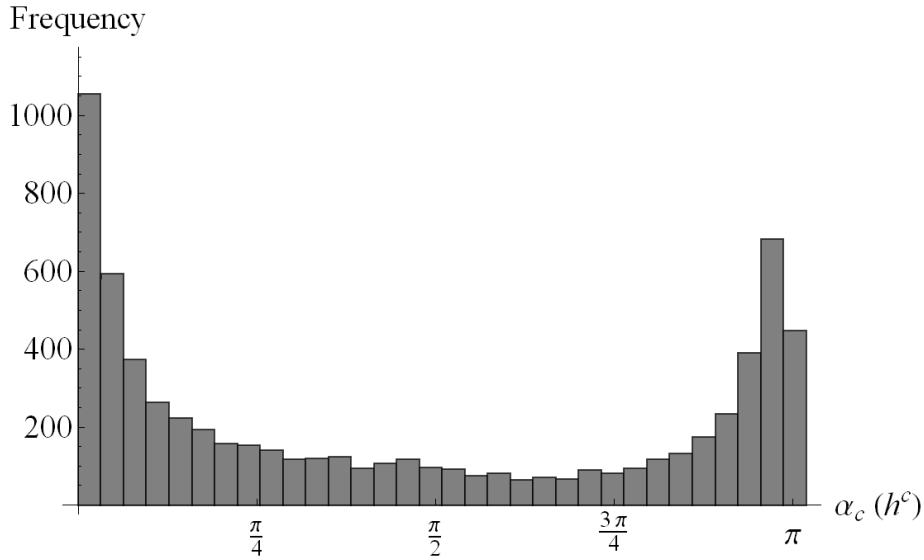

Figure 5-9. Raw distribution of angle α for fibers measured in cross flow direction sample expressed in cross flow sample coordinate system.

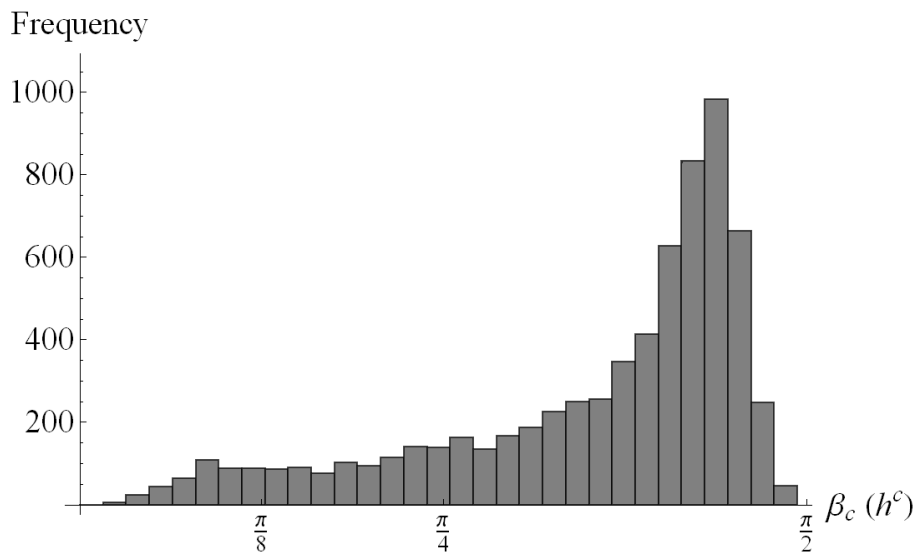

Figure 5-10. Raw distribution of angle β for fibers measured in cross flow direction sample expressed in cross flow sample coordinate system.

Equations 5.2-1 through 5.2-5 can then be used to calculate components of orientation vector for each fiber. Since we have measured the orientation over identical area, we can combine the results by transforming the cross-flow direction results to flow direction coordinate system using Equation 5.2-12

$$\begin{Bmatrix} h_1^f \\ h_2^f \\ h_3^f \end{Bmatrix} = \begin{bmatrix} 0 & 0 & -1 \\ 0 & 1 & 0 \\ 1 & 0 & 0 \end{bmatrix} \begin{Bmatrix} h_1^c \\ h_2^c \\ h_3^c \end{Bmatrix} \tag{5.2-12}$$

Equation 5.2-13 is then used to express the combined results in the global coordinate system

$$\begin{Bmatrix} e_1 \\ e_2 \\ e_3 \end{Bmatrix} = \begin{bmatrix} 1 & 0 & 0 \\ 0 & 0 & -1 \\ 0 & 1 & 0 \end{bmatrix} \begin{Bmatrix} h_1^f \\ h_2^f \\ h_3^f \end{Bmatrix} \tag{5.2-13}$$

To show the fiber orientation changing as a function of thickness, we will construct weight averged second order orientation tensor

$$a_{ij} = \frac{\sum (p_i p_j)_n \frac{1}{\cos\theta_n}}{\sum \frac{1}{\cos\theta_n}} \qquad i, j = 1, 2, 3 \tag{5.2-14}$$

Figure 5-11 shows combined results for all measured fibers as a function of normalized thickness. In this plot, the specimen surfaces lie at x=0 and x=1, while the middle of the sample is at x=0.5. We can clearly see the core-shell-skin structure typical of injection molded thermoplastics.

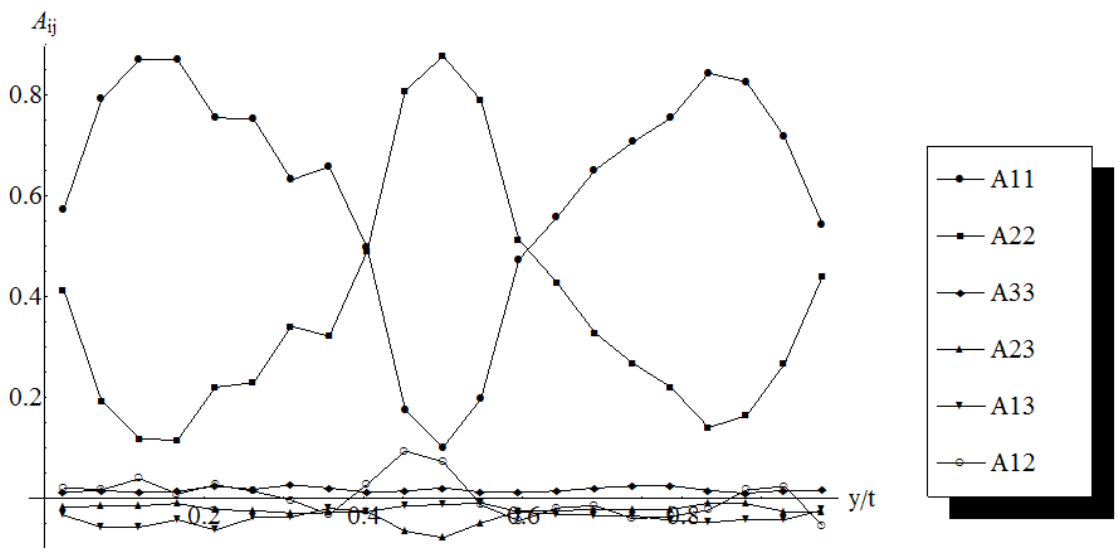

Figure 5-11. Combined results for all measured fibers as a function of normalized thickness.

It is comforting to note that results measured from cross-flow sample as well as from flow sample approximately match. Figure 5-12 shows comparison of flow and cross-flow sample measurements for orientation tensor component A_{11} and Figure 5-13 shows the same comparison for component A_{22}.

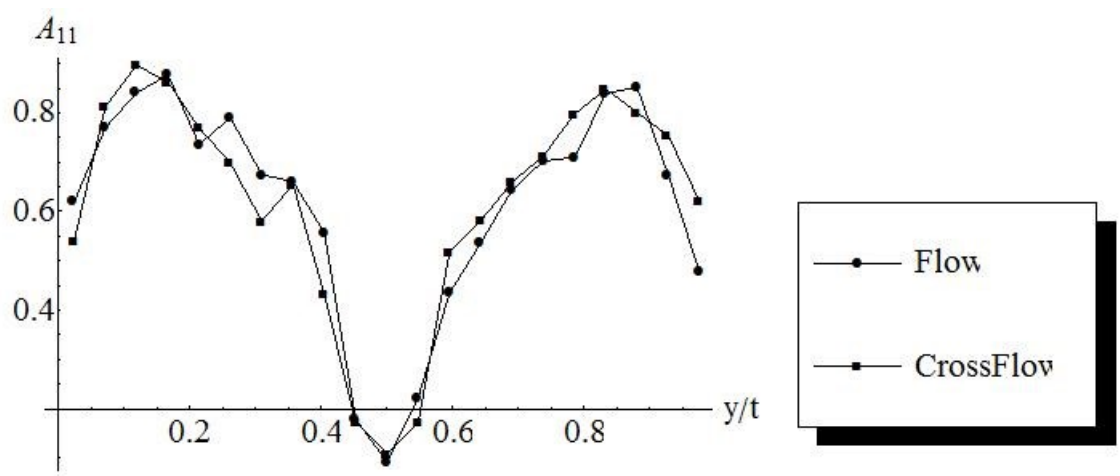

Figure 5-12. Fiber orientation tensor component A_{11} for flow and cross flow sample.

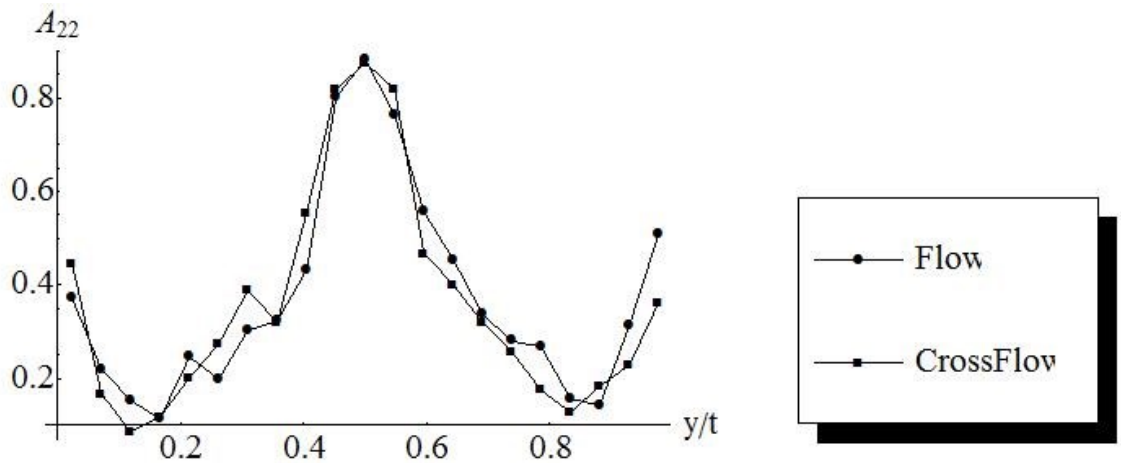

Figure 5-13. Fiber orientation tensor component A_{22} for flow and cross flow sample.

5.3 Fiber Length Measurement

This section presents fiber length distribution measurement for discontinuous fiber reinforced composites. The procedure was presented and published [7], however a brief summary is presented in this section. The objective in developing this procedure was to produce an un-biased method for fiber length distribution measurement in long fiber reinforced injection molded thermoplastics. The difficulty with measurement is that fiber diameter of glass and carbon fibers is measured in micrometers, while the fiber length spans fragments measured in tens of micrometers to nominally ten millimeter long fibers. This large fiber length span eliminated many non destructive techniques, such as X-ray tomography because of difficulties with achieving high resolution on micro-scale, while performing measurements in the meso-scale. This leads to refinement of destructive techniques, where the matrix is removed by digestion or pyrolysis and the fibers are measured individually, typically from a digital image. The bias encountered in the measurement as encountered in the industry usually comes from two sources. First, the selection of the physical fiber sample is typically performed with tweezers. This selection technique may be appropriate for screening, however there is no guarantee that the selected fibers represent the fiber length distribution in the material. If the sample is selected only from the surface of the fiber network, the results may represent fiber length distribution from the skin and shell of the sample and not the core. There is also high likelihood that short fibers may be discarded in this physical selection technique. The second source of the bias comes from preferential selection of long fibers, which will be discussed below in more detail. If the physical selection region is unknown, the bias cannot be accounted for and corrected for rigorously.

The procedure outlined below consists of five steps composite coupon isolation partially constrained removal of matrix material fiber sample isolation filament dispersion imaging and individual filament length measurement

This measurement is then followed by bias correction that assures Coupon isolation is usually necessary because pyrolysis of an entire composite part is impractical and unnecessary. The goal is to isolate a coupon by cutting a region of the composite part without cutting fibers that will be subsequently measured. This means that the minimum dimension of the sample will be no less than twice the maximum possible fiber length in the composite material. The maximum fiber length for injection-molded thermoplastics is the pellet size, however determination of maximum fiber length for other processes may be more involved.

The next step is partially constrained removal of matrix. The objective in this step is to remove matrix in a manner that would retain the fiber network structure and allow subsequent fiber sample isolation. Pyrolysis was shown to be effective for many thermoplastics. Figure 5-14 shows a sample after pyrolysis where the coupon was fully constrained during the procedure. Fully constraining the fiber often leads to a fiber sample that cannot be subsequently separated due to highly entangled nature of the fiber structure. Figure 5-15 fiber sample after unconstrained pyrolysis, where the fiber network structure was not retained due to long bent fibers straightening during the pyrolysis. Finding the proper level of partial constraint requires experimentation and depends on the specific material and fiber length distribution.

Figure 5-14. Network of glass fibers after fully constrained pyrolysis.

Figure 5-15. Network of carbon fibers after unconstrained pyrolysis.

The objective of fiber sample isolation step is to obtain a relatively small sample of fibers from a well defined region of the sample. The process involves inserting a needle attached to a hypodermic syringe with a liquid epoxy through the mass of fibers. The needle is withdrawn through the fiber structure while dispensing the epoxy through the needle at a constant rate. The continuous stream of epoxy results in an approximately cylindrical column of resin that extends through the entire thickness of the fiber network such as shown in Figure 5-16. The number of fibers collected from the specimen is proportional to the epoxy volume. Resin viscosity, the needle gage and the withdrawal rate of the needle through the fiber stack influence the selected region. Epon 828 resin mixed with 55 phr Versamid 125 supplied by Hexion along with an 18 gage hypodermic needle was used successfully for measurements of injection molded thermoplastics.

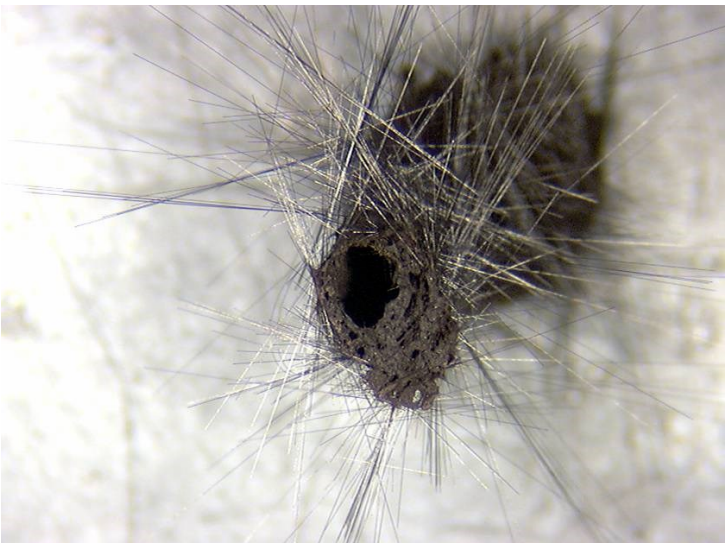

Figure 5-16. Isolated fibers with epoxy cylinder.

After this epoxy sets, the fibers not intersecting the cylinder can be removed and second pyrolysis is performed to obtain loose fibers.

The loose fibers obtained after the second pyrolysis need to be dispersed to allow identification and measurement of individual filaments. The procedure requires careful physical handling of the sample over appropriate surface. For glass fibers, glass surface allows good fiber dispersion. Corona field assisted dispersion over paper was developed [7] for carbon fibers.

The final step prior to actual measurement of individual filament length is digital imaging. This can be accomplished via high-resolution scanner (Figure 5-17) or a microscope. Scanners allow greater area to be scanned at once and the sample preparation is simple. Obtaining data from a digital microscope requires a motorized x-y stage, appropriate stitching algorithm and greater data storage, however the difficulties are offset by increased spatial resolution and an array of lighting options.

Figure 5-17. Digital image of dispersed carbon fibers obtained with a scanner.

After measurement of the fiber length is complete, correction of the fiber length distribution must be performed to account for preferentially selecting long fibers. Figure

5-18 shows two long fibers, of length L_1, that are captured in the sampling region and two shorter fibers, of length L_2 with similar centroid positions, one of which will not be part of the sample.

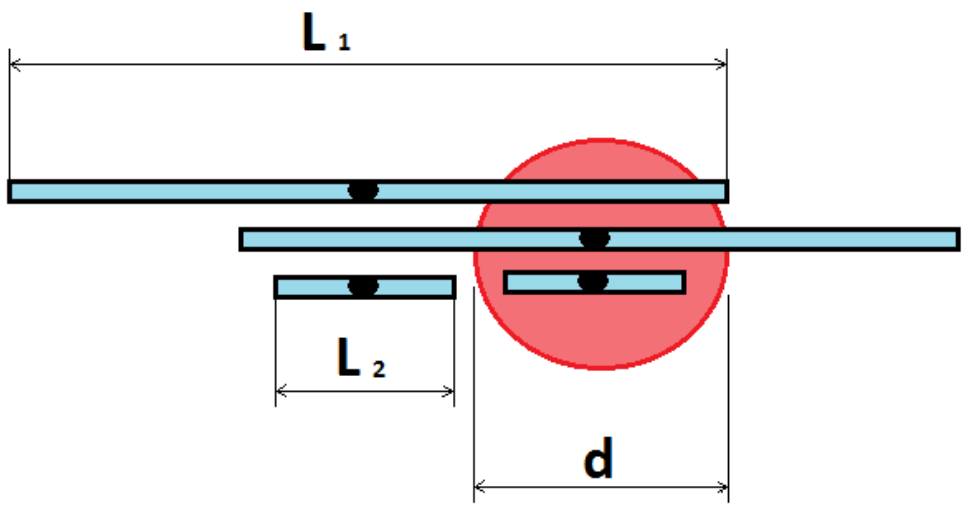

Figure 5-18. Sampling region of diameter d with three fibers captured for experimental measurement and only two centroids within the sampling region.

Assuming that the sampling region is a disk of diameter d and that all fibers lie in the same plane as the disk, then the actual number of centroids of fibers of length L_i within the sampling region $N(L_i)$ can be obtained from the raw measurement of number of fibers of length L_i that pass through the sampling region $N_r(L_i)$ using the formula given below:

$$N(L_i) = N_r(L_i)\left(1 + \frac{4L_i}{\pi d}\right)^{-1} \tag{5.3-1}$$

The results are typically interpreted as an average length or in the form a distribution. There are two common methods of calculating fiber length average. Number average fiber length L_n is calculated as

$$L_n = \frac{\sum N_i L_i}{\sum N_i} \tag{5.3-2}$$

where N_i is the number of fibers with length L_i. Weight average fiber length is calculated as

$$L_w = \frac{\sum N_i {L_i}^2}{\sum N_i L_i} \tag{5.3-3}$$

Similarly, histogram representation of FLD may be based on number or weight distribution. Since volume averaging is useful for micromechanical property analysis, weight average and weighted FLD is generally considered as more meaningful measure.

6 Articles

6.1 The Stiffness Tensor for Composites with Curved Discontinuous Fibers Part 1: A Formulation

Vlastimil Kunc[1], Srdjan Simunovic[1], Scott W. Case[2]

1. Oak Ridge National Laboratory, PO Box 2008 MS6053, Oak Ridge TN 37831-6053, USA
2. Virginia Polytechnic Institute and State University, Engineering Science and Mechanics, 225-A Norris Hall, Blacksburg, VA 24061, USA

Corresponding Author:

Vlastimil Kunc, kuncv@ornl.gov, Tel. 001 865 574 8010, Fax. 001 865 574 8257, Oak Ridge National Laboratory, PO Box 2008 MS6053, Oak Ridge, TN 37831-6053, USA

Author contact information:

Vlastimil Kunc: kuncv@ornl.gov, Srdjan Simunovic: simunovics@ornl.gov, Scott W. Case: scase@vt.edu

Abstract

In this paper we propose a method for calculating the fully anisotropic stiffness tensor for a composite material containing curved discontinuous fibers. To do so, we introduce the concept of configuration for a single curved fiber defined by five dimensionless parameters. An ensemble of the curved fibers within composite material is described by a configuration probability density function, which can be approximated by a set of even order tensors. The proposed stiffness tensor requires three tensors of fourth-order describing the microstructure of the composite material and a set of elastic constants. We introduce the concept of configuration averaging and present an analytical method for estimating elastic constants for materials containing curved fibers. Numerical results are presented to illustrate the application of the method. Additionally, we demonstrate that for materials containing only straight fibers, fiber configuration and configuration averaging reduces to standard fiber orientation and orientation averaging.

Keywords

B. Mechanical Properties C. Anisotropy, B. Modeling, Micro-mechanics

6.1.1 Introduction

Discontinuous fiber reinforced composites (DFCs) are materials in which fibers act as structural reinforcements and their aspect ratio, defined as fiber length divided by fiber diameter,

influences the resulting material properties. Examples of traditional production processes for DFCs are injection molding, compression molding, and spray-up. However, this work can be applied equally well to metal matrix composites and bio-composites. Our objective is to develop an improved description of microstructure of DFCs that accounts for curved fibers and to develop a method for obtaining the stiffness tensor. Since material stiffness is a common design driver, this work also provides a practical design tool.

In developing this work, we acknowledge that virtually any microstructure can be modeled using numerical techniques such the finite element method (FEM) [61, 62]. However, an obvious disadvantage of this approach is the need to generate a large, statistically significant number of representative volumes for quasi-random architectures and to subsequently perform analyses on all of them in order to obtain the statistics of the resulting response. Modeling of realistic DFCs using such an approach could require prohibitive computer resources and time.

An alternative modeling approach is to use statistical measures and homogenization methods for describing the fiber and matrix microstructure in the representative volumes of the composite. These measures and methods are largely driven by the nature of the subsequent analysis. The microstructure measures commonly used for composite stiffness prediction are fiber volume fraction, fiber length distribution (FLD), and fiber orientation distribution (FOD). Fiber volume fraction is a single parameter describing an average content of fiber and matrix material within the composite. FLD and FOD are functions describing an ensemble of fibers, represented as straight cylinders. Measurement techniques and results for traditional flow molded DFCs are discussed for example in [5-7] for FLD, [10, 56] for FOD and standards [63, 64] covering fiber volume fraction.

The orientation of a single straight fiber is described by an orientation vector. The probability density function (PDF) describing the orientation for an ensemble of fibers can be represented by a set of even order orientation tensors as described in [8]. Using a fourth order orientation tensor and the micromechanics-based material stiffness coefficients, Advani and Tucker [8] obtain the stiffness tensor using orientation averaging of transversely isotropic stiffness tensor.

In this work, we extend the work of Advani and Tucker for composites containing straight fibers [8] to composites containing assemblies of curved fibers with arbitrary orientation. The resulting stiffness tensor is fully anisotropic. This extension is motivated by experimental observations such as that shown in Figure 6-1.

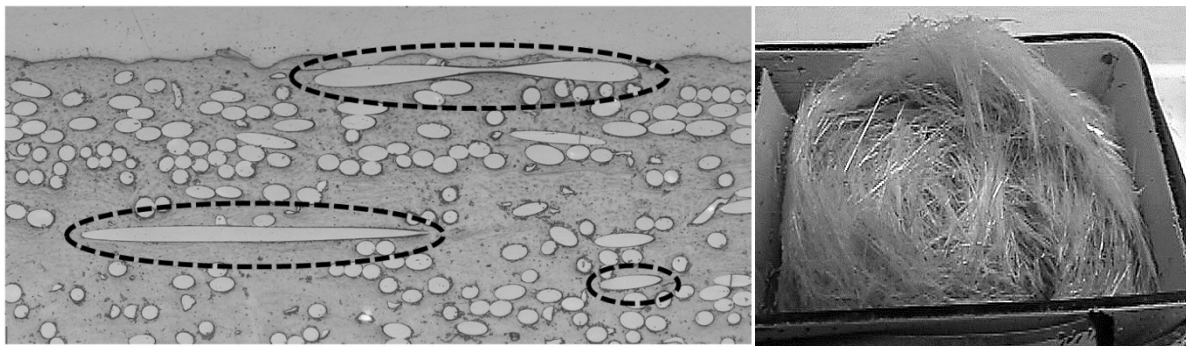

Figure 6-1. Injection molded composite containing glass fibers. Left: Polished cross-section - three cross-sections whose deviation from elliptical shape indicates fiber curvature are highlighted. Right: Entangled mass of curved fibers after matrix burn-off.

In order to rigorously account for the effect of fiber curvature on the composite properties, we introduce the concept of fiber configuration and a PDF of the configuration of ensemble of fibers. We then introduce a method of configuration averaging of the orthotropic stiffness tensor that results in a stiffness tensor containing 21 distinct components. To obtain numerical values of the material constants for the orthotropic stiffness tensor, we use the Halpin-Tsai equations [55] along with orientation averaging (although these constants could be generated by other methods). Finally, we demonstrate the developed method with numerical examples.

6.1.2 Description of Microstructure

6.1.2.1 Configuration of Single Fiber

The first step in our approach is to introduce the configuration description of a single curved fiber. We define a fiber coordinate system f = (**p**,**q**,**s**) as a Cartesian coordinate system defined by orthonormal vectors **p**,**q** and **s**. We assume straight cylindrical fiber of length L and diameter d and place it so that the center of gravity of the fiber coincides with the origin of the fiber coordinate system and fiber centerline is parallel to **p** as shown in Figure 6-2.

The fiber configuration is defined by a single dimensionless parameter $\xi = \frac{L}{d}$ and orientation vector (1,0,0) in coordinate system *f*.

Four successive geometry transformations will result in a curved fiber in general configuration with respect to a laboratory coordinate system. The operations consist of first changing the fiber from straight to curved shape and then rotating it using three Euler angles. We change the shape of the fiber so that the oriented curvature $\boldsymbol{\rho}$ is given by $= \frac{1}{R}\boldsymbol{q}$, where R is the radius of curvature. This is equivalent to describing a section of toroid in cylindrical coordinates $(r, \varphi, \bar{z})$ with cylindrical coordinate system origin at R**q**, z axis aligned with **s** and φ measured from $\bar{x}$ in mathematically positive sense as shown in Figure 6-2, right:

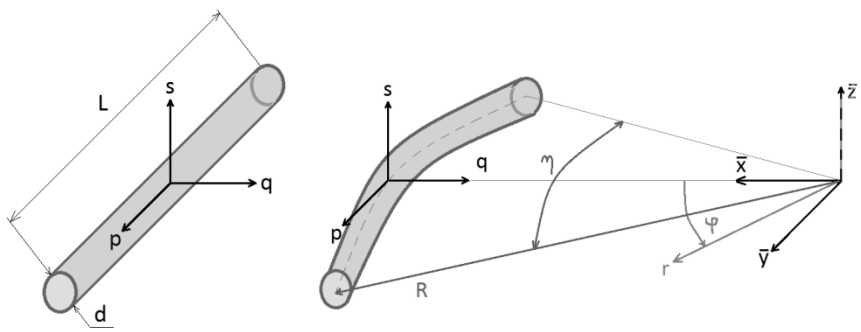

Figure 6-2. Left: Straight cylindrical fiber with coordinate system **f = (p,q,s)** Right: Bent fiber with radius R.

We assume that the fiber length and diameter remain the same, and the vector **p** remains tangent to the fiber centerline at its center. This fiber configuration is given by two dimensionless parameters, $\xi = \frac{L}{d}$ and $\eta = \frac{L}{R}$. We assume that fiber coordinates f_i are initially aligned with the laboratory coordinates x_i and perform three successive rotations through three Euler angles: rotation around **s** by α, rotation around **q** by β, and rotation around **p** by γ in mathematically positive sense. These operations are described by

$$f_l = R^x_{kl} R^y_{jk} R^z_{ij} x_i \qquad i,j,k,l = 1,2,3 \tag{6.1-1}$$

In (6.1-1) and all subsequent equations in this document, summation takes place over repeated indices unless otherwise noted. The direction cosines in (6.1-1) are given by

$$R^x_{kl} = \begin{bmatrix} 1 & 0 & 0 \\ 0 & \cos\gamma & \sin\gamma \\ 0 & -\sin\gamma & \cos\gamma \end{bmatrix}, R^y_{jk} = \begin{bmatrix} \cos\beta & 0 & \sin\beta \\ 0 & 1 & 0 \\ -\sin\beta & 0 & \cos\beta \end{bmatrix}, R^z_{ij} = \begin{bmatrix} \cos\alpha & \sin\alpha & 0 \\ -\sin\alpha & \cos\alpha & 0 \\ 0 & 0 & 1 \end{bmatrix} \tag{6.1-2}$$

We may obtain a unique description of a curved fiber in any configuration by placing the following limits on the rotations:

$$0 \le \alpha < 2\pi; \;\; -\frac{\pi}{2} \le \beta < \frac{\pi}{2}; \;\; 0 \le \gamma < 2\pi \tag{6.1-3}$$

Therefore, the configuration of a curved fiber can be described by five dimensionless parameters $\xi, \eta, \alpha, \beta, \gamma$ as illustrated in Figure 6-3. Parameters ξ, η describe the shape of the curved fiber, while three angles α, β, γ allow for arbitrary rotation of this shape with respect to laboratory coordinates.

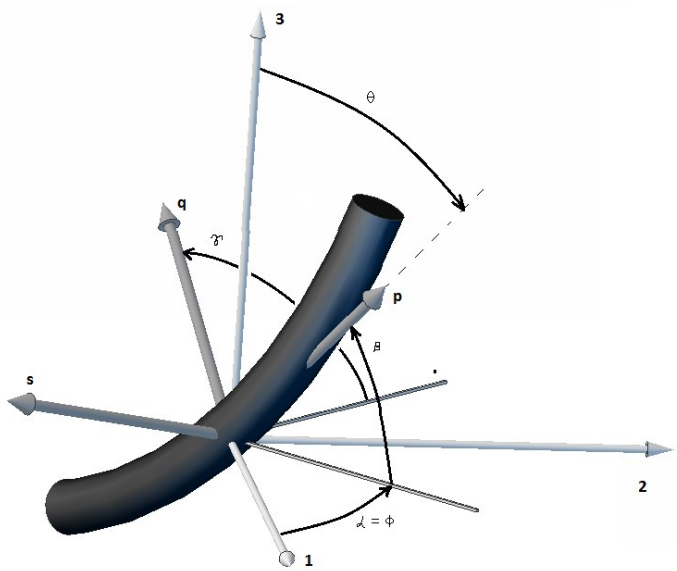

Figure 6-3. Curved fiber with coordinate system **f** = (**p**,**q**,**s**), defined by Euler angles α,β,γ.

Note that the limit case of a straight fiber ($\eta = 0$) reduces to the coordinate system of Advani-Tucker [8] (with spherical coordinate angles $\phi = \alpha$, $\theta = \frac{\pi}{2} - \beta$) where γ can be selected arbitrarily without affecting the configuration state. The components of the orientation vector p and the curvature vector q are:

$$p_1 = \cos\alpha\cos\beta = \cos\phi\sin\theta;\ p_2 = \sin\alpha\cos\beta = \sin\phi\sin\theta\,;\ p_3 = \sin\beta = \cos\theta \qquad (6.1\text{-}4)$$

$$q_1 = -\sin\alpha\cos\gamma - \cos\alpha\sin\beta\sin\gamma\,;\ q_2 = \cos\alpha\cos\gamma - \sin\alpha\sin\beta\sin\gamma\,;\ q_3 = \cos\beta\sin\gamma \qquad (6.1\text{-}5)$$

The configuration of a straight fiber is described by three parameters, namely the aspect ratio $\xi = \frac{L}{d}$ and two angles defining the orientation of fiber vector **p**. Equation (6.1-4) gives the orientation vector components with Euler angles α, β as well as with standard spherical coordinate angles ϕ, θ to allow for easy comparison with previously published work [8]. The configuration of curved fiber therefore requires one additional shape parameter and one additional angle. The shape parameter $\eta = \frac{L}{R}$ provides the magnitude of curvature, while angle γ provides the direction of the curvature vector **q**, which is by definition perpendicular to the orientation vector **p**.

6.1.2.2 Configuration Distribution Function for an Ensemble of Fibers

We now define the configuration distribution function for an ensemble of fibers $\psi_C(\alpha,\beta,\gamma,\xi,\eta)$. as a probability density function of finding a fiber with configuration given by angles and parameters $\alpha,\beta,\gamma,\xi,\eta$ in the intervals :

$$\begin{aligned} P(\alpha_1 \le \alpha \le \alpha_1 + d\alpha_1, \beta_1 \le \beta \le \beta_1 + d\beta_1, \gamma_1 \le \gamma \le \gamma_1 + d\gamma_1, \xi_1 \le \xi \\ \le +\xi_1 + d\xi_1, \eta_1 \le \eta \le +\eta_1 + d\eta_1) \\ = \psi(\alpha_1,\beta_1,\gamma_1,\xi_1,\eta_1)\cos\beta_1 \; d\alpha d\beta d\gamma d\xi d\eta \end{aligned} \tag{6.1-6}$$

The configuration distribution function ψ is normalized as:

$$\int_{\eta=0}^{\infty}\int_{\xi=0}^{\infty}\int_{\gamma=0}^{2\pi}\int_{\beta=-\pi/2}^{\pi/2}\int_{\alpha=0}^{2\pi} \psi_C(\alpha,\beta,\gamma,\xi,\eta)\cos\beta \;\; d\alpha d\beta d\gamma d\xi d\eta \; = 1 \tag{6.1-7}$$

Assuming the independence of fiber shape and rotation, ψ may be separated into two parts

$$\psi_C(\alpha,\beta,\gamma,\xi,\eta) = \psi_R(\alpha,\beta,\gamma)\psi_S(\xi,\eta) \tag{6.1-8}$$

where the rotation of fiber coordinate system with respect to laboratory system given by three angles α,β,γ and the shape of a fiber given by parameters ξ,η , are independent for an arbitrary configuration. We place the following normalization conditions on the rotation distribution function ψ_R and the shape distribution function ψ_S

$$\int_{\gamma=0}^{2\pi}\int_{\theta=0}^{\pi}\int_{\varphi=0}^{2\pi} \psi_R(\alpha,\beta,\gamma)\cos\beta \;\; d\alpha d\beta d\gamma = 1; \quad \int_{\eta=0}^{\infty}\int_{\xi=0}^{\infty} \psi_S(\xi,\eta) d\xi d\eta = 1 \tag{6.1-9}$$

Upon integration of ψ_R over all possible angles γ, the fiber orientation distribution function is:

$$\psi(\alpha,\beta) = \int_{\gamma=0}^{2\pi} \psi_R(\alpha,\beta,\gamma) d\gamma \tag{6.1-10}$$

The properties of ψ were explored in detail by Advani and Tucker [8].

6.1.2.3 Stiffness Tensor

In this section, we use the concept of fiber configuration to establish components of the anisotropic stiffness tensor C_{ijkl} for an ensemble of fibers in an arbitrary configuration. The generalized Hooke's law is given by

$$\sigma_{ij} = C_{ijkl}\varepsilon_{kl} \qquad i,j,k,l = 1,2,3 \tag{6.1-11}$$

where σ_{ij} and ε_{kl} are the components of symmetric fourth rank stress and strain tensors respectively. Assuming the existence of a strain energy density function and the symmetric stress and strain tensors, we note the following (standard) symmetry of the stiffness tensor

$$C_{ijkl} = C_{jikl} = C_{klij} \qquad i,j,k,l = 1,2,3 \tag{6.1-12}$$

which reduces the number of distinct components in C_{ijkl} from 81 to 21. In the following sections, our focus is on deriving these 21 components of C_{ijkl} for any material with its microstructure described by Equation (6.1-8).

Orthotropic stiffness tensor for material with fibers in single configuration

We now consider a material consisting of an ensemble of uniformly dispersed fibers of a single configuration within a matrix with no interactions between the fibers as illustrated in Figure 6-4.

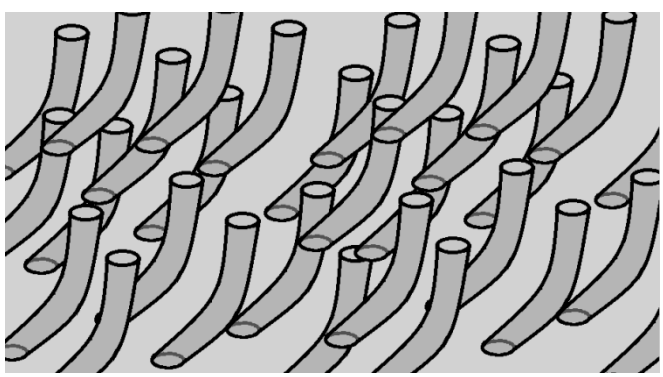

Figure 6-4. Material with fibers in single configuration.

For the material illustrated in Figure 6-4, the single fiber and surrounding matrix shown in Figure 6-3 would constitute a representative volume. We can inspect Figure 6-3 and conclude that there exists geometrical symmetry with respect to a plane with normal **p** and to a plane with normal **s**. Since our idealized material consists of fibers in single configuration, the resulting material will

also have two material planes of symmetry. We can write two transformations under which a stiffness tensor remains invariant

$$R_{ij}(\boldsymbol{p}) = \delta_{ij} - p_i p_j \; and \; R_{ij}(\boldsymbol{s}) = \delta_{ij} - s_i s_j \qquad i,j = 1,2,3 \tag{6.1-13}$$

Vectors **p** and **s** are normal, which was shown to imply a third material plane of symmetry [48] and result in orthotropic material stiffness tensor $\tilde{C}_{ijkl}$ with nine material constants

$$\begin{gathered}\tilde{C}_{ijkl} = \mu\left(\delta_{ik}\delta_{jl} + \delta_{il}\delta_{jk}\right) + \lambda\delta_{ij}\delta_{kl} + \kappa_{p2}\left(p_i p_j \delta_{kl} + \delta_{ij} p_k p_l\right) + \kappa_{q2}\left(q_i q_j \delta_{kl} + \right. \\ \left. \delta_{ij} q_k q_l\right) + 2\mu_1\left(\delta_{ik} p_j p_l + \delta_{il} p_j p_k + \delta_{jl} p_i p_k + \delta_{jk} p_i p_l\right) + 2\mu_2\left(\delta_{ik} q_j q_l + \delta_{il} q_j q_k + \right. \\ \left. \delta_{jl} q_i q_k + \delta_{jk} q_i q_l\right) + \kappa_{p4} p_i p_j p_k p_l + \kappa_{q4} q_i q_j q_k q_l + \kappa_{s4}\left(p_i p_j q_k q_l + q_i q_j p_k p_l\right) \\ i,j,k,l = 1,2,3\end{gathered} \tag{6.1-14}$$

This form of orthotropic stiffness tensor can be found for example in [54] and [65]. Spencer [65] also suggested that the vectors **p** and **q** may vary point to point for a material containing curved fibers. We extend this idea by introducing the concept of configuration averaging in a representative volume.

6.1.2.4 Configuration averaging for material with arbitrary fiber configuration

We now perform configuration averaging to obtain the stiffness tensor for material containing fibers described by a configuration distribution function ψ. This procedure is analogous to orientation averaging. We define the configuration average of the stiffness tensor as

$$\langle C_{ijkl} \rangle_C = \int_{\eta=0}^{\infty} \int_{\xi=0}^{\infty} \int_{\gamma=0}^{2\pi} \int_{\beta=-\pi/2}^{\pi/2} \int_{\alpha=0}^{2\pi} \tilde{C}_{ijkl} \psi_C(\alpha, \beta, \gamma, \xi, \eta) \cos\beta \; d\alpha d\beta d\gamma d\xi d\eta \qquad i,j,k,l = 1,2,3 \tag{6.1-15}$$

where we use $\langle \, \rangle_C$ brackets to indicate configuration averaging. Substituting Equation (6.1-14) into (6.1-15) results in the most general form of stiffness tensor for material containing curved fibers. We now use standard separation of variables in Equation (6.1-8) to describe independence of fiber shape and its rotation with respect to the laboratory system. This allows us to simplify configuration averaging (6.1-15) by separating rotation averaging and shape averaging as discussed below.

The material constants in Equation (6.1-14) are independent of orientation of fiber coordinate system with respect to laboratory system, however, they depend on parameters ξ and η for a particular configuration. Therefore for any of the material constants k of Equation (6.1-14) $k = k(\xi, \eta)$.

Since the orientation vector **p** for any configuration is obtained by two rotations through angles α, β and the curvature vector **q** is then obtained by additional rotation around orientation vector **p** through angle γ, we can write

$$\boldsymbol{p} = \boldsymbol{p}(\alpha, \beta\ ); \ \boldsymbol{q} = \boldsymbol{q}(\alpha, \beta\ , \gamma) \tag{6.1-16}$$

Performing the requisite integration, Equation (6.1-15) becomes

$$\begin{aligned} \langle C_{ijkl} \rangle_C = \bar{\mu}\left(\delta_{ik}\delta_{jl} + \delta_{il}\delta_{jk}\right) + \bar{\lambda}\delta_{ij}\delta_{kl} + \overline{\kappa_{p2}}\left(a_{ij}\delta_{kl} + \delta_{ij}a_{kl}\right) + \overline{\kappa_{q2}}\left(b_{ij}\delta_{kl} + \right. \\ \left. \delta_{ij}b_{kl}\right) + 2\overline{\mu_1}\left(\delta_{ik}a_{jl} + \delta_{il}a_{jk} + \delta_{jl}a_{ik} + \delta_{jk}a_{il}\ \right) + 2\overline{\mu_2}\left(\delta_{ik}b_{jl} + \delta_{il}b_{jk} + \delta_{jl}b_{ik} + \right. \\ \left. \delta_{jk}b_{il}\right) + \overline{\kappa_{p4}}a_{ijkl} + \overline{\kappa_{q4}}b_{ijkl} + \overline{\kappa_{s4}}(c_{ijkl} + c_{klij}) \quad i, j, k, l = 1, 2, 3 \end{aligned} \tag{6.1-17}$$

where

$$\bar{k} = \langle k \rangle_S = \int_{\xi=0}^{\infty} \int_{\eta=0}^{\infty} k(\xi, \eta)\psi_S(\xi, \eta)\ \ d\xi d\eta \tag{6.1-18}$$

with k representing any of the material constants in (6.1-18) and $\langle\ \rangle_S$ brackets denoting shape averaging. We use $\langle\ \rangle_R$ brackets for rotation averaging and standard definition of single brackets $\langle\ \rangle$ indicating orientation averaging to define a_{ij} and b_{ij} as second order orientation and curvature tensors respectively:

$$a_{ij} = \langle p_i p_j \rangle = \int_{\beta=-\pi/2}^{\pi/2} \int_{\alpha=0}^{2\pi} p_i p_j \psi(\alpha, \beta) \cos\beta\ \ d\alpha d\beta \quad i, j = 1, 2, 3 \tag{6.1-19}$$

$$b_{ij} = \langle q_i q_j \rangle_R = \int_{\gamma=0}^{2\pi} \int_{\beta=-\pi/2}^{\pi/2} \int_{\alpha=0}^{2\pi} q_i q_j \psi_R(\alpha, \beta, \gamma) \cos\beta\ \ d\alpha d\beta d\gamma \quad i, j = 1, 2, 3 \tag{6.1-20}$$

Similarly, we define a_{ijkl}, b_{ijkl} and c_{ijkl} as fourth order orientation, curvature and mixed tensors:

$$a_{ijkl} = \langle p_i p_j p_k p_l \rangle, \qquad b_{ijkl} = \langle q_i q_j q_k q_l \rangle_R,$$
$$c_{ijkl} = \langle p_i p_j q_k q_l \rangle_R \quad i,j,k,l = 1,2,3 \tag{6.1-21}$$

We have therefore defined all the terms in Equation (6.1-17) that allows us to obtain the form of a stiffness tensor for material containing curved fibers in arbitrary configuration. The remaining task is to find nine constants for material containing curved fibers in single configuration. Before doing this, however, we explore the properties of geometric configuration tensors and the resulting material anisotropy.

6.1.2.5 Properties of Geometric Configuration Tensors

In this section we investigate properties of second and fourth order orientation tensors a_{ij} and a_{ijkl}, second and fourth order curvature tensors b_{ij} and b_{ijkl}, and mixed tensor c_{ijkl}. In the absence of fiber curvature, definitions of a_{ij} and a_{ijkl} given in Equations (6.1-19) and (6.1-20) reduce to definitions identical to those provided by Advani and Tucker [8], and correspondingly all of the equations above reduce to previously developed theories. The orientation tensors are fully symmetric:

$$a_{ij} = a_{ji} \quad and \quad a_{ijkl} = a_{jikl} = a_{kijl} = a_{lijk} = a_{klij}, \qquad etc. \tag{6.1-22}$$

with information about second order tensor being contained within fourth order tensor and the trace of the second order tensor reducing to unity, i.e.:

$$a_{ijkk} = a_{ij}, \qquad a_{ii} = 1 \tag{6.1-23}$$

We can write identical expressions for fully symmetric curvature tensors b_{ij} and b_{ijkl}. Full symmetry for fourth-order tensors implies 15 distinct components.

The mixed tensor is not completely symmetric. However, it is symmetric with respect to the first pair and last pair of indexes.

$$c_{ijkl} = c_{ijlk} = c_{jilk} \tag{6.1-24}$$

Thus, there are 36 unique components in c_{ijkl}. Equation (6.1-14) imposes additional symmetry:

$$s_{ijkl} = \left(c_{ijkl} + c_{klij}\right) = \langle p_i p_j q_k q_l + p_k p_l q_i q_j \rangle_R \quad i,j,k,l = 1,2,3 \tag{6.1-25}$$

The tensor s_{ijkl} has the same symmetry as the elastic tensor and has 21 distinct components. We can therefore conclude that the stiffness tensor produced using configuration averaging contains the base tensor with 21 distinct components, while the stiffness tensor constructed via standard orientation averaging would contain a base tensor with only 15 distinct components corresponding to full symmetry of a_{ijkl}.

6.1.3 Obtaining Material Parameters for Material in Single Configuration

We now describe the procedure for obtaining the material parameters in Equation (6.1-17). If a material contains fibers in a limited range of configurations, these constants could be obtained experimentally. However, such an empirical approach would be impractical for realistic DFCs. Alternatively, one could perform a large number of numerical simulations to obtain the constants.

We propose an approach based on orientation averaging and semi-empirical Halpin-Kardos [55] equations. Regarding a curved fiber in an arbitrary configuration as an assembly of segments of straight fibers, we can assign an orientation tensor to any given segment. We will first define a planar orientation tensor for a bent fiber with shape given by ξ, η in fiber coordinate system **f** = (**p**,**q**,**s**), and subsequently rotate the result to obtain the solution for arbitrary configuration. From Figure 6-5, we note that $\phi = \varphi$ and $\theta = \frac{\pi}{2}$ for a segment of bent fiber with orientation given by vector $\tilde{\boldsymbol{p}}$.

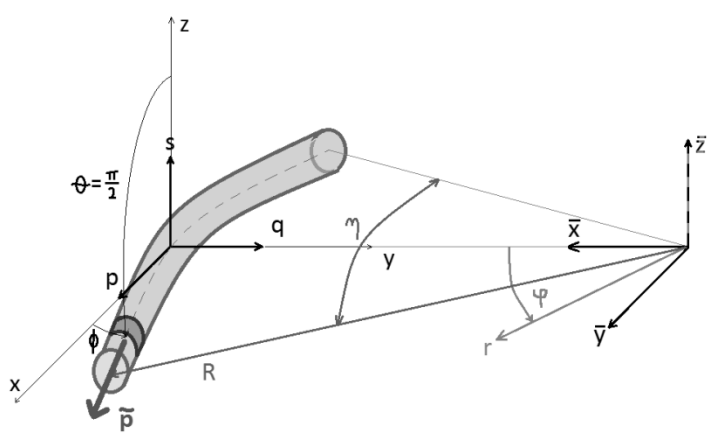

Figure 6-5. Orientation vector $\tilde{\boldsymbol{p}}$ for a segment of bent fiber.

The probability of finding a segment with given orientation is given by

$$\tilde{\psi}(\phi) = \begin{cases} \dfrac{1}{\pi\eta} & for\ \phi \in < -\dfrac{\eta}{2}, \dfrac{\eta}{2} > \\ 0 & elswhere \end{cases} \tag{6.1-26}$$

Components of orientation tensors $\tilde{a}_{ij}$ and $\tilde{a}_{ijkl}$ representing the segments of bent fiber can be calculated from definition given in Equations (6.1-19) and (6.1-20).

$$\begin{aligned} \tilde{a}_{1111} = \frac{3\eta + (4 + \cos\eta)\sin\eta}{8\eta}, \tilde{a}_{2222} = \frac{3\eta + (-4 + \cos\eta)\sin\eta}{8\eta}, \tilde{a}_{1122} = \tilde{a}_{2211} \\ = \tilde{a}_{1212} = \tilde{a}_{2112} = \tilde{a}_{2121} = \tilde{a}_{1221} = \frac{\eta - \sin\eta\cos\eta}{8\eta} \end{aligned} \tag{6.1-27}$$

with all other components reducing to zero. We now use planar orientation averaging over the transversely isotropic stiffness tensor

$$\begin{aligned} \langle \check{C}_{ijkl} \rangle = \ & \mu_s(\delta_{ik}\delta_{jl} + \delta_{il}\delta_{jk}) + \lambda_s(\delta_{ij}\delta_{kl}) + \varsigma_2(\tilde{a}_{ij}\delta_{kl} + \tilde{a}_{kl}\delta_{ij}) \\ & + (\mu_0 - \mu_s)(\tilde{a}_{ik}\delta_{jl} + \tilde{a}_{il}\delta_{jk} + \tilde{a}_{jl}\delta_{ik} + \tilde{a}_{jk}\delta_{il}) + \varsigma_4\tilde{a}_{ijkl} \\ & i, j, k, l = 1, 2, 3 \end{aligned} \tag{6.1-28}$$

where μ_s, λ_s, μ_0, ς_2, ς_4 are material constants for straight fibers obtained from the Halpin-Kardos [55] equations and the following relations:

$$\mu = G_{23}, \qquad \mu_0 = G_{12}, \qquad \lambda = \frac{-E_1E_2G_{23}}{E_1E_2 - 4E_1G_{23} + 4E_2G_{23}{\nu_{12}}^2} - G_{23},$$

$$\varsigma_2 = G_{23} + \frac{E_1E_2G_{23}(1-2\nu_{12})}{E_1E_2 - 4E_1G_{23} + 4E_2G_{23}{\nu_{12}}^2},$$

$$\varsigma_4 = G_{23} - 4G_{12} + \frac{{E_1}^2(E_2 - 4G_{23}) + E_1E_2G_{23}(4\nu_{12} - 1)}{E_1E_2 - 4E_1G_{23} + 4E_2G_{23}{\nu_{12}}^2} \tag{6.1-29}$$

The orientation averaging in Equation (6.1-28) results in an orthotropic stiffness tensor. Consequently, we can obtain nine material constants in Equation (6.1-14) for a material containing curved fibers:

$$\mu = \mu_s - \varsigma_4\tilde{a}_{1122};\ \ \lambda = \lambda_s + 2\,\varsigma_4\,\tilde{a}_{1122};\ \ \kappa_{p2} = \varsigma_2\tilde{a}_{11} - 2\,\tilde{a}_{1122}\,\varsigma_4;\ \ \kappa_{q2} = \varsigma_2\tilde{a}_{22} - 2\,\tilde{a}_{1122}\,\varsigma_4;\ \mu_1 = \frac{1}{2}((\mu_0 - \mu_s)\tilde{a}_{11} + 2\tilde{a}_{1122}\varsigma_4);\ \mu_2 = \frac{1}{2}((\mu_0 - \mu_s)\tilde{a}_{22} + 2\tilde{a}_{1122}\,\varsigma_4);\ \ \kappa_{p4} = \tilde{a}_{1111}\varsigma_4;\ \ \kappa_{q4} = \tilde{a}_{2222}\varsigma_4;\ \ \kappa_{s4} = 3\tilde{a}_{1122}\varsigma_4 \tag{6.1-30}$$

For straight fiber with $\eta \to 0$, the limiting process reduces an orthotropic material with nine material constants to a transversely isotropic material with five material constants as expected: $\mu = \mu_s, \lambda = \lambda_s, \kappa_{p2} = \varsigma_2, \kappa_{p4} = \varsigma_4, \mu_1 = \frac{1}{2}(\mu_0 - \mu_s), \mu_2 = \kappa_{q2} = \kappa_{q4} = \kappa_{s4} = 0$.

Examples

To illustrate the proposed approach on examples, we will follow our derivation in reverse. In

Table 6.1-1, we use numerical values for fiber and matrix properties given in an appendix of Reference [8].

Table 6.1-1. Fiber and matrix properties from reference [8].

E_f $[Pa]$($[psi]$)	ν_f	E_m $[Pa]$($[psi]$)	ν_m	V_f	ξ
7.24 10^{10} *(10.5 10^6)*	0.2	3.45 10^9*(0.5 10^6)*	0.35	0.2	100

To generate material constants for a material with fibers in single configuration, we use Halpin-Kardos [55] equations and Equations (6.1-29) and (6.1-30). Figure 6-6 shows material constants in Equation (6.1-17) as a function of curvature η for a material in with fibers single configuration.

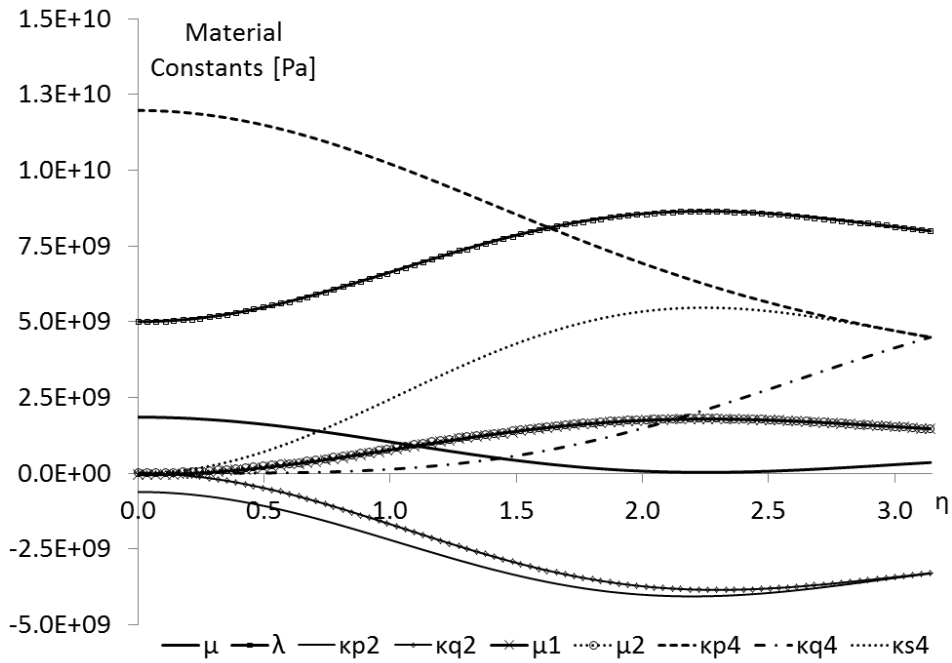

Figure 6-6. Material constants as a function of curvature η for a material in with fibers single configuration having aspect ratio $\xi = 100$ and constituent properties listed in Table 6.1-1.

Note that straight fibers and fibers forming half of a circle have five distinct material constants corresponding to a transversely isotropic material. Constants that will be used later are given in Table 6.1-2.

Table 6.1-2. Orthotropic material constants for a material with curved fibers in single configuration given by shape parameters $\xi = 100$ for straight fiber $\eta = 0$ and curved fiber with $\eta = \frac{\pi}{4}$.

η	$\mu\ [Pa]$	$\lambda\ [Pa]$	$\kappa_{p2}\ [Pa]$	$\kappa_{q2}\ [Pa]$	$\mu_1\ [Pa]$	$\mu_2 [Pa]$	$\kappa_{p4} [Pa]$	$\kappa_{q4} [Pa]$	$\kappa_{s4} [Pa]$
0	$1.85\ 10^9$	$5.00\ 10^9$	$-6.17\ 10^8$	0	$-5.28\ 10^7$	0	$1.20\ 10^{10}$	0	0
$\frac{\pi}{4}$	$1.31\ 10^9$	$6.09\ 10^9$	$-1.67\ 10^8$	$-1.12\ 10^9$	$2.22\ 10^8$	$2.69\ 10^8$	$1.08\ 10^{10}$	$5.29\ 10^7$	$1.63\ 10^9$

To provide a tool for better understanding of the influence of fiber curvature on material properties, we can use transformations listed in [54] to generate nine engineering constants in fiber coordinate system as shown in Figure 6-7.

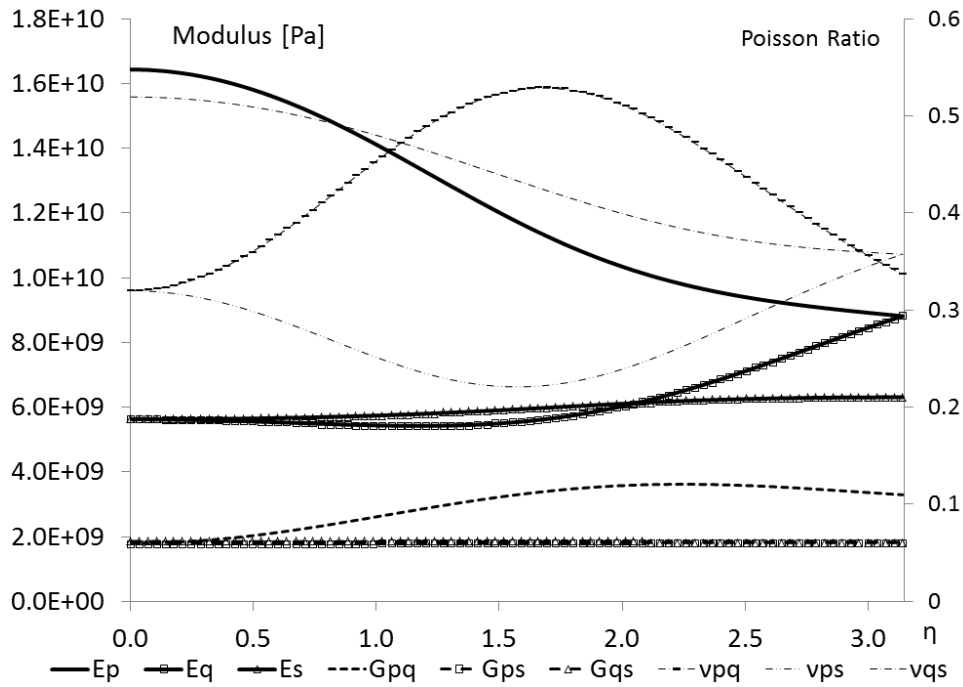

Figure 6-7. Engineering constants as a function of curvature η for a material in with fibers single configuration having aspect ratio $\xi = 100$ and constituent properties listed in Table 6.1-1.

All of the results above are obtained through orientation averaging of transversely isotropic stiffness tensor and represent material with fibers in single configuration. To demonstrate the concept of configuration averaging, we calculate geometric tensors for material with fibers in a finite set of configuration from the following definition:

$$a_{ijkl} = \sum_{K=1}^{N} \Upsilon_K \frac{p_i p_j p_k p_l}{Z}, b_{ijkl} = \sum_{K=1}^{N} \Upsilon_K \frac{q_i q_j\, q_k\, q_l}{Z},$$
$$s_{ijkl} = \sum_{K=1}^{N} \Upsilon_K \frac{p_i p_j\, q_k q_l + q_i q_j\, p_k p_l}{Z} \quad i,j,k,l = 1,2,3 \tag{6.1-31}$$

, where $Z = \sum_{L=1}^{N} \Upsilon_L \cos B_L$ and vectors $\boldsymbol{p} = \boldsymbol{p}(A_K, B_K), \boldsymbol{q} = \boldsymbol{q}(A_K, B_K, \Gamma_K)$ are calculated directly from Equation 6.1-4 and Equation 6.1-5 Υ_K indicates the fraction of fibers in given configuration. Second order-tensors can be obtained through contraction.

We consider a hypothetical material consisting of an ensemble of three fibers (N=3) with the geometric configuration parameters listed in Table 6.1-3.

Table 6.1-3. Geometric configuration parameters for three fibers.

	A_K	B_K	Γ_K	Υ_K
Fiber 1 (K=1)	0	0	0	$1/3$
Fiber 2 (K=2)	$\pi/32$	$\pi/32$	$\pi/32$	$1/3$
Fiber 3 (K=3)	$\pi/3$	$\pi/3$	$\pi/3$	$1/3$

Using standard representation of symmetric fourth order tensor with symmetry given in Equation (6.1-12) as 6x6 matrix, the configuration given in Table 6.1-3 results in the following geometric tensors:

$$a_{(4)} = \begin{bmatrix} 6.58\ 10^{-1} & 1.09\ 10^{-2} & 3.44\ 10^{-2} & 1.88\ 10^{-2} & 4.09\ 10^{-2} & 3.63\ 10^{-2} \\ 1.09\ 10^{-2} & 2.35\ 10^{-2} & 9.38\ 10^{-2} & 4.69\ 10^{-2} & 2.74\ 10^{-2} & 1.38\ 10^{-2} \\ 3.44\ 10^{-2} & 9.38\ 10^{-2} & 3.75\ 10^{-1} & 1.88\ 10^{-1} & 1.09\ 10^{-1} & 5.44\ 10^{-2} \\ 1.88\ 10^{-2} & 4.69\ 10^{-2} & 1.88\ 10^{-1} & 9.38\ 10^{-2} & 5.44\ 10^{-2} & 2.74\ 10^{-2} \\ 4.09\ 10^{-2} & 2.74\ 10^{-2} & 1.09\ 10^{-1} & 5.44\ 10^{-2} & 3.44\ 10^{-2} & 1.88\ 10^{-2} \\ 3.63\ 10^{-2} & 1.38\ 10^{-2} & 5.44\ 10^{-2} & 2.74\ 10^{-2} & 1.88\ 10^{-2} & 1.09\ 10^{-2} \end{bmatrix} \tag{6.1-32}$$

$$b_{(4)} = \begin{bmatrix} 2.84\ 10^{-1} & 7.32\ 10^{-2} & 8.16\ 10^{-2} & -7.49\ 10^{-2} & -1.52\ 10^{-1} & 1.40\ 10^{-1} \\ 7.32\ 10^{-2} & 6.71\ 10^{-1} & 2.31\ 10^{-2} & 1.32\ 10^{-2} & -4.07\ 10^{-2} & -4.00\ 10^{-4} \\ 8.16\ 10^{-2} & 2.31\ 10^{-2} & 2.35\ 10^{-2} & -2.13\ 10^{-2} & -4.38\ 10^{-2} & 4.00\ 10^{-2} \\ -7.49\ 10^{-2} & 1.32\ 10^{-2} & -2.13\ 10^{-2} & 2.31\ 10^{-2} & 4.00\ 10^{-2} & -4.07\ 10^{-2} \\ -1.52\ 10^{-1} & -4.07\ 10^{-2} & -4.38\ 10^{-2} & 4.00\ 10^{-2} & 8.16\ 10^{-2} & -7.49\ 10^{-2} \\ 1.40\ 10^{-1} & -4.00\ 10^{-4} & 4.00\ 10^{-2} & -4.07\ 10^{-2} & -7.49\ 10^{-2} & 7.32\ 10^{-2} \end{bmatrix} \tag{6.1-33}$$

$$s_{(4)} = \begin{bmatrix} 6.19\ 10^{-2} & 7.43\ 10^{-1} & 3.37\ 10^{-1} & 1.88\ 10^{-1} & 7.66\ 10^{-2} & 2.61\ 10^{-2} \\ 7.43\ 10^{-1} & 4.61\ 10^{-2} & 1.06\ 10^{-1} & 2.17\ 10^{-2} & 1.11\ 10^{-2} & 8.32\ 10^{-2} \\ 3.37\ 10^{-1} & 1.06\ 10^{-1} & 1.88\ 10^{-1} & -3.93\ 10^{-2} & -1.48\ 10^{-1} & 1.75\ 10^{-1} \\ 1.88\ 10^{-1} & 2.17\ 10^{-2} & -3.93\ 10^{-2} & -8.59\ 10^{-2} & -1.09\ 10^{-1} & 7.10\ 10^{-2} \\ 7.66\ 10^{-2} & 1.11\ 10^{-2} & -1.48\ 10^{-1} & -1.09\ 10^{-1} & -1.02\ 10^{-1} & 1.76\ 10^{-2} \\ 2.61\ 10^{-2} & 8.32\ 10^{-2} & 1.75\ 10^{-1} & 7.10\ 10^{-2} & 1.76\ 10^{-2} & 3.97\ 10^{-2} \end{bmatrix} \tag{6.1-34}$$

The reader may readily verify that Equations (6.1-23) hold and note that the mixed tensor contains 21 distinct constants. We consider two cases of fiber shapes. In our first hypothetical material, all three of our fibers are straight ($\eta = 0$) with aspect ratio $\xi = 100$, while in the second material, the fibers are curved with $\eta = \frac{\pi}{4}$. Shape averaging of identically shaped fibers will result in constants listed in nine material constants listed in Table 6.1-2. We can now use these constants with geometric tensors listed in Equations (6.1-32) through (6.1-33) in Equation (6.1-34) to assemble stiffness tensors. For the material with straight fibers:

$$C = \begin{bmatrix} 1.5410^{10} & 4.6210^{9} & 4.6710^{9} & 6.8610^{7} & 3.4410^{8} & 3.4810^{8} \\ 4.6210^{9} & 8.7810^{9} & 5.7410^{9} & 3.5210^{8} & 2.1910^{8} & 7.9210^{7} \\ 4.6710^{9} & 5.7410^{9} & 1.2410^{10} & 2.0410^{9} & 1.1510^{9} & 5.8810^{8} \\ 6.8610^{7} & 3.5210^{8} & 2.0410^{9} & 2.9110^{9} & 6.4110^{8} & 3.0910^{8} \\ 3.4410^{8} & 2.1910^{8} & 1.1510^{9} & 6.4110^{8} & 2.1410^{9} & 1.9810^{8} \\ 3.4810^{8} & 7.9210^{7} & 5.8810^{8} & 3.0910^{8} & 1.9810^{8} & 1.8910^{9} \end{bmatrix} \tag{6.1-35}$$

and for the material with curved fibers:

$$C = \begin{bmatrix} 1.4810^{10} & 4.6910^{9} & 4.3710^{9} & 1.7510^{8} & 4.3110^{8} & 3.5310^{8} \\ 4.6910^{9} & 8.8110^{9} & 5.2210^{9} & 3.4910^{8} & 2.8110^{8} & 1.9610^{8} \\ 4.3710^{9} & 5.2210^{9} & 1.2310^{10} & 1.7710^{9} & 8.0410^{8} & 5.0110^{8} \\ 1.7510^{8} & 3.4910^{8} & 1.7710^{9} & 2.9510^{9} & 5.5710^{8} & 3.6110^{8} \\ 4.3110^{8} & 2.8110^{8} & 8.0410^{8} & 5.5710^{8} & 2.3610^{9} & 2.9610^{8} \\ 3.5310^{8} & 1.9610^{8} & 5.0110^{8} & 3.6110^{8} & 2.9610^{8} & 2.5110^{9} \end{bmatrix} \tag{6.1-36}$$

It is apparent that for the material containing straight fibers, configuration averaging recovers the results of orientation averaging and results in stiffness tensor with 15 distinct constants. Configuration averaging of curved fibers gives a stiffness tensor with 21 distinct constants corresponding to full anisotropy.

6.1.4 Conclusions

We propose a new practical method for obtaining the stiffness tensor for discontinuous fiber composite materials containing curved fibers. The new concept of curved fiber configuration is introduced. This configuration is described by five dimensionless parameters. Two parameters describe the fiber shape and three parameters describe the rotation of this shape with respect to the laboratory coordinate system. An ensemble of fibers is described by configuration distribution function. For a system of non-interacting fibers, separation of variables is used to define the configuration distribution function as a product of shape distribution and rotation configuration functions. Furthermore, we propose a new method of configuration averaging for constructing a stiffness tensor for a material containing an ensemble of curved fibers. This configuration averaging leads us to the definition of orientation, curvature and mixed fourth order tensors. The fully anisotropic stiffness tensor for an ensemble of curved fibers can then be assembled using these three tensors and nine averaged elastic constants. We provide a method for predicting these material constants and show that our method of configuration averaging reduces to orientation averaging if all fibers within the material remain straight. The method is illustrated by numerical examples.

6.1.5 Acknowledgements

The authors would like to express gratitude to the American Chemistry Council, Plastics Division for supporting research and innovation in this area.

References

1. Lei, H. F., Z. Q. Zhang, and B. Liu, *Effect of fiber arrangement on mechanical properties of short fiber reinforced composites.* Composites Science and Technology, 2012. **72**(4): p. 506-514.

2. Tu, S. T., et al., *Numerical simulation of saturation behavior of physical properties in composites with randomly distributed second-phase.* Journal of Composite Materials, 2005. **39**(7): p. 617-631.

3. Thomason, J. L. and M. A. Vlug, *Influence of fibre length and concentration on the properties of glass fibre-reinforced polypropylene .1. Tensile and flexural modulus.* Composites Part a-Applied Science and Manufacturing, 1996. **27**(6): p. 477-484.

4. Thomason, J. L. and M. A. Vlug, *Influence of fibre length and concentration on the properties of glass fibre-reinforced polypropylene .4. Impact properties.* Composites Part a-Applied Science and Manufacturing, 1997. **28**(3): p. 277-288.

5. Kunc, V., Frame, B. J., Nguyen, B. N., Tucker III, C. L. and Velez-Garcia, G, *Fiber Length Distribution Measurement for Long Glass and Carbon Fiber Reinforced Injection*

Molded Thermoplastics, in *Composites Conference & Exposition, Society of Plastic Engineers*. 2007: Troy, Michigan.

6. Clarke, A. R., N. Davidson, and G. Archenhold, *A Multitransputer Image Analyzer for 3d-Fiber Orientation Studies in Composites.* Transactions of the Royal Microscopical Society : New Series, Vol 1, 1990. **1**: p. 305-308.

7. Bay, R. S. and C. L. Tucker, *Stereological Measurement and Error-Estimates for 3-Dimensional Fiber Orientation.* Polymer Engineering and Science, 1992. **32**(4): p. 240-253.

8. ASTM, *D2584 – 11 Standard Test Method for Ignition Loss of Cured Reinforced Resins*. 2011: West Conshohocken, PA.

9. ASTM, *D3171 – 11 Standard Test Methods for Constituent Content of Composite Materials*. 2011: West Conshohocken, PA.

10. Advani, S. G. and C. L. Tucker, *The Use of Tensors to Describe and Predict Fiber Orientation in Short Fiber Composites.* Journal of Rheology, 1987. **31**(8): p. 751-784.

11. Halpin, J. C. and J. L. Kardos, *Strength of Discontinuous Reinforced Composites .1. Fiber Reinforced Composites.* Polymer Engineering and Science, 1978. **18**(6): p. 496-504.

12. Chadwick, P., M. Vianello, and S. C. Cowin, *A new proof that the number of linear elastic symmetries is eight.* Journal of the Mechanics and Physics of Solids, 2001. **49**(11): p. 2471-2492.

13. Lubarda, V. A. and M. C. Chen, *On the elastic moduli and compliances of transversely isotropic and orthotropic materials.* Journal of Mechanics of Materials and Structures, 2008. **3**(1): p. 153-171.

14. Spencer, A. J. M., *The formulation of constitutive equation for anisotropic solids*, in *Mechanical behavior of anisotropic solids*, J. P. Boehler, Editor. 1982, Martinus Nijhoff Publishers: The Hague. p. 2-26.

6.2 The Stiffness Tensor for Composite with Curved Discontinuous Fibers Part 2: Effect of Curvature, Representative Volume and Comparison with Experiment

Vlastimil Kunc[1], Hector J. Santos-Villalobos[1], Srdjan Simunovic[1], Scott W. Case[2]

Oak Ridge National Laboratory, PO Box 2008 MS6053, Oak Ridge TN 37831-6053, USA

Virginia Polytechnic Institute and State University, Engineering Science & Mechanics, 225-A Norris Hall, Blacksburg, VA 24061, USA

Corresponding Author:

Vlastimil Kunc, kuncv@ornl.gov,Tel. 001 865 574 8010, Fax. 001 865 574 8257, Oak Ridge National Laboratory, PO Box 2008 MS6053, Oak Ridge, TN 37831-6053, USA

Author contact information:

Vlastimil Kunc: kuncv@ornl.gov, Srdjan Simunovic: simunovics@ornl.gov, Scott Case: scase@vt.edu

Abstract

We apply a method for obtaining fully anisotropic stiffness tensor for a composite material containing curved discontinuous fibers to several example cases and show the effect of curvature on the nature of anisotropy of the stiffness tensor. For a material with fibers in single configuration, we obtain transversely isotropic material for straight fibers and for fibers enclosing half of a circle. The planes of isotropy for these two limit cases are orthogonal with the stiffness tensor for a general case being orthotropic. We show that the effect of fiber curvature on stiffness is negligible for materials with perfectly random fiber rotation. We also establish the number of fibers, hence a volume, over which we need to average to approach desired material properties and avoid excessive scatter in numerical results. The new method for establishing stiffness tensor is tested against experimental results. Comparison of stiffness measurements using x-ray digital image correlation against stiffness calculated with fiber configuration obtained by x-ray tomography shows that accounting for fiber curvature provides better estimate of stiffness.

Keywords

A. Discontinuous reinforcement, B. Anisotropy, B. Microstructures, C. Micro-mechanics

6.2.1 Introduction

Modern rapid processing techniques for discontinuous fiber composites, such as direct in-line long fiber reinforced process, compression molding and long fiber injection molding, result in materials containing fibers with significant fiber length. Experimental observations point to the fact that long fiber does not stay straight in the material, yet the assumption of straight fibers is used for prediction of material properties [8, 43, 66]. The effect of fiber curvature on material properties is often debated, however few systematic studies of this subject exist. Bapanapalli and Nguyen [34] examined a special case of a single fiber via analytical and numerical results and presented useful engineering conclusions. Continuous curved fibers were also studied in [67] [68]. To the knowledge of the authors, there has been no systematic study of fiber curvature and resulting stiffness tensor anisotropy for material containing an ensemble of curved fibers. This can be attributed to the fact that curved fiber loses transversely isotropic symmetry, which was used for stiffness tensor prediction using orientation averaging. In Part 1 of this paper, we have introduced the concepts of fiber configuration for curved fiber with two planes of geometric symmetry and configuration averaging over orthotropic stiffness tensor resulting in fully anisotropic stiffness tensor. These concepts allow us to systematically evaluate the effect of curvature on stiffness tensor for material described by configuration distribution function.

A summary of our method is provided below, however the reader is encouraged to consult Part 1 of this paper for more detailed discussion.

We have provided explanation of configuration distribution function for an ensemble of fibers ψ_C, which may be separated into two parts

$$\psi_C(\alpha,\beta,\gamma,\xi,\eta) = \psi_R(\alpha,\beta,\gamma)\psi_S(\xi,\eta) \tag{6.2-1}$$

In Equation (6.2-1), the rotation of fiber coordinate system with respect to laboratory system given by three angles α,β,γ and the shape of a fiber given by parameters $\xi = \frac{L}{d}, \eta = \frac{L}{R}$, are independent for an arbitrary configuration. The shape parameters therefore depend on fiber length L, fiber diameter d and the radius of fiber curvature R.

Configuration averaging of orthotropic stiffness tensor leads to the following stiffness tensor:

$$\begin{aligned}\langle C_{ijkl}\rangle_C = \overline{\mu}(\delta_{ik}\delta_{jl} + \delta_{il}\delta_{jk}) + \overline{\lambda}\delta_{ij}\delta_{kl} + \overline{\kappa_{p2}}(a_{ijmm}\delta_{kl} + \delta_{ij}a_{klmm}) + \overline{\kappa_{q2}}(b_{ijmm}\delta_{kl} + \\ \delta_{ij}b_{klmm}) + 2\overline{\mu_1}(\delta_{ik}a_{jlmm} + \delta_{il}a_{jkmm} + \delta_{jl}a_{ikmm} + \delta_{jk}a_{ilmm}) + 2\overline{\mu_2}(\delta_{ik}b_{jlmm} + \\ \delta_{il}b_{jkmm} + \delta_{jl}b_{ikmm} + \delta_{jk}b_{ilmm}) + \overline{\kappa_{p4}}a_{ijkl} + \overline{\kappa_{q4}}b_{ijkl} + \overline{\kappa_{s4}}s_{ijkl} \quad i,j,k,l,m = 1,2,3\end{aligned} \tag{6.2-2}$$

Where δ_{ij} represents Kronecker delta and summation over repeating indexes is implied.

$$\overline{k} = \int_{\xi=0}^{\infty} \int_{\eta=0}^{\infty} k(\xi,\eta)\psi_S(\xi,\eta)\ d\xi d\eta \tag{6.2-3}$$

In Equation (6.2-3), $\overline{k}$ represents any of the constants in of Equation (6.2-2) and

$$t_{ijkl} = \int_{\gamma=0}^{2\pi} \int_{\beta=-\pi/2}^{\pi/2} \int_{\alpha=0}^{2\pi} t_{ijkl}(\alpha,\beta,\gamma)\psi_R(\alpha,\beta,\gamma)\cos\beta\ \ d\alpha d\beta d\gamma \quad i,j,k,l = 1,2,3 \tag{6.2-4}$$

Where t_{ijkl} in Equation (6.2-4) represents any of the fourth order tensors in Equation (6.2-2)

Because any fourth order tensor in Equation (6.2-2) possesses at least the symmetry of the stiffness tensor $C_{ijkl} = C_{jikl} = C_{klij}$, we can write any fourth order tensor as 6x6 matrix using the following scheme to assign the indexes during the transformation from three dimensional space to six dimensional space [48]:

$$11 \to 1, 22 \to 2, 33 \to 3, 23 = 32 \to 4, 31 = 13 \to 5, 12 = 21 \to 6 \tag{6.2-5}$$

This transformation brings the stiffness tensor into standard engineering notation also referred to as the Voigt notation.

6.2.2 The Effects of Curvature

6.2.2.1 Material with Fibers in Single Configuration

We turn our attention to material containing fibers in single configuration. All fibers in such material have the same rotation angles α, β, γ and the same shape parameters ξ, η. We can write the probability of finding a fiber of given configuration for such material in the following form:

$$\psi_R(\alpha,\beta,\gamma) = \delta(\alpha - A)\delta(\beta - B)\delta(\gamma - \Gamma) \tag{6.2-6}$$

$$\psi_S(\xi,\eta) = \delta(\xi - X)\delta(\eta - H) \tag{6.2-7}$$

Where δ is Dirac Delta function and parameters in capital Greek letters indicate the particular set of configuration parameters. We will use notation $a_{(4)}$, $b_{(4)}$ and $s_{(4)}$ for fourth order orientation, curvature and mixed tensors. These tensors will be represented in Voigt notation. We now provide specific examples:

For $A = 0$, $B = 0$ and $\Gamma = 0$ representing a fiber with vector p parallel to x axis of laboratory coordinate system:

$$a_{(4)} = \begin{bmatrix} 1 & 0 & 0 & 0 & 0 & 0 \\ 0 & 0 & 0 & 0 & 0 & 0 \\ 0 & 0 & 0 & 0 & 0 & 0 \\ 0 & 0 & 0 & 0 & 0 & 0 \\ 0 & 0 & 0 & 0 & 0 & 0 \\ 0 & 0 & 0 & 0 & 0 & 0 \end{bmatrix} b_{(4)} = \begin{bmatrix} 0 & 0 & 0 & 0 & 0 & 0 \\ 0 & 1 & 0 & 0 & 0 & 0 \\ 0 & 0 & 0 & 0 & 0 & 0 \\ 0 & 0 & 0 & 0 & 0 & 0 \\ 0 & 0 & 0 & 0 & 0 & 0 \\ 0 & 0 & 0 & 0 & 0 & 0 \end{bmatrix} s_{(4)} = \begin{bmatrix} 0 & 1 & 0 & 0 & 0 & 0 \\ 1 & 0 & 0 & 0 & 0 & 0 \\ 0 & 0 & 0 & 0 & 0 & 0 \\ 0 & 0 & 0 & 0 & 0 & 0 \\ 0 & 0 & 0 & 0 & 0 & 0 \\ 0 & 0 & 0 & 0 & 0 & 0 \end{bmatrix} \quad (6.2\text{-}8)$$

For the following examples we will use material properties from [8] listed in Table 6.2-1, where E_f and E_m are the Young's moduli for the fiber and matrix material, ν_f and ν_m are the Poisson's ratios and V_f is the fiber volume fraction.

Table 6.2-1. Constituent Material Properties.

$E_f\ [Pa]$ ($E_f\ [psi]$)	ν_f	$E_m\ [Pa]$ ($E_m\ [psi]$)	ν_m	V_f	ξ
$7.24\ 10^{10}$ *($10.5\ 10^6$)*	0.2	$3.45\ 10^9$ *($0.5\ 10^6$)*	0.35	0.2	100

Orientation averaging of transversely isotropic stiffness tensor with material constants obtained using Halpin-Kardos equations [55] results in the following parametric form of material constants for orthotropic stiffness tensor

$$\bar{\tau} = \frac{k_1 H + k_2 \mathrm{Sin}[H] + k_3 \mathrm{Cos}[H] \mathrm{Sin}[H]}{H}\ Pa \quad (6.2\text{-}9)$$

Where $\bar{\tau}$ represents any of the nine material constants. Values for obtaining nine material constants for $X = 100$ are given in 6.2-2.

Table 6.2-2. Parameters $k_1 k_2$ and k_3 for orthotropic material with fibers in single configuration and aspect ratio $X = 100$.

	$\bar{\mu}$	$\bar{\lambda}$	$\overline{\kappa_{p2}}$	$\overline{\kappa_{q2}}$	$\overline{\mu_1}$	$\overline{\mu_2}$	$\overline{\kappa_{p4}}$	$\overline{\kappa_{q4}}$	$\overline{\kappa_{s4}}$
k_1	$3.55\ 10^8$	$8.\ 10^9$	$-3.3\ 10^9$	$-3.3\ 10^9$	$1.47\ 10^9$	$1.47\ 10^9$	$4.49\ 10^9$	$4.49\ 10^9$	$4.49\ 10^9$
k_2	0	0	$-\ 3.08\ 10^8$	$3.08\ 10^8$	$-2.64\ 10^7$	$2.64\ 10^7$	$5.99\ 10^9$	$-\ 5.99\ 10^9$	0
k_3	$1.5\ 10^9$	$-2.99\ 10^9$	$2.99\ 10^9$	$2.99\ 10^9$	$-\ 1.5\ 10^9$	$-\ 1.5\ 10^9$	$1.5\ 10^9$	$1.5\ 10^9$	$4.49\ 10^9$

Values for coefficients corresponding to $H = \frac{\pi}{4}$ and straight fibers $H = 0$ obtained through limiting process are listed in 6.2-3.

6.2-3. Orthotropic material constants for material in single configuration given by shape parameters $X = 100, H = \frac{\pi}{4}$ and material with straight fibers $X = 100, H \to 0$.

	$\bar{\mu}$ [Pa]	$\bar{\lambda}$ [Pa]	$\overline{\kappa_{p2}}$ [Pa]	$\overline{\kappa_{q2}}$ [Pa]	$\overline{\mu_1}$ [Pa]	$\overline{\mu_2}$ [Pa]	$\overline{\kappa_{p4}}$ [Pa]	$\overline{\kappa_{q4}}$ [Pa]	$\overline{\kappa_{s4}}$ [Pa]
$H \to 0$	$1.85\ 10^9$	$5.00\ 10^9$	$-6.17\ 10^8$	0	$5.28\ 10^7$	0	$1.20\ 10^{10}$	0	0
$H = \frac{\pi}{4}$	$1.31\ 10^9$	$6.09\ 10^9$	$-1.67\ 10^9$	$-1.12\ 10^9$	$4.94\ 10^8$	$5.41\ 10^8$	$1.08\ 10^{10}$	$5.29\ 10^7$	$1.63\ 10^9$

Material with curved fibers in single configuration is therefore orthotropic in general as we have shown in Part 1. Figure 6.2-1 shows the material constants in graphical form.

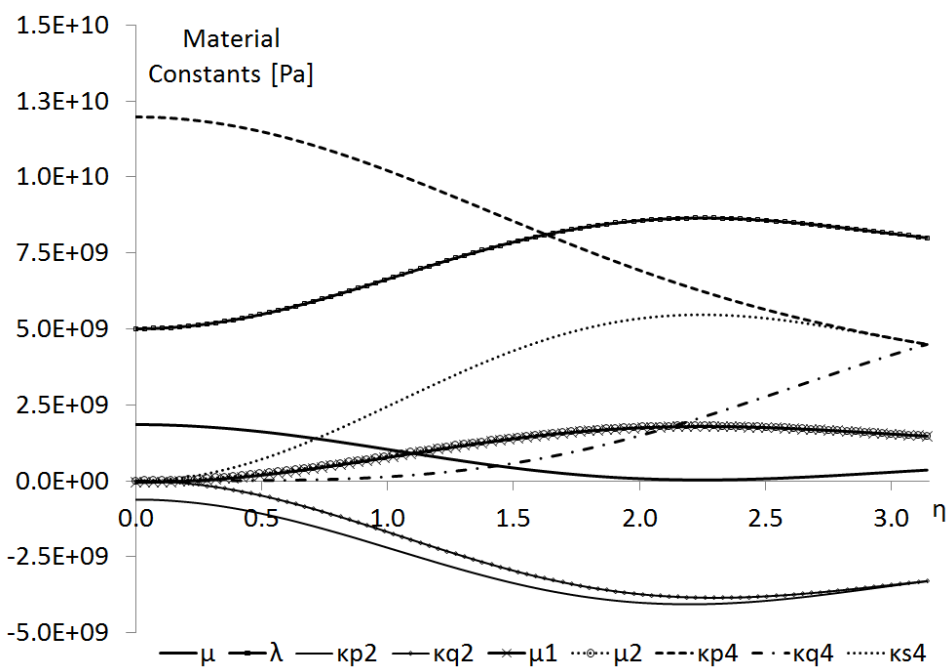

Figure 6.2-1. Material constants for orthotropic material with fibers in single configuration and aspect ratio $X = 100$.

Since the material is orthotropic, we can use relations given in [54] to generate engineering constants with respect to the principal axes of orthotropy, which coincide with the fiber coordinate. Figure 6.2-2 shows Young's moduli, shear moduli and Poisson ratios as a function of curvature.

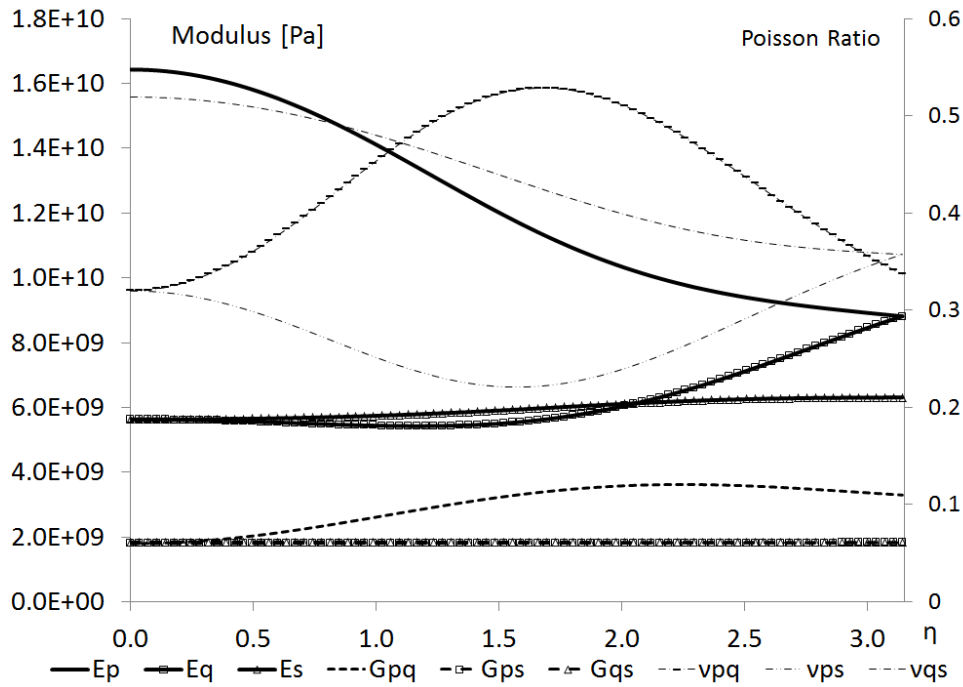

Figure 6.2-2. Young's moduli, shear Moduli and Poisson's ratios for orthotropic material with fibers in single configuration and aspect ratio $X = 100$.

6.2.2.2 Material with Perfectly Random Fiber Rotation

In this section, we consider material in which the fiber rotation is perfectly random over the entire range of angles α, β and γ. This distribution is represented by a constant function

$$\psi_R(\alpha,\beta,\gamma) = \frac{1}{8\,\pi^2}, \qquad \alpha \in \langle 0,2\pi\rangle, \beta \in \langle -\frac{\pi}{2},\frac{\pi}{2}\rangle, \gamma \in \langle 0,2\pi\rangle \tag{6.2-10}$$

And with the help of symbolic equation solver [69], the geometric tensors can be obtained analytically by performing integration as outlined in Equation (6.2-4).

$$a_{(4)} = \begin{bmatrix} \frac{1}{5} & \frac{1}{15} & \frac{1}{15} & 0 & 0 & 0 \\ \frac{1}{15} & \frac{1}{5} & \frac{1}{15} & 0 & 0 & 0 \\ \frac{1}{15} & \frac{1}{15} & \frac{1}{5} & 0 & 0 & 0 \\ 0 & 0 & 0 & \frac{1}{15} & 0 & 0 \\ 0 & 0 & 0 & 0 & \frac{1}{15} & 0 \\ 0 & 0 & 0 & 0 & 0 & \frac{1}{15} \end{bmatrix} \tag{6.2-11}$$

$$b_{(4)} = \begin{bmatrix} \frac{1}{5} & \frac{1}{15} & \frac{1}{15} & 0 & 0 & 0 \\ \frac{1}{15} & \frac{1}{5} & \frac{1}{15} & 0 & 0 & 0 \\ \frac{1}{15} & \frac{1}{15} & \frac{1}{5} & 0 & 0 & 0 \\ 0 & 0 & 0 & \frac{1}{15} & 0 & 0 \\ 0 & 0 & 0 & 0 & \frac{1}{15} & 0 \\ 0 & 0 & 0 & 0 & 0 & \frac{1}{15} \end{bmatrix} \tag{6.2-12}$$

$$s_{(4)} = \begin{bmatrix} \frac{2}{15} & \frac{4}{15} & \frac{4}{15} & 0 & 0 & 0 \\ \frac{4}{15} & \frac{2}{15} & \frac{4}{15} & 0 & 0 & 0 \\ \frac{4}{15} & \frac{4}{15} & \frac{2}{15} & 0 & 0 & 0 \\ 0 & 0 & 0 & -\frac{1}{15} & 0 & 0 \\ 0 & 0 & 0 & 0 & -\frac{1}{15} & 0 \\ 0 & 0 & 0 & 0 & 0 & -\frac{1}{15} \end{bmatrix} \tag{6.2-13}$$

The reader may verify that fiber changing the magnitude of fiber curvature does not influence the resulting stiffness tensor with material constants calculated listed above. For example, both sets of constants in Table 6.2-3 result in the same stiffness tensor:

$$C = \begin{bmatrix} 1.06\ 10^{10} & 5.39\ 10^{9} & 5.39\ 10^{9} & 0 & 0 & 0 \\ 5.39\ 10^{9} & 1.06\ 10^{10} & 5.39\ 10^{9} & 0 & 0 & 0 \\ 5.39\ 10^{9} & 5.39\ 10^{9} & 1.06\ 10^{10} & 0 & 0 & 0 \\ 0 & 0 & 0 & 2.61\ 10^{9} & 0 & 0 \\ 0 & 0 & 0 & 0 & 2.61\ 10^{9} & 0 \\ 0 & 0 & 0 & 0 & 0 & 2.61\ 10^{9} \end{bmatrix} \tag{6.2-14}$$

Our particular method of obtaining orthotropic material constants by orientation averaging of transversely isotropic stiffness tensor only accounts for changing orientation along the axis of the curved fiber and ensures that we obtain identical stiffness tensors regardless of fiber curvature. In general, the method of configuration averaging would result in different stiffness tensors for varying fiber curvature, however the form of the stiffness tensor would not change. It is clear that this material is isotropic with Young's modulus $\mathrm{E} = 6.99\ 10^{9}$ Pa and Poisson's ratio $\nu = 3.37\ 10^{-1}$.

We have therefore observed that changing the magnitude of fiber curvature in material with fibers in single configuration has significant influence on the stiffness tensor, while perfectly random fiber architecture negates the effects of fiber curvature.

6.2.2.3 Representative Volume

Since our method for stiffness tensor evaluation relies on averaging of configurations, we seek to establish in this section the size of a physical volume we need to average over to avoid stochastic nature of results dependent on particular volume selection.

For material with fibers in single configuration, we clearly need only the volume of a single fiber and surrounding matrix.

$$V_{1f} = \frac{\pi d^3}{4\nu_f}\xi \tag{6.2-15}$$

If our material contains fibers in finite set of N configurations, the representative volume necessary for exact determination of stiffness tensor is

$$V_{Nf} = \frac{\pi\ d^3}{4\ \nu_f}\sum_{i=1}^{N}\xi_{(i)} \tag{6.2-16}$$

Equation (6.2-16) contains the assumption that all fibers in our material have identical fiber diameter.

When the configuration distribution function is continuous for any of the five parameters, we need to average fibers of finite size over an infinite volume to obtain the exact stiffness tensor. Clearly, any realistic part or physical volume of material contains only a finite number of fibers, therefore continuous distribution function is merely a convenient approximation of reality. With the recognition that $1.0\ cm^3$ of material with glass fibers of $d = 1.5\ 10^{-5}\ m$ with aspect ratio and modest volume fraction given in Table 6.2-1 contains $7.55\ 10^5$ fibers, representation of microstructure for realistic DFCs with continuous distribution functions appears reasonable.

6.2.2.4 Approximation of Material by a Finite Number of Fibers

In the following discussion, we establish the number of fibers, hence the volume, over which we need to average to achieve acceptable error for materials containing very large number of fibers. The answers will naturally depend on the nature of configuration distribution.

The lower limit for averaging volume is a material with fibers in single configuration where we only need a single fiber to recover the exact stiffness tensor for such material. However for any material with a probability distribution function for any configuration parameter being continuous, we will recover only approximate stiffness tensor if we select a random set of fibers satisfying the configuration distribution.

We will estimate the approximation error for the previously presented example of material with perfectly arbitrary rotation distribution. We can use random number generator to produce 10^4 fiber configurations and subsequently evaluate isotropic Young's modulus obtained from configuration averaging over a selected set of fibers. The Young's moduli for approximations of isotropic material are obtained by calculating compliance matrix through inversion of stiffness matrix and subsequently inverting the first three diagonal terms. These three terms are identical for truly isotropic compliance matrix.

We start by evaluating the isotropic Young's modulus for the entire set of 10^4 fibers. Then we evaluate Young's moduli for randomly selected subset and continue reducing the size of the subset until we have only one fiber. We use the following formula to generate the number of fibers N_f that will be selected for in a given set

$$N_f = \text{Round}\left(10^{(i-1)/4}\right) \qquad i = 1 \ldots 17 \tag{6.2-17}$$

To obtain the number of fibers in our subsets

$$N_f = 1,2,3,6,10,18,32,56,100,178,316,562,1000,1778,3162,5623,10000 \tag{6.2-18}$$

Using Mathematica [69] random number generator for 10 sets of rotation configuration parameters with shape parameters $X = 100, H = \frac{\pi}{4}$, and perfectly random rotation we can generate plot shown in Figure 6.2-3.

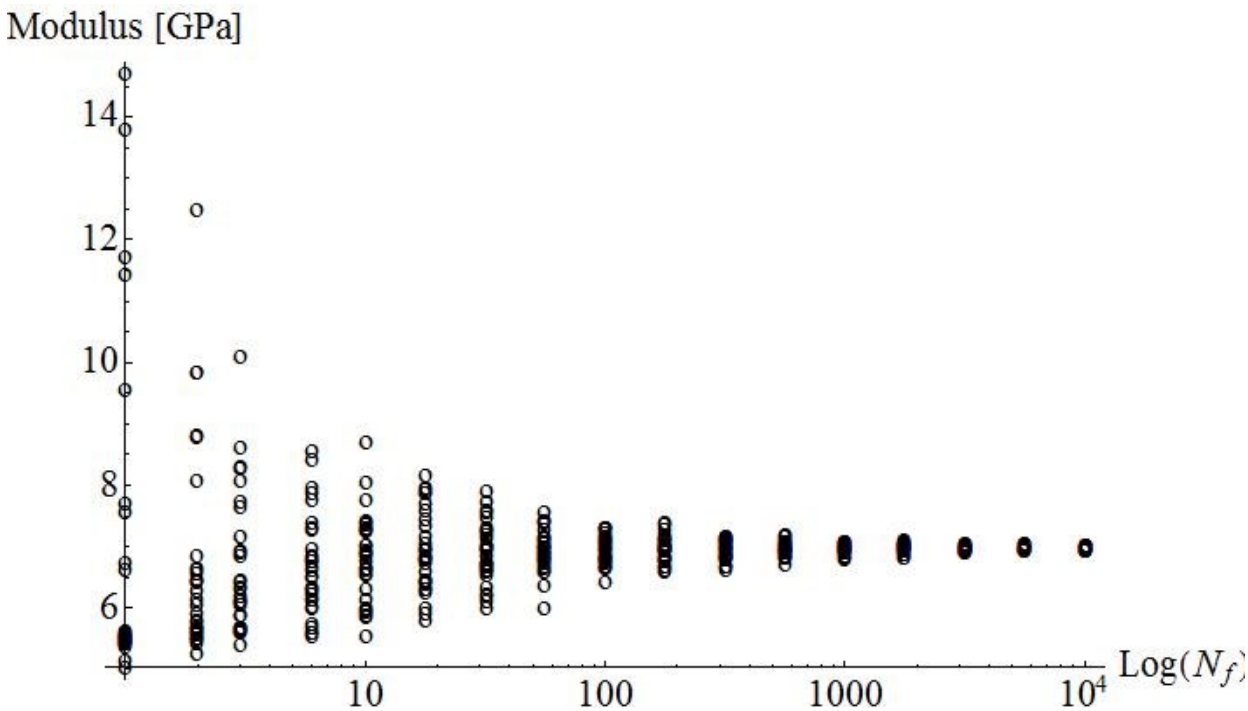

Figure 6.2-3. Isotropic Young's moduli for 10 randomly generated ensembles of fibers with shape parameters $X = 100, H = \frac{\pi}{4}$.

The reader may observe that we approach what can be considered an exact value $\underline{\mathrm{E}} = 6.99\ 10^9$ calculated for continuous fiber distribution as the number of fibers increases. Changing the fiber curvature results in plot nearly identical to Figure 6.2-3. We can now define error of approximation as

$$\overline{err}(N_f) = \frac{Max\left(E_{N_f}\right) - Min\left(E_{N_f}\right)}{2\underline{\mathrm{E}}} \tag{6.2-19}$$

Where we use maximum and minimum isotropic modulus calculated using approximation with N_f fibers exact isotropic modulus $\underline{\mathrm{E}}$ calculated with continuous distribution function. Figure 6.2-4 shows $\overline{err}$ for approximation of perfectly random fiber rotation of straight fibers and curved fibers with $H = \frac{\pi}{4}$. It is clear that both solutions converge to identical value and that 100 fibers

will result in $\overline{err}$ of less than 10%. We also note that configuration averaging and well established orientation averaging require comparable representative volume.

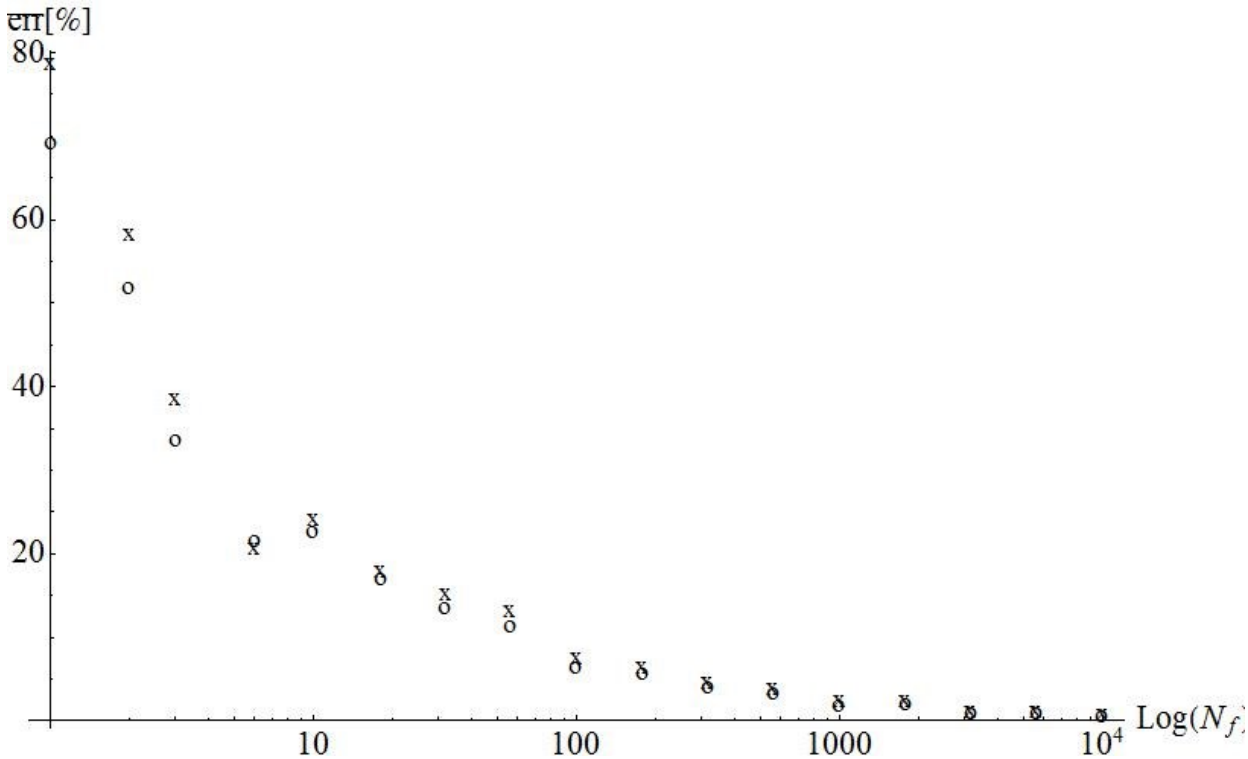

Figure 6.2-4. Error $\overline{err}$ for material with perfectly random rotation of straight (x) and curved (o) fibers approximated by a finite set of randomly generated fibers N_f.

We can use Equation (6.2-16) with 100 glass fibers of 15μm diameter in material with modest fiber volume fraction $\nu_f = 0.2$ to obtain material volume of V = 1.23 10^{-10} m^3. This is equivalent to the volume of a sphere with radius r = 3.16 10^{-4} m. This dimension is significantly smaller than any dimension of realistic DFC part.

6.2.2.5 Comparison with Experiments

Now we compare results of our method to against a realistic material produced with a common production technique. Polyamide 6,6 (PA6,6) material containing 50% of glass fibers by weight in the form of 12 mm long pulltruded pellets was injection molded into a an edge gated plaque cavity of 600mm x 600 mm and 2.8 mm thickness. Physical samples in this study were harvested from centers of these plaques. Figure 6.2-5 shows weighted fiber length distribution in the sample obtained by pyrolysis and measurements of digitized image of 2000 individual glass filaments [7].

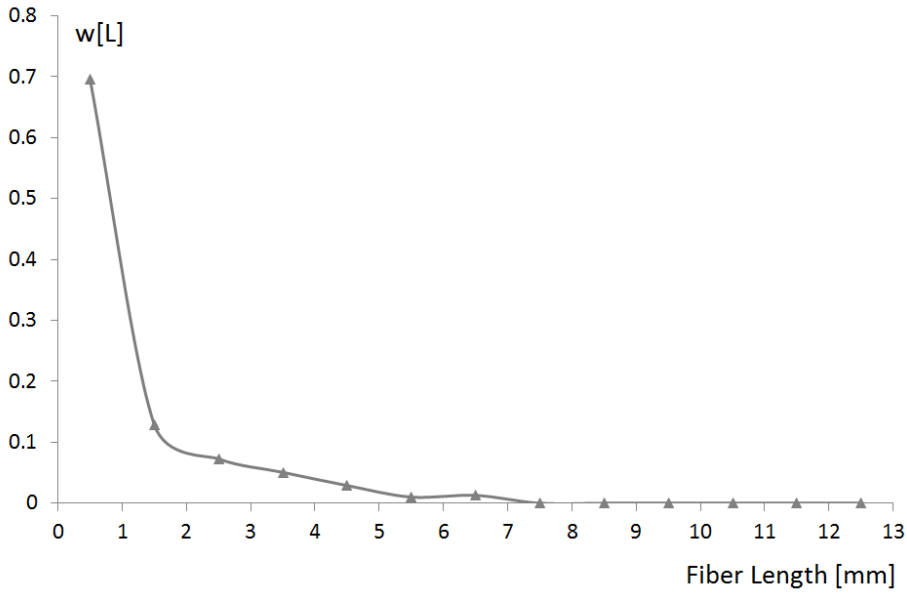

Figure 6.2-5. Weighted experimentally measured fiber length distribution.

Nominal diameter of 15 μm was measured for glass fibers in these samples using optical microscopy.

Experiments were performed using X-ray micro-tomography unit with a tensile testing machine [70]. This setup allows us to perform tomography at the beginning of the experiment and obtain fiber orientation as well as fiber curvature measurements. Measurements were performed on segments of 466 fibers with the best reconstruction. Although it is theoretically possible to obtain configuration of each individual filament using the setup presented in [70], reduced field of view and imperfect alignment of the testing machine in the tomography unit produces artifacts making tracking of each fiber difficult. Figure 6.2-6 shows histogram of fiber radius measured confirming the presence of curved fibers. Note that glass fiber subjected to pure bending can have minimum radius of approximately 147 μm.

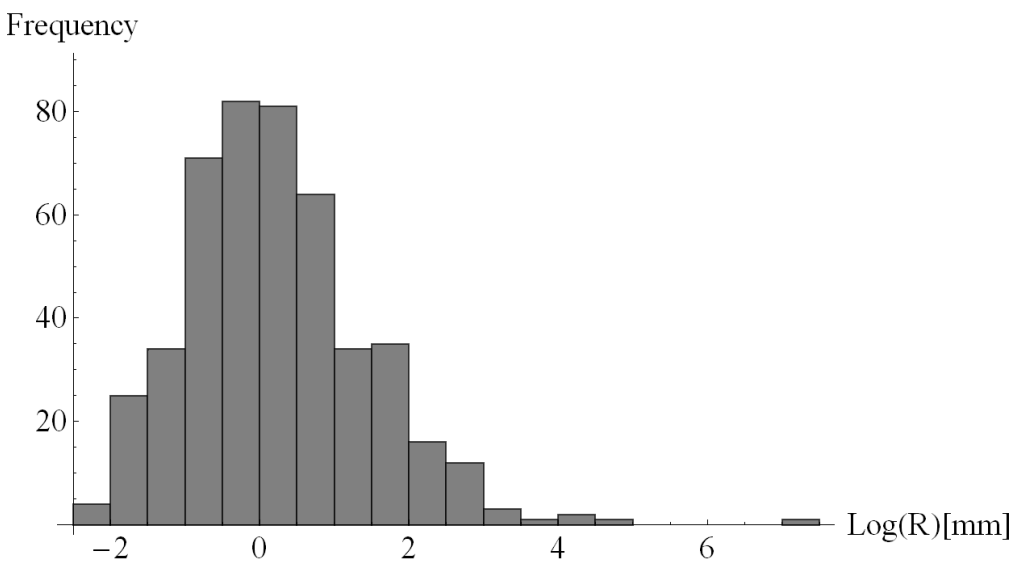

Figure 6.2-6. Histogram of fiber radius measured using x-ray micro-tomography.

Equations 6.2-20 through 6.2-22 provide geometric tensors reconstructed from the measurements on 466 filaments.

$$a_{(4)} = \begin{bmatrix} 8.62\ 10^{-2} & 1.38\ 10^{-2} & 1.07\ 10^{-1} & -2.79\ 10^{-3} & -3.21\ 10^{-2} & 9.66\ 10^{-3} \\ 1.38\ 10^{-2} & 3.27\ 10^{-2} & 1.13\ 10^{-2} & -1.4\ 10^{-3} & -2.94\ 10^{-3} & 4.02\ 10^{-3} \\ 1.07\ 10^{-1} & 1.13\ 10^{-2} & 6.17\ 10^{-1} & 1.27\ 10^{-3} & -1.27\ 10^{-1} & 4.28\ 10^{-3} \\ -2.79\ 10^{-3} & -1.4\ 10^{-3} & 1.27\ 10^{-3} & 1.13\ 10^{-2} & 4.28\ 10^{-3} & -2.94\ 10^{-3} \\ -3.21\ 10^{-2} & -2.94\ 10^{-3} & -1.27\ 10^{-1} & 4.28\ 10^{-3} & 1.07\ 10^{-1} & -2.79\ 10^{-3} \\ 9.66\ 10^{-3} & 4.02\ 10^{-3} & 4.28\ 10^{-3} & -2.94\ 10^{-3} & -2.79\ 10^{-3} & 1.38\ 10^{-2} \end{bmatrix} \tag{6.2-20}$$

$$b_{(4)} = \begin{bmatrix} 1.43\ 10^{-1} & 9.96\ 10^{-2} & 2.42\ 10^{-2} & -7.95\ 10^{-3} & 2.24\ 10^{-2} & -1.27\ 10^{-2} \\ 9.96\ 10^{-2} & 5.08\ 10^{-1} & 3.29\ 10^{-2} & -2.35\ 10^{-2} & 2.35\ 10^{-2} & -5.42\ 10^{-2} \\ 2.42\ 10^{-2} & 3.29\ 10^{-2} & 3.54\ 10^{-2} & -1.44\ 10^{-3} & 9.26\ 10^{-3} & -3.74\ 10^{-3} \\ -7.95\ 10^{-3} & -2.35\ 10^{-2} & -1.44\ 10^{-3} & 3.29\ 10^{-2} & -3.74\ 10^{-3} & 2.35\ 10^{-2} \\ 2.24\ 10^{-2} & 2.35\ 10^{-2} & 9.26\ 10^{-3} & -3.74\ 10^{-3} & 2.42\ 10^{-2} & -7.95\ 10^{-3} \\ -1.27\ 10^{-2} & -5.42\ 10^{-2} & -3.74\ 10^{-3} & 2.35\ 10^{-2} & -7.95\ 10^{-3} & 9.96\ 10^{-2} \end{bmatrix} \tag{6.2-21}$$

$$s_{(4)} = \begin{bmatrix} 7.17\ 10^{-2} & 1.59\ 10^{-1} & 2.43\ 10^{-1} & -7.25\ 10^{-3} & -2.48\ 10^{-2} & -1.22\ 10^{-2} \\ 1.59\ 10^{-1} & 2.77\ 10^{-2} & 5.12\ 10^{-1} & -7.27\ 10^{-4} & -1.06\ 10^{-1} & 8.34\ 10^{-3} \\ 2.43\ 10^{-1} & 5.12\ 10^{-1} & 7.33\ 10^{-2} & -2.79\ 10^{-2} & 2.36\ 10^{-2} & -4.89\ 10^{-2} \\ -7.25\ 10^{-3} & -7.27\ 10^{-4} & -2.79\ 10^{-2} & -1.46\ 10^{-2} & 3.87\ 10^{-3} & 1.14\ 10^{-3} \\ -2.48\ 10^{-2} & -1.06\ 10^{-1} & 2.36\ 10^{-2} & 3.87\ 10^{-3} & -5.87\ 10^{-2} & 2.86\ 10^{-2} \\ -1.22\ 10^{-2} & 8.34\ 10^{-3} & -4.89\ 10^{-2} & 1.14\ 10^{-3} & 2.86\ 10^{-2} & -1.31\ 10^{-2} \end{bmatrix} \quad (6.2\text{-}22)$$

Mechanical tests were performed on double dog-bone shoulder loaded samples with 1mm x 1 mm cross section [71]. Figure 6.2-6 shows stress strain curves from digital image correlation using X-ray images of sample deformed under known load. The solid lines in Figure 6.2-7 show fifth order polynomial least square fit that provide tangential Young's modulus summarized in Table 6.2-4.

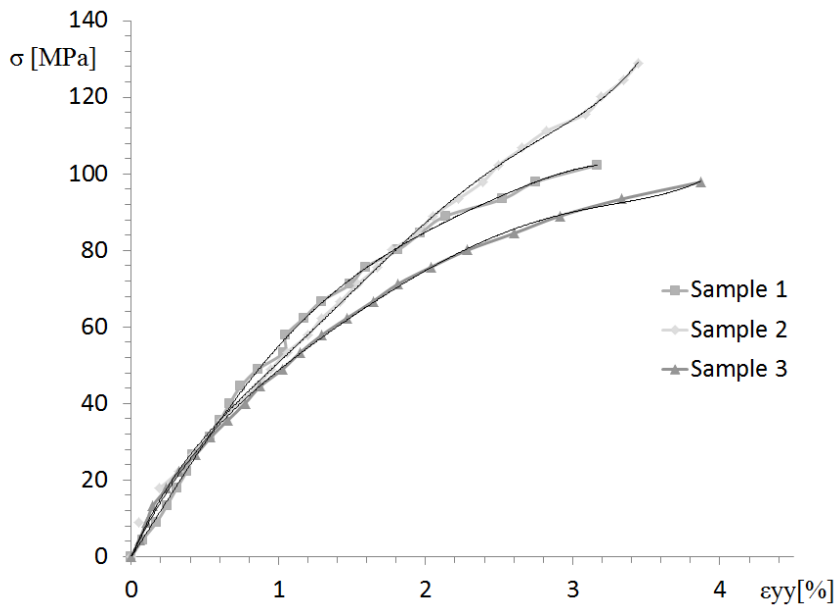

Figure 6.2-7. Stress-strain curves from digital image correlation.

Table 6.2-4. Tangential Young's moduli from digital image correlation of X-ray images of loaded samples.

	Sample1	*Sample 2*	*Sample 3*	*Average*
E [GPa]	8.88	5.84	8.09	7.61

Table 6.2-5 shows constituent material properties used for prediction of the stiffness tensor. The matrix properties were obtained by averaging tangential modulus of five PA6,6 samples containing resin identical to that used in the reinforced material.

Table 6.2-5. Constituent material properties for injection molded PA6,6 containing 50% glass fibers by weight

E_f $[Pa]$	ν_f	E_m $[Pa]$	ν_m	V_f
$7.24\ 10^{10}$	0.2	$2.63\ 10^{9}$	0.35	0.31

Averaging for material in with finite set of configurations, presented in Part 1, was used with number of fibers N=466. Random number generator in Mathematica [69] was used to select values from fiber length measurements and pair them with radii to generate values for ξ and η for each filament. Two stiffness tensors were calculated for one hundred randomly selected sets of 466 fibers. Due to the small sample size, the values of ξ for each filament were adjusted by randomly generating the intersection of the fiber with the sample and eliminating portions of the filament outside of the sample. One stiffness tensor, accounted for fiber curvature, while the other was calculated with the assumption of straight fibers. Figure 6.2-8 shows sample stiffness Ec for curved fibers and Es for straight fibers. The assumption of curved fibers resulted in mean sample stiffness prediction of 8.77 GPa, while the mean for straight fiber prediction was 9.05 GPa.

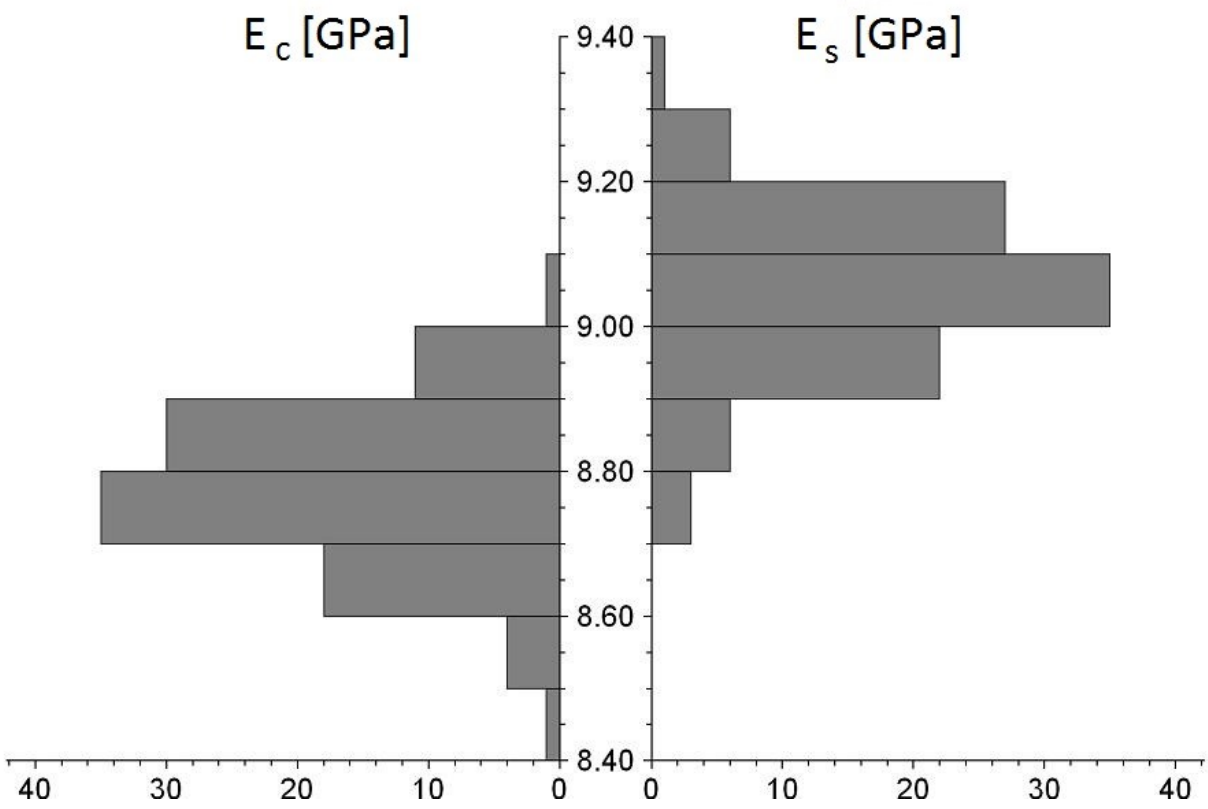

Figure 6.2-8. Predicted sample Young's moduli Ec and Es for curved fibers and straight fibers respectively.

The deviation from average experimental measurement is therefore 15% for model with curved fibers and 19% for model with straight fibers. It is likely that we would obtain closer match if we accounted for time dependent or non-linear behavior of the matrix material. It should also be noted that we have not performed any calibration of matrix material or arbitrary adjustment of parameters occasionally performed in engineering practice.

6.2.2.6 Conclusions

We have shown that the impact of fiber curvature on stiffness tensor properties depends on the rotation distribution function of the DFC material. The extreme examples are materials with fibers with perfectly random fiber rotation and materials with fibers in single configuration. For a material with perfectly random fiber rotation, where the local fiber coordinate system is oriented in any direction with equal probability, fiber curvature does not influence the stiffness tensor. For material with fibers in single configuration, fiber curvature influences not only the material properties.

We show that the representative volume over which we need to perform configuration averaging is comparable to the volume needed for orientation averaging and that this volume is small given reasonable expectation of acceptable error.

Finally, we compare results of configuration averaging and orientation averaging using experimentally obtained data. X-ray micro-tomography is used to obtain fiber orientation and curvature parameters, while x-ray digital image correlation is used to obtain stress-strain behavior of injection molded material. We demonstrate that configuration averaging produces closer match than orientation averaging.

6.2.2.7 Acknowledgements

The authors would like to express gratitude to the American Chemistry Council, Plastics Division for supporting research and innovation in this area.

6.2.2.8 References

1. Nguyen, B. N., et al., *Prediction of the Elastic-Plastic Stress/Strain Response for Injection-Molded Long-Fiber Thermoplastics.* Journal of Composite Materials, 2009. **43**(3): p. 217-246.
2. Advani, S. G. and C. L. Tucker, *The Use of Tensors to Describe and Predict Fiber Orientation in Short Fiber Composites.* Journal of Rheology, 1987. **31**(8): p. 751-784.
3. Nguyen, B. N. and V. Kunc, *An Elastic-Plastic Damage Model for Long-Fiber Thermoplastics.* International Journal of Damage Mechanics, 2009.
4. Bapanapalli, S. and B. N. Nguyen, *Prediction of elastic properties for curved fiber polymer composites.* Polymer Composites, 2008. **29**(5): p. 544-550.
5. Akbarov, S. D. and R. Kosker, *On a stress analysis in the infinite elastic body with two neighbouring curved fibres.* Composites Part B-Engineering, 2003. **34**(2): p. 143-150.
6. Kosker, R. and N. T. Cinar, *Stress distribution in an infinite elastic body containing two neighboring locally curved fibers.* Mechanics of Composite Materials, 2009. **45**(3): p. 315-330.
7. Chadwick, P., M. Vianello, and S. C. Cowin, *A new proof that the number of linear elastic symmetries is eight.* Journal of the Mechanics and Physics of Solids, 2001. **49**(11): p. 2471-2492.
8. Halpin, J. C. and J. L. Kardos, *Strength of Discontinuous Reinforced Composites .1. Fiber Reinforced Composites.* Polymer Engineering and Science, 1978. **18**(6): p. 496-504.
9. Lubarda, V. A. and M. C. Chen, *On the elastic moduli and compliances of transversely isotropic and orthotropic materials.* Journal of Mechanics of Materials and Structures, 2008. **3**(1): p. 153-171.
10. Wolfram Research, I., *Mathematica Edition: Version 7.0.* 2008, Champaign, Illinois Wolfram Research, Inc.
11. Kunc, V., Frame, B. J., Nguyen, B. N., Tucker III, C. L. and Velez-Garcia, G, *Fiber Length Distribution Measurement for Long Glass and Carbon Fiber Reinforced Injection*

Molded Thermoplastics, in *Composites Conference & Exposition, Society of Plastic Engineers*. 2007: Troy, Michigan.

12. Kunc, V., *Observation of Composite Materials Using Coupled Mechanical Testing and Computed Tomography*, in *SEM XI International Congress & Exposition on Experimental and Applied Mechanics*. 2008: Orlando, FL.
13. Kunc, V., *Tensile specimen design and experimental procedures for characterizing polymeric composites using X-ray based micro-tomography*, in *SAMPE-ASC*. 2008: Memphis, TN.

6.3 Observation of Composite Materials Using Coupled Mechanical Testing and Computed Tomography

Vlastimil Kunc[1,2], Donald Erdman [2], Barbara Frame[2], Robert Norris[2], Scott Case[3]

Abstract

A coupled load frame and x-ray micro-tomography unit was used to observe damage processes occurring within model composite specimens subjected to mechanical loading. These specimens consisted of two tows of glass fiber in the form of bound loops within an epoxy matrix of cylindrical form with 3-mm diameter cross-section. Computed tomography reconstruction was used to investigate internal structure of the specimens under load. This reconstruction revealed internal cracking and progressive failure in several experiments.

6.3.1 Introduction

The use of composites over the past six decades has been driven by high-end structural applications where design is governed by specific stiffness, strength or fatigue life considerations and where no single homogeneous material could be used [1]. To support these designs, investigations of damage processes in the composites were used primarily to establish failure criteria and in turn to design material with higher threshold for damage. Most studies in the field were oriented on design an analysis of composites under standard service conditions, therefore energy absorption of composite structures was not the primary concern. As composites are increasingly applied in automobiles and other structures where behavior during abnormal service events, such as crash, is of considerable importance, energy absorption is being investigated. Some composites have been found to possess good energy absorption properties; however, empirical investigations and phenomenological models for given material combinations and fiber architectures appear to dominate this field. Designers wishing to tailor the internal structure of composite material reinforced with continuous fibers can use readily available tools and design guidelines to investigate numerous options prior to making an actual test article. These tools will likely give good predictions for stiffness analyses and, when used with a large amount of published experimental data, provide reasonable predictions for strength analyses. Multi-scale modeling tools [2, 3] can be used to estimate energy absorption of composite structures, however confidence in predictive capabilities of these tools may suffer due to the inability to support assumptions about progressive damage on the microscopic scale by direct observation of multiple damage processes being active. When designing for maximum strength, it is usually preferable to delay initial damage in the material until high load is achieved in the structure and it is important to make sure that failure occurs in the fiber direction rather than relying on other, matrix property dominated, failure mode. Reducing the number of damage mechanisms being

[1] Author to whom correspondence should be addressed: kuncv@ornl.gov, (865) 574 - 8010
[2] Oak Ridge National Laboratory
[3] Virginia Polytechnic Institute and State University

active in the material prior to failure and increasing threshold load for initial damage is the usual objective in design and analysis of composite structures. As long as multi-scale modeling tools capture the limited number of dominant failure modes, they are useful for strength driven design. In contrast, the objectives in designing composite structures for maximum energy absorption differ significantly. Energy absorbing structures are often used to protect passengers in a vehicle or electronics in an enclosure by reducing inertial forces during incidents and rough handling. This is best achieved by triggering initial damage early and dissipating energy through multiple damage modes. Instead of minimizing the number of damage modes and maximizing the initial damage threshold as in strength driven design, maximum number of damage modes and early onset of damage is usually desirable in energy absorbing structures. A thorough understanding of possible damage modes is therefore necessary in order to develop reliable predictive tools for energy absorption modeling. This understanding is dependent on techniques used to observe the damage modes. Data collected on the surface of test articles via strain gages, extensometers or optical methods [4] along with visual observation of samples and microscopy of failure surface [5] are traditionally the primary tools for evaluation of processes being active within material. Acoustic emission can be used to monitor the nature and location of damage if the process is audible [6]. Micro-cracking is also often observed using x-ray imaging of a penetrating liquid deposited in the cracks [7]. The techniques listed above are well established and their use is widespread; however they do not allow direct observation of specimens subjected to load—one is left to infer and model the events that took place in the composite. To address this gap, a tensile testing machine capable of operating inside a 3-D x-ray tomography machine is being developed at ORNL. This new and unique capability allows examination or processes occurring in materials and viewing of specimens under load in various stages of damage in three dimensions.

6.3.2 Specimen preparation

Substantial effort was devoted to developing a procedure for sample manufacturing. The goal in specimen preparation was to obtain repeatable samples with controlled fiber architecture, material properties, interface properties and with geometry that would lead to failure in the area of interest. Three epoxy resin systems were evaluated in an effort to obtain desired "ductile" and "brittle" matrix behavior. While it was possible to achieve very brittle behavior in one system, it was not possible to manufacture specimens with this system without incurring damage prior to mounting of the sample in the testing machine. It was also not possible to obtain failure with necking with the epoxy systems under consideration. Preparation procedures were identical for all three epoxy systems, however handling and curing times may vary. The procedure is discussed in detail below for Epon 862 resin and 30 phr Ancamine 2167 hardener. Small tow E-glass [8] was used to make the desired fiber form. The fiber form had a shape of two interconnected loops. The loops were continuous (Figure 6.3-1) or interrupted at pre-determined location (Figure 6.3-2).

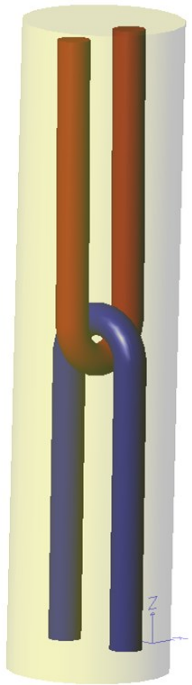

Figure 6.3-1. Schematic of fiber form within a specimen with continuous fiber tow loops.

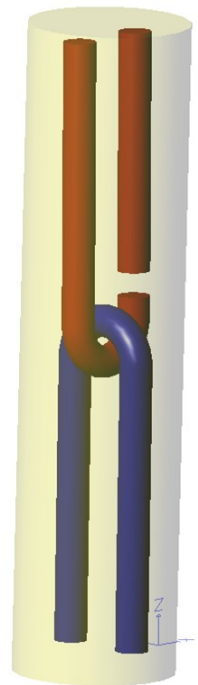

Figure 6.3-2. Schematic of fiber form within a specimen with interrupted fiber tow loops.

A cylindrical specimen rod was formed around the fiber form and grip pieces were bonded to the end of the specimen rod using a fixture. Several design iterations of grip pieces were conceived and experimented with to reduce excessive specimen relaxation under load, specimen rod pull-out and fracture near the grip piece (Figure 6.3-3).

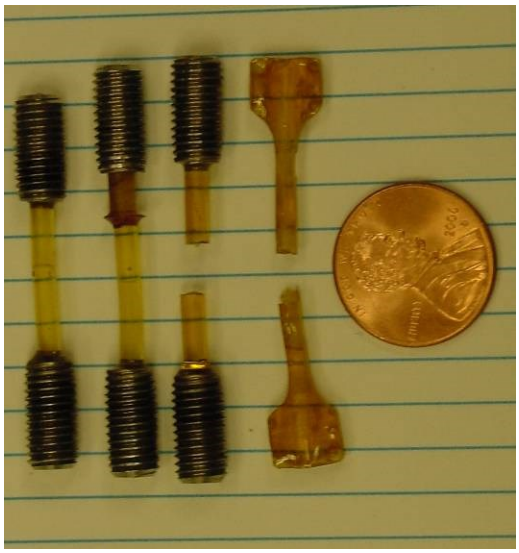

Figure 6.3-3. Untested specimen, specimen with pulled out grip piece, specimen with gage length grip failure and initial specimen design.

This effort was only partially successful since grip failures were not eliminated for any of the design iterations. The final design of the grip piece is illustrated in Figure 6.3-4. A stainless steel threaded rod (1/4-28) 0.25 inches long was drilled with a tapered drill bit and the wide part of the hole was subsequently plugged by welding it.

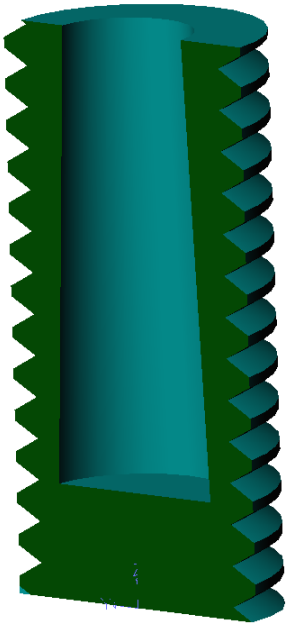

Figure 6.3-4. Cross-section of final design of the grip piece.

The following steps were followed to make "loop samples":

1. Cut two 18 inches long strands of glass tow and create a loop. Bond the ends of the strands with cyano-acrylate adhesive for easy handling. If reduced fiber matrix adhesion is desired, coat the tow in mold release and allow to dry.
2. Cover a flat surface with mold release film and affix stripes of high temperature tape 5 inches apart.
3. Mix epoxy, deposit loops in the resin and heat up to 60°C, until most bubbles disappear. De-gas resin with the loops.
4. Extract loops impregnated with resin and remove excess adhesive.
5. Affix stretched out loops with high temperature tape and cure the epoxy to obtain fiber form (Figure 6.3-5).

Figure 6.3-5. Fiber form with cured epoxy maintaining the shape.

6. Cut the fiber form into an appropriate length and cut the strands if desired. Insert the fiber form into a Teflon tube and seal the bottom with clay (Figure 6.3-6).

Figure 6.3-6. Fiber form (right) was inserted in Teflon tube and bottom sealed with clay (middle) to produce a specimen (left).

7. Mix epoxy, heat up to 60ºC until most bubbles disappear and de-gas. Fill syringe with the epoxy and attach hypodermic needle
8. Pierce the clay at the bottom of the tube and slowly inject the epoxy. Withdraw the needle and seal the opening thoroughly with clay to prevent leaks. Insert the Teflon tube in a copper tube in vertical position to make the Teflon tube straight and to prevent leaks. Let the epoxy gel and then cure.
9. Withdraw the Teflon tube from the copper tube. Pull out the specimen rod if possible. It may be necessary to cut away the Teflon tube. Cut the specimen rod to appropriate length.
10. Clean the grip pieces thoroughly, wrap the threads in Teflon tape and insert them in the alignment fixture. Mix epoxy, heat up to 60ºC along with an empty syringe, grip pieces and alignment fixture. Fill the syringe and deposit a few drops in a warm grip piece. Rotate the specimen rod while slowly inserting it in the grip piece. Place a loose grip piece at the top of the rod. Cure the epoxy. Remove specimens from the alignment fixture and repeat steps 21, 22, 23 and 25 to bond grip piece to the other end of the grip piece

6.3.2.1 Experimental Setup

The test setup consists of a micro-tomography unit produced by X-radia Inc. and a custom screw driven testing machine operating within the tomography unit (Figure 6.3-7) with accompanying data acquisition and control equipment.

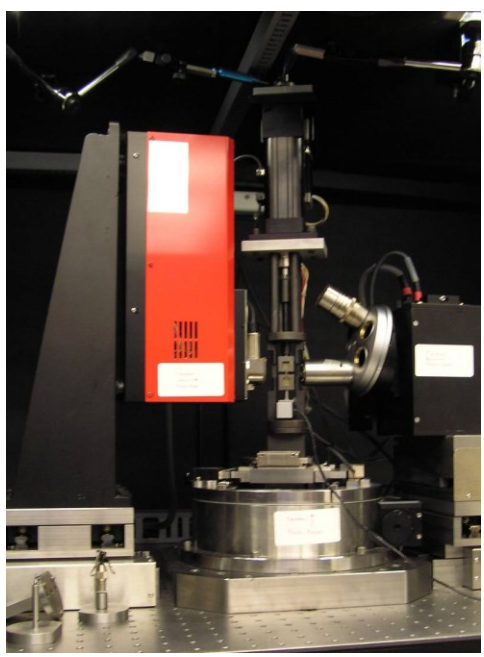

Figure 6.3-7. Testing machine within x-ray micro-tomography unit.

The primary components of the micro-tomography unit are the source, detector and x-y-z-rotate stage [9]. The source and the detector are also on stages to allow proper alignment. A 40–150 keV x-ray source allows through penetration imaging. The detector contains a 2048x2048 pixel, 16 bit CCD camera and two objectives (3.8x and 19.8x). The 3.8x objective was used for the study presented below.

The ORNL-designed test system is based on a screw driven testing machine with 1.33 kN (300 lb) capacity that can test specimens of up to 3 mm (0.118 in.) cross-section. An Interface load cell [10] is used to measure load and displacement is measured by the actuator encoder. Custom software was written in LabView [11] for data acquisition and control of the system.

The tomography unit and the testing machine are connected to two separate computers and synchronization is performed manually. Details about the experimental setup are available in [12].

6.3.2.2 Testing Procedure

Alignment of the system is performed once before a set of tests is performed. The testing machine is attached to a fixed bearing at the top and to the x-y-z-rotate stage at the bottom. The objective of alignment is to assure that the axis of the stage is aligned with the axis of the bearing. This will result in minimal forces on the stage positioning motors and minimal wobble of the sample during rotation of the instrument. The precision of alignment is judged from the movement of a small tungsten carbide ball deposited in an epoxy specimen rod. The specimen rod was made using technique discussed above with the fiber form not being present. The ball was deposited into a small hole that was drilled in the specimen rod and the hole subsequently sealed with an adhesive. During alignment, the specimen rod can be treated as transparent and only the movements of the ball was monitored. Figure 6.3-8 and Figure 6.3-9 show vertical and horizontal wobble of the ball through 150 degrees of rotation. The amount of wobble is less than for samples mounted on the stage without the testing machine present. This is likely due to the additional constraint being present at the top of the testing machine.

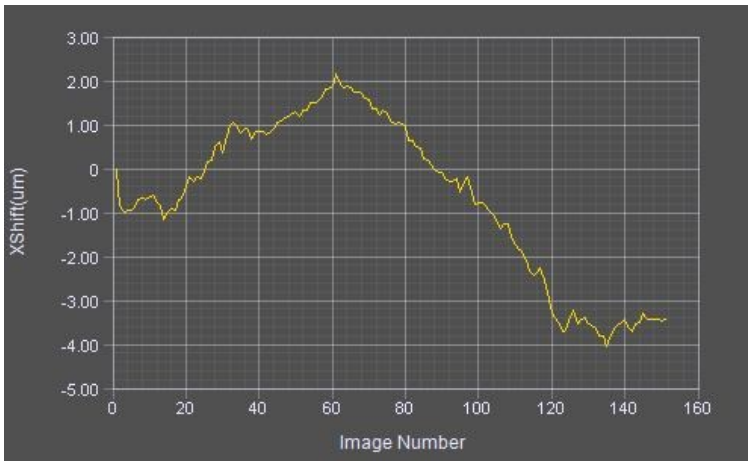

Figure 6.3-8. Horizontal wobble of alignment ball through 150 degrees of rotation.

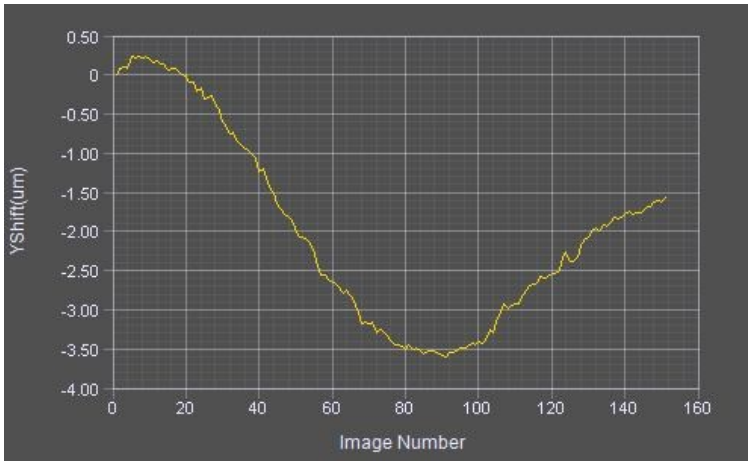

Figure 6.3-9. Vertical wobble of alignment ball through 150 degrees of rotation.

Once the alignment was performed, a set of tests was performed and the known wobble could be corrected using software.

After the specimen was mounted in the testing machine, it was loaded to a low load level to eliminate slack in the system. The sample was then loaded in displacement control with a stroke rate of 0.005 in./s. Loading was performed in steps with pauses in which displacement was held constant at initial pre-determined load levels. These pauses allowed imaging and examination of the sample. Although the sample relaxed and the load decreased during the pause, two-dimensional x-rays show individual fibers clearly and tomography reconstruction also provides

valuable insight into the processes in the material. The time to complete each individual x-ray, excluding manual operation of the computer, is 9.5 seconds for 5 second exposure with 4.5 seconds of data transfer overhead. With additional overhead for rotating the stage, the total time to complete tomography imaging with 1000 exposures is three hours. Tomography was performed before loading and at times when interesting behavior was observed during loading and after gage-length failure.

6.3.3 Results and Observations

As indicated in the above discussion, grip failures were not eliminated; therefore observation of processes occurring in the material leading to failure was not possible for some of the specimens. There were several preliminary tests performed, primarily to establish the testing procedure and to experiment with various epoxy formulations and gripping techniques. Three replicates of three types of samples were tested. The first type contained a fiber form with a continuous loop of un-modified tow. All of these specimens failed at the grip and no significant processes were observed prior to failure. The second type of specimens contained fiber form with a continuous loop of tow coated in mold release. Two of the three specimens failed at the gage length and some observations are discussed below. The third set of specimens contained fiber form with an un-modified, but interrupted tow. One tow was cut approximately 1 mm from the loop end (Figure 6.3-10).

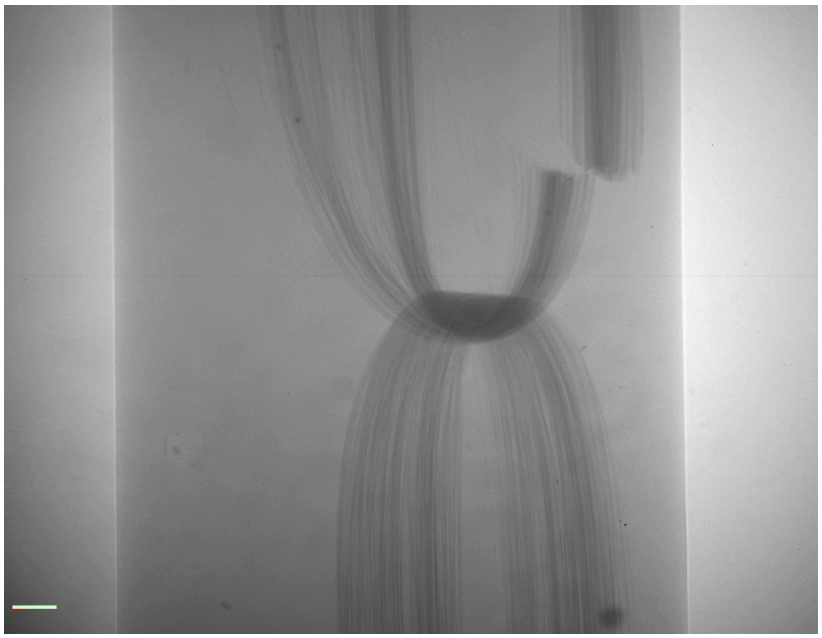

Figure 6.3-10. X-ray image of fiber form with interrupted tow (CutLoop1).

It was speculated that the fiber ends in close proximity of the loop would act as stress concentrators, which would initiate or alter failure mechanism of the sample. However, all specimens tested failed at the grip indicating the need to further refine the testing technique. Table 6.3-1 represents the final set of tests performed with the knowledge gained during the experimentation.

Table 6.3-1. Test Matrix

Specimen Name	Specimen Type	Test Notes
FullLoop1	Full loop, no mold release	Grip failure at 60.2 lb.
FullLoop2	Full loop, no mold release	Grip failure at 59.6 lb.
FullLoop3	Full loop, no mold release	Grip failure at 68.9 lb.
FullLoopMoldRel1	Full loop, mold release on tows	Observed white region at 30 lb. Gage length failure at 54.3 lb. Top loop failed completely.
FullLoopMoldRel2	Full loop, mold release on tows	Did not observe damage before failure. Gage length failure at 48.1 lb.
FullLoopMoldRel3	Full loop, mold release on tows	Observed crack at 24 lb. Data acquisition malfunction.
CutLoop1	Loop cut 1 mm from the loop end, no mold release	Grip failure at 60.2 lb.
CutLoop2	Loop cut 1 mm from the loop end, no mold release	Grip failure at 78.6 lb. Possible data acquisition malfunction during final loading.
CutLoop3	Loop cut 1 mm from the loop end, no mold release	Grip failure at 51.2 lb

Observations of FullLoopMoldRel1 (Figure 6.3-11) are presented below. Similar observations were made during testing of FullLoopMoldRel2 and experimental samples with fiber tow sizing not optimized for epoxy matrices.

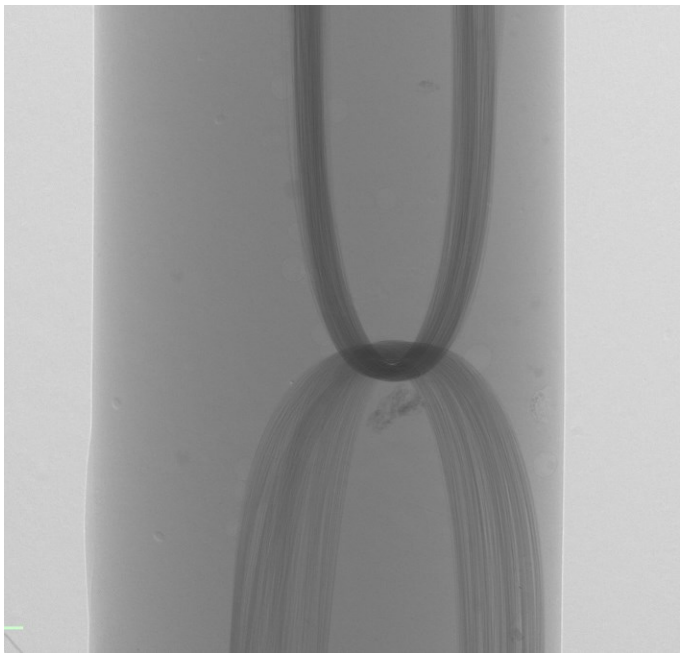

Figure 6.3-11. X-ray of FullLoopMoldRel1 specimen showing observable gage length.

Figure 6.3-12 shows the load-displacement curve for FullLoopMoldRel1 specimen. Loading of this sample was performed in 3 lb increments, which can be detected in the load-displacement curve. A large drop in load can be observed at 30 lb and another drop at 42 lb. These correspond to relaxation of the sample during tomography imaging at 30 lb and extended examination at 42 lb.

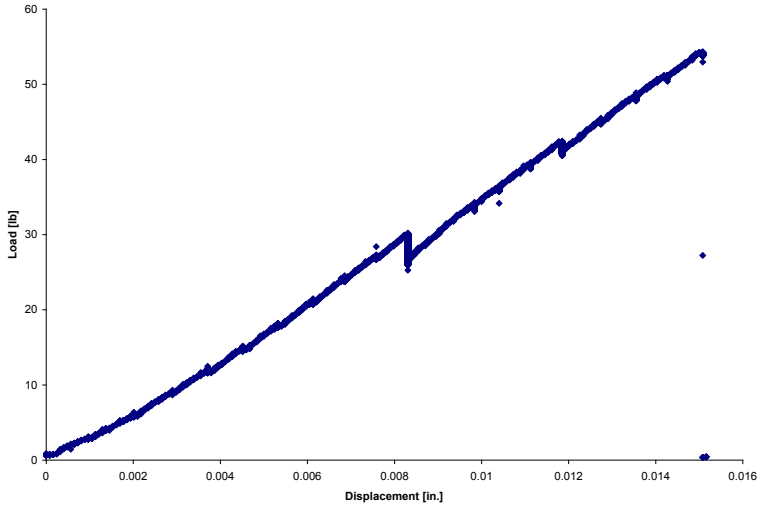

Figure 6.3-12. Load-displacement curve for the entire test of FullLoopMoldRel1.

A load-time curve shown in Figure 6.3-13 indicates relaxation of the specimen during each pause in loading leading up to the tomography imaging, which was started with the specimen carrying approximately 29 lb. This tomography was performed because a new crack was observed in the sample. Figure 6.3-14 shows relaxation of the specimen during tomography imaging.

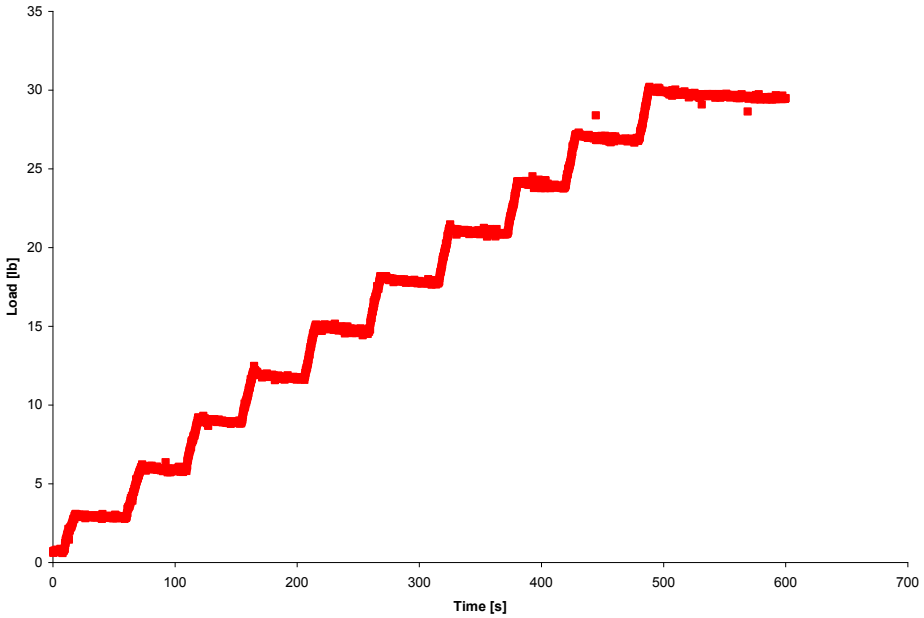

Figure 6.3-13. Initial ten minutes of loading leading up to tomography imaging at approximately 29 lb.

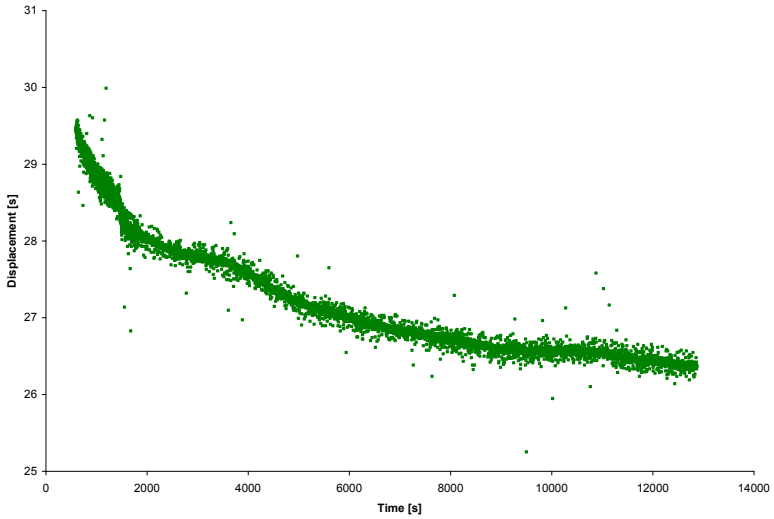

Figure 6.3-14. Relaxation of specimen during tomography imaging.

After the tomography imaging was completed, the specimen was again loaded in steps with an extended observation performed at 42 lb load level (Figure 6.3-15). Maximum achieved load was 54.3 lb

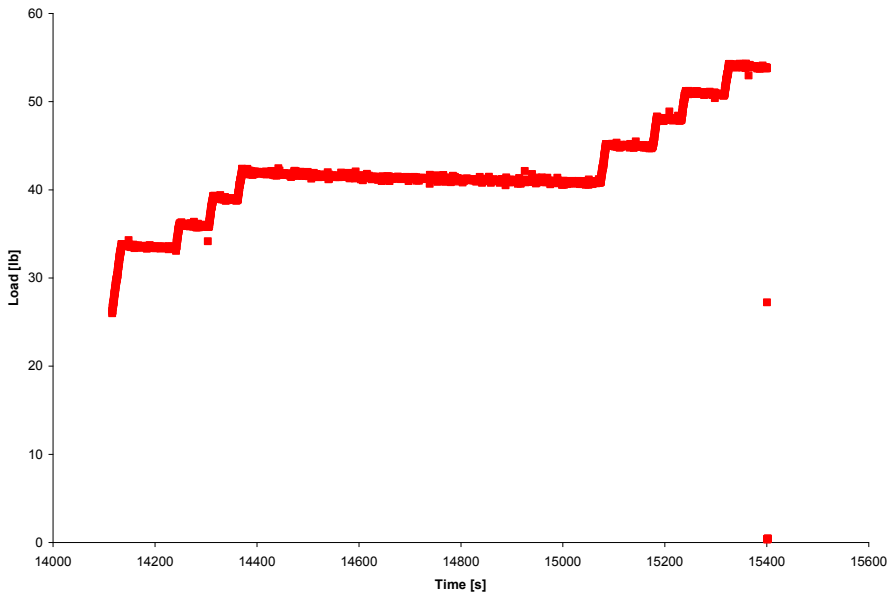

Figure 6.3-15. Loading after tomography taken at 29 lb with extended observation at 42 lb and failure.

Figure 6.3-16 and Figure 6.3-17 show details of x-ray images at no load and at approximately 29 lb. The specimen subjected to load exhibits a crack opening that was not present during the initial imaging before loading. This fact triggered the decision to perform tomography imaging. The quality of reconstruction suffers when the specimen relaxes during imaging as can be seen from Figure 6.3-18 and Figure 6.3-19, however single filaments can still be observed.

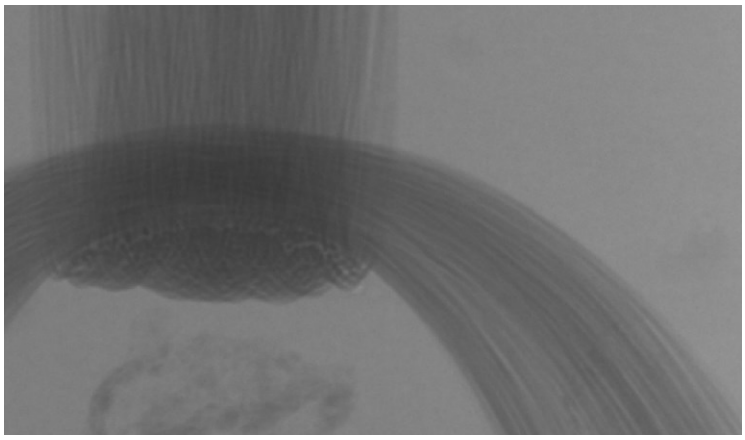

Figure 6.3-16. Detail of x-ray image of sample before loading.

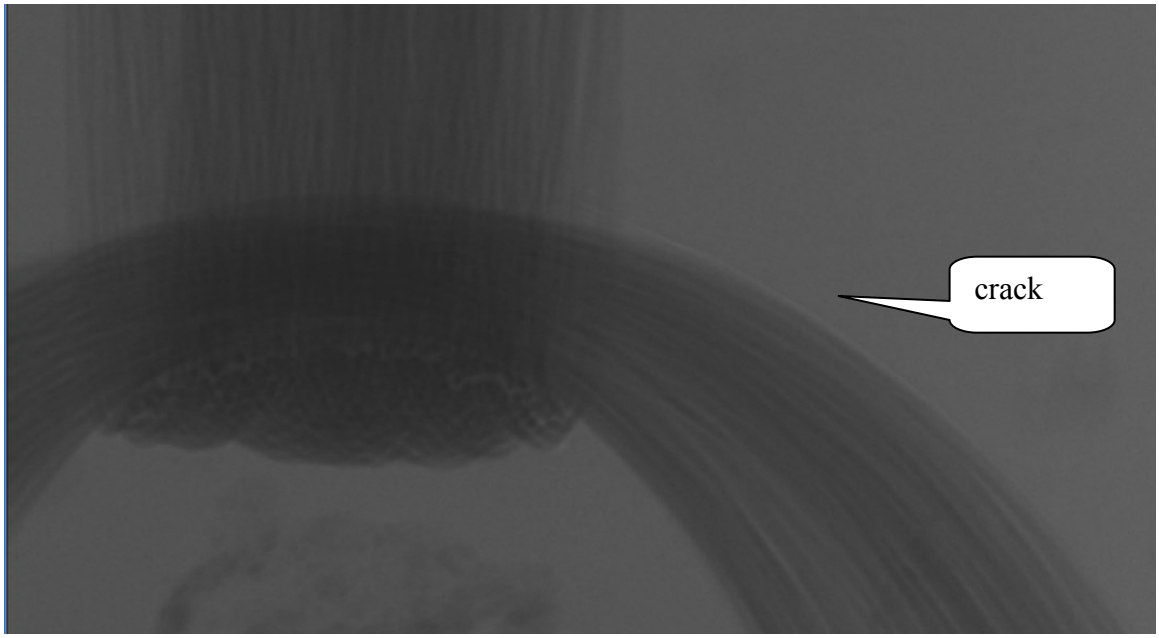

Figure 6.3-17. Detail of x-ray image of sample carrying approximately 29 lb of load.

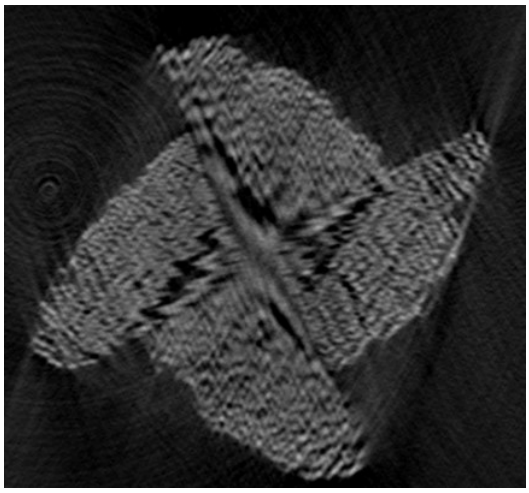

Figure 6.3-18. Detail of tomography reconstruction at no load - horizontal slice of the loop.

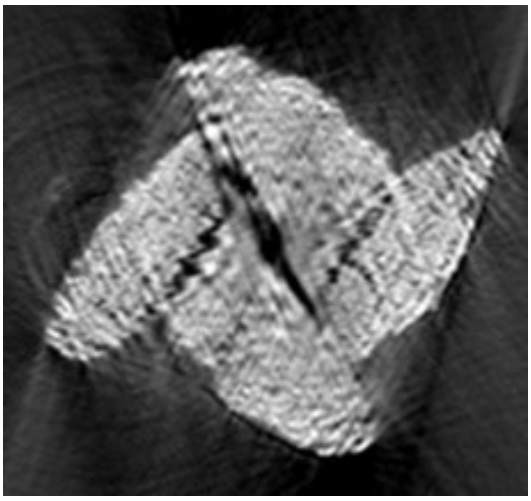

Figure 6.3-19. Detail of tomography reconstruction of sample subjected to load - horizontal slice of the loop.

Figure 6.3-20 and Figure 6.3-21 show slices of tomography reconstructions with no load and with specimen under load respectively. These slices are oriented at approximately 90 degrees to the imaging direction of Figure 6.3-16 and Figure 6.3-17. The crack can be tracked by inspecting multiple slices of the reconstruction.

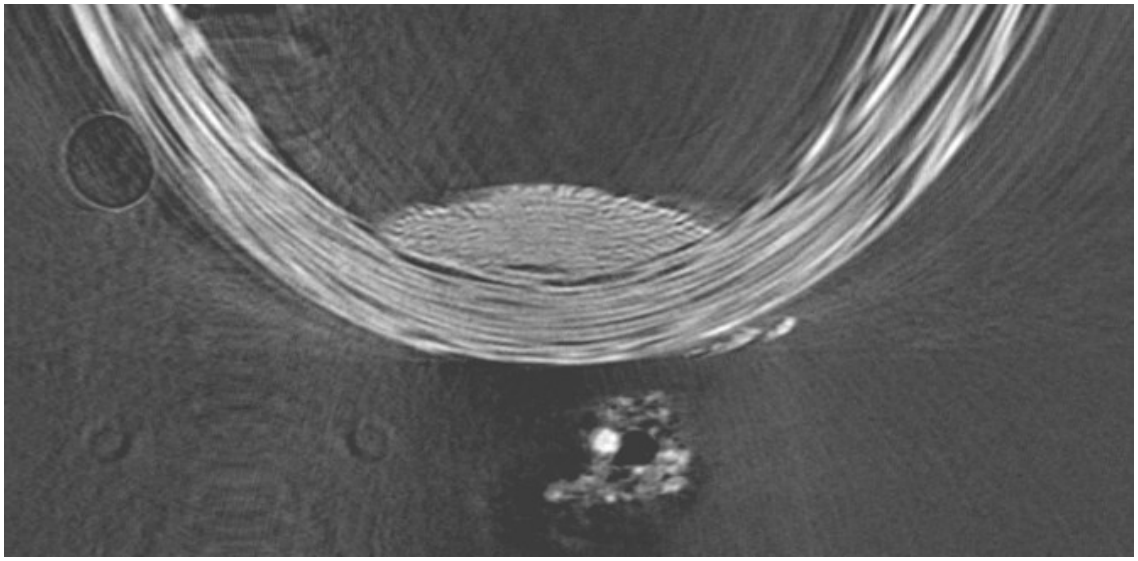

Figure 6.3-20. Vertical slice of tomography reconstruction at no load.

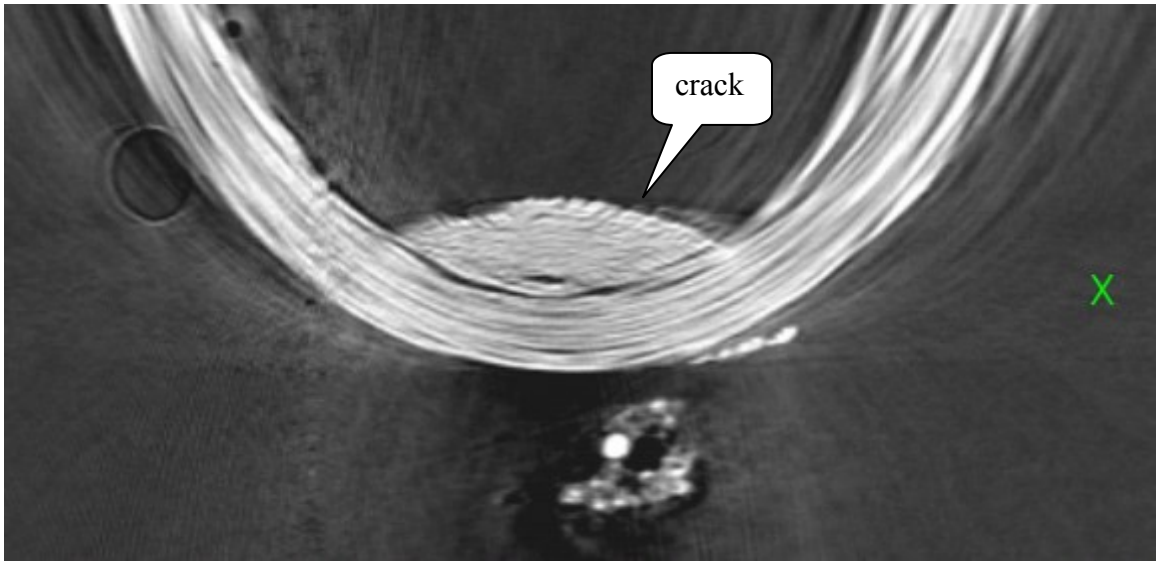

Figure 6.3-21. Vertical slice of tomography reconstruction of specimen under load showing crack within the specimen not observable prior to loading.

Another method of visualizing the internal structure of the sample is to render the tomography reconstruction and highlight certain features. Figure 6.3-22, Figure 6.3-23 and Figure 6.3-24 show rendering of tomography reconstruction of the fiber form at no load, at approximately 29 lb and after failure. This rendering can be achieved by making all parts of the reconstruction invisible with the exception of locations with the most x-ray absorption.

Figure 6.3-22. Rendering of fiber form at no load.

Figure 6.3-23. Rendering of fiber form inside specimen subjected to load.

Figure 6.3-24. Rendering of fiber form after failure.

Figure 6.3-25 and Figure 6.3-26 show rendering of locations with maximum and minimum x-ray transparency. As in previous images, the fiber form is rendered in red, while the areas of maximum x-ray transparency are displayed as blue and green. Air surrounding the cylindrical specimen is clearly visible along with two voids near the specimen rod surface. Closer examination reveals smaller voids and cracks in the vicinity of the fiber form, however these are obscured by reconstruction artifacts. Further work on data processing and visualization is necessary in order for us to clearly separate physical features and reconstruction artifacts.

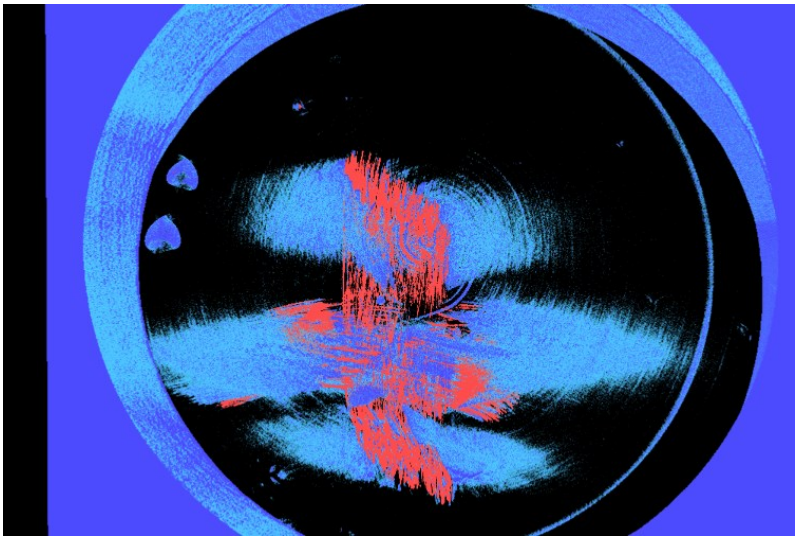

Figure 6.3-25. Rendering of fiber form and voids of specimen at no load, view from the top.

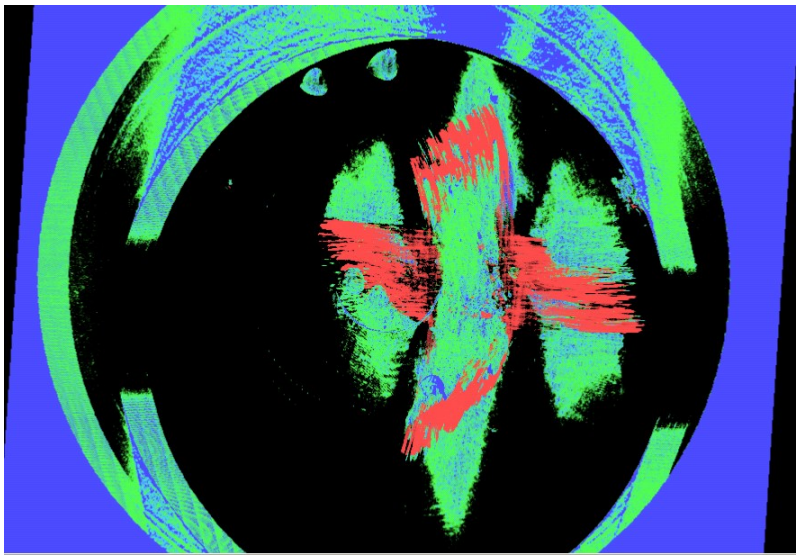

Figure 6.3-26. Rendering of fiber form and voids of specimen subjected to load, view from the top.

Visualization of areas with maximum x-ray transparency of the failed specimen does not yield useful results. Instead, locations with x-ray absorption close to that of the matrix material are visualized in green, while x-ray transparent locations are not viewed. It is possible to visualize crack surfaces of the failed sample using this rendering; however, examination of reconstruction slices provides a more accurate picture of the actual material-air boundary.

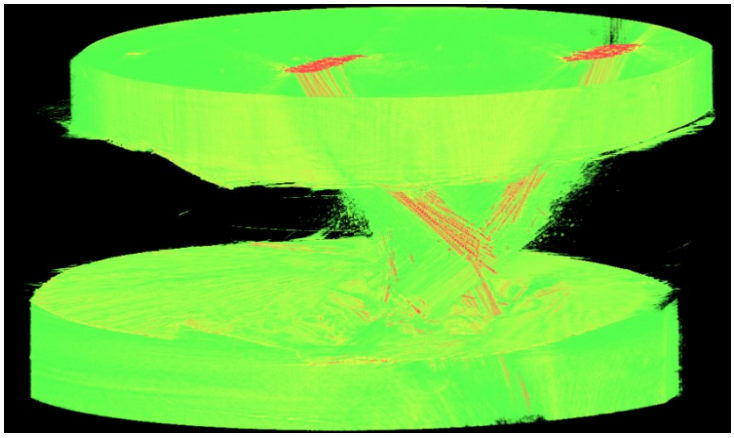

Figure 6.3-27. Rendering of fiber form and matrix after failure.

Figure 6.3-28 shows a selection of reconstruction slices of the failed specimen. The fiber form is clearly visible in light color, while crack surfaces are between the black regions (air) and gray regions (matrix). Examination of reconstruction slices reveals not only the shape of the primary crack surface, but also numerous internal cracks and cracks nearly perpendicular to the primary crack.

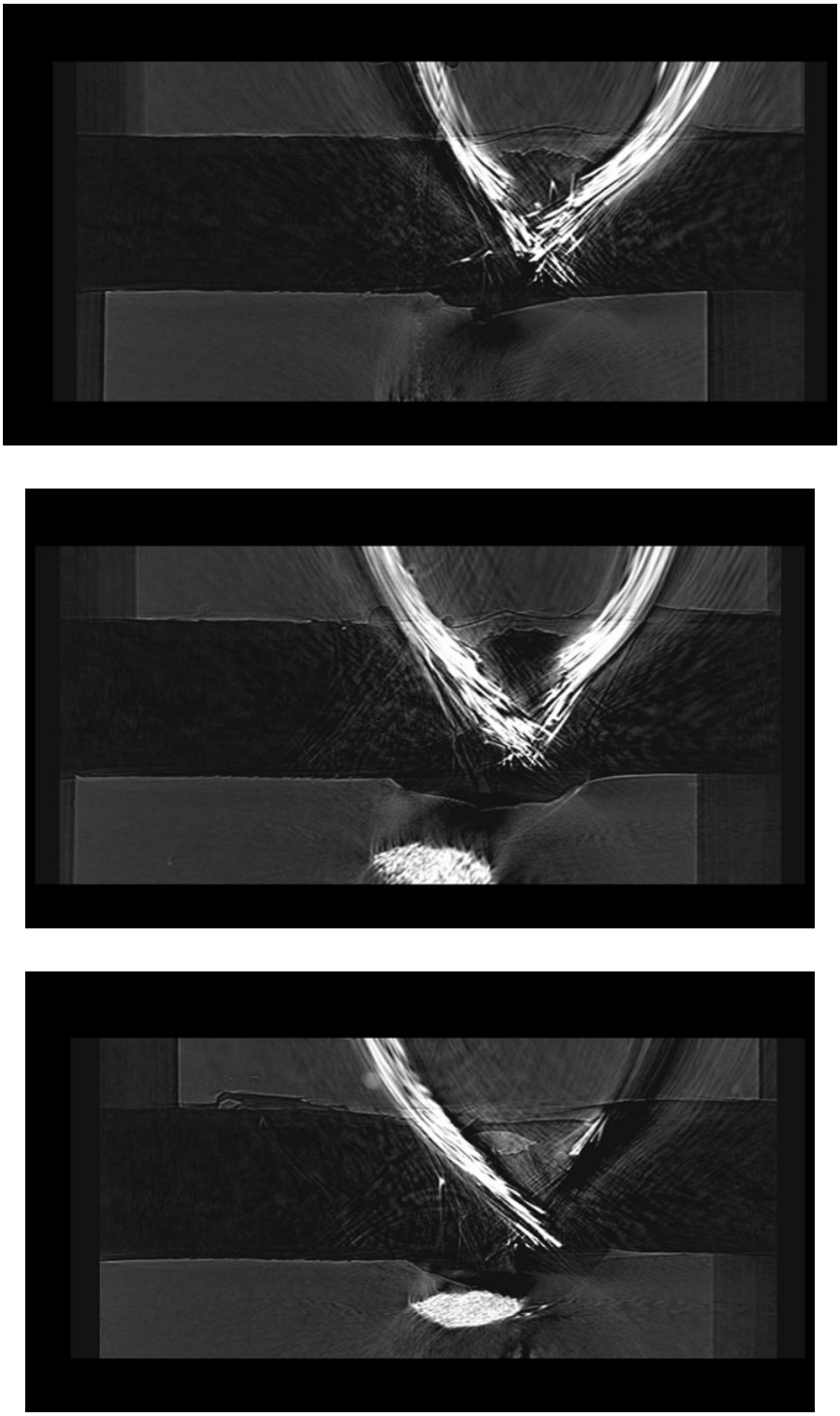

Figure 6.3-28. Selection of slices from a sequence of reconstruction slices showing failed specimen.

6.3.4 Conclusions

Test procedures and manufacturing techniques were developed for model composite specimens tested in a unique testing machine developed by ORNL within an x-ray micro-tomography unit. Three fiber forms were examined with failure occurring within the gage length for one of the fiber forms. Deformations within the material were observed using x-ray imaging as well as tomography reconstructions. Changes in the fiber form, as well as crack development was visualized. Brittle failure at the grips for fiber forms without mold release applied to the fiber tow did not yield useful information about damage processes within the model composite specimen. Samples with tow coated with mold release exhibited observable crack growth prior to failure as well as fiber bridging requiring subsequent loading after initial failure. Internal and exposed crack surfaces formed in various directions with respect to the fiber tow and loading direction. It is believed that the techniques developed and demonstrated in this work can be further developed and utilized to better understand damage meechanisms for a variety of materials and loading situations.

6.3.5 Acknowledgements

This work would not have been possible without funding provided by the Plastics Division of the American Chemistry Council. AGY supplied fibers used in the experiments at no charge.

6.3.6 References

1 Reinhart, T. J. et.al. (1987). *Engineered Materials Handbook Volume 1- Composites.* Metals Park, Ohio: ASM International.
2 Flesher, N. D. (2006). *Crash Energy Absorption of Braided Composite Tubes*. Ph.D. Thesis, Stanford University
3 Alpha Star Inc. (2003). *Genoa User's Manual*. Long Beach, California
4 Dally, J. W., & Riley W. F. (1991). *Experimental Stress Analysis* (3rd ed.). Knoxville, Tennessee: College House Enterprises
5 Gao, J., & Weitsman Y. J. (1998). *The Tensile Mechanical Properties and Failure Behavior of Stitched T300 Mat/Urethane 420 IMR Composite*. (Contract Technical Report). Knoxville, Tennessee: University of Tennessee
6 Glennie, A. M. G. Gulley, T. J. (1985). *Acoustic Emission Modulus Determination and Source Location in Unidirectional Fibre Reinforced Polymer Composites*. J. Acoustic Emission. 170-173.
7 Deng, S., & Weitsman Y.J. (2000). Mechanical Response of Stitched T300 Mat/Urethane 420 IMR Composite Laminates: Property/Orientation Dependence and Damage Evolution. ORNL/TM-2000/103
8 AGY. *Fiberglass Continuous Filament Yarn For the Weaving Industry*. (2007). [On-line] Available: http://www.agy.com/products/eglass/PDFs/TP227LD.pdf
9 Xradia Inc (2005). MicroXCT User's Manual Version 2.0 Issue 1.1.. Concord, California
10 Interface. *Model SML Low Height Load Cell*. (2007). [On-line] Available: http://www.interfaceforce.com/_products/documents/SML_51.pdf

11 National Instruments. *NI Lab View*. (2007). [On-line] Available: http://www.ni.com/labview/
12 Vlastimil Kunc et. al. Development of Coupled Mechanical Testing and Computed X-ray Tomography Unit. publication expected in 2008.

6.4 Tensile Specimen Design and Experimental Procedures for Characterizing Polymeric Composites Using X-Ray Based Micro-Tomography

Vlastimil Kunc, Barbara Frame

Oak Ridge National Laboratory, P.O. Box 2009, Oak Ridge, TN 37831

Ba Nghiep Nguyen

Pacific Northwest National Laboratory, P.O. Box 999, Richland, WA 99352

Scott Case

Virginia Polytechnic Institute and State University, Department of Engineering Science and Mechanics, 225 Norris Hall, Blacksburg, VA

Stephen Young, Dayakar Penumadu

University of Tennessee, Civil and Environmental Engineering, 223 Perkins Hall, Knoxville, TN 37996

ABSTRACT

The recent rapid increase in the use of continuous and chopped fiber composites for automotive, aerospace, and naval applications demands an increased understanding of microstructure evolution with stress in order to understand potential failure locations. X-ray imaging with micro-focus source and optics with high resolution shows promise for exploring such technology to study the microstructure. Initial tomography and radiography results will be presented that clearly show individual fibers and their interface with the resin as a function of tensile stress. In this study, we focus on the design of miniature fiber-reinforced polymer specimens suitable for examination during tensile loading using a micro-tomography system. Issues related to potential stress concentrations and experimental boundary conditions are examined using finite element analysis. Two gripping designs and specimen geometries are examined analytically and experimentally. Specimens with cylindrical cross section with specimen ends bonded to a metallic threaded grip were considered for thermoset materials. Grips containing cavities with cylindrical and conical shapes were also examined. A dog-bone shaped, shoulder loaded, square

cross section sample was considered for thermoplastic materials because of difficulties bonding them to a metallic threaded grip.

KEY WORDS: failure mechanisms, fiber composite materials-glass, optical testing

6.4.1 INTRODUCTION

Processes occurring within stressed material can be observed via x-ray imaging of a sample loaded in a testing machine. Location of internal features can be reconstructed in three dimensions from multiple, and usually a large number, of X-ray images taken at various locations. Such combination of mechanical testing with X-ray imaging and computed tomography can provide valuable insight into processes occurring within a material. A micro-tomography unit built by X-radia [1] was combined with a screw- driven testing machine at ORNL to observe internal deformation of fiber-reinforced polymer composites. Figure 6.4-1 shows an example of miniature sample tested in this setup.

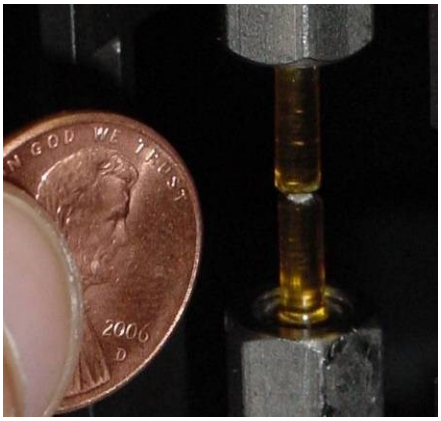

Figure 6.4-1. Miniature tensile sample.

In this particular example, the specimen was designed to observe behavior of two looped tows of glass filaments surrounded by epoxy matrix. An X-ray image of this sample after failure is shown in Figure 6.4-2. The two looped tows with individual filaments are dark, while the epoxy matrix is lighter gray color.

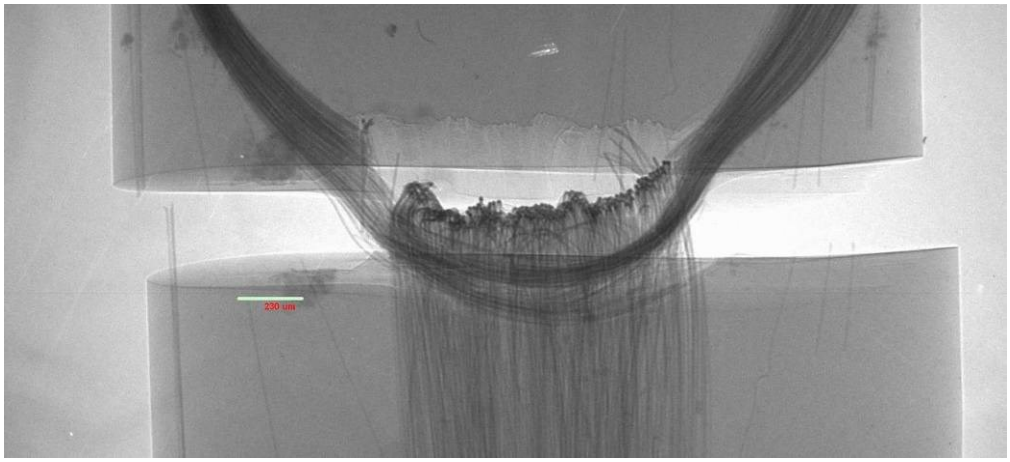

Figure 6.4-2. X-ray of failed miniature sample showing dark glass fibers and gray epoxy.

Figure 6.4-3 shows portion of a slice of reconstruction computed from multiple two-dimensional X-rays. Cross sections of individual fibers are visible in white, while the matrix appears black. Details of the observation can be found in [2].

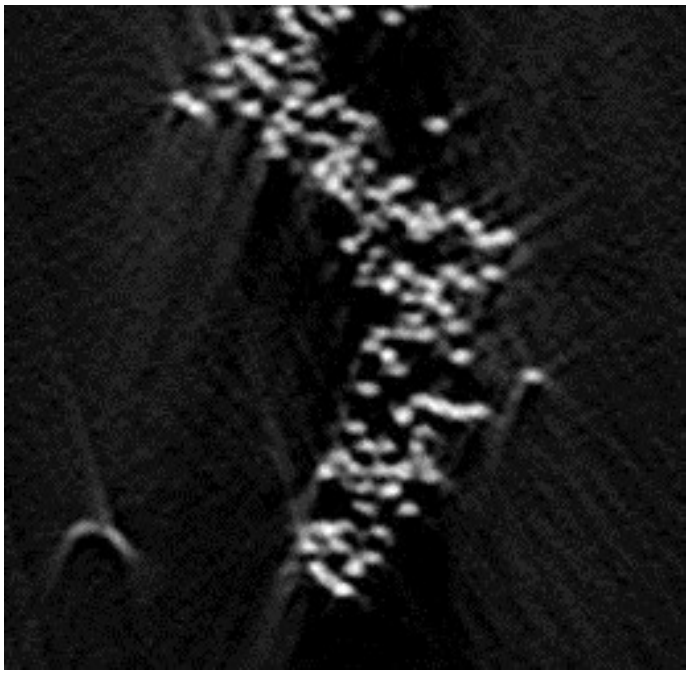

Figure 6.4-3. Reconstruction of filaments within a sample

Similar experiments can be performed at the European Synchotron Radiation Facility in Grenoble [3]. However, systematic design of specimens to study fiber-reinforced polymer composites has not been reported to the knowledge of the authors. Grip failure, significant relaxation and issues with precise dimensions of miniature samples were observed during initial experimentation at ORNL. The purpose of the subsequent discussion is to examine behavior of two specific sample designs that one may want to use in the coupled mechanical testing and X-ray tomography system.

There are two classes of samples that one may consider experimenting with using the system. The first class of samples, which we call "extracted", contains fiber architecture that is determined by manufacturing process, layup sequence, considerations unrelated to performing this experiment. Such samples are extracted from a larger existing structure. The second class of samples, which we call "designed", has fiber architecture specifically designed to observe certain phenomena with this instrument such as the effect of fiber curvature, fiber ends etc. While it would be possible to have single specimen geometry and gripping systems for both classes of samples, it is more convenient to consider two specimen designs which make manufacturing of extracted and designed samples easier.

Initial experiments were performed on both of these sample classes to validate feasibility of testing within the instrument and to uncover any issues that may arise due to gripping. Multiple samples have been manufactured to validate feasibility of manufacturing method and determine the nature of imprecision encountered due to small dimensions of the sample.

6.4.2 EXTRACTED SAMPLE E2-1: DOUBLE DOGBONE SAMPLE FOR HIGH RESOLUTION IMAGING

Figure 6.4-4 shows sample that is considered for study of polymeric composites with discontinuous fiber architecture. Such composites would be produced by injection molding, compression molding, sheet compound molding, programmable powder pre-form processing, spray-up or other techniques that result in quasi-random fiber architecture of discontinuous fibers. These materials are most often used in high volume non-structural or semi-structural applications where detailed understanding of material behavior near its load bearing limit is of little interest. However, understanding of physical behavior under load becomes important when these materials are called upon to absorb energy during accidental impact or are used applied in load bearing situations.

Initial design of the E2-1 specimen was inspired by a miniature SS-3 sheet tensile specimen [4] used for studies of irradiated materials. Specimen shoulder dimensions were replicated so that existing specimens and fixtures could complement the new experimental setup being investigated. Preliminary tests were performed on a dog-bone sample with nearly identical dimensions to that of the SS-3 sample. While there were no apparent gripping issues and specimens failed within the gage length, it was difficult to capture failure of the sample within the field of view of the instrument, because much of the gage length of the sample was outside of the field of view. Moreover, to take advantage of maximum resolution of the instrument, a thinner gage length was necessary so that the entire sample could lie within the field of view.

With these considerations in mind, the double dog-bone geometry E2-1 as shown in Figure 6.4-4 was conceived. The gage length is 1.5 mm and the volume in which observations should be made has a 1x1mm cross section.

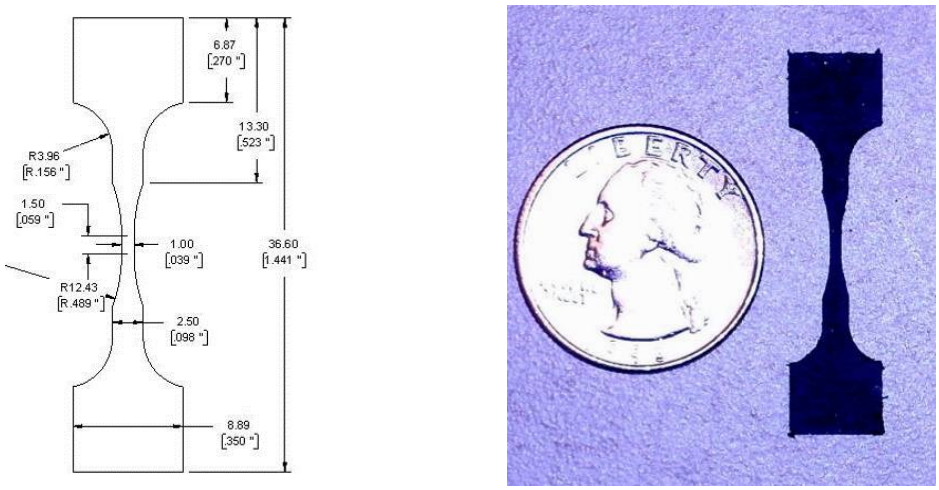

Figure 6.4-4. The miniature double dog-bone tensile specimen E2-1

Figure 6.4-5 shows grips used for these specimens and that fit the instrument. Note that these grips were designed to accommodate samples thicker than E2-1 and that the sample has to be offset from the backside of the grip so that the gage length of the sample can be rotated around the axis of the instrument. This is easily accomplished by adding layers of thin aluminum tape to the backside of the grip.

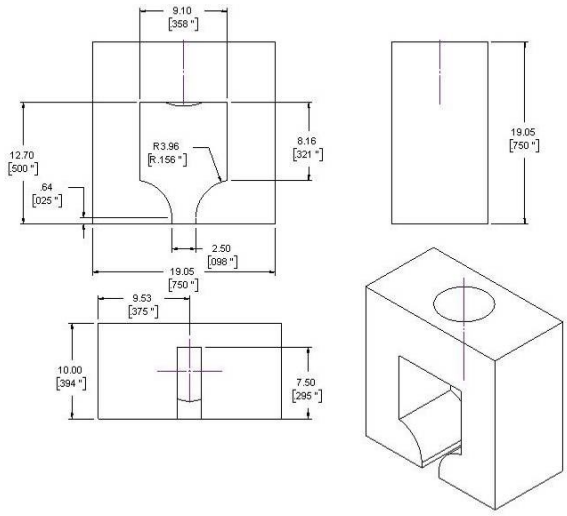

Figure 6.4-5. Grips for extracted samples.

Preliminary tests with this type of sample have shown significant load shedding during pauses in loading for imaging. A pause for a single X-ray lasts approximately 10 seconds, while a pause for tomography imaging lasts approximately 3 hours. It was unclear whether the load shedding was caused by relaxation of material in the gage length, relaxation of material in the grip region, sliding of the sample over the grip faces or due to other factors. It was also difficult to determine whether shoulder radius of the sample and the grip is the same and whether this mismatch played a significant role in the load shedding. Finite element analysis was used to estimate the effect of mismatch on load-displacement behavior and on load shedding during pauses.

6.4.3 FINITE ELEMENT ANALYSIS OF E2-1 SAMPLE

Loading of the E2-1 sample was modeled using finite element analysis. Abaqus 6.7-1 by Dassault Systems [5] was used to perform analysis involving contact between the grip and the sample. The grip was modeled as a rigid body, while the sample was modeled as a deformable solid with visco-elastic material properties. It was necessary to model only one-eighth of the geometry due to symmetry in the system, as shown in Figure 6.4-6. Frictionless contact was assumed between the grip and the specimen.

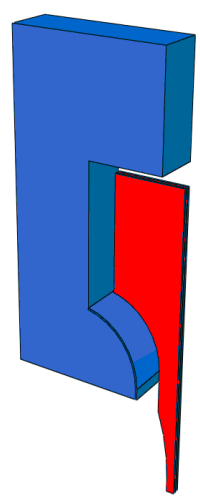

Figure 6.4-6. Assembly of grip and sample (shown in red) for finite element analysis.

It was assumed that material behavior can be adequately represented in this study by using isotropic elastic properties with power law creep model. $\dot{\bar{\varepsilon}} = A\tilde{q}^n t^m$, where $\dot{\bar{\varepsilon}}$ is the uniaxial equivalent creep strain rate, $\tilde{q}$ is the equivalent deviatoric stress, t is total time, A, n, and m are constants. The value of the constant n was assumed to be 1, while the constants A and m have been estimated using power-law fit of results from creep experiments performed on full size specimens (Figure 6.4-7) and taking a derivative with respect to time to obtain the desired rate form. Injection molded long glass fiber with a polypropylene matrix is considered in this section [6]. It should be noted that simplifying assumptions on material behavior were selected to

eliminate unnecessary modeling complexity. Different assumptions would be appropriate if the goal of the study was to accurately predict behavior of a particular material.

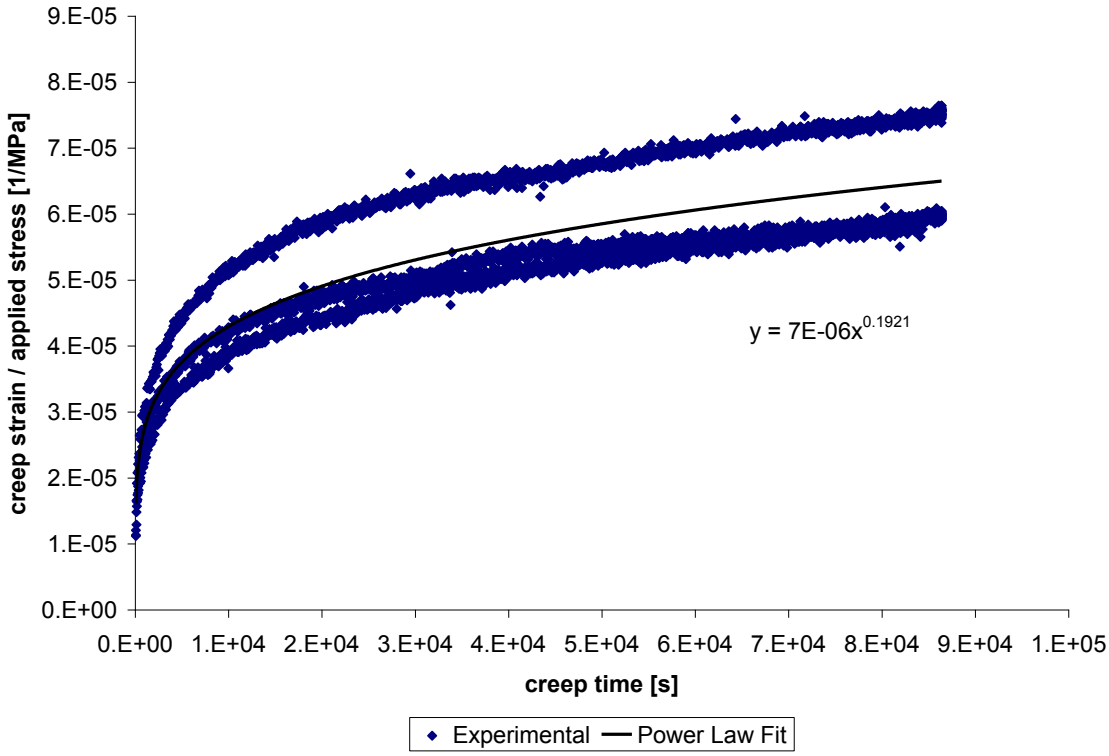

Figure 6.4-7. Power law fit of results from creep experiments for glass/polypropylene injection molded material.

The following constants were used for the analysis:

Young's modulus: E = 7.015 GPa

Poisson's ration: $\nu = 0.34$

Power-law creep constants with Pa as the unit of stress:

$$A = 1.345 \cdot 10^{-7}$$

$$n = 1$$

$$m = -0.8079$$

Manufacturing of precise grip-face radius is challenging on the E2-1 specimen, especially when the composite contains thermoplastic matrix. The effect of possible mismatch between the radius of the grip and radius of the specimen was studied by holding the grip radius constant at 3.96

mm and varying the radius on the specimen. Figure 6.4-8 shows Von-Mises stress contours in the model as a result of contact between the face of the grip and the sample, when 40N of tensile load is applied to the grip. In the calculations, instantaneous load application with no visco-elastic effects is assumed. The maximum von Mises stress within the sample and corresponding displacement of the grip that would be observed in experimental setup is also reported in Figure 6.4-8. It is assumed that one grip remains stationary, while the other grip moves. It is apparent that the location of maximum von Mises stress varies depending on the radius mismatch and it occurs in the specimen gage length only for perfect match of radii.

Radius	Radius	Radius	Radius	Radius
3.60 mm	3.80 mm	3.96 mm	4.20 mm	4.40 mm
Max Stress	Max Stress	Max Stress	Max Stress	Max Stress
1.63E+02 MPa	9.07E+01 MPa	4.10E+01 MPa	5.97E+01 MPa	6.73E+01 MPa
Grip Displacement	Grip Displacement	Grip Displacement	Grip Displacement	Grip Displacement
1.03E-01 mm	9.54E-02 mm	9.66E-02 mm	2.22E-01 mm	2.60E-01 mm

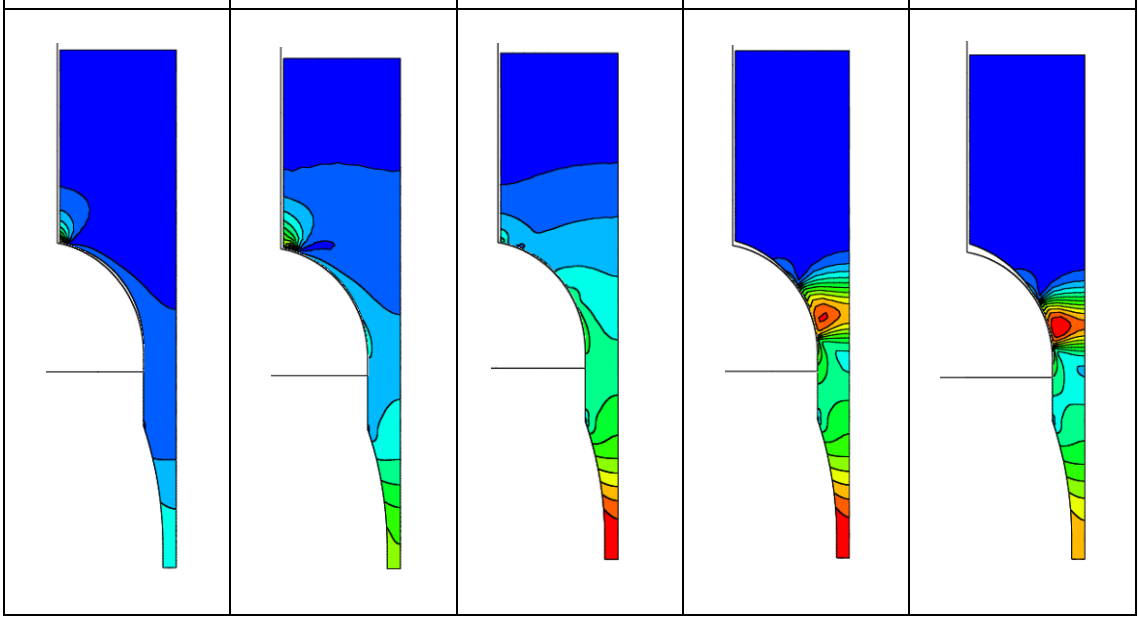

Figure 6.4-8. Contour plots of Von-Mises stress within E2-1 with corresponding shoulder radius, maximum Von-Misses stress and grip displacement.

Table 6.4-1 summarizes results of this static analysis. From this, we see that apparent sample stiffness decreases significantly as the shoulder radius of the sample increases. Therefore judgments on material performance should not be made based on load-displacement behavior

observed during experiments. The stress concentration factor increases significantly as the radius of the shoulder decreases. For the case of perfect radius match, the stress realized in the E2-1 sample is just three percent higher than an idealized straight bar under uniaxial tension.

Table 6.4-1. Results of static analysis for E2-1 specimen

Shoulder Radius [mm]	Nominal Stress [MPa]	Max. Von-Mises Stress [MPa]	Grip Displacement [mm]	Apparent Stiffness [Mpa/mm]	Stress Concentration Factor
3.60	40	163	.103	387	4.08
3.80	40	90.7	.095	419	2.27
3.96	40	41.0	.097	414	1.03
4.20	40	59.7	.220	180	1.49
4.40	40	67.3	.260	154	1.68

Shedding of load during pauses in loading for imaging was observed during initial experiments. These losses were significant during pauses for tomography imaging lasting approximately three hours. Table 6.4-2 summarizes results of viscoelastic analysis where the grip position was held constant for eleven thousand seconds. Loss of load increases with radius mismatch and maximum value of von Mises stress decreases and the locations of maximum stress remain the same. The gage length between the inner radii of the E2-1 sample contracts for shoulder radius smaller than that of the grip and expands for larger sample shoulder radii. Therefore no conclusions on material time-dependent behavior should be drawn directly from optical strain measurement during the test. The creep strain within the gage length clearly increases throughout the test because the sample remains loaded; however, deformation within the gage length reflects behavior of the sample and not the material. In addition, deformations of several microns may cause problems for the tomography reconstruction algorithm. It was experimentally observed that reconstruction is possible for samples under load, however its quality decreases.

Table 6.4-2. Results of visco-elastic analysis for E2-1 specimen.

Shoulder Radius [mm]	Grip Load Loss [%]	Max. Stress Decrease [%]	Gage Length Deformation [mm]
3.60	2.40E-02	2.63E-02	-1.74E-06
3.80	2.41E-02	2.50E-02	-4.00E-07
3.96	2.37E-02	2.36E-02	1.54E-06
4.20	2.41E-02	2.13E-02	5.32E-06
4.40	2.41E-02	2.38E-02	5.10E-06

6.4.4 DESIGNED SAMPLE D2-3:

Figure 6.4-9 shows Sample D2-3, that can be used to test fiber architectures designed for a specific purpose. An example of such architecture is given in the introduction of this paper and details are discussed in [2].

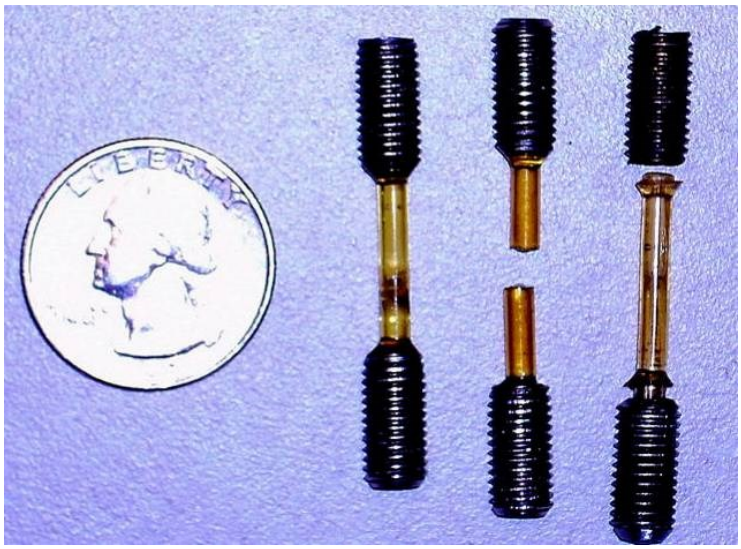

Figure 6.4-9. D2-3 samples (from left to right) untested, failed in gage length, grip failure and pull-out.

The sample is made by bonding a cylindrical sample rod inside a threaded steel grip that contains a cavity. It was experimentally determined that if this cavity is a right circular cylinder, the sample rod pulls out of the steel grip and any attempts to increase adhesion between the sample rod and the grip are not productive. Methods for mechanical locking were subsequently evaluated experimentally and a design with a conical cavity was viewed as the most promising. It is apparent from the sample pull-out observed in Figure 6.4-9 that the gripping issue has not been fully resolved.

6.4.5 FINITE ELEMENT ANALYSIS OF D2-3 SAMPLE

Loading of the D2-3 sample was modeled using finite element analysis. Once again, Abaqus 6.7-1 by Dassault Systems [5] was used to perform analysis involving contact between the grip and the sample. A two-dimensional axisymmetric analysis was performed on half of the sample due to symmetry (Figure 6.4-10). Both the grip and the sample rod were modeled as deformable bodies; however the deformation of the grip can be neglected. Since the primary issue for this sample as observed experimentally is the predominance of grip failures and grip pull outs, the effect of angle of the conical cavity on the performance of the sample was examined. Angles of 1^0,3^0,5^0 and 7^0 were investigated. Internal features of the specimen rod were neglected and linear elastic, isotropic properties of generic epoxy were assumed:

Young's modulus: E = 3.7 GPa

Poisson's ratio: ν = 0.34

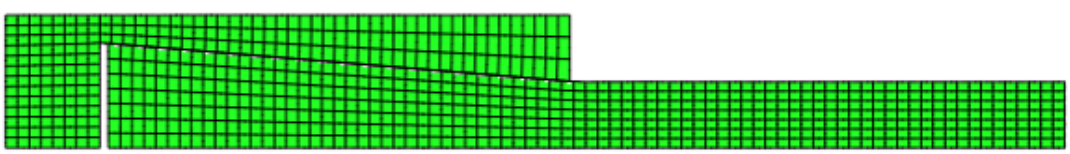

Figure 6.4-10. Mesh of axisymmetric model of D2-3 specimen.

A tensile load of 487 N was applied to the grip, resulting in a nominal applied stress of 68.9 MPa. First, perfect adhesion was assumed between the specimen rod and the grip. The maximum stress occurred at the junction of the specimen rod and the grip at the location where the cylindrical section of the specimen ends and conical section begins (Figure 6.4-11). Table 6.4-3 shows a summary of pertinent results. The calculated stress concentration factor ranges from 2.53 to 2.86. Therefore, a well- prepared D2-3 specimen should contain an internal feature within the gage length that results in a stress concentration factor of 2.9 or more if one wishes to observe the failure in the gage length.

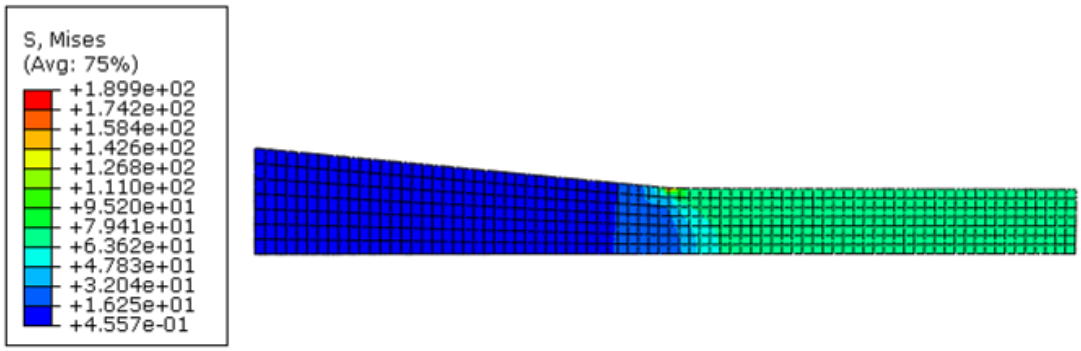

Figure 6.4-11. von Mises stress in a D2-3 specimen rod with perfect adhesion.

Table 6.4-3. Results of analysis for D2-3 specimen with perfect adhesion

Angle	Nominal Stress [MPa]	Max. von-Mises Stress [MPa]	Stress Concentration Factor
1	6.89E+01	1.74E+02	2.53
3	6.89E+01	1.78E+02	2.58
5	6.89E+01	1.90E+02	2.75
7	6.89E+01	1.97E+02	2.86

The second analysis assumed no adhesion between the specimen rod and the grip, therefore the transfer of load between the grip and the specimen rod occurs only due to mechanical locking. Frictionless contact was used to model this condition. Figure 6.4-12 shows a gap that develops between the end to the specimen rod and the grip. Table 6.4-4 provides a summary of the results.

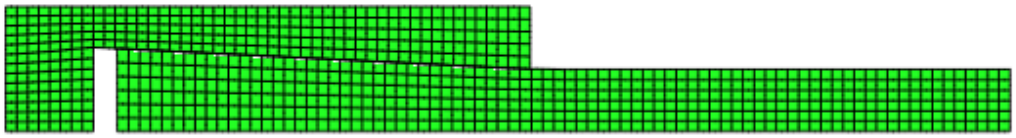

Figure 6.4-12. Pull-out gap in D2-3 specimen with no adhesion between the specimen rod and grip subjected to tensile load.

The specimen rod with 1^0 angle pulls out of the grip, before the applied load reaches 487 N. The gap becomes progressively smaller as the angle increases. The stress concentration factor reached at the fully loaded state decreases as the angle increases. The stress concentration factor for 5^0 and 7^0 specimens is smaller for samples with no interfacial bond, rather than for perfectly bonded interface. This result suggests that the specimen may either fail at the grip upon reaching a critical load or it can slide through the grip, before re-loading to higher level. This is consistent with experimental observations.

Table 6.4-4. Results of analysis for D2-3 specimen with no adhesion

Angle	Pull-out Gap [mm]	Max. von-Mises Stress [MPa]	Stress Concentration Factor
1	infinity	N/A	N/A
3	5.52E-01	2.39E+02	3.47
5	1.86E-01	1.59E+02	2.31
7	9.35E-02	1.54E+02	2.23

6.4.6 CONCLUSIONS

Analyses for two sample designs of miniature specimens has been presented. For double-dogbone specimens E2-1 with time-dependent material properties, care must be taken to separate the effects of specimen geometrical imperfections from material effects. Relaxation of the specimen may negatively influence reconstruction performed under load. Analysis of the D2-3 specimen confirmed experimentally observed behavior of the specimen. Internal features of the D2-3 specimen must produce a stress concentration of at least 2.9 if failure is to occur in the gage length due to this feature.

6.4.7 ACKNOWLEDGEMENT

This research was sponsored by the U.S. Department of Energy, Assistant Secretary for Energy Efficiency and Renewable Energy, Office of Vehicle Technologies, as part of the Automotive Lightweighting Materials Program, under contract DE-AC05-00OR22725 with UT-Battelle, LLC.

6.4.8 REFERENCES

1. Xradia Inc. MicroXCT User's Manual Version 2.0 Issue 1.1 Concord, California, 2005.
2. V. Kunc, D.L. Erdman, B.J. Frame, R.E. Norris. Observation of Composite Materials Using Coupled Mechanical Testing and Computed Tomography. Proceedings of the SEM World Congress. 2008. Orlando, FL.
3. D.R. Aroush, E. Marie, C. Gauthier, S. Youssef, P. Cloetens, H.D. Wagner. A Study of Fracture of Unidirectional Composites Using in Situ High-Resolution Synchotron X-ray microtomography. Composites Science and Technology. 2006. 66, 1248-1353.
4. R.L. Klueh. Miniature Tensile Test Specimens for Fusion Reactor Irradiation Studies. Nuclear Engineering and Design/Fusion 2 (1985). North-Holland, Amsterdam. 407-416.
5. Dassault Systemes, Abaqus User's Manual 2008. 6.7-1.
6. B.N. Nguyen, V. Kunc, J.H. Phelps, C.L. Tucker III and S.K. Banapalli. Prediction of the Elastic-Plastic Stress-Strain Response for Injection Molded Long Fiber Thermoplastics. Journal of Composite Materials. 2008, submitted.

Blank Page

6.5 On Fiber Curvature Measurements From Non-Elliptical Cross-Sections

Vlastimil Kunc[1], Srdjan Simunovic[1], Scott W. Case[2]

Oak Ridge National Laboratory, PO Box 2008 MS6053, Oak Ridge, TN 37831-6053, USA

Virginia Polytechnic Institute and State University, Engineering Science & Mechanics, 225-A Norris Hall, Blacksburg, VA 24061, USA

Corresponding Author:

Vlastimil Kunc, kuncv@ornl.gov,Tel. 001 865 574 8010, Fax. 001 865 574 8257, Oak Ridge National Laboratory, PO Box 2008 MS6053, Oak Ridge, TN 37831-6053, USA

Author contact information:

Vlastimil Kunc: kuncv@ornl.gov, Srdjan Simunovic: simunovics@ornl.gov, Scott W. Case: scase@vt.edu

Abstract

In this paper we present a new measurement technique for fiber curvature measurements in composites containing quasi-random fiber architecture. In this technique, fiber orientation and fiber curvature are determined from a fiber cross-section. Specifically, fiber curvature is determined based on the deviation of the cross-section outline from an elliptical shape. The spatial resolution necessary for the measurement of the fiber curvature distribution for an ensemble of fibers is determined. It is demonstrated that while curvature of individual filaments can be measured in a range of sectioning plane orientations, the measurement of fiber curvature distribution using optical microscopy would require a large number of sections. An example is provided for injection molded plaques with polypropylene (PP) and 40% of long glass fibers by weight.

Keywords

Composites, Micro-mechanics, Injection Molding

6.5.1 Introduction

The desire to improve the strength and stiffness of injection molded thermoplastic parts leads to an increased use of fiber reinforced materials with large fiber aspect ratio. For design purposes, the ability to predict the behavior of long fiber thermoplastic (LFT) materials requires accurate representation and prediction of the microstructure. Many research efforts in the area of injection molded LFTs modified existing definitions and models used for short fiber thermoplastic (SFT) materials. While this is a logical approach, we argue that the assumption of fibers being straight cylinders is applicable only to SFTs but not to LFTs with significantly larger aspect ratio. The aspect ratio, defined as fiber length divided by fiber diameter, in LFTs is on the order of 10^2 and

10^3, resulting in a situation where fibers do not remain in the form of straight cylinders in injection molded parts. While this fact has been recognized in the past by researchers attempting to generate models for flows containing suspended long fibers [14, 72, 73], quantitative experimental data describing the curvature has not yet been presented in the literature (to the knowledge of the so, would authors).

The method presented in this paper provides not only fiber curvature, but also fiber orientation in a manner consistent with a standard method of ellipses [56-58]. The authors have experimented with multiple methods of fiber microstructure measurements including methods providing three dimensional information such as x-ray tomography [12, 13] or neutron imaging[4]. X-ray tomography provides great qualitative information about the microstructure, especially for glass fibers, however noise in the data and reconstruction artifacts have prevented us from generating results for statistically significant number of fibers with an automated method. The contrast between carbon fibers and thermoplastic polymers also limits the use of this technique for carbon fiber filled materials, which are gaining popularity in the industry. Neutron tomography can be used for carbon fiber filled materials, however the physical equipment necessary for these experiments is currently scarce, which eliminates this technique from consideration for broad applicability.

Since method of ellipses has been developed and refined for many years for both glass and carbon fiber composites, its modification to measure fiber curvature potentially provides a useful tool for researchers and engineers in the field at minimum capital expense. Experimental data presented herein were obtained using an optical microscope; however, as we will demonstrate, the technique will work and could be enhanced by the use of a scanning electron microscope.

We start our discussion by presenting assumptions about the shape of fibers. Then we provide mathematical model of a curved fiber as well as its cross sections when intersected by an arbitrarily oriented plane. The limitations of the technique are established from analysis of sensitivity of results to spatial resolution of experimental data. We then describe physical preparation and imaging of composite sample and describe procedure by which we obtain fiber orientation and fiber curvature data. Then we apply this technique to injection molded plaque molded with commercially available polypropylene and glass fibers.

6.5.2 Fiber orientation and fiber curvature definitions.

The orientation of single fiber has been traditionally described by orientation vector **p**, which is aligned with the axis of the fiber, where the shape of the fiber is assumed to be a cylinder as shown in Figure 6.5-1 [7, 8, 56, 58, 74-76].

---

[4]The authors performed exploratory tests with carbon fiber reinforced composites at Spallation Neutron Source and High Flux Isotope Reactor of Oak Ridge National Laboratory concluding that currently available spatial resolution does not allow detection of individual filaments within the composite.

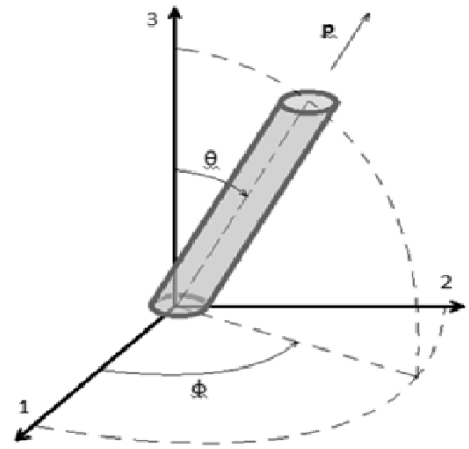

Figure 6.5-1. Standard assumption about fiber shape and definition or angles defining orientation vector **p**.

In this work, we assume that the fiber is in the shape of a section of a toroid. While the magnitude of curvature of such fiber is the same at any point along its centerline, the orientation vector **p** and curvature vector **q** depend on the location along the centerline. The measurement technique presented below generates orientation and curvature vectors at a point of intersection with a sectioning plane as shown in Figure 6.5-2 .

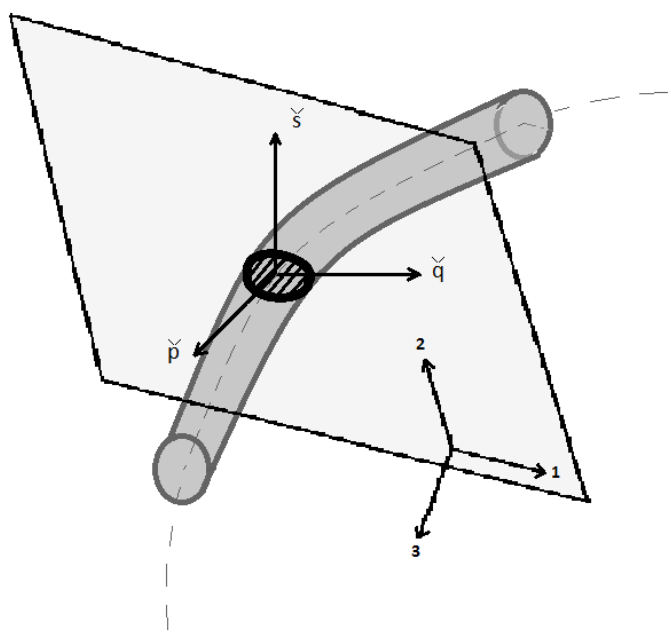

Figure 6.5-2. Non-elliptical cross section formed by intersection of toroid with an arbitrary plane.

In Figure 6.5-2, vector $\breve{\boldsymbol{p}}$ is a tangent to fiber centerline and vector $\breve{\boldsymbol{q}}$ points to the center of curvature with $\breve{\boldsymbol{s}}$ completing the right handed coordinate system at the intersection of the centerline with a plane. Given sufficient sample size, our method provides full information about the fiber orientation and curvature. Because the location of the sectioning plane is arbitrary, we measure fiber orientation and curvature with equal probability at any point along the centerline. If the radius of curvature is very large for fibers in the sample, the local shape of the fiber approaches that of a cylinder and this new method produces results identical to the method of ellipses.

We start by describing the coordinates **c** of the fiber centerline as a toroid arbitrarily oriented in space

$$\mathbf{c}(\alpha,\beta,\gamma,R,t) = \boldsymbol{R^z}(\alpha)\boldsymbol{R^y}(\beta)\boldsymbol{R^x}(\gamma)\mathbf{g}(R,t) \tag{6.5-1}$$

where **g** is parametric representation of a toroid

$$\mathbf{g} = (R\,\mathrm{Cos}(t), R\,\mathrm{Sin}(\mathrm{t}) + R, 0);\;\; R > 0, \qquad t \le 0 < 2\pi \tag{6.5-2}$$

and where R is the radius of the toroid and t is a parameter. The arbitrary orientation of the toroid is achieved through three successive rotations described by

$$\boldsymbol{R^x} = \begin{bmatrix} 1 & 0 & 0 \\ 0 & \cos\gamma & \sin\gamma \\ 0 & -\sin\gamma & \cos\gamma \end{bmatrix}, \boldsymbol{R^y} = \begin{bmatrix} \cos\beta & 0 & \sin\beta \\ 0 & 1 & 0 \\ -\sin\beta & 0 & \cos\beta \end{bmatrix}, \boldsymbol{R^z} = \begin{bmatrix} \cos\alpha & \sin\alpha & 0 \\ -\sin\alpha & \cos\alpha & 0 \\ 0 & 0 & 1 \end{bmatrix} \tag{6.5-3}$$

with the following limits on the on the rotations:

$$0 \le \alpha < 2\pi;\;\; -\frac{\pi}{2} \le \beta < \frac{\pi}{2};\;\; 0 \le \gamma < 2\pi \tag{6.5-4}$$

The parametric representation of the toroid can then be written as

$$\boldsymbol{\tau}(\alpha,\beta,\gamma,R,r,t,u) = \mathbf{c}(\alpha,\beta,\gamma,\mathrm{R},\mathrm{t}) + \mathbf{A}(\alpha,\beta,\gamma)\mathrm{h}(r,u) \tag{6.5-5}$$

where **h** is the parametric representation of the circular shape of the fiber

$$\mathbf{h} = (0, r\,\mathrm{Cos}(u), r\,\mathrm{Sin}(u))\ ; \quad \mathrm{u} \leq 0 < 2\pi \tag{6.5-6}$$

and **A** is the matrix of unit vectors of a moving frame along the centerline

$$\mathbf{A} = [\breve{\boldsymbol{p}}, \breve{\boldsymbol{q}}, \breve{\boldsymbol{s}}] \tag{6.5-7}$$

where

$$\breve{\boldsymbol{p}} = \frac{\dot{\mathbf{c}}}{\|\dot{\mathbf{c}}\|}, \breve{\boldsymbol{q}} = \frac{(\dot{\mathbf{c}}\dot{\mathbf{c}})\ddot{\mathbf{c}} - (\dot{\mathbf{c}}\ddot{\mathbf{c}})\dot{\mathbf{c}}}{\|\dot{\mathbf{c}}\|\|\dot{\mathbf{c}}\ \mathbf{x}\ \ddot{\mathbf{c}}\|}, \breve{\boldsymbol{s}} = \frac{\dot{\mathbf{c}}\ \mathbf{x}\ \ddot{\mathbf{c}}}{\|\dot{\mathbf{c}}\ \mathbf{x}\ \ddot{\mathbf{c}}\|} \tag{6.5-8}$$

and where $\dot{\mathbf{c}} = \frac{d\mathbf{c}}{dt}$, $\ddot{\mathbf{c}} = \frac{d\dot{\mathbf{c}}}{dt}$. (The double bars $\|\ \|$ indicate the norm of a vector and **x** denotes the cross product between two vectors). Note that **A** is independent of *R* and *t* for our specific definition of centerline **c**.

To obtain the parametric representation of the toroid cross-sections with the x-y plane, we solve equation

$$\tau_3 = 0 \tag{6.5-9}$$

for the parameter *t* and substitute the expected two solutions into expressions for τ_1 and τ_2. To allow the cross-section to appear anywhere in the x-y plane, we add arbitrary constants to the two non-zero coordinates and write the final expressions for the cross sections. We have therefore obtained two parametric solutions for the cross sections in the following form

$$\mathbf{k}_i(\alpha, \beta, \gamma, r, \rho, \mathrm{u}) = \mathbf{q} + r\,\hat{\mathbf{k}}_i(\alpha, \beta, \gamma, \rho, \mathrm{u}) \qquad i = 1,2 \tag{6.5-10}$$

where $\boldsymbol{q}$ is the vector of arbitrary constants

$$\mathbf{q} = (\mathrm{x}_c, \mathrm{y}_c, 0) \tag{6.5-11}$$

and the non-dimensional parameter of curvature ρ is defined as

$$\rho = \frac{r}{R} \tag{6.5-12}$$

We do not list the full form of $\bar{\mathbf{k}}$ due to space limitations. The two solutions $\mathbf{k_1}$ and $\mathbf{k_2}$ represent either two distinct cross-sections, one of which is located over the origin, or both solutions represent separate sections of a single cross-section. As ρ approaches zero, the cross sections become nearly elliptical. A single solution for a cross section of a straight fiber with the x-y plane can be written as

$$\bar{\mathbf{k}}(\alpha, \beta, \gamma, r, \mathrm{u}) = \mathbf{q} + r\,\bar{\bar{\mathbf{k}}}(\alpha, \beta, \gamma, u) \tag{6.5-13}$$

where

$$\bar{\bar{\mathbf{k}}} = -(\cos(u+\gamma)\sin(\alpha) + \cos(\alpha)\csc(\beta)\sin(u+\gamma), \csc(\beta)\sin(\alpha)\sin(u+\gamma) - \cos(\alpha)\cos(u+\gamma), 0) \tag{6.5-14}$$

The reader should note that the coordinates of the ellipse are independent of γ and that the angles α and β correspond to standard definition of fiber orientation vector **p** with components

$$\begin{aligned} p_1 &= \cos\alpha\cos\beta = \cos\phi\sin\theta \\ p_2 &= \sin\alpha\cos\beta = \sin\phi\sin\theta \\ p_3 &= \sin\beta = \cos\theta \end{aligned} \tag{6.5-15}$$

Therefore measurements performed on composite with straight or nearly straight fibers will generate fiber orientation results identical to one obtained by previously reported methods [56, 58]. We can now discuss how we obtain $\alpha, \beta, \gamma, r, \rho$ for each fiber cross section in a physical sample.

6.5.3 Limits on Physically Achievable Measurements

The measurement of fiber orientation from nearly circular fiber cross-sections results in greater error compared to measurements from elongated ellipses [56]. Similarly, determining fiber curvature is easier from elongated fiber cross sections. We will show in this section that our ability to distinguish curved fiber is dependent several parameters. We define two measures for deviation of the measured profile and calculated profile that best fits the measured profile. First measure describes average deviation of N discrete points along the boundary

$$\bar{\delta} = \frac{1}{N}\sum_{i=1}^{N} \left\| \boldsymbol{x_i} - \underline{\boldsymbol{k_i}} \right\| \tag{6.5-16}$$

Our second measure captures the greatest distance between the boundaries

$$\delta_{max} = Max(\left\| \boldsymbol{x_i} - \underline{\boldsymbol{k_i}} \right\|) \tag{6.5-17}$$

Where$\underline{k_i}$ is the closest point along the calculated to the measured point x_i

$$\underline{k_i} = Min(\|\boldsymbol{x_i} - \mathbf{k}(\mathrm{u})\|) \qquad 0 \leq u < 2\pi \tag{6.5-18}$$

We can now generate cross sections for a large number of parameters, fit them with ellipses as well as non-elliptical shapes as if they were measured experimentally. This allows us to characterize errors that we can expect from our measurement. To accomplish this effectively, we limit our search to reasonable parameter limits. First, we recognize that parameter sets $(\alpha, \beta, \gamma, \mathrm{r}, \rho, \mathrm{u})$ and $(\alpha + \pi, -\beta, -\gamma, \mathrm{r}, \rho, \mathrm{u})$ describe the same fiber and fiber cross sections, therefore our angles span the following intervals without a loss of generality

$$0 \leq \alpha < 2\pi; \;\; 0 \leq \beta < \frac{\pi}{2}; \;\; 0 \leq \gamma < 2\pi \tag{6.5-19}$$

Since angle α describes the orientation of the cross section shape in the plane, it will not influence our results and we can choose a single arbitrary value for error analysis. We also restrict our search for the magnitude of curvature between ρ_{min} and ρ_{max}. Assuming isotropic properties of fiber, we can estimate ρ_{max}, corresponding to a fiber in pure bending at the point of breaking, using mechanics of materials

$$\rho_{max} = \frac{\sigma_{uf}}{E_f} \tag{6.5-20}$$

Where σ_{uf} and E_f are the strength and Young's modulus of the fiber material. Note that the definition of ρ coincides with strain at the surface of the fiber in pure bending. We will consider fibers for which $0 \leq \rho < \rho_{min}$ as straight. The value of ρ_{min} can be estimated for example as curvature at which the difference in longitudinal modulus between composite with straight aligned fibers and slightly curved aligned fibers is less than 1%. Using values for glass fiber [1] and values for polypropylene [77] $E_f = 72.4\ 10^9\ Pa$, $\nu_f = 0.2$, $\sigma_{uf} = 3445\ 10^6\ Pa$, $E_m = 1.6\ 10^9\ Pa$, $\nu_m = 0.43$ and fiber fraction by weight in the composite $\mathrm{f}_w = 0.4$. This results in

$$\rho_{max} = 4.758\ 10^{-2} \text{ and } \rho_{min} = 9.398\ 10^{-5} \tag{6.5-21}$$

We further restrict our evaluation to fibers with $\beta < \frac{\pi}{4}$, since fitting non-elliptical shape to nearly circular fibers results in artificially large curvatures due to the inevitable noise in experimental data. We place no restriction on angle γ. The results below are presented based on sampling of the parameter space for cross sections described by a single solution given in (6.5-10) with the following parameter values:

$$\beta_k = \frac{\pi}{36} * k \qquad k = 1,2,\ldots,9 \tag{6.5-22}$$

$$\gamma_k = \frac{\pi}{8} * k \qquad k = 1,2,\ldots,16 \tag{6.5-23}$$

$$\rho_k = e^{-k} \qquad k = 2,3,\ldots,10 \tag{6.5-24}$$

To visualize the process, we consider an example of cross sections centered over the origin given by $\alpha = 0$ and $\beta = 20°$ sweeping all of the remaining parameters as shown in Figure 6.5-3.

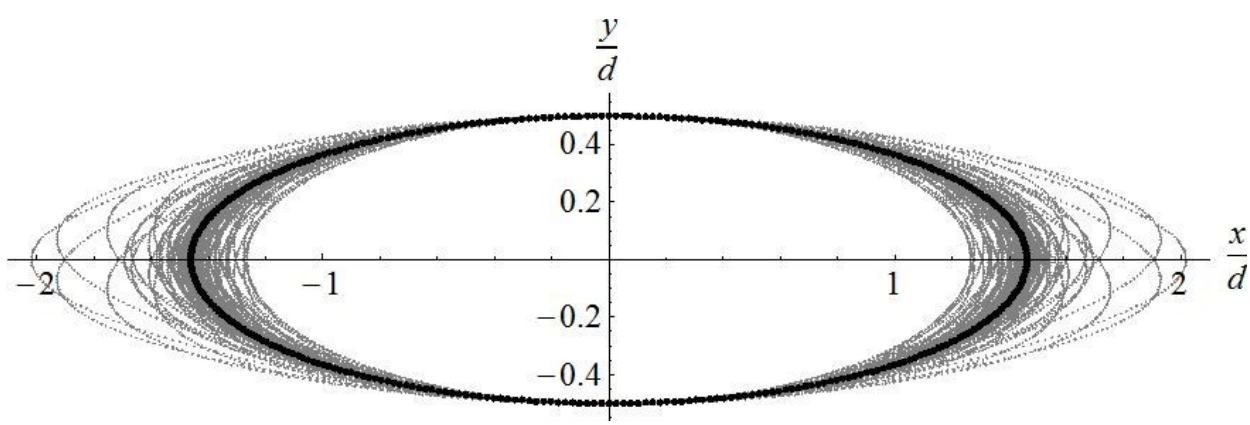

Figure 6.5-3. Black elliptical cross section for $\alpha = 0$ and $\beta = 20°$, gray non-elliptical cross sections for $9.398\ 10^{-5} < \rho < 4.758\ 10^{-2}$and $0 \leq \gamma < 2\pi$.

It is apparent from Figure 6.5-3 that if the non-elliptical cross sections were approximated by an ellipse, we would generally obtain different than those specified to generate the ellipse. This error is most pronounced for the ellipse center location and for parameter β. To quantify the shift of the center, we simply calculate the distance between the center of the cross section $\boldsymbol{q}$ and the center of the ellipse $\boldsymbol{q_e}$ that is fitted to this cross-section.

$$C_{err} = \|\boldsymbol{q_e} - \boldsymbol{q}\| \tag{6.5-25}$$

This result is normalized with respect to fiber diameter as shown in Figure 6.5-4 for $\beta = 20°$.

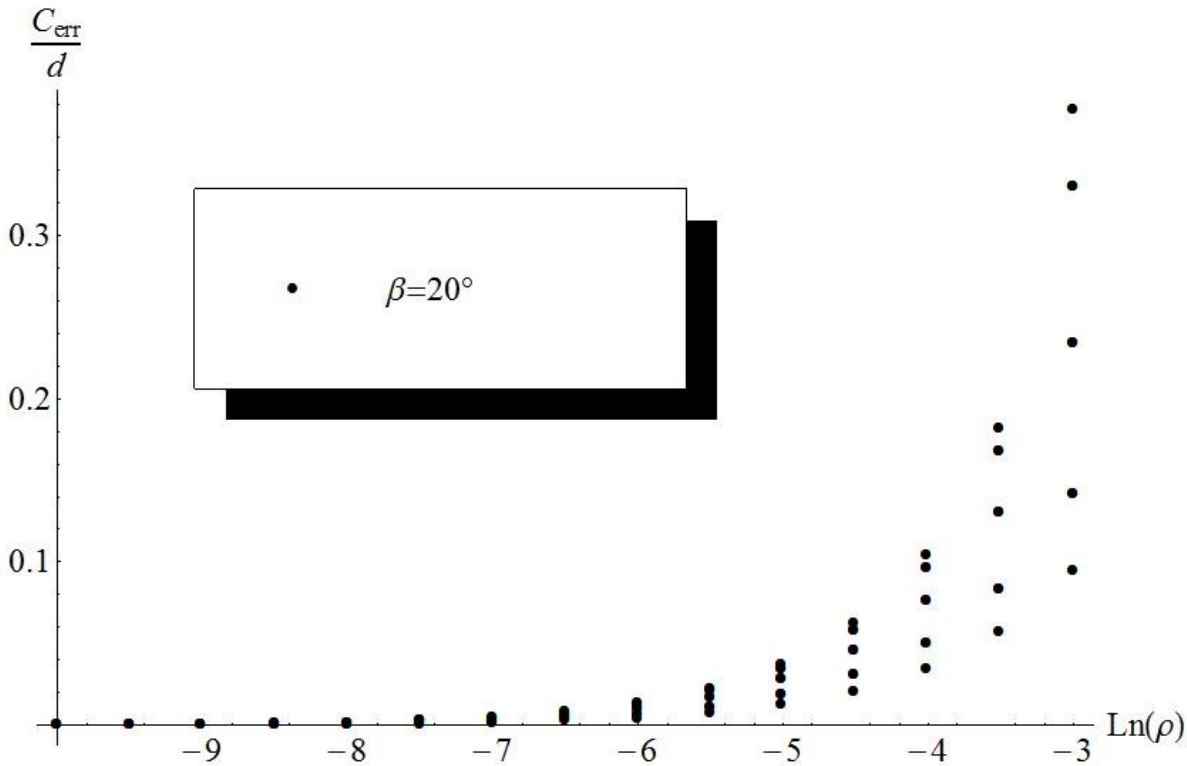

Figure 6.5-4. Normalized distance between center of non-elliptical cross section q and center of best fit ellipse q_e for sections with $\beta = 20°$.

Figure 6.5-5 shows β_{err}, which is defined as the absolute value of difference between β for the non-elliptical cross section and β_e of the best fit ellipse.

$$\beta_{err} = |\beta_e - \beta| \tag{6.5-26}$$

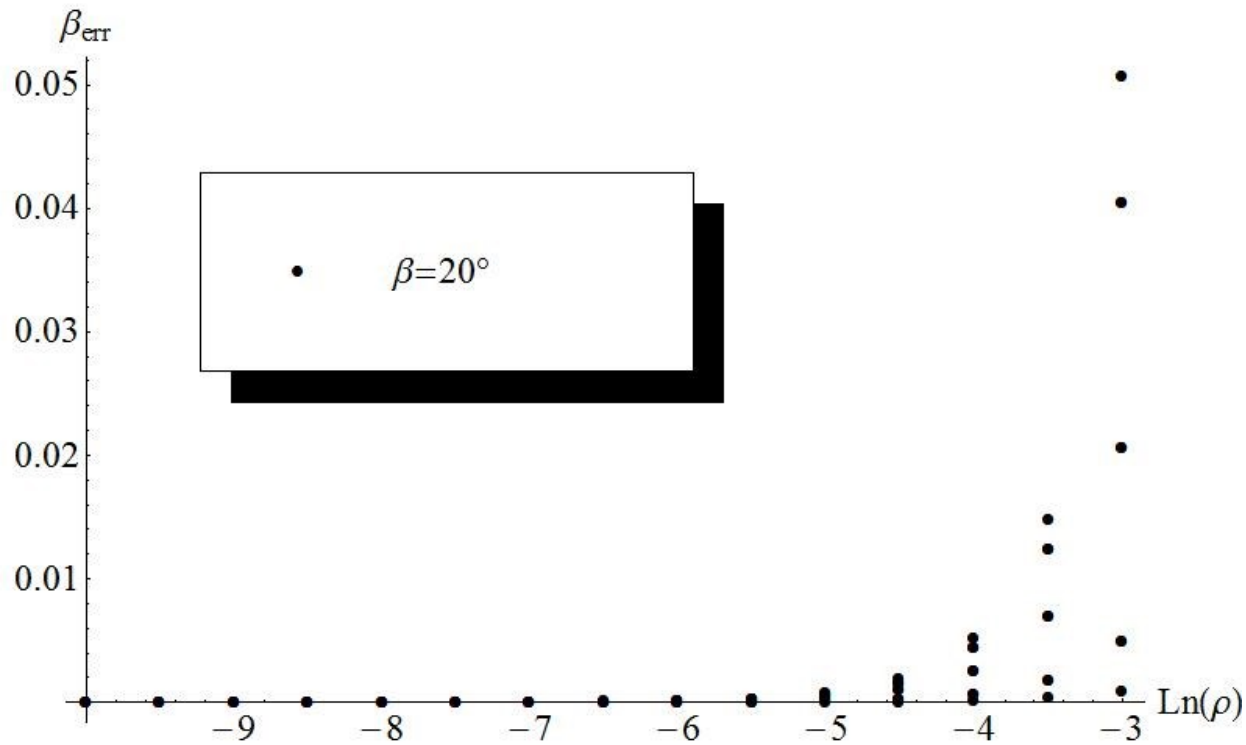

Figure 6.5-5. Difference between $\beta = 20°$ for non-elliptical cross sections and β_e of best fit ellipse.

We also note that the area of the cross section changes as a function of curvature. Figure 6.5-6 shows non-elliptical cross sections for $\beta = 20°$ normalized to a circular cross section of the same fiber. The area of circular cross section obtained at $\beta = \frac{\pi}{2}$ is

$$A_{\frac{\pi}{2}} = \frac{\pi d^2}{4} \tag{6.5-27}$$

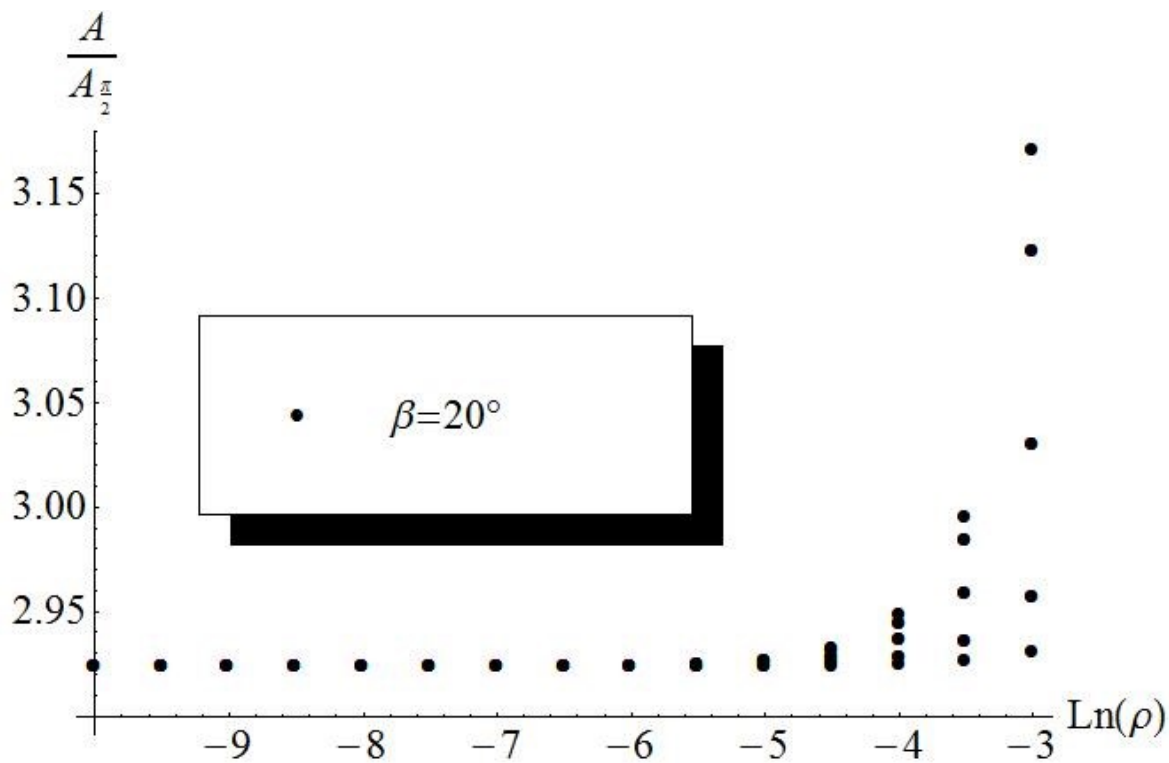

Figure 6.5-6. Area of non-elliptical cross sections for $\beta = 20°$ normalized with respect to the area of circular cross section for the same fiber.

Now we can evaluate the deviation of the non-elliptical cross section from the best fit ellipse. Figure 6.5-7 and Figure 6.5-8 show deviations $\bar{\delta}$ and δ_{max} normalized with respect to fiber diameter d as a function of curvature ρ. To do this, we assume that in Equation (6.5-18) points along the non-elliptical cross section are $\boldsymbol{x_i}$ and $\mathbf{k}(\mathrm{u})$ approaches $\bar{\mathbf{k}}(\mathrm{u})$ for an ellipse.

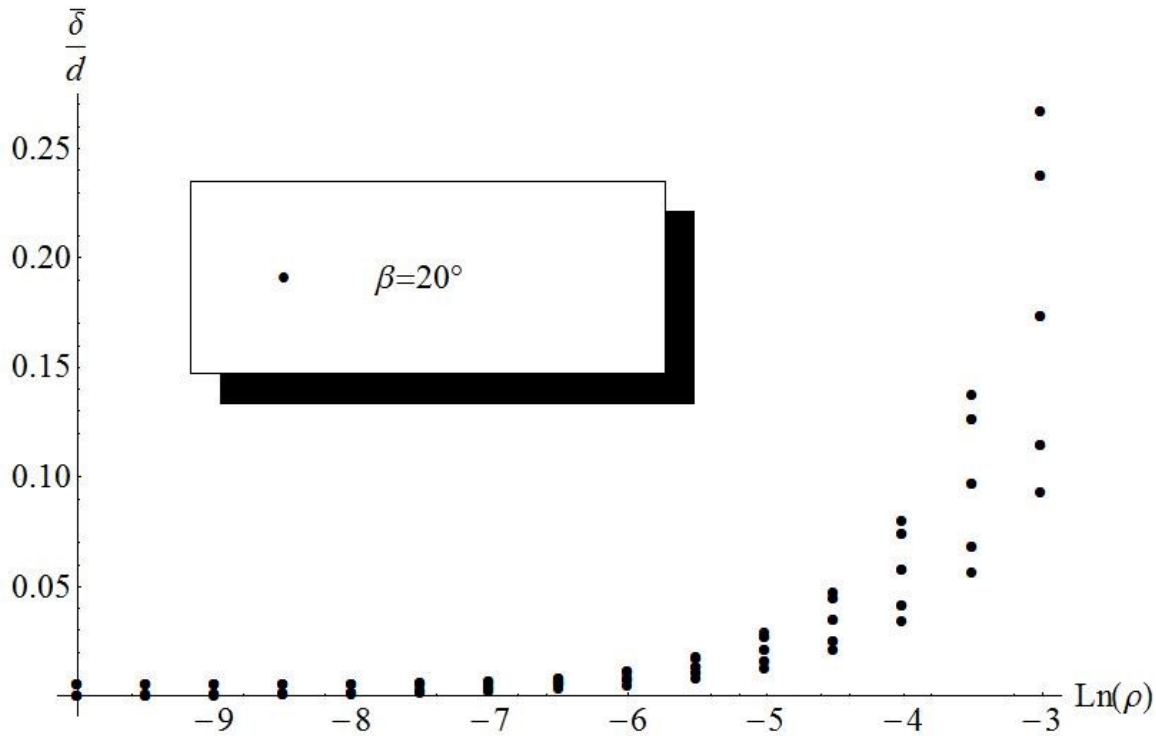

Figure 6.5-7. Normalized deviation $\bar{\delta}$ for fiber with $\beta = 20°$.

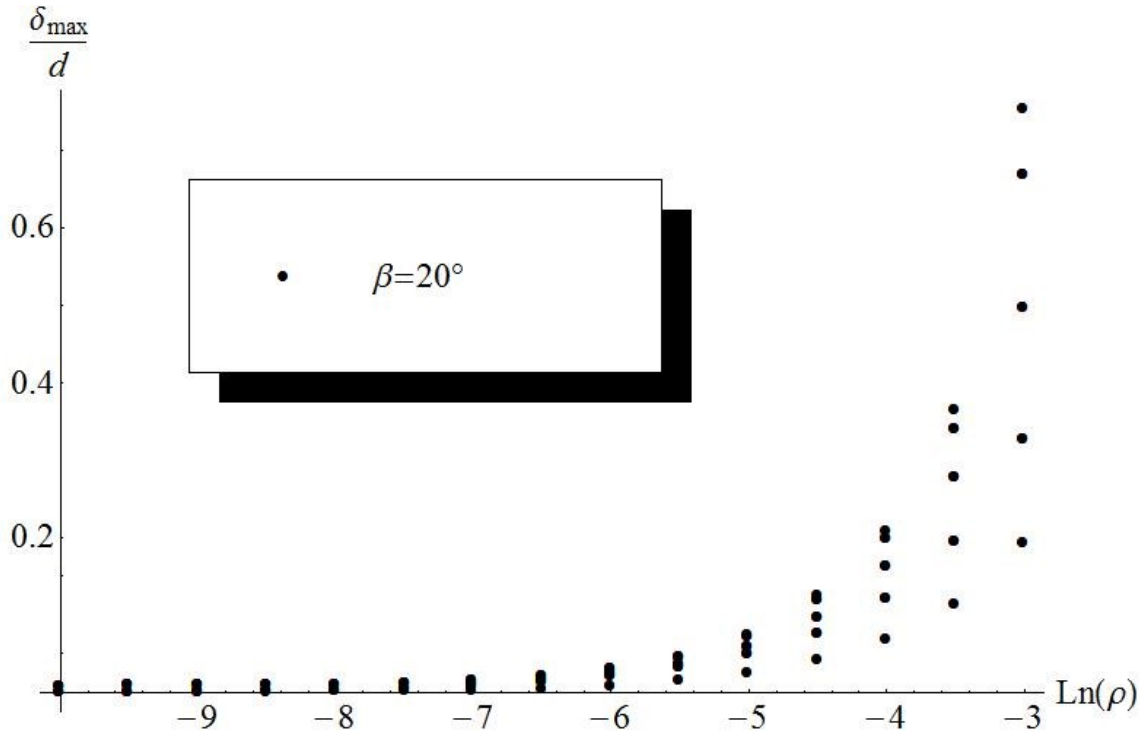

Figure 6.5-8. Normalized deviation δ_{max} for fiber with $\beta = 20°$.

The pattern of both $\bar{\delta}$ and δ_{max} is similar and we note that the deviations vary significantly depending on the angle γ. Large values of deviations $\bar{\delta}$ and δ_{max} mean that the presence of fiber curvature is easier to detect. To evaluate the limitations of our measurement method, we must assume the worst case scenario in which the fiber is curved in such a way that the deviation from the ellipse cross section is at its minimum. With this assumption, we can plot the minima of normalized deviations for several angles β as shown in Figure 6.5-9 and Figure 6.5-10.

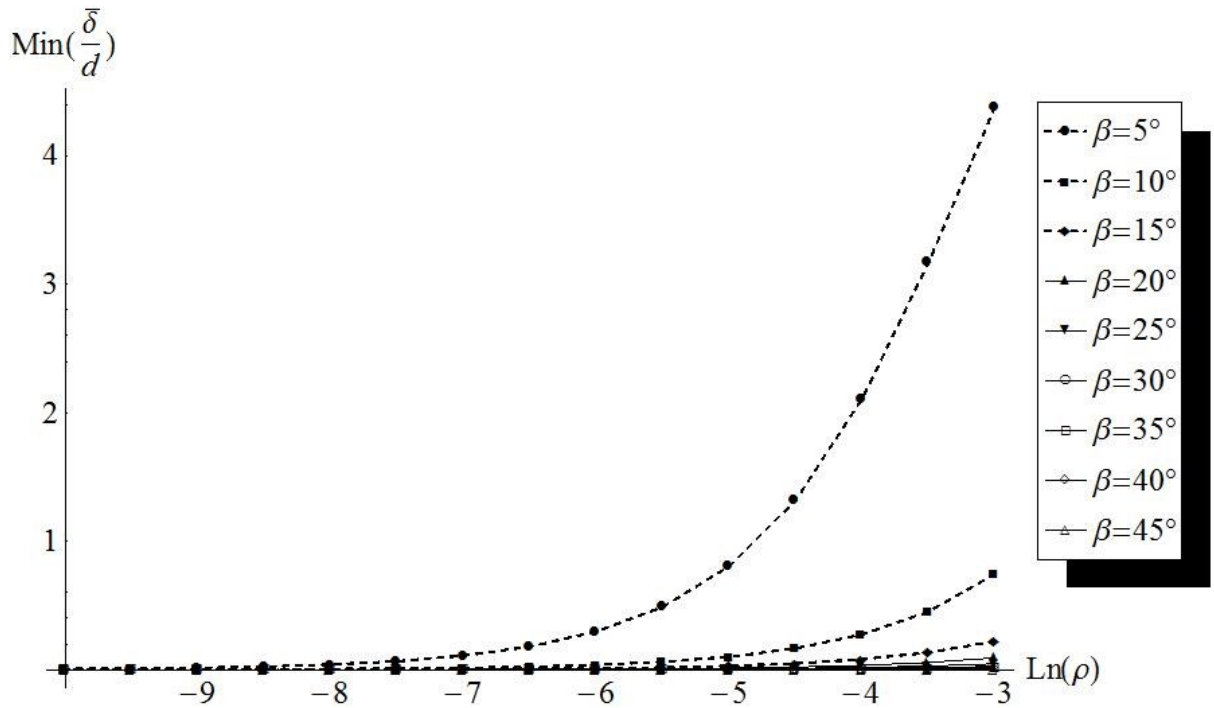

Figure 6.5-9. Minimum of normalized $\bar{\delta}$ deviation as a function of curvature for a range of angles β.

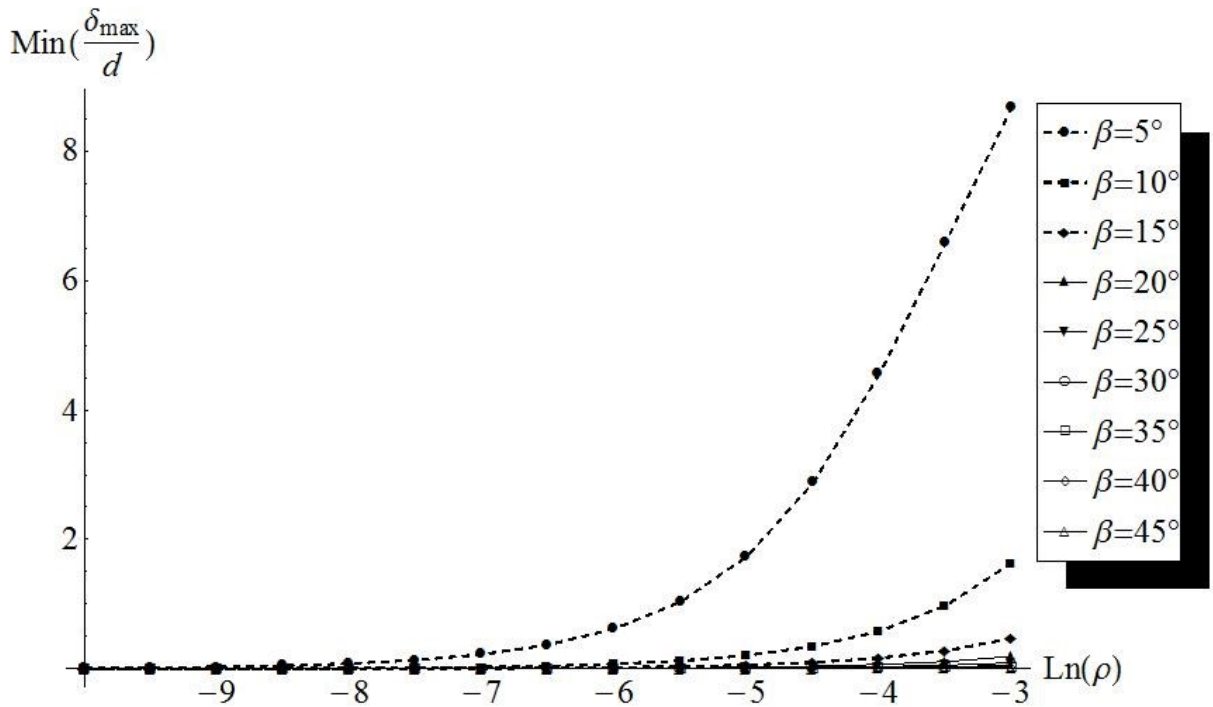

Figure 6.5-10. Minimum of normalized δ_{max} deviation as a function of curvature for a range of angles β.

A small angle β implies a large aspect ratio for an elliptical cross section of a straight fiber and large deviation from this cross section for curved fiber. It would be convenient if all fibers conformed to our assumption of their centerline forming a semi-circle, which would allow us to measure fiber curvature for in-plane fibers with high precision. Real fibers however usually do not conform exactly to this assumption and we are likely to encounter fiber ends and out of plane curvatures at small angles of β. Additionally with decreasing angle β, the likelihood of finding a single cross-section described by both $\mathbf{k_1}$ and $\mathbf{k_2}$ increases for an arbitrary angle γ. Fitting a single cross section to parameters from two solutions is difficult and does not lend itself to automation. We have identified angles at which single solutions for cross sections for our selected range of curvature exist by using dashed line in the plots. Figure 6.5-11 and Figure 6.5-12 show the same data as Figure 6.5-9 and Figure 6.5-10 with modified limits on y axis values. The dotted line in Figure 6.5-11 and Figure 6.5-12 indicates optical microscope spatial resolution at 1000x magnification, or 4.94 μm/pixel.

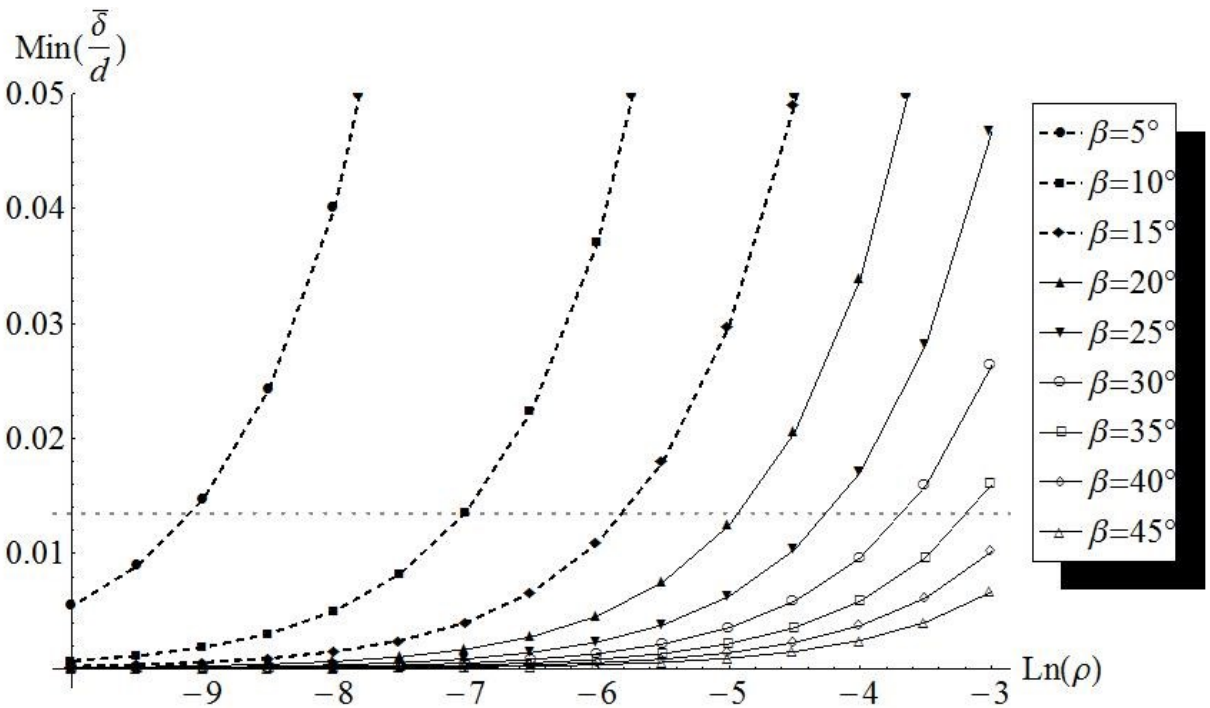

Figure 6.5-11. Minimum of normalized $\bar{\delta}$ deviation as a function of curvature for a range of angles β with dotted line indicating optical microscope spatial resolution at 1000x magnification.

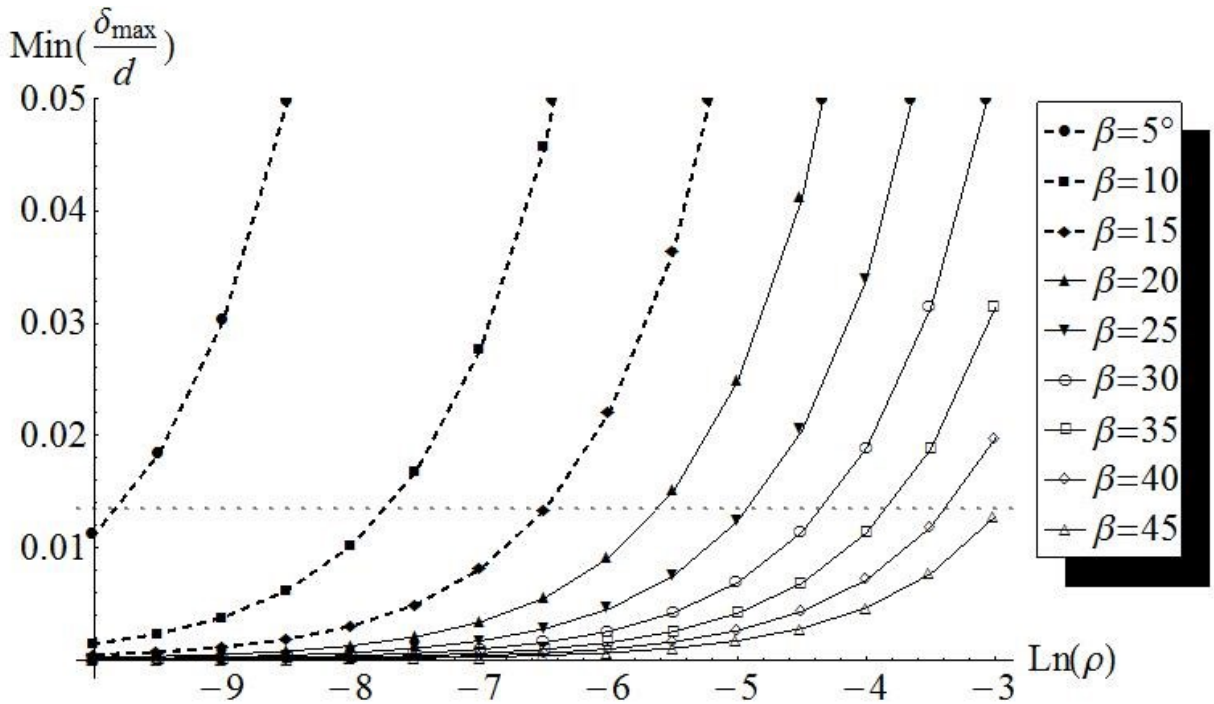

Figure 6.5-12. Minimum of normalized δ_{max} deviation as a function of curvature for a range of angles β with dotted line indicating optical microscope spatial resolution at 1000x magnification.

It is possible to implement algorithms for fitting non-elliptical shapes to experimentally measured cross-sections. Since distinguishing a fiber described by both solutions given in Equation 6.5-10 appears physically and computationally difficult, we will assume that we can only fit fibers which are described by a single solution given in Equation 6.5-10. We would therefore not be able to fit fibers with $\beta < 15°$ for any combination of ρ and γ.

If the algorithm relied on average deviation of the measured profile, we may infer achievable measurements from Figure 6.5-11. Let's assume that the algorithm would consider average deviation of less than one pixel as acceptable. We can see that we would generally not be able to make conclusion about fiber curvature for fibers with $\beta > 35°$, since all of the minimum deviations are below our microscope resolution indicated by the dotted line. It is also clear that we could not be confident in distinguishing curvature below approximately $\rho = e^{-5}$ even if we limited our measurement to fibers with $\beta < 25°$.

Similarly, if our algorithm fitted experimental profiles so that no point along the experimental fiber cross section boundary would be more than one pixel apart from the fitted solution, Figure 6.5-12 would provide insight into achievable measurements. Since this measure is more restrictive, we could detect curvature easier. It is important to point out that inevitable imperfections in experimentally measured profiles would likely prevent us from fitting experimental profiles with sub-pixel accuracy for each point measured along the boundary as suggested by this measure.

The reader should not conclude that measurement of fiber curvature from its cross section is impossible. Rather, we have demonstrated that measurement of general state of fiber orientation and fiber curvature would require analysis of multiple cross sections from the experimental sample. Based on our analysis presented above, we are able to evaluate fiber cross section and establish our confidence in the measurement of fiber orientation and fiber curvature. We demonstrate this in a small example.

6.5.4 Example measurement from a physical sample

The material used in this study was commercially available polypropylene with 40% of glass fibers by weight. The samples were injection molded with nominally 12.5 mm long pultruded pellets into a plaque mold with 3 mm thickness. The samples were harvested 280 mm from the injection point, which is approximately a mid-point between the injection point and an edge of the sample. The sample preparation consists of cutting out samples, polishing a plane of interest and etching the sample. The technique has been documented in the past [58, 59], therefore we only point out differentiating details allowing us to obtain measurements of curvature. Figure 6.5-13 shows typical section of image collected for our technique.

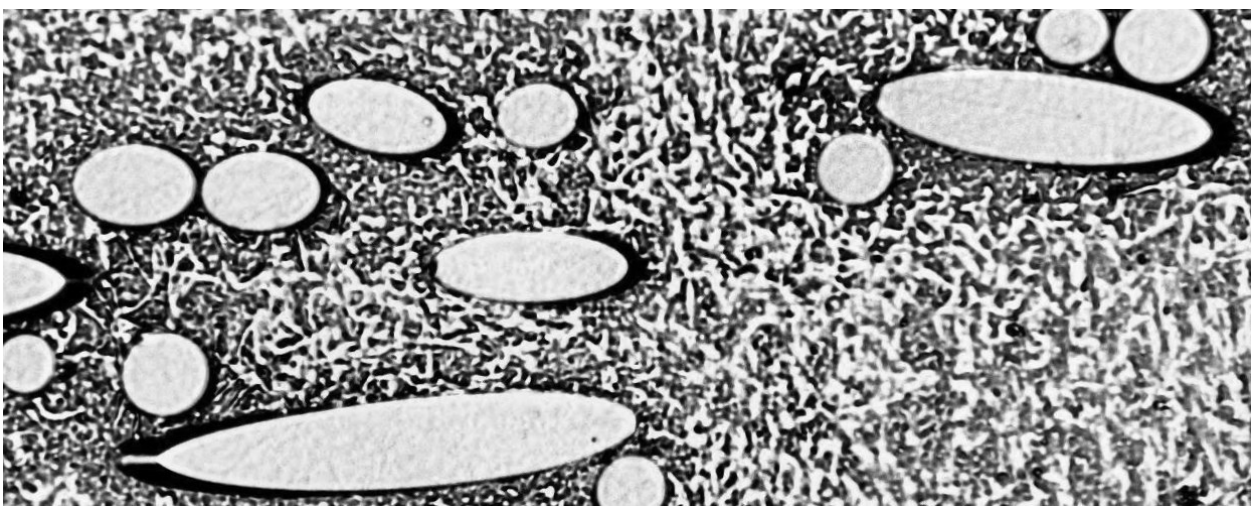

Figure 6.5-13. Example fiber cross-sections showing white fibers, dark shadows identifying fiber end protruding above the etched surface and rough matrix surface obtained by etching.

We start the measurement analysis by characterizing the parameters of the cross section and eliminating fragmented fibers. This step can be augmented by visual inspection and manual elimination of fragments that were not automatically filtered from the measurement sample. We then fit an ellipse to each fiber, a process which gives us an estimate for angles α and β, fiber radius r and ellipse center coordinates xc and yc. Since there is an ambiguity in the results [58], we use the automated shadow detection method illustrated in Figure 6.5-14 to resolve the ambiguity.

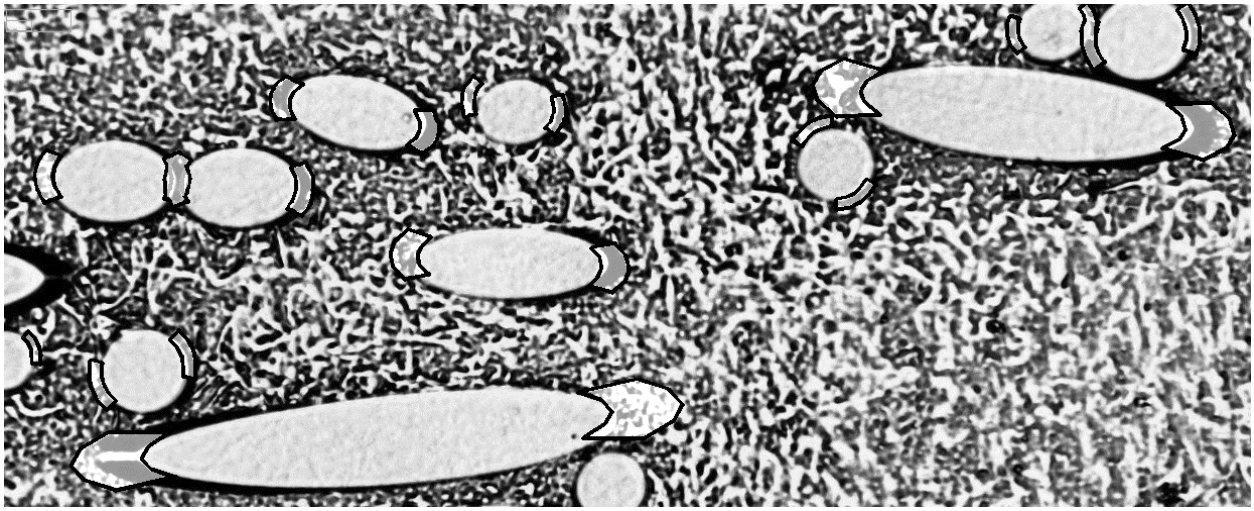

Figure 6.5-14. Illustration of automated shadow detection.

Having determined un-ambiguous orientation of each fiber by obtaining angles α and β, we can now proceed with an iterative method of finding the magnitude of fiber curvature given by ρ and the direction of the curvature vector, which requires specification of angle γ. This is done by estimating deviation of the fiber cross-section from elliptical cross section and fitting a non-elliptical cross section in the form of Figure 6.5-15. This search is conducted only for selected fibers due to limited resolution that can be obtained with measurement equipment. Figure 6.5-15 shows elliptical and non-elliptical fit for fibers with $\beta < \frac{\pi}{4}$.

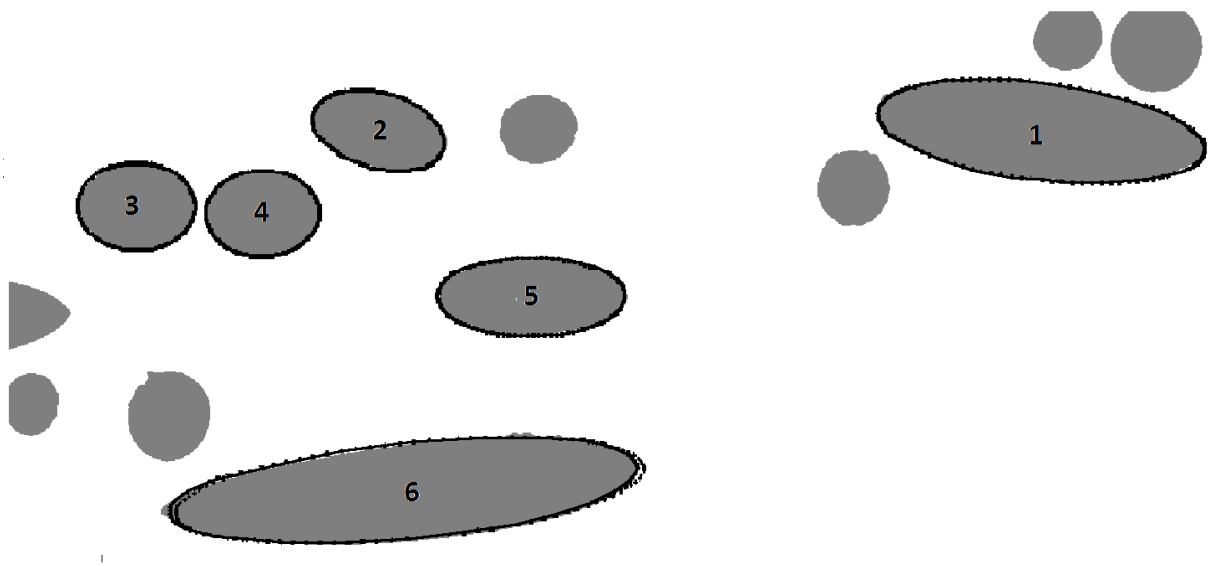

Figure 6.5-15. Fibers (gray) with overlay of ellipse fit (points) and curved fiber fit (solid line).

We were able to achieve better than elliptical fit for fibers that are apparently curved and converge to nearly elliptical fit for fibers that do not display significant curvature. Table 6.5-1 shows parameters for the fibers shown in Figure 6.5-15.

Table 6.5-1. Parameters for six fibers shown in Figure 6.5-15.

Fiber	d [μm]	α	β	γ	$\rho \,.\, 10^3$	Log(ρ)	R[mm]	$\frac{\bar{\delta}}{d}$
1	17.6	6.18	0.27	2.84	3.87	-5.55	4.55	0.015
2	13.8	6.06	0.53	6.12	16.51	-4.10	0.83	0.006
3	15.9	6.28	0.74	0.20	7.35	-4.91	2.17	0.003
4	15.6	0.02	0.74	3.55	14.51	-4.23	1.07	0.013
5	14.1	0.00	0.38	3.16	1.45	-6.54	9.76	0.031
6	17.7	3.23	0.19	0.52	3.92	-5.54	4.51	0.049

We can see that for fibers with larger β (fibers 2,3,4) the deviation is at or below the instrument resolution (nominally $\frac{\bar{\delta}}{d} = 0.012$). Fibers 1 and 6 have clearly non-elliptical cross sections. Both of these fibers show similar magnitude of curvature ρ indicating nominally 0.4% strain at their surface, however the remaining fiber cross section parameters vary significantly.

6.5.5 Conclusions

A method for fiber curvature measurement from non-elliptical fiber cross section was developed. The sensitivity of this method to experimentally obtained cross-section spatial resolution is documented. While the method works well for fibers conveniently oriented with respect to the sectioning plane, very high resolution would be necessary to establish fiber curvature state in a network of fibers from relatively few experimental cross sections. Large number of sections would be necessary if optical microscope were used for data collection, which limits the practicality of this method.

6.5.6 References

1. Baird, D. G., *Simulating Injection Molding of Thermoplastics Reinforced with Short and Long Fibers*, in *DOE Report*. 2008.
2. Strautins, U. and A. Latz, *Flow-driven orientation dynamics of semiflexible fiber systems.* Rheologica Acta, 2007. **46**(8): p. 1057-1064.
3. Ortman, K., et al., *Prediction of fiber orientation in the injection molding of long fiber suspensions.* Polymer Composites, 2012. **33**(8): p. 1360-1367.
4. Bay, R. S. and C. L. Tucker, *Stereological Measurement and Error-Estimates for 3-Dimensional Fiber Orientation.* Polymer Engineering and Science, 1992. **32**(4): p. 240-253.
5. Velez-Garcia, G. M., et al., *Unambiguous orientation in short fiber composites over small sampling area in a center-gated disk.* Composites Part a-Applied Science and Manufacturing, 2012. **43**(1): p. 104-113.
6. Hine, P. J., et al., *Measuring the Fiber Orientation and Modeling the Elastic Properties of Injection-Molded Long-Glass-Fiber-Reinforced Nylon.* Composites Science and Technology, 1995. **53**(2): p. 125-131.
7. Eberhardt, C. N. and A. R. Clarke, *Automated reconstruction of curvilinear fibres from 3D datasets acquired by X-ray microtomography.* Journal of Microscopy-Oxford, 2002. **206**: p. 41-53.
8. Svensson, S. and M. Aronsson, *Using distance transform based algorithms for extracting measures of the fiber network in volume images of paper.* Ieee Transactions on Systems Man and Cybernetics Part B-Cybernetics, 2003. **33**(4): p. 562-571.
9. Advani, S. G. and C.L. Tucker, *The Use of Tensors to Describe and Predict Fiber Orientation in Short Fiber Composites.* Journal of Rheology, 1987. **31**(8): p. 751-784.
10. Phelps, J. H. and C.L. Tucker III, *An anisotropic rotary diffusion model for fiber orientation in short- and long-fiber thermoplastics* Journal of Non-Newtonian Fluid Mechanics, 2009. **156**(3): p. 165-176.
11. Nguyen, B. N. and V. Kunc, *An elastic-plastic damage model for long-fiber thermoplastics.* International Journal of Damage Mechanics, 2010. **19**(6): p. 691-725.
12. Nguyen, B. N., et al., *Fiber length and orientation in long-fiber injection-molded thermoplastics - Part I: Modeling of microstructure and elastic properties.* Journal of Composite Materials, 2008. **42**(10): p. 1003-1029.
13. Kunc, V., Frame, B.J., Nguyen, B.N., Tucker III, C.L. and Velez-Garcia, G, *Fiber Length Distribution Measurement for Long Glass and Carbon Fiber Reinforced Injection Molded Thermoplastics*, in *Composites Conference & Exposition, Society of Plastic Engineers*. 2007: Troy, Michigan.
14. Hyer, M. W., *Stress Analysis of Fiber-Reinforced Composite Materials*. 1998: WCB/McGraw-Hill.
15. Tscharnuter, D., et al., *Time-dependent poisson's ratio of polypropylene compounds for various strain histories.* Mechanics of Time-Dependent Materials, 2011. **15**(1): p. 15-28.
16. Velez-Garcia, G. M., et al., *Sample preparation and image acquisition using optical-reflective microscopy in the measurement of fiber orientation in thermoplastic composites.* Journal of Microscopy, 2012. **248**(1): p. 23-33.

Blank Page

7 Conclusions

7.1 Review

Chapter 2 contains broad review of DFC material background, scales involved as well as microstructure-property models for stiffness and strength. It is noted that existing theories assume straight fibers, which is inconsistent with physical observations. Chapter 3 contains mathematical background relevant to the development of new model of stiffness tensor for materials containing curved fibers. The background contains several anisotropic stiffness tensor decompositions. Not all of the decompositions are necessary for the development of new stiffness tensor model, however they are included due to their potential usefulness for study of the structure of the stiffness tensor or because they have not appeared previously in English literature. Chapter 5 contains overview of current experimental techniques used to establish fiber orientation distribution and fiber length distribution within DFCs.

7.2 Development

Chapter 4 introduces the concept of configuration for single curved fiber, representation of configuration distribution for an ensemble of fibers by a set of even order tensors and an averaging technique used for obtaining fully anisotropic stiffness tensor. The concepts reduce to currently well known concepts of fiber orientation distribution and orientation averaging for material containing only straight fibers. Paper in Chapter 6.1 summarizes the theoretical development and demonstrates that configuration averaging results in fully anisotropic stiffness tensor, whereas orientation averaging for straight fibers produced at most orthotropic symmetry. Paper in Chapter 6.2 demonstrates the effect of curvature on stiffness tensor for materials of three different configuration distributions and contains comparison to experimental results. It is shown that application of configuration averaging results in better match with experiments compared to orientation averaging.

The experimental results were obtained with X-ray micro-tomography unit allowing observation of material under load. The setup is discussed in Chapter 6.3 and the design of miniature specimens is discussed in Chapter 6.4. Paper in Chapter 6.5 discusses development of fiber curvature measurement technique. The development is complete and the technique can be theoretically used, however the resolution of optical microscope currently available to the researcher did not allow generation of useful data.

7.3 Summary

This dissertation presents a new method for obtaining fully anisotropic stiffness tensor for materials containing discontinuous curverd fibers. It is demonstrated that the definition of fiber configuration and configuration averaging allow us to obtain better match with experimental results when compared to theory relying on the assumption of straight fibers. The experimental results are obtained using novel X-ray micro-tomography setup allowing observation of material microstructure under load.

7.4 Future Work

The dissertation opens areas for future research in several areas. Strictly theoretical examination of anisotropy, multiplicity of Kelvin moduli and eigen-states could provide valuable insight into the nature of anisotropic stiffness tensor obtained by configuration averaging. Semi-empirical Halpin-Kardos equations form the basis for obtaining material constants for our stiffness tensor. Evaluation of other experimental and numerical methods could produce interesting results. Changes in anisotropy and description of internal material structure also clearly open the possibility to improve time dependent, non-linear and strength models for DFCs. Verification of the model is documented in this dissertation, however substantial effort is necessary for validation against experimental data for various classes of DFCs. Development of technique allowing characterization of fiber configuration distribution in a realistic sample is clearly necessary.

Bibliography

1. Hyer, M. W., *Stress Analysis of Fiber-Reinforced Composite Materials*. 1998: WCB/McGraw-Hill.
2. Reinhart, T., ed. *Engineered Materials Handbook*. Composites. Vol. 1. 1987, ASM International: Ohio.
3. Epel, J.N., ed. *Engineered Materials Handbook*. Engineering Plastics. Vol. 2. 1987, ASM International: Ohio.
4. Kaw, A. K., ed. *Mechanics of Composite Materials*. 1997, CRC Press LLC: Boca Raton, Florida.
5. Thomason, J. L. and M. A. Vlug, *Influence of fibre length and concentration on the properties of glass fibre-reinforced polypropylene .4. Impact properties.* Composites Part a-Applied Science and Manufacturing, 1997. **28**(3): p. 277-288.
6. Thomason, J. L. and M. A. Vlug, *Influence of fibre length and concentration on the properties of glass fibre-reinforced polypropylene .1. Tensile and flexural modulus.* Composites Part a-Applied Science and Manufacturing, 1996. **27**(6): p. 477-484.
7. Kunc, V., Frame, B. J., Nguyen, B. N., Tucker III, C.L. and Velez-Garcia, G, *Fiber Length Distribution Measurement for Long Glass and Carbon Fiber Reinforced Injection Molded Thermoplastics*, in *Composites Conference & Exposition, Society of Plastic Engineers*. 2007: Troy, Michigan.
8. Advani, S. G. and C. L. Tucker, *The Use of Tensors to Describe and Predict Fiber Orientation in Short Fiber Composites.* Journal of Rheology, 1987. **31**(8): p. 751-784.
9. Advani, S. G. and C. L. Tucker, *Closure Approximations for 3-Dimensional Structure Tensors.* Journal of Rheology, 1990. **34**(3): p. 367-386.
10. Clarke, A. R., N. Davidson, and G. Archenhold, *A Multitransputer Image Analyzer for 3d-Fiber Orientation Studies in Composites.* Transactions of the Royal Microscopical Society : New Series, Vol 1, 1990. **1**: p. 305-308.
11. VerWeyst, B. E., et al., *Fiber orientation in 3-D injection molded features - Prediction and experiment.* International Polymer Processing, 1999. **14**(4): p. 409-420.
12. Eberhardt, C. N. and A. R. Clarke, *Automated reconstruction of curvilinear fibres from 3D datasets acquired by X-ray microtomography.* Journal of Microscopy-Oxford, 2002. **206**: p. 41-53.

13. Svensson, S. and M. Aronsson, *Using distance transform based algorithms for extracting measures of the fiber network in volume images of paper.* Ieee Transactions on Systems Man and Cybernetics Part B-Cybernetics, 2003. **33**(4): p. 562-571.
14. Baird, D. G., *Simulating Injection Molding of Thermoplastics Reinforced with Short and Long Fibers*, in *DOE Report*. 2008.
15. Jones, R. M., *Mechanics of Composite Materials*. 1975: Scripta Book Company.
16. Tsai, S. W., *Introduction to Composite Materials*. 1980, Westport, CT: Technomic Publishing Co.
17. Manson, J. A. and L. H. Sperling, *Polymer blends and composites*. 1976, New York: Plenum Press.
18. Cox, H. L., *The elasticity and strength of paper and other fibrous materials.* Brit. J. Appl. Phys., 1952. **3**: p. 72-79.
19. Rosen, B. W., *Tensile Failure of Fiborous Composites.* AIAA Journal, 1964. **2**(11): p. 1985-1991.
20. Batdorf, S. B., *Tensile Strength of Unidirectionally Rreinforced Composites - 1.* Journal of Reinforced Plastics and Composites, 1982. **1**(2): p. 153-164.
21. Batdorf, S. B. and S. R. G. Hammamkar, *Tensile Strength of Unidirectionally Reinforced Composites - 2.* Journal of Reinforced Plastics and Composites, 1982. **1**(2): p. 165-176.
22. Kelly, A. and W. R. Tyson, *Tensile Properties of Fibre-Reinforced Metals - Copper/Tungsten And Copper/Molybdenum.* Journal of the Mechanics and Physics of Solids, 1965. **13**(6): p. 329-350.
23. Eshelby, J. D., *The determination of the elastic field of an ellipsoidal inclusion and related problems.* Proc Roy Soc A, 1957. **241**: p. 376-396.
24. Mori T, T. K., *Average stress in matrix and average elastic energy of materials with misfitting inclusions.* Acta Metallurgica Et Materialia, 1973. **21**: p. 571-574.
25. Nielsen, L. E. and P. E. Chen, *Youngs Modulus of Composites Filled with Randomly Oriented Fibers.* Journal of Materials, 1968. **3**(2): p. 352.
26. Tandon, G. P. and G. J. Weng, *Average Stress in the Matrix and Effective Moduli of Randomly Oriented Composites.* Composites Science and Technology, 1986. **27**(2): p. 111-132.
27. Tucker, C. L. and E. Liang, *Stiffness predictions for unidirectional short-fiber composites: Review and evaluation.* Composites Science and Technology, 1999. **59**(5): p. 655-671.
28. Thomason, J. L., *The influence of fibre length and concentration on the properties of glass fibre reinforced polypropylene: 5. Injection moulded long and short fibre PP.* Composites Part a-Applied Science and Manufacturing, 2002. **33**(12): p. 1641-1652.
29. Thomason, J. L., *The influence of fibre length and concentration on the properties of glass fibre reinforced polypropylene. 6. The properties of injection moulded long fibre PP at high fibre content.* Composites Part a-Applied Science and Manufacturing, 2005. **36**(7): p. 995-1003.
30. Thomason, J. L., *Structure-property relationships in glass-reinforced polyamide, part 1: The effects of fiber content.* Polymer Composites, 2006. **27**(5): p. 552-562.
31. Thomason, J. L., *Structure-property relationships in glass reinforced polyamide, Part 2: The effects of average fiber diameter and diameter distribution.* Polymer Composites, 2007. **28**(3): p. 331-343.

32. Thomason, J. L., *The influence of fibre length, diameter and concentration on the modulus of glass fibre reinforced polyamide 6,6.* Composites Part a-Applied Science and Manufacturing, 2008. **39**(11): p. 1732-1738.
33. Thomason, J. L., *The influence of fibre length, diameter and concentration on the impact performance of long glass-fibre reinforced polyamide 6,6.* Composites Part a-Applied Science and Manufacturing, 2009. **40**(2): p. 114-124.
34. Bapanapalli, S. and B. N. Nguyen, *Prediction of elastic properties for curved fiber polymer composites.* Polymer Composites, 2008. **29**(5): p. 544-550.
35. Schapery, R. A., *On Characterization of Nonlinear Viscoelastic Materials.* Polymer Engineering and Science, 1969. **9**(4): p. 295.
36. Riedel, H., *Fracture at High Temperatures*. 1987, Heidelberg: Springer-Verlag.
37. Zdenek Bazant, J. P., *Fracture and Size Effect in Concrete and Other Quasibritle Materials*. 1997, Boca Raton: CRC Press.
38. Hinton, M.J. and P.D. Soden, *Predicting failure in composite laminates: The background to the exercise.* Composites Science and Technology, 1998. **58**(7): p. 1001-1010.
39. DeBoest, J. F., *Reinforced Polypropylenes*, in *Engineering Plastics*. 1987, ASM International: Metals Park. p. 193.
40. Al-Rub, R. K. A., *Material Length Scales in Gradient-Dependent Plasticity / Damage and Size Effects: Theory and Computation*, in *Department of Civil & Environmental Engineering*. 2004, Louisiana State University: Baton Rouge.
41. Krajcinovic, D., *Damage Mechanics* 1996, Amsterdam: Elsevier.
42. Lee, H. K. and S. Simunovic, *Modeling of progressive damage in aligned and randomly oriented discontinuous fiber polymer matrix composites.* Composites Part B-Engineering, 2000. **31**(2): p. 77-86.
43. Nguyen, N. and V. Kunc, *An Elastic-Plastic Damage Model for Long-Fiber Thermoplastics.* International Journal of Damage Mechanics, 2009.
44. Kobayashi, A. S., ed. *Handbook on Experimental Mechanics*. 2 ed. 1993, Society of Experimental Mechanics: Bethel.
45. Jenkins, C. H., ed. *Manual on Experimental Methods of Mechanical Testing of Composites*. 2 ed. 1998, The Fairmont Press, Inc.: Lilburn.
46. Sutton, M. A., *Image Correlation for Shape, Motion and Deformation Measurements*. 2009, New York: Springer.
47. Dally, J. W. and W. F. Riley, *Experimental Stress Analysis*. 2005: College House Enterprises Llc
48. Chadwick, P., M. Vianello, and S. C. Cowin, *A new proof that the number of linear elastic symmetries is eight.* Journal of the Mechanics and Physics of Solids, 2001. **49**(11): p. 2471-2492.
49. Annin, B. D. and N. I. Ostrosablin, *Anisotropy of elastic properties of materials.* Journal of Applied Mechanics and Technical Physics, 2008. **49**(6): p. 998-1014.
50. Reuter, R. C., *Concise Property Transformation Relations for an Anisotropic Lamina.* Journal of Composite Materials, 1971. **5**(Apr): p. 270.
51. Thomson, A. W., *Elements of a Mathematical Theory of Elasticity*. 1856: Royal Society of Edinburgh.
52. Rychlewski, J., *ON HOOKE LAW.* Pmm Journal of Applied Mathematics and Mechanics, 1984. **48**(3): p. 303-314.

53. Ostrosablin, N. I., *Linear invariant irreducible decompositions of the fourth-rank tensor of elasticity moduli.* Dynamics of Continuous Media (collected scientific papers), 2002. **120**: p. 149-160.
54. Lubarda, V. A. and M. C. Chen, *On the elastic moduli and compliances of transversely isotropic and orthotropic materials.* Journal of Mechanics of Materials and Structures, 2008. **3**(1): p. 153-171.
55. Halpin, J. C. and J. L. Kardos, *Strength of Discontinuous Reinforced Composites .1. Fiber Reinforced Composites.* Polymer Engineering and Science, 1978. **18**(6): p. 496-504.
56. Bay, R. S. and C. L. Tucker, *Stereological Measurement and Error-Estimates for 3-Dimensional Fiber Orientation.* Polymer Engineering and Science, 1992. **32**(4): p. 240-253.
57. Hine, P. J., et al., *Measuring the Fiber Orientation and Modeling the Elastic Properties of Injection-Molded Long-Glass-Fiber-Reinforced Nylon.* Composites Science and Technology, 1995. **53**(2): p. 125-131.
58. Velez-Garcia, G. M., et al., *Unambiguous orientation in short fiber composites over small sampling area in a center-gated disk.* Composites Part a-Applied Science and Manufacturing, 2012. **43**(1): p. 104-113.
59. Velez-Garcia, G. M., et al., *Sample preparation and image acquisition using optical-reflective microscopy in the measurement of fiber orientation in thermoplastic composites.* Journal of Microscopy, 2012. **248**(1): p. 23-33.
60. Konicek, T. S., *A method to determine three-dimensional fiber orientation in fiber reinforced polymers*. 1987, University of Illinois at Urbana-Champaign: Urbana-Champaign.
61. Lei, H. F., Z. Q. Zhang, and B. Liu, *Effect of fiber arrangement on mechanical properties of short fiber reinforced composites.* Composites Science and Technology, 2012. **72**(4): p. 506-514.
62. Tu, S. T., et al., *Numerical simulation of saturation behavior of physical properties in composites with randomly distributed second-phase.* Journal of Composite Materials, 2005. **39**(7): p. 617-631.
63. ASTM, *D2584 – 11 Standard Test Method for Ignition Loss of Cured Reinforced Resins*. 2011: West Conshohocken, PA.
64. ASTM, *D3171 – 11 Standard Test Methods for Constituent Content of Composite Materials*. 2011: West Conshohocken, PA.
65. Spencer, A. J. M., *The formulation of constitutive equation for anisotropic solids*, in *Mechanical behavior of anisotropic solids*, J.P. Boehler, Editor. 1982, Martinus Nijhoff Publishers: The Hague. p. 2-26.
66. Nguyen, B. N., et al., *Prediction of the Elastic-Plastic Stress/Strain Response for Injection-Molded Long-Fiber Thermoplastics.* Journal of Composite Materials, 2009. **43**(3): p. 217-246.
67. Akbarov, S. D. and R. Kosker, *On a stress analysis in the infinite elastic body with two neighbouring curved fibres.* Composites Part B-Engineering, 2003. **34**(2): p. 143-150.
68. Kosker, R. and N. T. Cinar, *Stress distribution in an infinite elastic body containing two neighboring locally curved fibers.* Mechanics of Composite Materials, 2009. **45**(3): p. 315-330.

69. Wolfram Research, I., *Mathematica Edition: Version 7.0*. 2008, Champaign, Illinois Wolfram Research, Inc.
70. Kunc, V., *Observation of Composite Materials Using Coupled Mechanical Testing and Computed Tomography*, in *SEM XI International Congress & Exposition on Experimental and Applied Mechanics*. 2008: Orlando, FL.
71. Kunc, V., *Tensile specimen design and experimental procedures for characterizing polymeric composites using X-ray based micro-tomography*, in *SAMPE-ASC*. 2008: Memphis, TN.
72. Strautins, U. and A. Latz, *Flow-driven orientation dynamics of semiflexible fiber systems.* Rheologica Acta, 2007. **46**(8): p. 1057-1064.
73. Ortman, K., et al., *Prediction of fiber orientation in the injection molding of long fiber suspensions.* Polymer Composites, 2012. **33**(8): p. 1360-1367.
74. Phelps, J. H. and C. L. Tucker III, *An anisotropic rotary diffusion model for fiber orientation in short- and long-fiber thermoplastics* Journal of Non-Newtonian Fluid Mechanics, 2009. **156**(3): p. 165-176.
75. Nguyen, B. N. and V. Kunc, *An elastic-plastic damage model for long-fiber thermoplastics.* International Journal of Damage Mechanics, 2010. **19**(6): p. 691-725.
76. Nguyen, B. N., et al., *Fiber length and orientation in long-fiber injection-molded thermoplastics - Part I: Modeling of microstructure and elastic properties.* Journal of Composite Materials, 2008. **42**(10): p. 1003-1029.
77. Tscharnuter, D., et al., *Time-dependent poisson's ratio of polypropylene compounds for various strain histories.* Mechanics of Time-Dependent Materials, 2011. **15**(1): p. 15-28.

8 Appendixes

8.1 Appendix A: Curved Fiber Stiffness Model Verification Cases

8.1.1 Introduction

In this section, test numerical examples are provided to verify that the new model for stiffness fiber provides expected results. The model was implemented in Mathematica and results provided herein are directly taken from Mathematica code without modification. For brevity, the code is not included, however some comments on implementation are provided when appropriate. Numerical values are given to high digit precision to aid code verification.

8.1.2 Halpin-Tsai-Kardos Equations

We first verify that our implementation of Equations 3.9-3 through 3.9-11. We use numerical values for fiber and matrix properties given in an appendix of [8] and reproduce identical numerical values for composite material.

Table 8-1. Fiber and matrix properties from [8]

$E_f\ [psi]$	ν_f	$E_m\ [psi]$	ν_m	V_f	ξ
$10.5\ 10^6$	.2	$0.5\ 10^6$	.35	.2	100

In metric units:

$E_f\ [Pa]$	ν_f	$E_m\ [Pa]$	ν_m	V_f	ξ
$7.24\ 10^{10}$	.2	$3.45\ 10^9$	.35	.2	100

We reproduce identical results for engineering constants:

Table 8-2. Composite engineering properties calculated from Halpin-Tsai Equations.

$E_1[psi]$	$E_2\ [psi]$	$G_{12}\ [psi]$	ν_{12}	$G_{23}[psi]$	ν_{23}
$2.35\ 10^6$	$0.82\ 10^6$	$0.268\ 10^6$	0.32	$0.253\ 10^6$	0.519

In metric units:

$E_1[Pa]$	$E_2\ [Pa]$	$G_{12}\ [psi]$	ν_{12}	$G_{23}[psi]$	ν_{23}
$1.62\ 10^{10}$	$5.62\ 10^9$	$1.75\ 10^9$	0.32	$1.85\ 10^9$	0.519

Now we can generate numerical values for transversely isotropic material using Equations 3.9-13:

Table 8-3. Composite material constants.

$\mu\ [psi]$	$\mu_0\ [psi]$	$\lambda\ [psi]$	$\alpha_\lambda\ [psi]$	$\beta_\lambda\ [psi]$
$2.53\ 10^5$	$2.69\ 10^5$	$7.26\ 10^5$	$-8.94\ 10^4$	$1.737\ \ 10^6$

In metric units

$\mu\ [Pa]$	$\mu_0\ [Pa]$	$\lambda\ [Pa]$	$\alpha_\lambda\ [Pa]$	$\beta_\lambda\ [Pa]$
$1.85\ 10^9$	$1.75\ 10^9$	$5.00\ 10^9$	$-6.165\ 10^8$	$1.19\ \ 10^{10}$

This results in the following stiffness tensor in Voigt notation

$$C_{ij}^{HK} = \begin{bmatrix} 1.9210^{10} & 4.3910^9 & 4.3910^9 & 0 & 0 & 0 \\ 4.3910^9 & 8.7110^9 & 5.10^9 & 0 & 0 & 0 \\ 4.3910^9 & 5.10^9 & 8.7110^9 & 0 & 0 & 0 \\ 0 & 0 & 0 & 1.8510^9 & 0 & 0 \\ 0 & 0 & 0 & 0 & 1.810^9 & 0 \\ 0 & 0 & 0 & 0 & 0 & 1.810^9 \end{bmatrix} \tag{8.1-1}$$

And in Kelvin Notation

$$\hat{C}_{ij}^{HK} = \begin{bmatrix} 1.9210^{10} & 4.3910^9 & 4.3910^9 & 0 & 0 & 0 \\ 4.3910^9 & 8.7110^9 & 5.10^9 & 0 & 0 & 0 \\ 4.3910^9 & 5.10^9 & 8.7110^9 & 0 & 0 & 0 \\ 0 & 0 & 0 & 3.710^9 & 0 & 0 \\ 0 & 0 & 0 & 0 & 3.610^9 & 0 \\ 0 & 0 & 0 & 0 & 0 & 3.610^9 \end{bmatrix} \tag{8.1-2}$$

8.1.3 Material with Fibers in Single Configuration

Now we turn our attention to material containing fibers in single configuration. We can write the probability of finding a fiber of given configuration for such material in the following form:

$$\psi_R(\alpha,\beta,\gamma) = \frac{\delta(\alpha - A)\delta(\beta - B)\delta(\gamma - \Gamma)}{\cos B} \tag{8.1-3}$$

$$\psi_S(\xi,\eta) = \delta(\xi - \Xi)\delta(\eta - H) \tag{8.1-4}$$

Where δ is Dirac Delta function and parameters in capital Greek letters indicate the particular set of configuration parameters. Normalization condition shown in Equation 4.5-3 was satisfied by

$$\int_{\gamma=0}^{2\pi}\int_{\beta=-\frac{\pi}{2}}^{\frac{\pi}{2}}\int_{\alpha=0}^{2\pi}\delta(\alpha-A)\delta(\beta-B)\delta(\gamma-\Gamma)\cos\beta\ d\alpha d\beta d\gamma$$

$$= \int_{\alpha=0}^{2\pi}\delta(\alpha-A)d\alpha\int_{\beta=-\frac{\pi}{2}}^{\frac{\pi}{2}}\delta(\beta-B)\cos\beta\, d\beta\int_{\gamma=0}^{2\pi}\delta(\gamma-\Gamma)d\gamma \tag{8.1-5}$$

$$= \cos B$$

It follows directly from Equation 4.5-5 that

$$\psi(\alpha,\beta) = \frac{\delta(\alpha-A)\delta(\beta-B)}{\cos B}\int_{\gamma=0}^{2\pi}\delta(\gamma-\Gamma)d\gamma = \frac{\delta(\alpha-A)\delta(\beta-B)}{\cos B} \tag{8.1-6}$$

for material with fibers in single configuration.

8.1.4 Geometric Tensors for Material with fibers in single configuration

We can then evaluate orientation tensor directly from definitions shown in Equations 4.6-4 and 4.6-5:

$$a_{ij} = \int_{\beta=-\frac{\pi}{2}}^{\frac{\pi}{2}}\int_{\alpha=0}^{2\pi}p_i(\alpha,\beta)p_j(\alpha,\beta)\frac{\delta(\alpha-A)\delta(\beta-B)}{\cos B}\cos\beta\, d\alpha d\beta$$

$$= p_i(A,B)p_j(A,B) \tag{8.1-7}$$

$$i,j = 1,2,3$$

$$a_{ijkl} = \int_{\beta=-\frac{\pi}{2}}^{\frac{\pi}{2}}\int_{\alpha=0}^{2\pi}p_i(\alpha,\beta)p_j(\alpha,\beta)p_k(\alpha,\beta)p_l(\alpha,\beta)\frac{\delta(\alpha-A)\delta(\beta-B)}{\cos B}\cos\beta\ d\alpha d\beta$$

$$= p_i(A,B)p_j(A,B)\,p_k(A,B)p_l(A,B)\ \ i,j,k,l = 1,2,3 \tag{8.1-8}$$

The results are identical to evaluating Equations 4.6-8 through 4.6-13 for second order orientation tensor and Equations 4.6-15 through 4.6-29 for fourth order orientation tensor with $\alpha = A$ and $\beta = B$.

Similarly, for curvature tensor, we use Equations 4.6-35 and 4.6-36 and evaluate:

$$b_{ij} = \int_{\gamma=0}^{2\pi} \int_{\beta=-\frac{\pi}{2}}^{\frac{\pi}{2}} \int_{\alpha=0}^{2\pi} q_i(\alpha,\beta,\gamma) q_j(\alpha,\beta,\gamma) \frac{\delta(\alpha-A)\delta(\beta-B)\delta(\gamma-\Gamma)}{\cos B} \cos\beta \; d\alpha d\beta d\gamma$$
$$= q_i(A,B,\Gamma) q_j(A,B,\Gamma) \quad i,j = 1,2,3 \tag{8.1-9}$$

$$b_{ijkl} = \int_{\gamma=0}^{2\pi} \int_{\beta=-\frac{\pi}{2}}^{\frac{\pi}{2}} \int_{\alpha=0}^{2\pi} q_i q_j q_k q_l \frac{\delta(\alpha-A)\delta(\beta-B)\delta(\gamma-\Gamma)}{\cos B} \cos\beta \; d\alpha d\beta d\gamma$$
$$= q_i(A,B,\Gamma) q_j(A,B,\Gamma)\, q_k(A,B,\Gamma)\, q_l(A,B,\Gamma) \quad i,j,k,l$$
$$= 1,2,3 \tag{8.1-10}$$

We can also arrive at the same results using Equations 4.6-39 through 4.6-44 and 4.6-46 through 4.6-60 with $\alpha = A$, $\beta = B$ and $\gamma = \Gamma$.

For mixed tensor s_{ijkl}, we write

$$s_{ijkl}$$
$$= \int_{\gamma=0}^{2\pi} \int_{\beta=-\frac{\pi}{2}}^{\frac{\pi}{2}} \int_{\alpha=0}^{2\pi} \Big(p_i(\alpha,\beta) p_j(\alpha,\beta) q_k(\alpha,\beta,\gamma) q_l(\alpha,\beta,\gamma)$$
$$+ q_i(\alpha,\beta,\gamma) q_j(\alpha,\beta,\gamma) p_k(\alpha,\beta) p_l(\alpha,\beta) \Big) \frac{\delta(\alpha-A)\delta(\beta-B)\delta(\gamma-\Gamma)}{\cos B} \cos\beta \; d\alpha d\beta d\gamma \tag{8.1-11}$$
$$= p_i(A,B) p_j(A,B)\, q_k(A,B,\Gamma) q_l(A,B,\Gamma)$$
$$+ q_i(A,B,\Gamma) q_j(A,B,\Gamma)\, p_k(A,B) p_l(A,B) \quad i,j,k,l = 1,2,3$$

Again, this is equivalent to evaluating Equations 4.6-67 through 4.6-87 with $\alpha = A$, $\beta = B$ and $\gamma = \Gamma$.

We will use notation $a_{(2)}$, $b_{(2)}$ for second order orientation and curvature tensors and $a_{(4)}$, $b_{(4)}$ and $s_{(4)}$. These tensors will be represented in Voigt notation. We now provide specific examples:

For $A = 0$, $B = 0$ and $\Gamma = 0$ representing a fiber with vector p parallel to x axis of laboratory coordinate system:

$$a_{(2)} = \begin{bmatrix} 1 \\ 0 \\ 0 \\ 0 \\ 0 \\ 0 \end{bmatrix} a_{(4)} = \begin{bmatrix} 1 & 0 & 0 & 0 & 0 & 0 \\ 0 & 0 & 0 & 0 & 0 & 0 \\ 0 & 0 & 0 & 0 & 0 & 0 \\ 0 & 0 & 0 & 0 & 0 & 0 \\ 0 & 0 & 0 & 0 & 0 & 0 \\ 0 & 0 & 0 & 0 & 0 & 0 \end{bmatrix} \tag{8.1-12}$$

$$b_{(2)} = \begin{bmatrix} 0 \\ 1 \\ 0 \\ 0 \\ 0 \\ 0 \end{bmatrix} b_{(4)} = \begin{bmatrix} 0 & 0 & 0 & 0 & 0 & 0 \\ 0 & 1 & 0 & 0 & 0 & 0 \\ 0 & 0 & 0 & 0 & 0 & 0 \\ 0 & 0 & 0 & 0 & 0 & 0 \\ 0 & 0 & 0 & 0 & 0 & 0 \\ 0 & 0 & 0 & 0 & 0 & 0 \end{bmatrix} \tag{8.1-13}$$

$$s_{(4)} = \begin{bmatrix} 0 & 1 & 0 & 0 & 0 & 0 \\ 1 & 0 & 0 & 0 & 0 & 0 \\ 0 & 0 & 0 & 0 & 0 & 0 \\ 0 & 0 & 0 & 0 & 0 & 0 \\ 0 & 0 & 0 & 0 & 0 & 0 \\ 0 & 0 & 0 & 0 & 0 & 0 \end{bmatrix} \tag{8.1-14}$$

We can see that curvature tensors $b_{(2)}$ and $b_{(4)}$ represent oriented curvature aligned with the y axis of the laboratory coordinate system. The same geometric tensors can be obtained with parameters $A = \pi$, $B = 0$, $\Gamma = 0$ or $A = \pi$, $B = 0$, $\Gamma = \pi$.

A fiber with identical orientation, but different oriented curvature can be obtained by assigning various values of angle γ. For $A = 0$ or $A = \pi$, $B = 0$ and $\Gamma = \frac{\pi}{2}$:

$$a_{(2)} = \begin{bmatrix} 1 \\ 0 \\ 0 \\ 0 \\ 0 \\ 0 \end{bmatrix} a_{(4)} = \begin{bmatrix} 1 & 0 & 0 & 0 & 0 & 0 \\ 0 & 0 & 0 & 0 & 0 & 0 \\ 0 & 0 & 0 & 0 & 0 & 0 \\ 0 & 0 & 0 & 0 & 0 & 0 \\ 0 & 0 & 0 & 0 & 0 & 0 \\ 0 & 0 & 0 & 0 & 0 & 0 \end{bmatrix} \tag{8.1-15}$$

$$b_{(2)} = \begin{bmatrix} 0 \\ 0 \\ 1 \\ 0 \\ 0 \\ 0 \end{bmatrix} b_{(4)} = \begin{bmatrix} 0 & 0 & 0 & 0 & 0 & 0 \\ 0 & 0 & 0 & 0 & 0 & 0 \\ 0 & 0 & 1 & 0 & 0 & 0 \\ 0 & 0 & 0 & 0 & 0 & 0 \\ 0 & 0 & 0 & 0 & 0 & 0 \\ 0 & 0 & 0 & 0 & 0 & 0 \end{bmatrix} \tag{8.1-16}$$

$$s_{(4)} = \begin{bmatrix} 0 & 0 & 1 & 0 & 0 & 0 \\ 0 & 0 & 0 & 0 & 0 & 0 \\ 1 & 0 & 0 & 0 & 0 & 0 \\ 0 & 0 & 0 & 0 & 0 & 0 \\ 0 & 0 & 0 & 0 & 0 & 0 \\ 0 & 0 & 0 & 0 & 0 & 0 \end{bmatrix} \tag{8.1-17}$$

We can see that orientation tensors did not change for these configurations, however curvature and mixed tensors changed. The curvature tensors $b_{(2)}$ and $b_{(4)}$ now represent oriented curvature parallel with the z axis of the laboratory coordinate system.

Curvature and mixed tensors for configuration with oriented curvature not aligned with laboratory coordinate system have more general form. For example, we can assume $A = 0,\ B = 0$ and $\Gamma = \frac{\pi}{6}$:

$$a_{(2)} = \begin{bmatrix} 1 \\ 0 \\ 0 \\ 0 \\ 0 \\ 0 \end{bmatrix} a_{(4)} = \begin{bmatrix} 1 & 0 & 0 & 0 & 0 & 0 \\ 0 & 0 & 0 & 0 & 0 & 0 \\ 0 & 0 & 0 & 0 & 0 & 0 \\ 0 & 0 & 0 & 0 & 0 & 0 \\ 0 & 0 & 0 & 0 & 0 & 0 \\ 0 & 0 & 0 & 0 & 0 & 0 \end{bmatrix} \tag{81.18}$$

$$b_{(2)} = \begin{bmatrix} 0 \\ \frac{3}{4} \\ \frac{1}{4} \\ \frac{\sqrt{3}}{4} \\ 0 \\ 0 \end{bmatrix} b_{(4)} = \begin{bmatrix} 0 & 0 & 0 & 0 & 0 & 0 \\ 0 & \frac{9}{16} & \frac{3}{16} & \frac{3\sqrt{3}}{16} & 0 & 0 \\ 0 & \frac{3}{16} & \frac{1}{16} & \frac{\sqrt{3}}{16} & 0 & 0 \\ 0 & \frac{3\sqrt{3}}{16} & \frac{\sqrt{3}}{16} & \frac{3}{16} & 0 & 0 \\ 0 & 0 & 0 & 0 & 0 & 0 \\ 0 & 0 & 0 & 0 & 0 & 0 \end{bmatrix} \tag{8.1-19}$$

$$s_{(4)} = \begin{bmatrix} 0 & \frac{3}{4} & \frac{1}{4} & \frac{\sqrt{3}}{4} & 0 & 0 \\ \frac{3}{4} & 0 & 0 & 0 & 0 & 0 \\ \frac{1}{4} & 0 & 0 & 0 & 0 & 0 \\ \frac{\sqrt{3}}{4} & 0 & 0 & 0 & 0 & 0 \\ 0 & 0 & 0 & 0 & 0 & 0 \\ 0 & 0 & 0 & 0 & 0 & 0 \end{bmatrix} \tag{8.1-20}$$

For $A = \frac{\pi}{2}$ or $A = \frac{3\pi}{2}$, $B = 0$ and $\Gamma = 0$ representing fiber with vector **p** aligned with y axis:

$$a_{(2)} = \begin{bmatrix} 0 \\ 1 \\ 0 \\ 0 \\ 0 \\ 0 \end{bmatrix} a_{(4)} = \begin{bmatrix} 0 & 0 & 0 & 0 & 0 & 0 \\ 0 & 1 & 0 & 0 & 0 & 0 \\ 0 & 0 & 0 & 0 & 0 & 0 \\ 0 & 0 & 0 & 0 & 0 & 0 \\ 0 & 0 & 0 & 0 & 0 & 0 \\ 0 & 0 & 0 & 0 & 0 & 0 \end{bmatrix} \tag{8.1-21}$$

$$b_{(2)} = \begin{bmatrix} 1 \\ 0 \\ 0 \\ 0 \\ 0 \\ 0 \end{bmatrix} b_{(4)} = \begin{bmatrix} 1 & 0 & 0 & 0 & 0 & 0 \\ 0 & 0 & 0 & 0 & 0 & 0 \\ 0 & 0 & 0 & 0 & 0 & 0 \\ 0 & 0 & 0 & 0 & 0 & 0 \\ 0 & 0 & 0 & 0 & 0 & 0 \\ 0 & 0 & 0 & 0 & 0 & 0 \end{bmatrix} \tag{8.1-22}$$

$$s_{(4)} = \begin{bmatrix} 0 & 1 & 0 & 0 & 0 & 0 \\ 1 & 0 & 0 & 0 & 0 & 0 \\ 0 & 0 & 0 & 0 & 0 & 0 \\ 0 & 0 & 0 & 0 & 0 & 0 \\ 0 & 0 & 0 & 0 & 0 & 0 \\ 0 & 0 & 0 & 0 & 0 & 0 \end{bmatrix} \tag{8.1-23}$$

Finally, fiber aligned with z axis given by angles $A = 0$, $B = \frac{\pi}{2}$: and $\Gamma = 0$:

$$a_{(2)} = \begin{bmatrix} 0 \\ 0 \\ 1 \\ 0 \\ 0 \\ 0 \end{bmatrix} a_{(4)} = \begin{bmatrix} 0 & 0 & 0 & 0 & 0 & 0 \\ 0 & 0 & 0 & 0 & 0 & 0 \\ 0 & 0 & 1 & 0 & 0 & 0 \\ 0 & 0 & 0 & 0 & 0 & 0 \\ 0 & 0 & 0 & 0 & 0 & 0 \\ 0 & 0 & 0 & 0 & 0 & 0 \end{bmatrix} \tag{8.1-24}$$

$$b_{(2)} = \begin{bmatrix} 0 \\ 1 \\ 0 \\ 0 \\ 0 \\ 0 \end{bmatrix} b_{(4)} = \begin{bmatrix} 0 & 0 & 0 & 0 & 0 & 0 \\ 0 & 1 & 0 & 0 & 0 & 0 \\ 0 & 0 & 0 & 0 & 0 & 0 \\ 0 & 0 & 0 & 0 & 0 & 0 \\ 0 & 0 & 0 & 0 & 0 & 0 \\ 0 & 0 & 0 & 0 & 0 & 0 \end{bmatrix} \tag{8.1-25}$$

$$s_{(4)} = \begin{bmatrix} 0 & 0 & 0 & 0 & 0 & 0 \\ 0 & 0 & 1 & 0 & 0 & 0 \\ 0 & 1 & 0 & 0 & 0 & 0 \\ 0 & 0 & 0 & 0 & 0 & 0 \\ 0 & 0 & 0 & 0 & 0 & 0 \\ 0 & 0 & 0 & 0 & 0 & 0 \end{bmatrix} \tag{8.1-26}$$

And more general case with $A = 0$, $B = \frac{\pi}{2}$: and $\Gamma = \frac{\pi}{6}$:

$$a_{(2)} = \begin{bmatrix} 0 \\ 0 \\ 1 \\ 0 \\ 0 \\ 0 \end{bmatrix} a_{(4)} = \begin{bmatrix} 0 & 0 & 0 & 0 & 0 & 0 \\ 0 & 0 & 0 & 0 & 0 & 0 \\ 0 & 0 & 1 & 0 & 0 & 0 \\ 0 & 0 & 0 & 0 & 0 & 0 \\ 0 & 0 & 0 & 0 & 0 & 0 \\ 0 & 0 & 0 & 0 & 0 & 0 \end{bmatrix} \tag{8.1-27}$$

$$b_{(2)} = \begin{bmatrix} \frac{1}{4} \\ \frac{3}{4} \\ 0 \\ 0 \\ 0 \\ -\frac{\sqrt{3}}{4} \end{bmatrix} b_{(4)} = \begin{bmatrix} \frac{1}{16} & \frac{3}{16} & 0 & 0 & 0 & -\frac{\sqrt{3}}{16} \\ \frac{3}{16} & \frac{9}{16} & 0 & 0 & 0 & -\frac{3\sqrt{3}}{16} \\ 0 & 0 & 0 & 0 & 0 & 0 \\ 0 & 0 & 0 & 0 & 0 & 0 \\ 0 & 0 & 0 & 0 & 0 & 0 \\ -\frac{\sqrt{3}}{16} & -\frac{3\sqrt{3}}{16} & 0 & 0 & 0 & \frac{3}{16} \end{bmatrix} \tag{8.1-28}$$

$$s_{(4)} = \begin{bmatrix} 0 & 0 & \frac{1}{4} & 0 & 0 & 0 \\ 0 & 0 & \frac{3}{4} & 0 & 0 & 0 \\ \frac{1}{4} & \frac{3}{4} & 0 & 0 & 0 & -\frac{\sqrt{3}}{4} \\ 0 & 0 & 0 & 0 & 0 & 0 \\ 0 & 0 & 0 & 0 & 0 & 0 \\ 0 & 0 & -\frac{\sqrt{3}}{4} & 0 & 0 & 0 \end{bmatrix} \tag{8.1-29}$$

8.1.5 Parameters for a Material with Fibers in Single Configuration

We can recall that material with fibers in single configuration is orthotropic material. We therefore need nine constants. Using previously suggested approach for obtaining material parameters through planar orientation averaging of transversely isotropic material obtained using semi-empirical Halpin-Tsai-Kardos [55] Equations.

For single configuration, we use ψ_S in the form given by Equation 8.1-4 and calculate material constants from Equations 4.5-36 through 4.5-44 in the following form

$$\bar{k} = \langle\langle\langle k \rangle\rangle\rangle = \int_{\eta=0}^{\infty}\int_{\xi=0}^{\infty} k(\xi,\eta)\psi_S(\xi,\eta)d\xi d\eta = \int_{\eta=0}^{\infty}\int_{\xi=0}^{\infty} k(\xi,\eta)\delta(\xi - \Xi)\delta(\eta - H)\, d\xi d\eta = k(\Xi, H) \tag{8.1-30}$$

We can therefore calculate five parameters $\mu_s(\Xi), \mu_0(\Xi)$, $\lambda_s(\Xi), \alpha_\lambda(\Xi), \beta_\lambda(\Xi)$ for transversely isotropic material using Halpin-Tsai-Kardos [55] Equation from Section 3.9 and then obtain orientation tensor $\tilde{a}_{ijkl}(H)$ using Equations 4.7-12 through 4.7-14. Then we can use Equations 4.7-45 through 4.7-53 to obtain parameters for a material with fibers in single configuration.

We can use fiber and matrix properties from Section 8.1.2 along with three values of Ξ to provide examples of five parameters $\mu_s(\Xi), \mu_0(\Xi),\ \lambda_s(\Xi), \alpha_\lambda(\Xi), \beta_\lambda(\Xi)$

$$\Xi = 10\text{: } \mu_s = 1.85\ 10^9\ Pa, \mu_0 = 1.75\ 10^9\ Pa\ ,\ \lambda_s = 5.57\ 10^9\ Pa, \alpha_\lambda = -8.19\ 10^8\ Pa, \beta_\lambda = 7.10\ 10^9\ Pa \tag{8.1-31}$$

$$\Xi = 505\text{: } \mu_s = 1.85\ 10^9\ Pa, \mu_0 = 1.75\ 10^9\ Pa\ ,\ \lambda_s = 4.95\ 10^9\ Pa, \alpha_\lambda = -5.97\ 10^8\ Pa, \beta_\lambda = 1.28\ 10^{10}\ Pa \tag{8.1-32}$$

$$\Xi = 1000\text{: } \mu_s = 1.85\ 10^9\ Pa, \mu_0 = 1.75\ 10^9\ Pa\ ,\ \lambda_s = 4.94\ 10^9\ Pa, \alpha_\lambda = -5.94\ 10^8\ Pa, \beta_\lambda = 1.29\ 10^{10}\ Pa \tag{8.1-33}$$

Examples of $\tilde{a}_{ijkl}(H)$ are given below. For straight fiber $H = 0$

$$\tilde{a}_{(2)} = \begin{bmatrix} 1 \\ 0 \\ 0 \\ 0 \\ 0 \\ 0 \end{bmatrix}, \quad \tilde{a}_{(4)} = \begin{bmatrix} 1 & 0 & 0. & 0. & 0. & 0. \\ 0 & 0 & 0. & 0. & 0. & 0. \\ 0. & 0. & 0. & 0. & 0. & 0. \\ 0. & 0. & 0. & 0. & 0. & 0. \\ 0. & 0. & 0. & 0. & 0. & 0. \\ 0. & 0. & 0. & 0. & 0. & 0 \end{bmatrix} \tag{8.1-34}$$

For slightly curved fiber $H = \frac{\pi}{18}$

$$\tilde{a}_{(2)} = \begin{bmatrix} 9.97\ 10^{-1} \\ 2.53\ 10^{-3} \\ 0. \\ 0. \\ 0. \\ 0. \end{bmatrix}, \quad \tilde{a}_{(4)} = \begin{bmatrix} 9.94\ 10^{-1} & 2.52\ 10^{-3} & 0. & 0. & 0. & 0. \\ 2.52\ 10^{-3} & 1.15\ 10^{-5} & 0. & 0. & 0. & 0. \\ 0. & 0. & 0. & 0. & 0. & 0. \\ 0. & 0. & 0. & 0. & 0. & 0. \\ 0. & 0. & 0. & 0. & 0. & 0. \\ 0. & 0. & 0. & 0. & 0. & 2.52\ 10^{-3} \end{bmatrix} \tag{8.1-35}$$

For significantly curved fiber enclosing quarter of a circle $H = \frac{\pi}{2}$

$$\tilde{a}_{(2)} = \begin{bmatrix} 0.818 \\ 0.183 \\ 0. \\ 0. \\ 0. \\ 0. \end{bmatrix}, \quad \tilde{a}_{(4)} = \begin{bmatrix} 0.693 & 0.125 & 0. & 0. & 0. & 0. \\ 0.125 & 0.0567 & 0. & 0. & 0. & 0. \\ 0. & 0. & 0. & 0. & 0. & 0. \\ 0. & 0. & 0. & 0. & 0. & 0. \\ 0. & 0. & 0. & 0. & 0. & 0. \\ 0. & 0. & 0. & 0. & 0. & 0.125 \end{bmatrix} \tag{8.1-36}$$

And for a fiber enclosing half of a circle $H = \pi$

$$\tilde{a}_{(2)} = \begin{bmatrix} 0.5 \\ 0.5 \\ 0. \\ 0. \\ 0. \\ 0. \end{bmatrix}, \quad \tilde{a}_{(4)} = \begin{bmatrix} 0.375 & 0.125 & 0. & 0. & 0. & 0. \\ 0.125 & 0.375 & 0. & 0. & 0. & 0. \\ 0. & 0. & 0. & 0. & 0. & 0. \\ 0. & 0. & 0. & 0. & 0. & 0. \\ 0. & 0. & 0. & 0. & 0. & 0. \\ 0. & 0. & 0. & 0. & 0. & 0.125 \end{bmatrix} \tag{8.1-37}$$

Note that $\tilde{a}_{1111}$ and $\tilde{a}_{2222}$ are equal in the last example. We can now generate nine material constants for orthotropic stiffness tensor using Equations 4.7-45 through 4.7-53. In examples below, we use $\Xi = 505$, and examine cases from straight fiber ($H = 0$) to a fiber enclosing half of a circle ($H = \pi$).

$\Xi = 505, H = 0$:

$$\mu = 1.85\ 10^9\ Pa, \lambda = 4.95\ 10^9\ Pa, \alpha_{\lambda 1} = -5.97\ 10^8\ Pa, \alpha_{\lambda 2} = 0.0\ Pa, \mu_1 = -5.28\ 10^7\ Pa, \mu_2 = 0.0\ Pa, \beta_{\lambda 1} = 1.28\ 10^{10}\ Pa, \beta_{\lambda 2} = 0.0\ Pa, \beta_{\lambda 3} = 0.0\ Pa \tag{8.1-38}$$

$\Xi = 505, H = \frac{\pi}{18}$:

$$\mu = 1.82\ 10^9\ Pa, \lambda = 5.01\ 10^9\ Pa, \alpha_{\lambda 1} = -6.59\ 10^8\ Pa, \alpha_{\lambda 2} = -6.59\ 10^7\ Pa, \mu_1 = -2.05\ 10^7\ Pa, \mu_2 = 3.21\ 10^7\ Pa, \beta_{\lambda 1} = 1.27\ 10^{10}\ Pa, \beta_{\lambda 2} = 1.48\ 10^5\ Pa, \beta_{\lambda 3} = 9.67\ 10^7\ Pa \tag{8.1-39}$$

$\Xi = 505, H = \frac{\pi}{2}$:

8.1-1

$$\mu = 2.55\ 10^8\ Pa, \lambda = 8.14\ 10^9\ Pa, \alpha_{\lambda 1} = -3.68\ 10^9\ Pa, \alpha_{\lambda 2} = -3.3\ 10^9\ Pa, \mu_1 = 1.55\ 10^9\ Pa, \mu_2 = 1.58\ 10^9\ Pa, \beta_{\lambda 1} = 8.85\ 10^9\ Pa, \beta_{\lambda 2} = 7.24\ 10^8\ Pa, \beta_{\lambda 3} = 4.79\ 10^9\ Pa \tag{8.1-40}$$

$\Xi = 505, H = \pi$:

$$\mu = 2.55\ 10^8\ Pa, \lambda = 8.14\ 10^9\ Pa, \alpha_{\lambda 1} = -3.49\ 10^9\ Pa, \alpha_{\lambda 2} = -3.49\ 10^9\ Pa, \mu_1 = 1.57\ 10^9\ Pa, \mu_2 = 1.57\ 10^9\ Pa, \beta_{\lambda 1} = 4.79\ 10^9\ Pa, \beta_{\lambda 2} = 4.79\ 10^8\ Pa, \beta_{\lambda 3} = 4.79\ 10^9\ Pa \tag{8.1-41}$$

Note that for a fiber enclosing half of a circle, there are only five unique constants. This suggests that we obtain transversely isotropic form of the stiffness tensor.

8.1.6 Stiffness tensor for Material in Single Confguration

We can now examine stiffness tensors for several materials with fibers in single configuration. We will use examples of geometric tensors and material constants obtained above.

The first example provides stiffness tensor for material with straight fibers aligned along x axis. We can use geometric tensors from Equations 8.1-12 through 8.1-14 with material constants from Equation 8.1-38.

The stiffness tensor in Voigt notation:

$$\boldsymbol{C} = \begin{bmatrix} 2.10^{10} & 4.3510^{9} & 4.3510^{9} & 0 & 0 & 0 \\ 4.3510^{9} & 8.6510^{9} & 4.9510^{9} & 0 & 0 & 0 \\ 4.3510^{9} & 4.9510^{9} & 8.6510^{9} & 0 & 0 & 0 \\ 0 & 0 & 0 & 1.8510^{9} & 0 & 0 \\ 0 & 0 & 0 & 0 & 1.810^{9} & 0 \\ 0 & 0 & 0 & 0 & 0 & 1.810^{9} \end{bmatrix} \tag{8.1-42}$$

The stiffness tensor in Kelvin notation:

$$\widehat{\boldsymbol{C}} = \begin{bmatrix} 2.10^{10} & 4.3510^{9} & 4.3510^{9} & 0 & 0 & 0 \\ 4.3510^{9} & 8.6510^{9} & 4.9510^{9} & 0 & 0 & 0 \\ 4.3510^{9} & 4.9510^{9} & 8.6510^{9} & 0 & 0 & 0 \\ 0 & 0 & 0 & 3.710^{9} & 0 & 0 \\ 0 & 0 & 0 & 0 & 3.610^{9} & 0 \\ 0 & 0 & 0 & 0 & 0 & 3.610^{9} \end{bmatrix} \tag{8.1-43}$$

Kelvin eigen-moduli:

$$\boldsymbol{\lambda} = [2.3810^{10}, 9.8710^{9}, 3.710^{9}, 3.710^{9}, 3.610^{9}, 3.610^{9}] \tag{8.1-44}$$

This is clearly transversely isotropic material with $\boldsymbol{e}_1$ defining the plane of isotropy and four distinct Kelvin moduli as expected.

In the next example, we let the fibers slightly bend. We use geometric tensors from Equations 8.1-12 through 8.1-14 with material constants from Equation 8.1-39.

The stiffness tensor in Voigt notation:

$$\boldsymbol{C} = \begin{bmatrix} 2.10^{10} & 4.3810^{9} & 4.3510^{9} & 0 & 0 & 0 \\ 4.3810^{9} & 8.6510^{9} & 4.9510^{9} & 0 & 0 & 0 \\ 4.3510^{9} & 4.9510^{9} & 8.6510^{9} & 0 & 0 & 0 \\ 0 & 0 & 0 & 1.8510^{9} & 0 & 0 \\ 0 & 0 & 0 & 0 & 1.810^{9} & 0 \\ 0 & 0 & 0 & 0 & 0 & 1.8310^{9} \end{bmatrix} \tag{8.1-45}$$

The stiffness tensor in Kelvin notation:

$$\widehat{\boldsymbol{C}} = \begin{bmatrix} 2.10^{10} & 4.3810^{9} & 4.3510^{9} & 0 & 0 & 0 \\ 4.3810^{9} & 8.6510^{9} & 4.9510^{9} & 0 & 0 & 0 \\ 4.3510^{9} & 4.9510^{9} & 8.6510^{9} & 0 & 0 & 0 \\ 0 & 0 & 0 & 3.710^{9} & 0 & 0 \\ 0 & 0 & 0 & 0 & 3.610^{9} & 0 \\ 0 & 0 & 0 & 0 & 0 & 3.6610^{9} \end{bmatrix} \tag{8.1-46}$$

Kelvin eigen-moduli

$$\boldsymbol{\lambda} = [3.93\ 10^{6}, 1.59\ 10^{6}, 5.46\ 10^{5}, 5.37\ 10^{5}, 5.07\ 10^{5}, 5.07\ 10^{5}] \tag{8.1-47}$$

This material is orthotropic, although one could reasonably approximate it as transversely isotropic.

Now we allow the fibers to bend significantly so that the fiber centerline spans quarter of a circle. We use geometric tensors from Equations 8.1-12 through 8.1-14 with material constants from Equation 8.1-40.

The stiffness tensor in Voigt notation:

$$\boldsymbol{C} = \begin{bmatrix} 1.6410^{10} & 5.9510^{9} & 4.4610^{9} & 0 & 0 & 0 \\ 5.9510^{9} & 9.1210^{9} & 4.8410^{9} & 0 & 0 & 0 \\ 4.4610^{9} & 4.8410^{9} & 8.6510^{9} & 0 & 0 & 0 \\ 0 & 0 & 0 & 1.8410^{9} & 0 & 0 \\ 0 & 0 & 0 & 0 & 1.8110^{9} & 0 \\ 0 & 0 & 0 & 0 & 0 & 3.410^{9} \end{bmatrix} \tag{8.1-48}$$

The stiffness tensor in Kelvin notation:

$$\widehat{\boldsymbol{C}} = \begin{bmatrix} 1.6410^{10} & 5.9510^{9} & 4.4610^{9} & 0 & 0 & 0 \\ 5.9510^{9} & 9.1210^{9} & 4.8410^{9} & 0 & 0 & 0 \\ 4.4610^{9} & 4.8410^{9} & 8.6510^{9} & 0 & 0 & 0 \\ 0 & 0 & 0 & 3.6810^{9} & 0 & 0 \\ 0 & 0 & 0 & 0 & 3.6210^{9} & 0 \\ 0 & 0 & 0 & 0 & 0 & 6.7910^{9} \end{bmatrix} \tag{8.1-49}$$

Kelvin eigen-moduli

$$\boldsymbol{\lambda} = [2.2610^{10}, 7.6310^{9}, 6.7910^{9}, 3.9310^{9}, 3.6810^{9}, 3.6210^{9}] \tag{8.1-50}$$

This material is clearly orthotropic with six distinct Kelvin moduli.

We can bend the fibers further, until they form half of a circle. Again, we use geometric tensors from Equations 8.1-12 through 8.1-14 with material constants from Equation 8.1-41.

The stiffness tensor in Voigt notation:

$$C = \begin{bmatrix} 1.2710^{10} & 5.9510^{9} & 4.6510^{9} & 0 & 0 & 0 \\ 5.9510^{9} & 1.2710^{10} & 4.6510^{9} & 0 & 0 & 0 \\ 4.6510^{9} & 4.6510^{9} & 8.6510^{9} & 0 & 0 & 0 \\ 0 & 0 & 0 & 1.8310^{9} & 0 & 0 \\ 0 & 0 & 0 & 0 & 1.8310^{9} & 0 \\ 0 & 0 & 0 & 0 & 0 & 3.410^{9} \end{bmatrix} \tag{8.1-51}$$

The stiffness tensor in Kelvin notation:

$$\hat{C} = \begin{bmatrix} 1.2710^{10} & 5.9510^{9} & 4.6510^{9} & 0 & 0 & 0 \\ 5.9510^{9} & 1.2710^{10} & 4.6510^{9} & 0 & 0 & 0 \\ 4.6510^{9} & 4.6510^{9} & 8.6510^{9} & 0 & 0 & 0 \\ 0 & 0 & 0 & 3.6510^{9} & 0 & 0 \\ 0 & 0 & 0 & 0 & 3.6510^{9} & 0 \\ 0 & 0 & 0 & 0 & 0 & 6.7910^{9} \end{bmatrix} \tag{8.1-52}$$

Kelvin eigen-moduli

$$\lambda = [2.1910^{10}, 6.7910^{9}, 6.7910^{9}, 5.410^{9}, 3.6510^{9}, 3.6510^{9}] \tag{8.1-53}$$

This material is transversely isotropic with e_3 definig the plane of isotropy.

We have therefore transformed transversely isotropic material with plane of symmetry defined by $e_1$to orthotropic material and finally to transversely isotropic material with plane of symmetry defined by e_3 by simply bending the fibers in single plane.

We can also demonstrate that changing rotation configuration of the material does not change the nature of the material. We use geometric tensors from Equations 8.1-27 through 8.1-29 with material constants from Equation 8.1-40.

The stiffness tensor in Voigt notation:

$$C = \begin{bmatrix} 8.6310^{9} & 4.9810^{9} & 4.8310^{9} & 0 & 0 & -2.3110^{7} \\ 4.9810^{9} & 8.8710^{9} & 5.5810^{9} & 0 & 0 & -1.810^{8} \\ 4.8310^{9} & 5.5810^{9} & 1.6410^{10} & 0 & 0 & -6.4410^{8} \\ 0 & 0 & 0 & 3.10^{9} & -6.8710^{8} & 0 \\ 0 & 0 & 0 & -6.8710^{8} & 2.2110^{9} & 0 \\ -2.3110^{7} & -1.810^{8} & -6.4410^{8} & 0 & 0 & 1.9810^{9} \end{bmatrix} \tag{8.1-54}$$

The stiffness tensor in Kelvin notation:

$$\hat{\mathbb{C}} = \begin{bmatrix} 8.6310^9 & 4.9810^9 & 4.8310^9 & 0 & 0 & -3.2710^7 \\ 4.9810^9 & 8.8710^9 & 5.5810^9 & 0 & 0 & -2.5410^8 \\ 4.8310^9 & 5.5810^9 & 1.6410^{10} & 0 & 0 & -9.1110^8 \\ 0 & 0 & 0 & 6.10^9 & -1.3710^9 & 0 \\ 0 & 0 & 0 & -1.3710^9 & 4.4110^9 & 0 \\ -3.2710^7 & -2.5410^8 & -9.1110^8 & 0 & 0 & 3.9610^9 \end{bmatrix} \tag{8.1-55}$$

Kelvin eigen-moduli

$$\lambda = [2.2610^{10}, 7.6310^9, 6.7910^9, 3.9310^9, 3.6810^9, 3.6210^9] \tag{8.1-56}$$

Although the tensors in Equations 8.1-48 and 8.1-54 are noticeably different, they represent material with the same properties as evidenced by comparison of Kelvin moduli in Equations 8.1-50 and 8.1-56.

8.1.7 Material with Fibers in Finite Set of Configurations

We now consider material consisting of fibers in finite set of configurations. Let's assume that we can find fibers of N configurations within a material. The probability of finding a configuration within the material is given by Υ_K. Since we must find each fiber in the material, we can write

$$\sum_{K=1}^{N} \Upsilon_K = 1 \tag{8.1-57}$$

Then we can write the rotation and shape distribution functions in the following form:

$$\psi_R(\alpha, \beta, \gamma) = \sum_{K=1}^{N} \Upsilon_K \frac{\delta(\alpha - A_K)\delta(\beta - B_K)\delta(\gamma - \Gamma_K)}{\sum_{L=1}^{N} \Upsilon_L \cos B_L} \tag{8.1-58}$$

$$\psi_S(\xi, \eta) = \sum_{K=1}^{N} \Upsilon_K \, \delta(\xi - \Xi_K)\delta(\eta - H_K) \tag{8.1-59}$$

Where δ is Dirac Delta function and parameters in capital Greek letters with a subscript indicate the particular set of configuration parameters. Normalization condition in Equation 4.5-3 was satisfied by

$$\int_{\gamma=0}^{2\pi}\int_{\beta=-\frac{\pi}{2}}^{\frac{\pi}{2}}\int_{\alpha=0}^{2\pi}\sum_{K=1}^{N}\Upsilon_K\,\delta(\alpha-A_K)\delta(\beta-B_K)\delta(\gamma-\Gamma_K)\cos\beta\;d\alpha d\beta d\gamma$$

$$=\sum_{K=1}^{N}\Upsilon_K\left(\int_{\alpha=-0}^{2\pi}\delta(\alpha-A_K)d\alpha\int_{\beta=-\frac{\pi}{2}}^{\frac{\pi}{2}}\delta(\beta-B_K)\cos\beta\,d\beta\int_{\gamma=0}^{2\pi}\delta(\gamma-\Gamma_K)d\gamma\right)=\sum_{K=1}^{N}\Upsilon_K\cos B_K \tag{8.1-60}$$

It follows directly from Equation 4.5-5 that

$$\psi(\alpha,\beta)=\sum_{K=1}^{N}\Upsilon_K\left(\frac{\delta(\alpha-A_K)\delta(\beta-B_K)}{\sum_{L=1}^{N}\Upsilon_L\cos B_L}\int_{\gamma=0}^{2\pi}\delta(\gamma-\Gamma_K)d\gamma\right)=\sum_{K=1}^{N}\Upsilon_K\frac{\delta(\alpha-A_K)\delta(\beta-B_K)}{\sum_{L=1}^{N}\Upsilon_L\cos B_L} \tag{8.1-61}$$

For material with fibers in finite set of configurations. For N=1, Equations 8.1-57 through 8.1-61 reduce to Equations 8.1-3 through 8.1-6 for material with fibers in single configuration.

8.1.8 Geometric Tensors for Material With Fibers in Finite Set of Configurations

We can then evaluate orientation tensor directly from definitions shown in Equations 4.6-4 and 4.6-5:

$$a_{ij}=\int_{\beta=-\frac{\pi}{2}}^{\frac{\pi}{2}}\int_{\alpha=0}^{2\pi}p_i(\alpha,\beta)p_j(\alpha,\beta)\sum_{K=1}^{N}\Upsilon_K\frac{\delta(\alpha-A_K)\delta(\beta-B_K)}{\sum_{L=1}^{N}\Upsilon_L\cos B_L}\cos\beta\,d\alpha d\beta=\sum_{K=1}^{N}\Upsilon_K\frac{p_i(A,B_K)p_j(A,B_K)}{\sum_{L=1}^{N}\Upsilon_L\cos B_L} \tag{8.1-62}$$

$$i,j=1,2,3$$

$$a_{ijkl}$$

$$= \int_{\beta=-\frac{\pi}{2}}^{\frac{\pi}{2}} \int_{\alpha=0}^{2\pi} p_i(\alpha,\beta)p_j(\alpha,\beta)p_k(\alpha,\beta)p_l(\alpha,\beta) \sum_{K=1}^{N} \Upsilon_K \frac{\delta(\alpha - A_K)\delta(\beta - B_K)}{\sum_{L=1}^{N} \Upsilon_L \cos B_L} \cos\beta \; d\alpha d\beta$$

$$= \sum_{K=1}^{N} \Upsilon_K \frac{p_i(A,B_K)p_j(A,B_K)p_k(A,B_K)p_l(A,B_K)}{\sum_{L=1}^{N} \Upsilon_L \cos B_L} \quad i,j,k,l = 1,2,3 \tag{8.1-63}$$

The results are identical to evaluating Equations 4.6-8 through 4.6-13 for second order orientation tensor and in Equestions 4.6-15 through 4.6-29 for fourth order orientation tensor with $\alpha = A_K$ and $\beta = B_K$for N configurations and performing requisite normalization.

Similarly, for curvature tensor, we can transform Equations 4.6-35 and 4.6-36 and evaluate:

$$b_{ij}$$

$$= \int_{\gamma=0}^{2\pi} \int_{\beta=-\frac{\pi}{2}}^{\frac{\pi}{2}} \int_{\alpha=0}^{2\pi} q_i(\alpha,\beta,\gamma)q_j(\alpha,\beta,\gamma) \sum_{K=1}^{N} \Upsilon_K \frac{\delta(\alpha - A_K)\delta(\beta - B_K)\delta(\gamma - \Gamma_K)}{\sum_{L=1}^{N} \Upsilon_L \cos B_L} \cos\beta \; d\alpha d\beta d\gamma$$

$$= \sum_{K=1}^{N} \Upsilon_K \frac{q_i(A,B,\Gamma)q_j(A,B,\Gamma)}{\sum_{L=1}^{N} \Upsilon_L \cos B_L} \quad i,j = 1,2,3 \tag{8.1-64}$$

$$b_{ijkl}$$

$$= \int_{\gamma=0}^{2\pi} \int_{\beta=-\frac{\pi}{2}}^{\frac{\pi}{2}} \int_{\alpha=0}^{2\pi} q_i q_j q_k q_l \sum_{K=1}^{N} \Upsilon_K \frac{\delta(\alpha - A_K)\delta(\beta - B_K)\delta(\gamma - \Gamma_K)}{\sum_{L=1}^{N} \Upsilon_L \cos B_L} \cos\beta \; d\alpha d\beta d\gamma$$

$$= \sum_{K=1}^{N} \Upsilon_K \frac{q_i(A,B,\Gamma)q_j(A,B,\Gamma)\, q_k(A,B,\Gamma)\, q_l(A,B,\Gamma)}{\sum_{L=1}^{N} \Upsilon_L \cos B_L} \quad i,j,k,l = 1,2,3 \tag{8.1-65}$$

We can also arrive at the same results using Equations 4.6-39 through 4.6-44 and 4.6-46 through 4.6-60 with $\alpha = A_K$, $\beta = B_K$ and $\gamma = \Gamma_K$ for N configurations along with normalization condition.

For mixed tensor s_{ijkl}, we write

$$
\begin{aligned}
& s_{ijkl} \\
&= \int_{\gamma=0}^{2\pi} \int_{\beta=-\frac{\pi}{2}}^{\frac{\pi}{2}} \int_{\alpha=0}^{2\pi} \Big(p_i(\alpha,\beta) p_j(\alpha,\beta) q_k(\alpha,\beta,\gamma) q_l(\alpha,\beta,\gamma) \\
&+ q_i(\alpha,\beta,\gamma) q_j(\alpha,\beta,\gamma) p_k(\alpha,\beta) p_l(\alpha,\beta) \Big) \sum_{K=1}^{N} \Upsilon_K \frac{\delta(\alpha - A_K)\delta(\beta - B_K)\delta(\gamma - \Gamma_K)}{\sum_{L=1}^{N} \Upsilon_L \cos B_L} \cos\beta \; d\alpha d\beta d\gamma \\
&= \sum_{K=1}^{N} \Upsilon_K \frac{p_i(A,B) p_j(A,B)\, q_k(A,B,\Gamma) q_l(A,B,\Gamma) + q_i(A,B,\Gamma) q_j(A,B,\Gamma)\, p_k(A,B) p_l(A,B)}{\sum_{L=1}^{N} \Upsilon_L \cos B_L} \quad i,j,k,l \\
&= 1,2,3
\end{aligned}
\tag{8.1-66}
$$

Again, this is equivalent to evaluating Equations 4.6-67 through 4.6-87 with $\alpha = A_K$, $\beta = B_K$ and $\gamma = \Gamma_K$ for N configurations and normalization condition listed above.

We can generate a hypothetical material consisting of an ensemble of 10,000 fibers with random fiber parameters in the following ranges $A_K \in \langle 0,2\pi \rangle, B_K \in \langle -\frac{\pi}{2}, \frac{\pi}{2} \rangle, \Gamma_K \in \langle 0,2\pi \rangle$. An example of geometric tensors generated is given below:

$$
a_{(2)} = \begin{bmatrix} 3.35\ 10^{-1} \\ 3.28\ 10^{-1} \\ 3.36\ 10^{-1} \\ -5.39\ 10^{-6} \\ -2.37\ 10^{-3} \\ 2.38\ 10^{-4} \end{bmatrix}
$$

$$
a_{(4)} = \begin{bmatrix} 2.02\ 10^{-1} & 6.64\ 10^{-2} & 6.72\ 10^{-2} & 1.33\ 10^{-4} & -9.14\ 10^{-4} & 1.8\ 10^{-3} \\ 6.64\ 10^{-2} & 1.94\ 10^{-1} & 6.74\ 10^{-2} & 1.44\ 10^{-5} & 3.39\ 10^{-4} & -1.55\ 10^{-3} \\ 6.72\ 10^{-2} & 6.74\ 10^{-2} & 2.02\ 10^{-1} & -1.53\ 10^{-4} & -1.79\ 10^{-3} & -1.42\ 10^{-5} \\ 1.33\ 10^{-4} & 1.44\ 10^{-5} & -1.53\ 10^{-4} & 6.74\ 10^{-2} & -1.42\ 10^{-5} & 3.39\ 10^{-4} \\ -9.14\ 10^{-4} & 3.39\ 10^{-4} & -1.79\ 10^{-3} & -1.42\ 10^{-5} & 6.72\ 10^{-2} & 1.33\ 10^{-4} \\ 1.8\ 10^{-3} & -1.55\ 10^{-3} & -1.42\ 10^{-5} & 3.39\ 10^{-4} & 1.33\ 10^{-4} & 6.64\ 10^{-2} \end{bmatrix}
\tag{8.1-67}
$$

$$
b_{(2)} = \begin{bmatrix} 3.32\ 10^{-1} \\ 3.38\ 10^{-1} \\ 3.3\ 10^{-1} \\ 1.\ 10^{-3} \\ 3.94\ 10^{-4} \\ -3.62\ 10^{-3} \end{bmatrix}
$$

$$
b_{(4)} = \begin{bmatrix} 1.99\ 10^{-1} & 6.72\ 10^{-2} & 6.51\ 10^{-2} & 9.52\ 10^{-4} & -2.14\ 10^{-4} & -6.75\ 10^{-4} \\ 6.72\ 10^{-2} & 2.05\ 10^{-1} & 6.68\ 10^{-2} & -6.5\ 10^{-4} & 1.59\ 10^{-4} & -2.42\ 10^{-3} \\ 6.51\ 10^{-2} & 6.68\ 10^{-2} & 1.98\ 10^{-1} & 7.02\ 10^{-4} & 4.49\ 10^{-4} & -5.24\ 10^{-4} \\ 9.52\ 10^{-4} & -6.5\ 10^{-4} & 7.02\ 10^{-4} & 6.68\ 10^{-2} & -5.24\ 10^{-4} & 1.59\ 10^{-4} \\ -2.14\ 10^{-4} & 1.59\ 10^{-4} & 4.49\ 10^{-4} & -5.24\ 10^{-4} & 6.51\ 10^{-2} & 9.52\ 10^{-4} \\ -6.75\ 10^{-4} & -2.42\ 10^{-3} & -5.24\ 10^{-4} & 1.59\ 10^{-4} & 9.52\ 10^{-4} & 6.72\ 10^{-2} \end{bmatrix}
\tag{8.1-68}
$$

$$s_{(4)} = \begin{bmatrix} 1.33\ 10^{-1} & 2.67\ 10^{-1} & 2.67\ 10^{-1} & -1.55\ 10^{-4} & -5.35\ 10^{-4} & -3.09\ 10^{-3} \\ 2.67\ 10^{-1} & 1.34\ 10^{-1} & 2.66\ 10^{-1} & 1.75\ 10^{-3} & -1.79\ 10^{-3} & 2.32\ 10^{-3} \\ 2.67\ 10^{-1} & 2.66\ 10^{-1} & 1.33\ 10^{-1} & -5.99\ 10^{-4} & 3.52\ 10^{-4} & -2.61\ 10^{-3} \\ -1.55\ 10^{-4} & 1.75\ 10^{-3} & -5.99\ 10^{-4} & -6.7\ 10^{-2} & 7.66\ 10^{-4} & 1.82\ 10^{-4} \\ -5.35\ 10^{-4} & -1.79\ 10^{-3} & 3.52\ 10^{-4} & 7.66\ 10^{-4} & -6.6\ 10^{-2} & -1.15\ 10^{-3} \\ -3.09\ 10^{-3} & 2.32\ 10^{-3} & -2.61\ 10^{-3} & 1.82\ 10^{-4} & -1.15\ 10^{-3} & -6.68\ 10^{-2} \end{bmatrix} \quad (8.1\text{-}69)$$

It is apparent from second order orientation and curvature tensors that this is an approximation of material with random sub-structure.

A more general example may be given by generating an ensemble of 10,000 fibers with random fiber parameters in the following ranges $A_K \in \langle \frac{5\pi}{6}, \frac{7\pi}{6} \rangle, B_K \in \langle -\frac{\pi}{6}, \frac{\pi}{6} \rangle, \Gamma_K \in \langle \frac{5\pi}{6}, \frac{7\pi}{6} \rangle$. An example of geometric tensors generated is given below:

$$a_{(2)} = \begin{bmatrix} 8.72\ 10^{-1} \\ 8.3\ 10^{-2} \\ 9.47\ 10^{-2} \\ -3.36\ 10^{-4} \\ -7.27\ 10^{-3} \\ 2.43\ 10^{-3} \end{bmatrix}$$

$$a_{(4)} = \begin{bmatrix} 7.34\ 10^{-1} & 6.44\ 10^{-2} & 7.29\ 10^{-2} & -3.04\ 10^{-4} & -5.94\ 10^{-3} & 1.62\ 10^{-3} \\ 6.44\ 10^{-2} & 1.16\ 10^{-2} & 7.03\ 10^{-3} & -6.34\ 10^{-5} & -3.95\ 10^{-4} & 3.94\ 10^{-4} \\ 7.29\ 10^{-2} & 7.03\ 10^{-3} & 1.47\ 10^{-2} & 3.08\ 10^{-5} & -9.32\ 10^{-4} & 4.2\ 10^{-4} \\ -3.04\ 10^{-4} & -6.34\ 10^{-5} & 3.08\ 10^{-5} & 7.03\ 10^{-3} & 4.2\ 10^{-4} & -3.95\ 10^{-4} \\ -5.94\ 10^{-3} & -3.95\ 10^{-4} & -9.32\ 10^{-4} & 4.2\ 10^{-4} & 7.29\ 10^{-2} & -3.04\ 10^{-4} \\ 1.62\ 10^{-3} & 3.94\ 10^{-4} & 4.2\ 10^{-4} & -3.95\ 10^{-4} & -3.04\ 10^{-4} & 6.44\ 10^{-2} \end{bmatrix} \quad (8.1\text{-}70)$$

$$b_{(2)} = \begin{bmatrix} 9.14\ 10^{-2} \\ 8.76\ 10^{-1} \\ 8.16\ 10^{-2} \\ 2.57\ 10^{-3} \\ 1.27\ 10^{-3} \\ -1.75\ 10^{-3} \end{bmatrix}$$

$$b_{(4)} = \begin{bmatrix} 1.51\ 10^{-2} & 6.94\ 10^{-2} & 6.99\ 10^{-3} & 3.76\ 10^{-4} & 2.64\ 10^{-4} & -3.22\ 10^{-4} \\ 6.94\ 10^{-2} & 7.44\ 10^{-1} & 6.33\ 10^{-2} & 2.02\ 10^{-3} & 8.29\ 10^{-4} & -1.01\ 10^{-3} \\ 6.99\ 10^{-3} & 6.33\ 10^{-2} & 1.13\ 10^{-2} & 1.78\ 10^{-4} & 1.79\ 10^{-4} & -4.19\ 10^{-4} \\ 3.76\ 10^{-4} & 2.02\ 10^{-3} & 1.78\ 10^{-4} & 6.33\ 10^{-2} & -4.19\ 10^{-4} & 8.29\ 10^{-4} \\ 2.64\ 10^{-4} & 8.29\ 10^{-4} & 1.79\ 10^{-4} & -4.19\ 10^{-4} & 6.99\ 10^{-3} & 3.76\ 10^{-4} \\ -3.22\ 10^{-4} & -1.01\ 10^{-3} & -4.19\ 10^{-4} & 8.29\ 10^{-4} & 3.76\ 10^{-4} & 6.94\ 10^{-2} \end{bmatrix} \quad (8.1\text{-}71)$$

$$s_{(4)} = \begin{bmatrix} 1.41\,10^{-1} & 7.45\,10^{-1} & 7.71\,10^{-2} & 2.12\,10^{-3} & 3.1\,10^{-4} & -7.68\,10^{-4} \\ 7.45\,10^{-1} & 1.29\,10^{-1} & 8.54\,10^{-2} & -9.79\,10^{-5} & -5.84\,10^{-3} & 1.23\,10^{-3} \\ 7.71\,10^{-2} & 8.54\,10^{-2} & 1.37\,10^{-2} & 2.16\,10^{-4} & -4.66\,10^{-4} & 2.1\,10^{-4} \\ 2.12\,10^{-3} & -9.79\,10^{-5} & 2.16\,10^{-4} & -7.58\,10^{-4} & -4.66\,10^{-4} & 1.55\,10^{-4} \\ 3.1\,10^{-4} & -5.84\,10^{-3} & -4.66\,10^{-4} & -4.66\,10^{-4} & -1.3\,10^{-2} & -1.18\,10^{-4} \\ -7.68\,10^{-4} & 1.23\,10^{-3} & 2.1\,10^{-4} & 1.55\,10^{-4} & -1.18\,10^{-4} & -1.28\,10^{-1} \end{bmatrix} \quad (8.1\text{-}72)$$

8.1.9 Parameters for a Material with Fibers in Finite Set of Configurations

We use planar orientation averaging of transversely isotropic material obtained using semi-empirical Halpin-Tsai-Kardos [55] Equations.

For single configuration, we use ψ_S in the form given by Equation 8.1-59 and calculate material constants from Equations 4.5-36 through 4.5-44 in the following form

$$\bar{k} = \langle\langle\langle k \rangle\rangle\rangle = \int_{\eta=0}^{\infty}\int_{\xi=0}^{\infty} k(\xi,\eta)\sum_{K=1}^{N}[\Upsilon_K \psi_S(\xi,\eta)]\, d\xi d\eta = \sum_{K=1}^{N}\left[\Upsilon_K \int_{\eta=0}^{\infty}\int_{\xi=0}^{\infty} k(\xi,\eta)\delta(\xi - \Xi_K)\delta(\eta - H_K)\, d\xi d\eta\right] = \sum_{K=1}^{N}[\Upsilon_K k(\Xi_K, H_K)] \quad (8.1\text{-}73)$$

We can therefore calculate five parameters $\mu_s(\Xi_K), \mu_0(\Xi_K),\ \lambda_s(\Xi_K), \alpha_\lambda(\Xi_K), \beta_\lambda(\Xi_K)$ for transversely isotropic material using Halpin-Tsai-Kardos Equation from Section 3.9 and then obtain orientation tensor $\tilde{a}_{ijkl}(H_K)$ for each fiber shape using Equations 4.7-12 through 4.7-14. Then we can use Equations 4.7-45 through 4.7-53 to obtain nine parameters for a material with fibers in single configuration $\mu(\Xi_K, H_K),\ \mu_1(\Xi_K, H_K),\ \mu_2(\Xi_K, H_K),\ \lambda(\Xi_K, H_K),\ \alpha_{\lambda 1}(\Xi_K, H_K),\ \alpha_{\lambda 2}(\Xi_K, H_K),\ \alpha_{\lambda 3}(\Xi_K, H_K),\ \beta_{\lambda 1}(\Xi_K, H_K),\ \beta_{\lambda 2}(\Xi_K, H_K),\ \beta_{\lambda 3}(\Xi_K, H_K)$. These parameters are then averaged using Equation 8.1-73 to obtain parameters for material with fibers in finite set of configurations.

For N=1, Equation 8.1-73 reduces to Equation 8.1-30 and all examples from previous section are applicable.

For a general case, we can use fiber and matrix properties from Section 8.1.2 along with randomly generated shape parameters for 10,000 fibers to produce nine material constants. Using Mathematica random number generator with

$$N = 10{,}000,\ \ 10^1 < \Xi_K < 10^3, 10^{-9} < H_K < \pi, \Upsilon_K = \frac{1}{N} \quad (8.1\text{-}74)$$

In Equation 8.1-73 we can obtain the following material constants

$$\mu = 6.5\ 10^8\ Pa, \lambda = 7.37\ 10^9\ Pa, \alpha_{\lambda 1} = -2.89\ 10^9\ Pa, \alpha_{\lambda 2} = -2.53\ 10^9\ Pa, \mu_1 = 1.16\ 10^9\ Pa, \mu_2 = 1.19\ 10^9\ Pa, \beta_{\lambda 1} = 8.78\ 10^9\ Pa, \beta_{\lambda 2} = 1.34\ 10^9\ Pa, \beta_{\lambda 3} = 3.61\ 10^9\ Pa \tag{8.1-75}$$

8.1.10 Stiffness Tensor for Material with Fibers in Finite Set of Configurations

Geometric tensors and material constants generated above can now be used to produce stiffness tensors. We start with geometric tensors representing 10,000 fibers with completely random rotation configuration with geometric tensors given by Equations 8.1-67 through 8.1-69 and with material constants given by Equation 8.1-75.

The stiffness tensor in Voigt notation:

$$\mathrm{C} = \begin{bmatrix} 1.0710^{10} & 5.410^{9} & 5.4110^{9} & -4.1510^{6} & -3.5810^{6} & 9.0610^{6} \\ 5.410^{9} & 1.0710^{10} & 5.410^{9} & 4.6910^{6} & 5.1510^{5} & 1.5210^{7} \\ 5.4110^{9} & 5.410^{9} & 1.0710^{10} & 1.7710^{6} & 3.10^{6} & 1.0210^{7} \\ -4.1510^{6} & 4.6910^{6} & 1.7710^{6} & 2.6510^{9} & 1.210^{7} & 5.1110^{5} \\ -3.5810^{6} & 5.1510^{5} & 3.10^{6} & 1.210^{7} & 2.6610^{9} & -4.0310^{6} \\ 9.0610^{6} & 1.5210^{7} & 1.0210^{7} & 5.1110^{5} & -4.0310^{6} & 2.6510^{9} \end{bmatrix} \tag{8.1-76}$$

The stiffness tensor in Kelvin notation:

$$\hat{\mathrm{C}} = \begin{bmatrix} 1.0710^{10} & 5.410^{9} & 5.4110^{9} & -5.8710^{6} & -5.0610^{6} & 1.2810^{7} \\ 5.410^{9} & 1.0710^{10} & 5.410^{9} & 6.6310^{6} & 7.2810^{5} & 2.1510^{7} \\ 5.4110^{9} & 5.410^{9} & 1.0710^{10} & 2.510^{6} & 4.2410^{6} & 1.4410^{7} \\ -5.8710^{6} & 6.6310^{6} & 2.510^{6} & 5.310^{9} & 2.4110^{7} & 1.0210^{6} \\ -5.0610^{6} & 7.2810^{5} & 4.2410^{6} & 2.4110^{7} & 5.3110^{9} & -8.0610^{6} \\ 1.2810^{7} & 2.1510^{7} & 1.4410^{7} & 1.0210^{6} & -8.0610^{6} & 5.310^{9} \end{bmatrix} \tag{8.1-77}$$

Kelvin eigen-moduli

$$\lambda = [2.1510^{10}, 5.3410^{9}, 5.3110^{9}, 5.310^{9}, 5.2910^{9}, 5.2810^{9}] \tag{8.1-78}$$

This material is numerically isotropic with two distinct Kelvin moduli. The values vary depending on the particular configurations generated by the Mathematica random number generator. Although many of the off-axis values should be zero for perfectly isotropic material, we can see that in our approximation the appropriate off-axis stiffness tensor values remain two orders of magnitudes below the values on the components appearing on the tensor axis. In the next example, we use geometric tensors from Equations 8.1-70 through 8.1-72, which were produced by random generation of 10,000 fibers where the rotation configuration for each fiber falls within $\frac{\pi}{6}$ of a median value of given rotation angle. Again, we use material constants given by Equation 8.1-75. The stiffness tensor in Voigt notation:

$$C = \begin{bmatrix} 1.46 10^{10} & 5.52 10^{9} & 5.08 10^{9} & -5.78 10^{4} & -4.68 10^{7} & 9.86 10^{6} \\ 5.52 10^{9} & 9.89 10^{9} & 4.89 10^{9} & 1.61 10^{6} & -5.66 10^{6} & 5.43 10^{6} \\ 5.08 10^{9} & 4.89 10^{9} & 8.74 10^{9} & 1.11 10^{6} & -5.7 10^{6} & 1.3 10^{6} \\ -5.78 10^{4} & 1.61 10^{6} & 1.11 10^{6} & 2.14 10^{9} & 2.17 10^{6} & -8.71 10^{6} \\ -4.68 10^{7} & -5.66 10^{6} & -5.7 10^{6} & 2.17 10^{6} & 2.58 10^{9} & 8.15 10^{4} \\ 9.86 10^{6} & 5.43 10^{6} & 1.3 10^{6} & -8.71 10^{6} & 8.15 10^{4} & 3.11 10^{9} \end{bmatrix} \tag{8.1-79}$$

The stiffness tensor in Kelvin notation:

$$\hat{C} = \begin{bmatrix} 1.46 10^{10} & 5.52 10^{9} & 5.08 10^{9} & -8.18 10^{4} & -6.61 10^{7} & 1.41 0^{7} \\ 5.52 10^{9} & 9.89 10^{9} & 4.89 10^{9} & 2.28 10^{6} & -8.\ 10^{6} & 7.68 10^{6} \\ 5.08 10^{9} & 4.89 10^{9} & 8.74 10^{9} & 1.57 10^{6} & -8.06 10^{6} & 1.84 10^{6} \\ -8.18 10^{4} & 2.28 10^{6} & 1.57 10^{6} & 4.28 10^{9} & 4.34 10^{6} & -1.74 10^{7} \\ -6.61 10^{7} & -8.\ 10^{6} & -8.06 10^{6} & 4.34 10^{6} & 5.16 10^{9} & 1.63 10^{5} \\ 1.41 0^{7} & 7.68 10^{6} & 1.84 10^{6} & -1.74 10^{7} & 1.63 10^{5} & 6.21 10^{9} \end{bmatrix} \tag{8.1-80}$$

Kelvin eigen-moduli

$$\lambda = [2.19 10^{10}, 6.94 10^{9}, 6.21 10^{9}, 5.16 10^{9}, 4.38 10^{9}, 4.28 10^{9}] \tag{8.1-81}$$

We can see that we have generated anisotropic material.

8.1.11 Material with Continuous Distribution of Fiber Configurations

Sections 8.1.3 and 8.1.7 focused on distribution functions which could be thought of as representations of individual fibers within discontinuous fiber composite. We have shown that if we consider very large number of fibers with random configuration within certain parameter bounds, we can approach special cases of material symmetry. In this section, we focus on distribution functions given by continuous functions. Clearly, our choice of functions is infinite, however we can select one example function to demonstrate the concept of generating anisotropic stiffness tensor for materials with known continuous distribution of fiber configurations.

8.1.12 Constant δ Sequence Function

In this section, we consider distribution functions of the following form

$$\psi_R(\alpha, \beta, \gamma) = \frac{\bar{b}}{\sin \bar{b}} \bar{\delta}_a(\alpha) \bar{\delta}_b(\beta) \bar{\delta}_c(\gamma) \tag{8.1-82}$$

$$\psi_S(\xi, \eta) = \bar{\delta}_e(\xi) \bar{\delta}_h(\eta) \tag{8.1-83}$$

Where

$$\bar{\delta}_a(\alpha) = \begin{cases} \frac{1}{2\bar{a}}, & \alpha \in \langle \pi - \bar{a}, \pi + \bar{a} \rangle; \quad \bar{a} \in \langle 0, \pi \rangle \\ 0, & \alpha \notin \langle \pi - \bar{a}, \pi + \bar{a} \rangle \end{cases} \tag{8.1-84}$$

$$\bar{\delta}_b(\beta) = \begin{cases} \frac{1}{2\bar{b}}, & \beta \in \langle -\bar{b}, \bar{b} \rangle; \quad \bar{b} \in \langle 0, \frac{\pi}{2} \rangle \\ 0, & \beta \notin \langle \bar{b}, \bar{b} \rangle \end{cases} \tag{8.1-85}$$

$$\bar{\delta}_c(\gamma) = \begin{cases} \frac{1}{2\bar{c}}, & \gamma \in \langle \pi - \bar{c}, \pi + \bar{c} \rangle; \quad \bar{c} \in \langle 0, \pi \rangle \\ 0, & \gamma \notin \langle \pi - \bar{c}, \pi + \bar{c} \rangle \end{cases} \tag{8.2-86}$$

$$\bar{\delta}_e(\xi) = \begin{cases} \frac{1}{2\bar{e}}, & \xi \in \langle \bar{l} - \bar{e}, \bar{l} + \bar{e} \rangle; \quad \bar{l} - \bar{e} > 0 \ \wedge \ \bar{l} > 0 \\ 0, & \xi \notin \langle \bar{l} - \bar{e}, \bar{l} + \bar{e} \rangle \end{cases} \tag{8.1-86}$$

$$\bar{\delta}_h(\eta) = \begin{cases} \frac{1}{2\bar{h}}, & \eta \in \langle \bar{\rho} - \bar{h}, \bar{\rho} + \bar{h} \rangle; \quad \bar{\rho} - \bar{h} \geq 0 \ \wedge \ \bar{\rho} - \bar{h} < \pi \\ 0, & \eta \notin \langle \bar{\rho} - \bar{h}, \bar{\rho} + \bar{h} \rangle \end{cases} \tag{8.1-87}$$

This definition assigns a constant probability of finding a fiber within intervals symmetric around configuration $\alpha = \pi$, $\beta = 0$, $\gamma = \pi$, $\xi = \bar{l}$ and $\eta = \bar{\rho}$. Completely random rotation with equal probability of fiber coordinate system being oriented in any direction is given by $\bar{a} = \pi$, $\bar{b} = \frac{\pi}{2}$ and $\bar{c} = \pi$. In a limit case of infinitesimally small intervals given by $\bar{a} \to 0$, $\bar{b} \to 0$, $\bar{c} \to 0$, $\bar{e} \to 0$ and $\bar{h} \to 0$, the functions above approach delta function with ψ_R an ψ_S describing material with fibers in single configuration. Normalization condition shown in Equation 4.5-3 was satisfied by

$$\begin{aligned} &\int_{\gamma=0}^{2\pi} \int_{\beta=-\frac{\pi}{2}}^{\frac{\pi}{2}} \int_{\alpha=0}^{2\pi} \bar{\delta}_a(\alpha)\bar{\delta}_b(\beta)\bar{\delta}_c(\gamma) \ \cos\beta \ d\alpha d\beta d\gamma \\ &\qquad = \frac{1}{2\bar{a}} \frac{1}{2\bar{b}} \frac{1}{2\bar{c}} \int_{\alpha=\pi-\bar{a}}^{\pi+\bar{a}} d\alpha \int_{\beta=-\bar{b}}^{\bar{b}} \cos\beta \, d\beta \int_{\gamma=\pi-\bar{c}}^{\pi+\bar{c}} d\gamma = \frac{\sin\bar{b}}{\bar{b}} \end{aligned} \tag{8.1-88}$$

We can obtain the orientation distribution function from Equation 4.5-5:

$$\begin{aligned} \psi(\alpha,\beta) &= \frac{\bar{b}}{\sin\bar{b}} \bar{\delta}_a(\alpha)\bar{\delta}_b(\beta) \int_{\gamma=0}^{2\pi} \bar{\delta}_c(\gamma) d\gamma = \frac{\bar{b}}{\sin\bar{b}} \bar{\delta}_a(\alpha)\bar{\delta}_b(\beta) \frac{1}{2\bar{c}} \int_{\gamma=\pi-\bar{c}}^{\pi+\bar{c}} d\gamma \\ &= \frac{\bar{b}}{\sin\bar{b}} \bar{\delta}_a(\alpha)\bar{\delta}_b(\beta) \end{aligned} \tag{8.1-89}$$

For material represented by delta sequence function.

8.1.13 Geometric Tensors for Material with Fibers Represented by Constant δ Sequence Function

Components of geometric tensors are not listed in this section due to the effort necessary to perform symbolic integration. Listing all the resulting components would take significant space. Given a continuous distribution function, one would likely employ numerical integration scheme, which is what we choose to do.

We use definitionsin Equations 4.6-4 and 4.6-5 to arrive at integrals giving us second and fourth order orientation tensors:

$$a_{ij} = \int_{\beta=-\frac{\pi}{2}}^{\frac{\pi}{2}} \int_{\alpha=0}^{2\pi} p_i(\alpha,\beta)p_j(\alpha,\beta)\frac{\bar{b}}{\sin\bar{b}}\bar{\delta}_a(\alpha)\bar{\delta}_b(\beta)\cos\beta\, d\alpha d\beta$$
$$= \frac{1}{4\bar{a}\sin\bar{b}} \int_{\beta=-\bar{b}}^{\bar{b}} \int_{\alpha=\pi-\bar{a}}^{\pi+\bar{a}} p_i(\alpha,\beta)p_j(\alpha,\beta)\cos\beta\, d\alpha d\beta\ , \quad (8.1\text{-}90)$$
$$i,j = 1,2,3$$

$$a_{ijkl} \quad (8.1\text{-}91)$$
$$= \int_{\beta=-\frac{\pi}{2}}^{\frac{\pi}{2}} \int_{\alpha=-\infty}^{2\pi} p_i(\alpha,\beta)p_j(\alpha,\beta)p_k(\alpha,\beta)p_l(\alpha,\beta)\frac{\bar{b}}{\sin\bar{b}}\bar{\delta}_a(\alpha)\bar{\delta}_b(\beta)\cos\beta\ d\alpha d\beta$$
$$= \frac{1}{4\bar{a}\sin\bar{b}} \int_{\beta=-\bar{b}}^{\bar{b}} \int_{\alpha=\pi-\bar{a}}^{\pi+\bar{a}} p_i(\alpha,\beta)p_j(\alpha,\beta)p_k(\alpha,\beta)p_l(\alpha,\beta)\cos\beta\ d\alpha d\beta\ ,\ \ i,j,k,l$$
$$= 1,2,3$$

Similarly, for curvature tensor, we can transform Equations 4.6-35 and 4.6-36 and evaluate:

$$b_{ij}$$
$$= \int_{\gamma=0}^{2\pi} \int_{\beta=-\frac{\pi}{2}}^{\frac{\pi}{2}} \int_{\alpha=0}^{2\pi} q_i(\alpha,\beta,\gamma)q_j(\alpha,\beta,\gamma)\frac{\bar{b}}{\sin\bar{b}}\bar{\delta}_a(\alpha)\bar{\delta}_b(\beta)\bar{\delta}_c(\gamma)\cos\beta\ d\alpha d\beta d\gamma \quad (8.1\text{-}92)$$
$$= \frac{1}{8\bar{a}\bar{c}\sin\bar{b}} \int_{\gamma=\pi-\bar{c}}^{\pi+\bar{c}} \int_{\beta=-\bar{b}}^{\bar{b}} \int_{\alpha=\pi-\bar{a}}^{\pi+\bar{a}} q_i q_j \cos\beta\ d\alpha d\beta d\gamma \qquad i,j = 1,2,3$$

$$b_{ijkl} = \int_{\gamma=0}^{2\pi} \int_{\beta=-\frac{\pi}{2}}^{\frac{\pi}{2}} \int_{\alpha=0}^{2\pi} q_i q_j q_k q_l \frac{\bar{b}}{\sin \bar{b}} \bar{\delta}_a(\alpha) \bar{\delta}_b(\beta) \bar{\delta}_c(\gamma) \cos\beta \; d\alpha d\beta d\gamma$$

$$= \frac{1}{8\bar{a}\bar{c}\sin\bar{b}} \int_{\gamma=\pi-\bar{c}}^{\pi+\bar{c}} \int_{\beta=-\bar{b}}^{\bar{b}} \int_{\alpha=\pi-\bar{a}}^{\pi+\bar{a}} q_i q_j q_k q_l \cos\beta \; d\alpha d\beta d\gamma \qquad i,j,k,l = 1,2,3 \tag{8.1-93}$$

For mixed tensor s_{ijkl}, we write

$$s_{ijkl}$$

$$= \int_{\gamma=0}^{2\pi} \int_{\beta=-\frac{\pi}{2}}^{\frac{\pi}{2}} \int_{\alpha=0}^{2\pi} \Big(p_i(\alpha,\beta) p_j(\alpha,\beta) q_k(\alpha,\beta,\gamma) q_l(\alpha,\beta,\gamma)$$

$$+ q_i(\alpha,\beta,\gamma) q_j(\alpha,\beta,\gamma) p_k(\alpha,\beta) p_l(\alpha,\beta) \Big) \frac{\bar{b}}{\sin\bar{b}} \bar{\delta}_a(\alpha) \bar{\delta}_b(\beta) \bar{\delta}_c(\gamma) \cos\beta \; d\alpha d\beta d\gamma \tag{81.94}$$

$$= \frac{1}{8\bar{a}\bar{c}\sin\bar{b}} \int_{\gamma=\pi-\bar{c}}^{\pi+\bar{c}} \int_{\beta=-\bar{b}}^{\bar{b}} \int_{\alpha=\pi-\bar{a}}^{\pi+\bar{a}} \left(p_i p_j q_k q_l + q_i q_j p_k p_l \right) \cos\beta \; d\alpha d\beta d\gamma \quad i,j,k,l$$

$$= 1,2,3$$

Again, this is equivalent to evaluating Equations 4.6-67 through 4.6-87 with $\alpha = A$, $\beta = B$ and $\gamma = \Gamma$.

We now provide three specific examples.

As noted above, completely random material is given by by $\bar{a} = \pi$, $\bar{b} = \frac{\pi}{2}$ and $\bar{c} = \pi$.

$$a_{(2)} = \begin{bmatrix} \frac{1}{3} \\ \frac{1}{3} \\ \frac{1}{3} \\ 0 \\ 0 \\ 0 \end{bmatrix} a_{(4)} = \begin{bmatrix} \frac{1}{5} & \frac{1}{15} & \frac{1}{15} & 0 & 0 & 0 \\ \frac{1}{15} & \frac{1}{5} & \frac{1}{15} & 0 & 0 & 0 \\ \frac{1}{15} & \frac{1}{15} & \frac{1}{5} & 0 & 0 & 0 \\ 0 & 0 & 0 & \frac{1}{15} & 0 & 0 \\ 0 & 0 & 0 & 0 & \frac{1}{15} & 0 \\ 0 & 0 & 0 & 0 & 0 & \frac{1}{15} \end{bmatrix} \tag{8.1-95}$$

$$b_{(2)} = \begin{bmatrix} \frac{1}{3} \\ \frac{1}{3} \\ \frac{1}{3} \\ 0 \\ 0 \\ 0 \end{bmatrix} \tag{8.196}$$

$$b_{(4)} = \begin{bmatrix} 2.10^{-1} & 6.67\ 10^{-2} & 6.67\ 10^{-2} & 0 & 0 & -5.38\ 10^{-9} \\ 6.67\ 10^{-2} & 2.10^{-1} & 6.67\ 10^{-2} & 0 & 0 & 0 \\ 6.67\ 10^{-2} & 6.67\ 10^{-2} & 2.10^{-1} & -1.56\ 10^{-9} & 3.67\ 10^{-8} & 0 \\ 0 & 0 & -1.56\ 10^{-9} & 6.67\ 10^{-2} & 0 & 0 \\ 0 & 0 & 3.67\ 10^{-8} & 0 & 6.67\ 10^{-2} & 0 \\ -5.38\ 10^{-9} & 0 & 0 & 0 & 0 & 6.67\ 10^{-2} \end{bmatrix}$$

$$s_{(4)} = \begin{bmatrix} 1.33\ 10^{-1} & 2.67\ 10^{-1} & 2.67\ 10^{-1} & -3.63\ 10^{-8} & 0 & -2.93\ 10^{-8} \\ 2.67\ 10^{-1} & 1.33\ 10^{-1} & 2.67\ 10^{-1} & 0 & 0 & 0 \\ 2.67\ 10^{-1} & 2.67\ 10^{-1} & 1.33\ 10^{-1} & 3.01\ 10^{-9} & 0 & 0 \\ -3.63\ 10^{-8} & 0 & 3.01\ 10^{-9} & -6.67\ 10^{-2} & 0 & 2.46\ 10^{-8} \\ 0 & 0 & 0 & 0 & -6.67\ 10^{-2} & 0 \\ -2.93\ 10^{-8} & 0 & 0 & 2.46\ 10^{-8} & 0 & -6.67\ 10^{-2} \end{bmatrix} \tag{8.1-97}$$

We can consider a more general case given by $\bar{a} = \frac{\pi}{6}$, $\bar{b} = \frac{\pi}{6}$and $\bar{c} = \frac{\pi}{6}$:

$$a_{(2)} = \begin{bmatrix} 8.37\ 10^{-1} \\ 7.93\ 10^{-2} \\ 8.33\ 10^{-2} \\ 0. \\ 0. \\ 0. \end{bmatrix}$$

$$a_{(4)} = \begin{bmatrix} 7.11\ 10^{-1} & 6.2\ 10^{-2} & 6.47\ 10^{-2} & 0. & 0. & 0. \\ 6.2\ 10^{-2} & 1.12\ 10^{-2} & 6.13\ 10^{-3} & 0. & 0. & 0. \\ 6.47\ 10^{-2} & 6.13\ 10^{-3} & 1.25\ 10^{-2} & 0. & 0. & 0. \\ 0. & 0. & 0. & 6.13\ 10^{-3} & 0. & 0. \\ 0. & 0. & 0. & 0. & 6.47\ 10^{-2} & 0. \\ 0. & 0. & 0. & 0. & 0. & 6.2\ 10^{-2} \end{bmatrix} \tag{8.1-98}$$

$$b_{(2)} = \begin{bmatrix} 8.56\ 10^{-2} \\ 8.35\ 10^{-1} \\ 7.93\ 10^{-2} \\ 0. \\ 0. \\ 0. \end{bmatrix}$$

$$b_{(4)} = \begin{bmatrix} 1.39\ 10^{-2} & 6.5\ 10^{-2} & 6.67\ 10^{-3} & 8.3\ 10^{-10} & 0 & 0 \\ 6.5\ 10^{-2} & 7.09\ 10^{-1} & 6.15\ 10^{-2} & 0 & -7.03\ 10^{-10} & 0 \\ 6.67\ 10^{-3} & 6.15\ 10^{-2} & 1.12\ 10^{-2} & 0 & 0 & 1.55\ 10^{-9} \\ 8.3\ 10^{-10} & 0 & 0 & 6.15\ 10^{-2} & 1.55\ 10^{-9} & -7.03\ 10^{-10} \\ 0 & -7.03\ 10^{-10} & 0 & 1.55\ 10^{-9} & 6.67\ 10^{-3} & 8.3\ 10^{-10} \\ 0 & 0 & 1.55\ 10^{-9} & -7.03\ 10^{-10} & 8.3\ 10^{-10} & 6.5\ 10^{-2} \end{bmatrix} \tag{8.1-99}$$

$$s_{(4)} = \begin{bmatrix} 1.33\ 10^{-1} & 7.15\ 10^{-1} & 7.44\ 10^{-2} & -7.77\ 10^{-9} & 0 & 0 \\ 7.15\ 10^{-1} & 1.23\ 10^{-1} & 7.6\ 10^{-2} & -2.93\ 10^{-9} & 2.75\ 10^{-9} & 0 \\ 7.44\ 10^{-2} & 7.6\ 10^{-2} & 1.23\ 10^{-2} & 0 & 0 & -1.53\ 10^{-8} \\ -7.77\ 10^{-9} & -2.93\ 10^{-9} & 0 & -1.06\ 10^{-3} & 0 & 0 \\ 0 & 2.75\ 10^{-9} & 0 & 0 & -1.12\ 10^{-2} & 3.6\ 10^{-9} \\ 0 & 0 & -1.53\ 10^{-8} & 0 & 3.6\ 10^{-9} & -1.22\ 10^{-1} \end{bmatrix} \tag{8.1-100}$$

Now we can examine a case with very narrow parameter interval, which approaches delta function. We use $\bar{a} = 0.001$, $\bar{b} = 0.001$ and $\bar{c} = 0.001$:

$$a_{(2)} = \begin{bmatrix} 1. \\ 3.33\ 10^{-7} \\ 3.33\ 10^{-7} \\ 0 \\ 0 \\ 0 \end{bmatrix}$$

$$a_{(4)} = \begin{bmatrix} 1. & 3.33\ 10^{-7} & 3.33\ 10^{-7} & 0 & 0 & 0 \\ 3.33\ 10^{-7} & 0 & 0 & 0 & 0 & 0 \\ 3.33\ 10^{-7} & 0 & 0 & 0 & 0 & 0 \\ 0 & 0 & 0 & 0 & 0 & 0 \\ 0 & 0 & 0 & 0 & 3.33\ 10^{-7} & 0 \\ 0 & 0 & 0 & 0 & 0 & 3.33\ 10^{-7} \end{bmatrix} \tag{8.1-101}$$

$$b_{(2)} = \begin{bmatrix} 3.33\ 10^{-7} \\ 1. \\ 3.33\ 10^{-7} \\ 0 \\ 0 \\ 0 \end{bmatrix} \tag{8.1-102}$$

$$b_{(4)} = \begin{bmatrix} 0 & 3.33\ 10^{-7} & 0 & 0 & 0 & 0 \\ 3.33\ 10^{-7} & 1. & 3.33\ 10^{-7} & 0 & 0 & 0 \\ 0 & 3.33\ 10^{-7} & 0 & 0 & 0 & 0 \\ 0 & 0 & 0 & 3.33\ 10^{-7} & 0 & 0 \\ 0 & 0 & 0 & 0 & 0 & 0 \\ 0 & 0 & 0 & 0 & 0 & 3.33\ 10^{-7} \end{bmatrix}$$

$$s_{(4)} = \begin{bmatrix} 6.67\ 10^{-7} & 1. & 3.33\ 10^{-7} & 0 & 0 & 0 \\ 1. & 6.67\ 10^{-7} & 3.33\ 10^{-7} & 0 & 0 & 0 \\ 3.33\ 10^{-7} & 3.33\ 10^{-7} & 0 & 0 & 0 & 0 \\ 0 & 0 & 0 & 0 & 0 & 0 \\ 0 & 0 & 0 & 0 & 0 & 0 \\ 0 & 0 & 0 & 0 & 0 & -6.67\ 10^{-7} \end{bmatrix} \tag{8.1-103}$$

8.1.14 Parameters for Material with Fibers Represented by Constant δ Sequence Function

We can recall that material with fibers in single configuration is orthotropic material. We therefore need nine constants. Using previously suggested approach for obtaining material parameters through planar orientation averaging of transversely isotropic material obtained using semi-empirical Halpin-Tsai-Kardos [55] Equations.

For single configuration, we use ψ_S in the form given by Equation8.1-4 and calculate material constants from Equations 4.5-36 through 4.5-44 in the following form

$$\begin{gathered} \bar{k} = \langle\langle\langle k \rangle\rangle\rangle = \\ \int_{\eta=0}^{\infty}\int_{\xi=0}^{\infty} k(\xi,\eta)\psi_S(\xi,\eta)d\xi d\eta = \int_{\eta=0}^{\infty}\int_{\xi=0}^{\infty} k(\xi,\eta)\bar{\delta}_e(\xi)\bar{\delta}_h(\eta)\ \ d\xi d\eta = \\ \frac{1}{4\bar{e}\bar{h}}\int_{\eta=\bar{\rho}-\bar{h}}^{\bar{\rho}+\bar{h}}\int_{\xi=\bar{l}-\bar{e}}^{\bar{l}+\bar{e}} k(\xi,\eta)d\xi d\eta \end{gathered} \tag{8.1-104}$$

Using composite constants from Table 8-3 in Equations 4.7-45 through 4.7-53 and integrating over a narrow range of shape parameters approximating slightly curved fibers of the same length:

$$\bar{l} = 505, \bar{e} = 1, \bar{\rho} = \frac{\pi}{18}, \bar{h} = \frac{\pi}{10^3} \tag{8.1-105}$$

We obtain

$$\begin{aligned} \mu = 1.82\ 10^9\ Pa, \lambda = 5.01\ 10^9\ Pa, \alpha_{\lambda 1} = -6.59\ 10^8\ Pa, \alpha_{\lambda 2} \\ = -6.59\ 10^7\ Pa, \mu_1 = -2.05\ 10^7\ Pa, \mu_2 = 3.21\ 10^7\ Pa, \beta_{\lambda 1} \\ = 1.27\ 10^{10}\ Pa, \beta_{\lambda 2} = 1.48\ 10^5\ Pa, \beta_{\lambda 3} = 9.67\ 10^7\ Pa \end{aligned} \tag{8.1-106}$$

which is numerically nearly identical to results obtained for material with fibers in single configuration in Equation 8.1-39.

We can use parameters equivalent to a large number of fibers in Equation 8.1-74, where fiber lengths and curvatures span a large interval:

$$\bar{l} = 505, \bar{e} = 495, \bar{\rho} = \frac{\pi}{2}, \bar{h} = \frac{\pi}{2} \tag{8.1-107}$$

We obtain

$$\begin{aligned} \mu = 6.38\ 10^8\ Pa, \lambda = 7.4\ 10^9\ Pa, \alpha_{\lambda 1} = -2.91\ 10^9\ Pa, \alpha_{\lambda 2} \\ = -2.55\ 10^9\ Pa, \mu_1 = 1.17\ 10^9\ Pa, \mu_2 = 1.2\ 10^9\ Pa, \beta_{\lambda 1} \\ = 8.75\ 10^9\ Pa, \beta_{\lambda 2} = 1.36\ 10^9\ Pa, \beta_{\lambda 3} = 3.64\ 10^9\ Pa \end{aligned} \tag{8.1-108}$$

Which is numerically close to the results obtained for an ensemble of 10,000 fibers in Equation 8.1-75.

8.1.15 Stiffness Tensor for Material with Fibers Represented by Constant δ Sequence Function

In this section, we examine stiffness tensors and Kelvin moduli for six cases, which can be obtained using material parameters and geometric tensors listed above.

In the first case, we use narrow intervals for delta sequence functions to approximate material with fibers in single configuration. We use material parameters from Equation 8.1-106 for straight fibers and geometric tensors in Equations 8.1-101 through 8.1-103 approximating single configuration.

The stiffness tensor in Voigt notation:

$$\boldsymbol{C} = \begin{bmatrix} 2.10^{10} & 4.3810^9 & 4.3510^9 & 1.1810^{-8} & 0 & 1.1810^{-8} \\ 4.3810^9 & 8.6510^9 & 4.9510^9 & 0 & 0 & -1.1810^{-8} \\ 4.3510^9 & 4.9510^9 & 8.6510^9 & 0 & 0 & 0 \\ 1.1810^{-8} & 0 & 0 & 1.8510^9 & 0 & 0 \\ 0 & 0 & 0 & 0 & 1.810^9 & 0 \\ 1.1810^{-8} & -1.1810^{-8} & 0 & 0 & 0 & 1.8310^9 \end{bmatrix} \tag{8.1-109}$$

The stiffness tensor in Kelvin notation:

$$\widehat{\boldsymbol{C}} = \begin{bmatrix} 2.10^{10} & 4.3810^9 & 4.3510^9 & 1.6710^{-8} & 0 & 1.6710^{-8} \\ 4.3810^9 & 8.6510^9 & 4.9510^9 & 0 & 0 & -1.6710^{-8} \\ 4.3510^9 & 4.9510^9 & 8.6510^9 & 0 & 0 & 0 \\ 1.6710^{-8} & 0 & 0 & 3.710^9 & 0 & 0 \\ 0 & 0 & 0 & 0 & 3.610^9 & 0 \\ 1.6710^{-8} & -1.6710^{-8} & 0 & 0 & 0 & 3.6610^9 \end{bmatrix} \tag{8.1-110}$$

Kelvin eigen-moduli

$$\boldsymbol{\lambda} = [2.3710^{10}, 9.8310^{9}, 3.710^{9}, 3.710^{9}, 3.6610^{9}, 3.610^{9}] \tag{8.1-111}$$

This material is nearly transversely isotropic and the values are numerically identical to the case of fibers in single configuration, which is approximated by the narrow intervals for delta sequence functions – see Equations 8.1-45 through 8.1-47.

Now we keep the length of the fibers and geometric configuration the same as in the previous case, except that we allow the fibers to bend with random curvature. Since all of the fibers have nearly identical geometric configuration, the fibers are curved only in one plane. We use large interval for material parameter delta function with resulting material parameters listed in Equation 8.1-108 with geometric tensors Equations 8.1-101 through 8.1-103 approximating single configuration.

The stiffness tensor in Voigt notation:

$$\boldsymbol{C} = \begin{bmatrix} 1.6310^{10} & 5.5810^{9} & 4.4910^{9} & 4.4610^{-7} & 0 & 4.4610^{-7} \\ 5.5810^{9} & 9.7410^{9} & 4.8410^{9} & 1.6710^{-7} & 1.2510^{-10} & -2.7910^{-7} \\ 4.4910^{9} & 4.8410^{9} & 8.6710^{9} & 0 & 0 & -4.310^{-8} \\ 4.4610^{-7} & 1.6710^{-7} & 0 & 1.8410^{9} & -4.310^{-8} & 0 \\ 0 & 1.2510^{-10} & 0 & -4.310^{-8} & 1.8110^{9} & 0 \\ 4.4610^{-7} & -2.7910^{-7} & -4.310^{-8} & 0 & 0 & 3.0110^{9} \end{bmatrix} \tag{8.1-112}$$

The stiffness tensor in Kelvin notation:

$$\widehat{\boldsymbol{C}} = \begin{bmatrix} 1.6310^{10} & 5.5810^{9} & 4.4910^{9} & 6.3110^{-7} & 0 & 6.310^{-7} \\ 5.5810^{9} & 9.7410^{9} & 4.8410^{9} & 2.3610^{-7} & 1.7610^{-10} & -3.9510^{-7} \\ 4.4910^{9} & 4.8410^{9} & 8.6710^{9} & 0 & 0 & -6.0810^{-8} \\ 6.3110^{-7} & 2.3610^{-7} & 0 & 3.6810^{9} & -8.610^{-8} & 0 \\ 0 & 1.7610^{-10} & 0 & -8.610^{-8} & 3.6210^{9} & 0 \\ 6.310^{-7} & -3.9510^{-7} & -6.0810^{-8} & 0 & 0 & 6.0310^{9} \end{bmatrix} \tag{8.1-113}$$

Kelvin eigen-moduli

$$\boldsymbol{\lambda} = [2.2410^{10}, 7.9710^{9}, 6.0310^{9}, 4.3110^{9}, 3.6810^{9}, 3.6210^{9}] \tag{8.1-114}$$

We can see that allowing the fibers to be curved in a single plane resulted in orthotropic stiffness tensor as expected. In the following example, we look at slightly curved fibers of the same length with completely random geometric configuration. Narrow delta function for shape parameters was used with resulting material parameters given in Equation 8.1-106. Geometric tensors for randomly configured fibers are given in Equations 8.1-95 through 8.1-97.

The stiffness tensor in Voigt notation:

$$\boldsymbol{C} = \begin{bmatrix} 1.0710^{10} & 5.410^{9} & 5.410^{9} & -3.51 & 6.0710^{-5} & -2.84 \\ 5.410^{9} & 1.0710^{10} & 5.410^{9} & 6.0910^{-7} & 9.4610^{-5} & 2.2410^{-6} \\ 5.410^{9} & 5.410^{9} & 1.0710^{10} & 2.910^{-1} & 5.4210^{-3} & -1.1510^{-5} \\ -3.51 & 6.0910^{-7} & 2.910^{-1} & 2.6710^{9} & 3.1710^{-6} & 2.37 \\ 6.0710^{-5} & 9.4610^{-5} & 5.4210^{-3} & 3.1710^{-6} & 2.6710^{9} & 2.5310^{-9} \\ -2.84 & 2.2410^{-6} & -1.1510^{-5} & 2.37 & 2.5310^{-9} & 2.6710^{9} \end{bmatrix} \tag{8.1-115}$$

The stiffness tensor in Kelvin notation:

$$\widehat{\boldsymbol{C}} = \begin{bmatrix} 1.0710^{10} & 5.410^{9} & 5.410^{9} & -4.96 & 8.5810^{-5} & -4.01 \\ 5.410^{9} & 1.0710^{10} & 5.410^{9} & 8.6210^{-7} & 1.3410^{-4} & 3.1710^{-6} \\ 5.410^{9} & 5.410^{9} & 1.0710^{10} & 4.1110^{-1} & 7.6710^{-3} & -1.6310^{-5} \\ -4.96 & 8.6210^{-7} & 4.1110^{-1} & 5.3410^{9} & 6.3410^{-6} & 4.75 \\ 8.5810^{-5} & 1.3410^{-4} & 7.6710^{-3} & 6.3410^{-6} & 5.3410^{9} & 5.0510^{-9} \\ -4.01 & 3.1710^{-6} & -1.6310^{-5} & 4.75 & 5.0510^{-9} & 5.3410^{9} \end{bmatrix} \tag{8.1-116}$$

Kelvin eigen-moduli

$$\boldsymbol{\lambda} = [2.1510^{10}, 5.3410^{9}, 5.3410^{9}, 5.3410^{9}, 5.3410^{9}, 5.3410^{9}] \tag{8.1-117}$$

As expected, we have generated nearly isotropic material with two distinct Kelvin moduli.

Now we consider an example of material where fiber length and curvature parameters span large intervals with resulting material parameters shown in Equation 8.1-108 with rotation configuration given in Equations 8.1-98 through 8.1-100.

The stiffness tensor in Voigt notation:

$$\boldsymbol{C} = \begin{bmatrix} 1.0710^{10} & 5.410^{9} & 5.410^{9} & -1.3210^{2} & -1.1210^{-3} & -1.1410^{2} \\ 5.410^{9} & 1.0710^{10} & 5.410^{9} & -1.1910^{-4} & 3.5610^{-3} & 8.7410^{-5} \\ 5.410^{9} & 5.410^{9} & 1.0710^{10} & 8.83 & 4.9910^{1} & -4.3410^{-4} \\ -1.3210^{2} & -1.1910^{-4} & 8.83 & 2.6510^{9} & 1.210^{-4} & 8.9410^{1} \\ -1.1210^{-3} & 3.5610^{-3} & 4.9910^{1} & 1.210^{-4} & 2.6510^{9} & -1.8610^{-7} \\ -1.1410^{2} & 8.7410^{-5} & -4.3410^{-4} & 8.9410^{1} & -1.8610^{-7} & 2.6510^{9} \end{bmatrix} \tag{8.1-118}$$

The stiffness tensor in Kelvin notation:

$$\widehat{\boldsymbol{C}} = \begin{bmatrix} 1.0710^{10} & 5.410^{9} & 5.410^{9} & -1.8710^{2} & -1.5910^{-3} & -1.6110^{2} \\ 5.410^{9} & 1.0710^{10} & 5.410^{9} & -1.6810^{-4} & 5.0410^{-3} & 1.2410^{-4} \\ 5.410^{9} & 5.410^{9} & 1.0710^{10} & 1.2510^{1} & 7.0610^{1} & -6.1410^{-4} \\ -1.8710^{2} & -1.6810^{-4} & 1.2510^{1} & 5.3110^{9} & 2.3910^{-4} & 1.7910^{2} \\ -1.5910^{-3} & 5.0410^{-3} & 7.0610^{1} & 2.3910^{-4} & 5.3110^{9} & -3.7210^{-7} \\ -1.6110^{2} & 1.2410^{-4} & -6.1410^{-4} & 1.7910^{2} & -3.7210^{-7} & 5.3110^{9} \end{bmatrix} \tag{8.1-119}$$

Kelvin eigen-moduli

$$\boldsymbol{\lambda} = [2.1510^{10}, 5.3110^{9}, 5.3110^{9}, 5.3110^{9}, 5.3110^{9}, 5.3110^{9}] \tag{8.1-120}$$

Again, we have arrived at isotropic material with two identical Kelvin moduli. We can see that the results are comparable to the case of 10,000 randomly generated fibers Equations 8.1-79 through 8.1-81 with identical parameter constraints.

8.2 Appendix B: Solutions for toroid cross-sections

Solutions for cross section(s) $\mathbf{k_1}$ and $\mathbf{k_2}$ of a toroid with a plane are provided below.

$$\mathbf{k_1} = (k_{1x}, k_{1y}) \tag{8.2-1}$$

$$\begin{aligned} k_{1x} = \mathrm{x}_c + \frac{1}{\rho} r(\mathrm{Sin})\alpha)(\mathrm{Cos})\gamma)(-1 + (-1 + \rho\mathrm{Cos})u))\mathrm{Sin})\mathrm{f1})) \\ + \rho\mathrm{Sin})u)\mathrm{Sin})\gamma)) \\ -\mathrm{Cos})\alpha)(\mathrm{Cos})\mathrm{f1})(-1 + \rho\mathrm{Cos})u))\mathrm{Cos})\beta) + \mathrm{Sin})\beta)(\rho\mathrm{Cos})\gamma)\mathrm{Sin})u) \\ +(1 + (1 - \rho\mathrm{Cos})u))\mathrm{Sin})\mathrm{f1}))\mathrm{Sin})\gamma)))) \end{aligned} \tag{8.2-2}$$

$$\begin{aligned} k_{1y} = \mathrm{y}_c + \frac{1}{\rho} r(\mathrm{Cos})\alpha)(\mathrm{Cos})\gamma)(1 + (1 - \rho\mathrm{Cos})u))\mathrm{Sin})\mathrm{f1})) \\ - \rho\mathrm{Sin})u)\mathrm{Sin})\gamma)) - \mathrm{Sin})\alpha)(\mathrm{Cos})\mathrm{f1})(-1 + \rho\mathrm{Cos})u))\mathrm{Cos})\beta) \\ + \mathrm{Sin})\beta)(\rho\mathrm{Cos})\gamma)\mathrm{Sin})u) + (1 + (1 \\ - \rho\mathrm{Cos})u))\mathrm{Sin})\mathrm{f1}))\mathrm{Sin})\gamma)))) \end{aligned} \tag{8.2-3}$$

$$\mathrm{f}_1 = 2\mathrm{ArcTan}(a_1) \tag{8.2-4}$$

$$\mathbf{k_1} = (k_{1x}, k_{1y}) \tag{8.2-5}$$

$$a_1 = \frac{(-1 + \rho\mathrm{Cos}(u))\mathrm{Cos}(\beta)\mathrm{Sin}(\gamma)}{(-1 + \rho\mathrm{Cos}(u))\mathrm{Sin}(\beta) + \mathrm{Cos}(\beta)(\rho\mathrm{Cos}(\gamma)\mathrm{Sin}(u) + \mathrm{Sin}(\gamma))} - \frac{\sqrt{(-1 + \rho\mathrm{Cos}(u))^2\mathrm{Sin}(\beta)^2 - \rho\mathrm{Cos}(\beta)^2(\rho\mathrm{Sin}(u - \gamma) + 2\mathrm{Sin}(\gamma))\mathrm{Sin}(u + \gamma)}}{(-1 + \rho\mathrm{Cos}(u))\mathrm{Sin}(\beta) + \mathrm{Cos}(\beta)(\rho\mathrm{Cos}(\gamma)\mathrm{Sin}(u) + \mathrm{Sin}(\gamma))} \tag{8.2-6}$$

$$\mathbf{k_2} = (k_{2x}, k_{2y}) \tag{8.2-7}$$

$$\begin{aligned} k_{2x} = \mathrm{x}_c + \frac{1}{\rho} r(&\mathrm{Sin}(\alpha)(\mathrm{Cos}(\gamma)(-1 + (-1 + \rho\mathrm{Cos}(u))\mathrm{Sin}(\mathrm{f2})) \\ &+ \rho\mathrm{Sin}(u)\mathrm{Sin}(\gamma)) - \mathrm{Cos}(\alpha)(\mathrm{Cos}(\mathrm{f2})(-1 + \rho\mathrm{Cos}(u))\mathrm{Cos}(\beta) \\ &+ \mathrm{Sin}(\beta)(\rho\mathrm{Cos}(\gamma)\mathrm{Sin}(u) + (1 + \mathrm{Sin}(\mathrm{f2}) \\ &- \rho\mathrm{Cos}(u)\mathrm{Sin}(\mathrm{f2}))\mathrm{Sin}(\gamma)))) \end{aligned} \tag{8.2-8}$$

$$\begin{aligned} k_{2y} = \mathrm{y}_c - \frac{1}{\rho} r(&\mathrm{Cos}(\alpha)(\mathrm{Cos}(\gamma)(-1 + (-1 + \rho\mathrm{Cos}(u))\mathrm{Sin}(\mathrm{f2})) \\ &+ \rho\mathrm{Sin}(u)\mathrm{Sin}(\gamma)) + \mathrm{Sin}(\alpha)(\mathrm{Cos}(\mathrm{f2})(-1 + \rho\mathrm{Cos}(u))\mathrm{Cos}(\beta) \\ &+ \mathrm{Sin}(\beta)(\rho\mathrm{Cos}(\gamma)\mathrm{Sin}(u) + (1 + \mathrm{Sin}(\mathrm{f2}) \\ &- \rho\mathrm{Cos}(u)\mathrm{Sin}(\mathrm{f2}))\mathrm{Sin}(\gamma)))) \end{aligned} \tag{8.2-9}$$

$$\mathrm{f}_2 = 2\mathrm{ArcTan}(a_2) \tag{8.2-10}$$

$$\begin{aligned} a_2 = \\ &\frac{(-1 + \rho\mathrm{Cos}(u))\mathrm{Cos}(\beta)\mathrm{Sin}(\gamma)}{(-1 + \rho\mathrm{Cos}(u))\mathrm{Sin}(\beta) + \mathrm{Cos}(\beta)(\rho\mathrm{Cos}(\gamma)\mathrm{Sin}(u) + \mathrm{Sin}(\gamma))} \\ &+ \frac{\sqrt{(-1 + \rho\mathrm{Cos}(u))^2\mathrm{Sin}(\beta)^2 - \rho\mathrm{Cos}(\beta)^2(\rho\mathrm{Sin}(u - \gamma) + 2\mathrm{Sin}(\gamma))\mathrm{Sin}(u + \gamma)}}{(-1 + \rho\mathrm{Cos}(u))\mathrm{Sin}(\beta) + \mathrm{Cos}(\beta)(\rho\mathrm{Cos}(\gamma)\mathrm{Sin}(u) + \mathrm{Sin}(\gamma))} \end{aligned} \tag{8.2-11}$$